PhD-FSTC-2016-23
The Faculty of Sciences, Technology and Communication

DISSERTATION

Defense held on 27/06/2016 in Esch-sur-Alzette (Luxembourg)

to obtain the degree of

DOCTEUR DE L'UNIVERSITÉ DU LUXEMBOURG

EN PHYSIQUE

by

Christian HÖNES
Born on 13th March 1987 in Hamburg, (Germany)

INFLUENCE OF INTERFACE CONDITIONING AND DOPANTS ON CD-FREE BUFFERS FOR CU(IN,GA)(S,SE)$_2$ SOLAR CELLS

Dissertation defense committee

Dr Susanne SIEBENTRITT, Dissertation Supervisor
Professor, Université du Luxembourg

Dr Ludger WIRTZ, Chairman
Professor, Université du Luxembourg

Dr Phillip DALE, Vice Chairman
Professor, Université du Luxembourg

Dr Hans-Werner SCHOCK
Professor, Helmholtz Zentrum Berlin

Dr Jürgen HACKENBERG
Robert Bosch GmbH, Stuttgart

Contents

Abstract

In the search for a non-toxic replacement of the commonly employed CdS buffer layer for Cu(In,Ga)(S,Se)$_2$ (CIGSSe) based solar cells, indium sulfide thin films, deposited via thermal evaporation, and chemical bath deposited (CBD) Zn(O,S) thin films are promising materials. However, while both materials have already been successfully utilized in highly efficient cells, solar cells with both materials usually need an ill-defined post-treatment step in order to reach maximum efficiencies, putting them at a disadvantage for mass production.
In this thesis the influence of interface conditioning and dopants on the need for post-treatments is investigated for both materials, giving new insights into the underlying mechanisms and paving the way for solar cells with higher initial efficiencies.
First, CIGSSe solar cells with In_2S_3 thin film buffer layers, deposited by thermal evaporation, are presented in Chapter 3. The distinctive improvement of these buffer layers upon annealing of the completed solar cell and the change of this annealing behavior when the CIGSSe surface is treated with wet-chemical means prior to buffer layer deposition is investigated. Additional model simulations lead to a two-part explanation for the observed effects, involving a reduction of interface recombination, and the removal of a highly p-doped CIGSSe surface layer.
Chapter 4 introduces a novel, fast process for the deposition of Zn(O,S) buffer layers on submodule sized substrates. The resulting solar cell characteristics and the effects of annealing and prolonged illumination are discussed within the framework of theoretical considerations involving an electronic barrier for generated charge carriers. The most important influences on such an electronic barrier are investigated by model simulations and an experimental approach to each parameter. This leads to an improved window layer deposition process, absorber optimization, and intentional buffer layer doping, all reducing the electronic barrier and therefore the necessity for post-treatments to some extent.
The energetic barrier discussed above may be avoided altogether by effective interface engineering. Therefore, the controlled incorporation of indium as an additional cation into CBD-Zn(O,S) buffer layers by means of a newly developed alkaline chemical bath deposition process is presented in Chapter 5. With increasing amount of incorporated indium, the energetic barrier in the conduction band can be reduced. This is quantitatively assessed by a combination of photoelectron spectroscopy measurements and the determination of the buffer layer's optical band gap. This barrier lowering leads to less distorted current–voltage characteristics and efficiencies above 14 %, comparable to CdS reference cells, without extensive light-soaking.

Publications

Parts of this thesis have already been published ...
... in scientific journals:

- C. Hönes, S. Siebentritt, "Annealing of wet treated Cu(In,Ga)(S,Se)$_2$ solar cells with an indium sulfide buffer", *Thin Solid Films*, Vol. **582** (2015), 313–316
- C. Hönes, J. Hackenberg, S.Zweigart, A. Wachau, F. Hergert, and S. Siebentritt, "A comparative study of the annealing behavior of Cu(In,Ga)(S,Se)$_2$ based solar cells with an indium sulfide buffer layer, partly submitted to wet chemical treatments", *Journal of Applied Physics*, Vol. **117** (2015), 094503
- C. Hönes, A. Fuchs, S. Zweigart, and S. Siebentritt, "Improved Chemically Deposited Zn(O,S) Buffers for Cu(In,Ga)(S,Se)$_2$ Solar Cells by Controlled Incorporation of Indium", *IEEE Journal of Photovoltaics*, Vol. **6** (2016), No. 1, 319–325

... at scientific conferences:

- C. Hönes, S. Siebentritt, "Annealing of wet treated Cu(In,Ga)(S,Se)$_2$ solar cells with an indium sulfide buffer" (poster), EMRS 2014, Lille, France, May 2014
- C. Hönes, A. Fuchs, S. Zweigart, and S. Siebentritt, "Reducing the Necessity of Light Soaking by Controlled Incorporation of Indium into Chemically Deposited Zn(O,S) Buffer Layers for Cu(In,Ga)(S,Se)$_2$ Solar Cells" (talk), EU PVSEC, Hamburg, Germany, September 2015

Chapter 1

1 Introduction

At the time of writing this thesis, there is a broad consensus in the scientific community regarding the causal relation of CO_2 emissions into the atmosphere and rising temperatures in the last century. Most political leaders of the world's largest industries have acknowledged this fact and measures to reduce emissions of CO_2 and other greenhouse gases are under discussion or already implemented. The core problem, however, is that the emission of CO_2 is closely linked to the world's power consumption, as carbon based (fossil) fuels are with ~80 % still by far the largest energy source utilized around the world [1]. While the attempt to reduce the absolute power consumption, thereby reducing emission of CO_2, is certainly laudable in its purpose, there is another fundamental relation undermining these attempts: the production of every good is accompanied by power consumption. In the end a significant reduction of power consumption can only be achieved by a reduction of production, which essentially means a reduction of wealth. Thus, while there is a notable reduction of power consumption in Germany [2], even a constant wealth implies an increase of externalization of power consumption to other countries. In contrast to stagnating western industrial nations, emerging nations all over the world will inevitably increase their direct or indirect power consumption as they strive to increase the wealth of their people by an increase of available goods.
The more sensible solution is therefore to break the link between power generation and CO_2 emission, by employing nuclear fission/fusion and the so-called 'renewable energies' (hydropower, biomass, wind power, solar energy, geothermal energy). Nuclear power generation is staying almost constant in the last years, the renewable energies on the other hand have grown significantly [1]. While the direct burning of fossil fuels has the advantage of providing power directly where it is needed (heating, driving a motor, generation of electricity in remote areas), most renewable power sources rely on the generation and transfer of electric power. A most prominent example, where this is not the case is distributed solar power generation (thermal energy or electricity). This, while fundamentally disrupting the business models of existing large utilities, certainly adds to the appeal of solar energy for the customer, which (apart from subsidies) is probably one major reason for the significant growth of this renewable energy source in the last ten years.

1.1 Motivation for this thesis

The question of rapid growth of solar power generation is mainly a question of the price. Although electricity produced with photovoltaic systems reached grid-parity in a number of states in the last years [3], the key to further growth of this renewable energy source without relying on markets with high subsidies remains lowering production costs while raising the module efficiency. While crystalline and multicrystalline silicon are the dominant materials for solar cell production, competing thin-film technologies, especially the materials CdTe and $Cu(In,Ga)(S,Se)_2$ (CIGSSe), offer an alternative, combining the possibility for large scale production (lowering the cost) with high efficiencies. The latest record efficiency for a $Cu(In,Ga)(S,Se)_2$ based solar cell was certified with 22.3 % [4], surpassing multicrystalline silicon cells, albeit on a smaller cell size. This high potential for CIGSSe based technology is the reason for the research efforts that were undertaken by the Robert Bosch GmbH and its subsidiary Bosch Solar CISTech GmbH.
A CIGSSe solar cell is relying on efficient interplay of several semiconducting thin films, realizing a p–n heterojunction solar cell. One of these thin films is the so-called buffer layer, an n-type layer between the p-type CIGSSe absorber and the highly n-doped window layer. This layer should improve the band alignment between absorber and window layer, reduce interface defects, and in the best case pin the Fermi level close to the conduction band at the very CIGSSe surface, reducing interface recombination and increasing the open circuit voltage. A material, that seems to satisfy these requirements and is therefore utilized in most high efficient CIGSSe based solar cells is chemically deposited CdS. CdS was consequently also the buffer layer material in the CISTech baseline process. CdS is, however, not perfect as a buffer layer material. In terms of maximum efficiencies, the bandgap energy of CdS is with 2.4 eV too small and the number of photons transmitted to the CIGSSe absorber is reduced by absorption in the buffer layer. Recent developments reduce this loss by utilizing thinner CdS layers [5], but generally a material with higher band gap energy would be desirable. The second problem of utilizing CdS is the toxicity of elemental Cd but also of most Cd containing compounds, Cd containing compounds are also classified as carcinogenic. This will lead to an eventual ban of CdS in solar cell manufacture in Europe, when there is a possible non-toxic replacement. Such replacements were already presented in large scale manufacture with Zn(O,S) by Solar Frontier K.K. in Japan and with In_2S_3 by the Avancis GmbH in Germany. There are, however, several problems, occurring when these Cd-free buffer layers are employed, some of which will be discussed in this work. The economic pressure combined with the need for a deeper understanding of effects, that are still under scientific debate, is the outset for this dissertation work in cooperation of the Corporate Research of the Robert Bosch GmbH and the Laboratory for Photovoltaics at the University of Luxembourg. The aim of this work is to provide new insights into the particularities of CIGSSe based solar cells with Cd-free

buffers, and provide a guideline how to use these insights for the advance of Cd-free manufacturing processes.
My hope is, that the results of this work will provide an additional impulse towards a non-toxic future of thin-film photovoltaics.

1.2 Structure of this thesis

The structure of this theses is due to its nature as dissertation work in the industry. It is basically divided into two parts, where the first is concerned with the description of In_2S_3 based buffer layers (Chapter 3) and the second is concerned with the description of Zn(O,S) based buffer layers (Chapters 4 and 5). At the beginning of my work both material systems were under research at the Robert Bosch GmbH and I started out with focus on the In_2S_3 system and the influence of wet-chemical treatments on the interface to the CIGSSe absorber. However, it was decided to discontinue the work on In_2S_3, urging me to switch the focus towards Zn(O,S) and leave some of the questions, that arise in the first part of this work unanswered. As my work on In_2S_3 based buffer layers is nevertheless a substantial part of this dissertation work as a whole, it is included into this thesis. While the cells with In_2S_3 buffer layer show an intriguing behavior when heat is applied, the cells with Zn(O,S) buffer layer show a very pronounced alteration of current-voltage characteristics under illumination. Although these effects are different in nature, the key to eliminate both is the alteration of the interfaces to the absorber and the window layer. The attempt to understand the influence of the two interfaces to the buffer layer and to alter the relevant parameters experimentally is the frame of this dissertation work.
Chapter 4 is devoted to the description of a new chemical deposition process for Zn(O,S) buffer layer, that was developed at the Robert Bosch GmbH. The resulting cells show a large light-soaking effect and the influence of absorber composition, window layer deposition, and the possibility of additional n-type doping of the buffer layer are examined both in simulation and experiment.
Chapter 5, finally presents a newly developed process for the deposition of ZnInOS buffer layers, by controlled incorporation of indium into a chemical bath deposition process for Zn(O,S). The aim is to reduce the necessity of light-soaking by lowering the positive conduction band offset at the CIGSSe/Zn(O,S) interface. As a result, solar cells with ZnInOS buffer are presented, that show only a negligible effect of light-soaking.
Additional information on theoretical and technological background of this thesis is given in Chapter 2, while each of the main chapters will contain its own literature survey. Some information, such as simulation parameters is not included in the main body of the text, but can be found in the appendix.
Concluding this work, a summary of all results can be found in Chapter 6.

I encourage the reader to use the digital version of this work because of my extensive use of cross-referencing in the main body of the text. I also took care to

insert hyper-references for every citation (using digital object identifiers, where possible), which will hopefully facilitate access to the cited literature.

References

[1] World Energy Council, *Energy Resources*, https://www.worldenergy.org/data/resources/ (visited on 03/29/2016) (Cited on page 1).

[2] Umweltbundesamt der Bundesrepublik Deutschland, *Entwicklung des Energieverbrauchs*, http://www.umweltbundesamt.de/daten/ (visited on 03/29/2016) (Cited on page 1).

[3] Deutsche Bank - Markets Research, *2014 Outlook: Let the Second Gold Rush Begin*, Jan. 2014, https://www.deutschebank.nl/nl/docs/Solar_-_2014_Outlook_Let_the_Second_Gold_Rush_Begin.pdf (visited on 03/29/2016) (Cited on page 2).

[4] Solar Frontier K.K., *Solar Frontier Achieves World Record Thin-Film Solar Cell Efficiency: 22.3%*, online press release, Dec. 2015, http://www.solar-frontier.com/eng/news/2015/C051171.html (visited on 03/15/2016) (Cited on page 2).

[5] A. Chirilă, P. Reinhard, F. Pianezzi, P. Bloesch, A. R. Uhl, C. Fella, L. Kranz, D. Keller, C. Gretener, H. Hagendorfer, D. Jaeger, R. Erni, S. Nishiwaki, S. Buecheler, and A. N. Tiwari, "Potassium-induced surface modification of Cu(In,Ga)Se_2 thin films for high-efficiency solar cells", Nature Materials Letter **12**, 1107–1111 (2013) (Cited on page 2).

Chapter 2

2 Background

From basic semiconductor physics to measurement methods, the most important background of Cu(In,Ga)(S,Se)$_2$ based solar cells in the context of this work is covered in this chapter. Most of the content presented here can be found in the relevant literature (e.g. [6–9]) and is considered common knowledge. As this introductory chapter is meant to provide the basis for the discussion of the results in Chapters 3 to 5, it is covered nonetheless, albeit with less detail compared to standard textbooks.

2.1 Semiconductor basics

Generally, the Fermi-Dirac distribution describes the probability of the population of electronic states in solids. These states are forming energy bands, which are not covering the whole energy space. In semiconductors, the edge of the Fermi-Dirac distribution, the Fermi level E_F, is lying in the gap between two energy bands, which are denoted as 'conduction band' and 'valence band'. At room temperature, there are mobile electrons in the conduction band and as a counterpart mobile holes in the valence band. When the Fermi level is not too close to either of the bands, Boltzmann statistics apply and the concentration of electrons n and the concentration of holes p are

$$n = N_{CB} \exp\left(-\frac{E_{CB} - E_F}{k_B T}\right) \quad \text{and} \quad p = N_{VB} \exp\left(-\frac{E_F - E_{VB}}{k_B T}\right), \tag{2.1}$$

where N_{CB} and N_{VB} are the temperature dependent effective densities of state in the conduction band and valence band. E_{CB} and E_{VB} are the positions of the conduction band minimum and the valence band maximum, k_B is the Boltzmann constant and T is the temperature.
In the intrinsic case, that is, when $n = p$, the position of the Fermi Level can be calculated from Eq. (2.1) to be slightly off from the middle of the band gap:

$$E_F = E_i = \frac{E_{CB} + E_{VB}}{2} + \frac{k_B T}{2} \ln\left(\frac{N_{VB}}{N_{CB}}\right) \tag{2.2}$$

From Eq. (2.1) it also follows for the carrier concentration in the intrisic case:

$$pn = n_i^2 = N_{CB} N_{VB} \exp\left(-\frac{E_g}{k_B T}\right). \tag{2.3}$$

In the case of shallow n-type doping, when the donors with density N_D are almost completely ionized at room temperature, the electron and hole densities are approaching

$$n \approx N_D \qquad p = \frac{n_i^2}{n} \approx \frac{n_i^2}{N_D} \qquad E_F \approx E_C - k_B T \ln\left(\frac{N_{VB}}{N_D}\right), \tag{2.4}$$

and vice versa in the case of p-type doping with an acceptor density N_A. The Fermi level is approaching the respective band according to the new distribution of charges with $n \neq p$. In case of non-degenerate doping Eq. (2.3) still holds in equilibrium without generation or external supply of charge carriers.
External supply of electrons to the conduction band or holes to the valence band (e.g. by generation from absorbed photons, or by applying a voltage) leads to an alteration of their energetic distribution. Even if they are supplied with excess energy, thermalization quickly leads to the formation of two separate Fermi-Dirac distributions, one for the holes, and one for the electrons. The densities n and p are then calculated as

$$n = N_{CB} \exp\left(-\frac{E_C - E_{F,e}}{k_B T}\right) \qquad p = N_{VB} \exp\left(-\frac{E_{F,h} - E_V}{k_B T}\right), \tag{2.5}$$

where $E_{F,e}$ and $E_{F,h}$ are the quasi Fermi levels for electrons and holes respectively. The product np is now necessarily larger than the squared intrinsic density:

$$np = n_i^2 \exp\left(\frac{E_{F,e} - E_{F,h}}{k_B T}\right) \tag{2.6}$$

When the equilibrium $np = n_i^2$ is disturbed, recombination (and thermal generation) processes occur, restoring this equilibrium. Recombination of electron-hole pairs in a semiconductor can be separated into the two groups of radiative and non-radiative recombination.
For radiative recombination, the recombination rate R_r is given by

$$R_r = r_r np = \frac{G_{th}}{n_i^2} np \quad , \tag{2.7}$$

where the radiative recombination coefficient r_r is connected to the thermal generation rate G_{th} such that there is no net recombination in the case of equilibrium $np = n_i^2$. If $np \neq n_i^2$, for a small surplus of holes Δp (low excitation) in an n-type material, the net recombination rate results in

$$R_{net} = R_r - G_{th} = r_r \left(np - n_i^2\right) \approx r_r N_D \Delta p = \frac{\Delta p}{\tau_p}, \tag{2.8}$$

where the hole lifetime is $\tau_p = 1/(r_r N_D)$. The calculation for p-type doping can be done accordingly. The result is a recombination rate that is solely dependent on the excess minority carrier concentration.

Non-radiative recombination via recombination centers at the single energy E_t in the band gap is described by Shockley-Read-Hall statistics, resulting in a net recombination rate R_t of

$$R_t = \frac{(np - n_i^2)}{\tau_n \left(n + n_i \exp\left(\frac{E_t - E_i}{k_B T}\right)\right) + \tau_p \left(p + n_i \exp\left(\frac{E_i - E_t}{k_B T}\right)\right)} \tag{2.9}$$

This rate is at its maximum, when $E_t = E_i$. The lifetimes are defined here for low injection as $\tau_{n/p} = 1/\left(\sigma_{n/p} v_{th,n/p} N_t\right)$, where σ is the capture cross section, v_{th} is the thermal velocity and N_t is the density of recombination centers. Again, with doping, this leads to recombination rates proportional only to the excess minority carrier concentration.

2.1.1 *The p–n junction*

The junction of n-doped and p-doped materials are of special importance for the discussion of semiconductor devices. While the general heterojunction case allows for different band gaps with varying band offsets at the junction, most of the physics can be discussed for the p–n homojunction, assuming the same material on the p-doped and n-doped side of the junction.

At the junction, a depletion region is forming on both sides, the initial driving force for the exchange of charge carriers is the concentration gradient. The ionized dopants within the depletion region lead to a space charge, the depletion region is therefore also called 'space charge region' (SCR). In electrochemical equilibrium, the electric field on both sides far from the depletion region vanishes, the width of the space charge regions $W_{D,p/n}$ on both sides of the junction must fulfill the relation

$$N_A W_{D,p} = N_D W_{D,n} \quad \Rightarrow \quad \frac{W_{D,p}}{W_{D,n}} = \frac{N_D}{N_A} \tag{2.10}$$

As a result, with asymmetric doping, the space charge width in the n-doped region is different from the space charge region in the p-doped region. In the depletion approximation, it is assumed that the depletion region is characterized by abrupt transitions from no to maximum space charge. This is displayed in Fig. 2.1. As a consequence, the electric field is increasing linearly from both sides to a maximum at the junction. The electrical potential is parabolic on both sides, joining at the junction. This leads to the band diagram displayed in the lower part of Fig. 2.1, where the built-in potential of the p–n junction is the result of integrating over the electric field, and denoted here as V_{bi}.

In the case of a one-sided junction with $N_D \gg N_A$, the depletion width $W_{D,p}$ can be approximated by

$$W_{D,p} = \sqrt{\frac{2\epsilon(V_{bi} - V)}{eN_A}}, \tag{2.11}$$

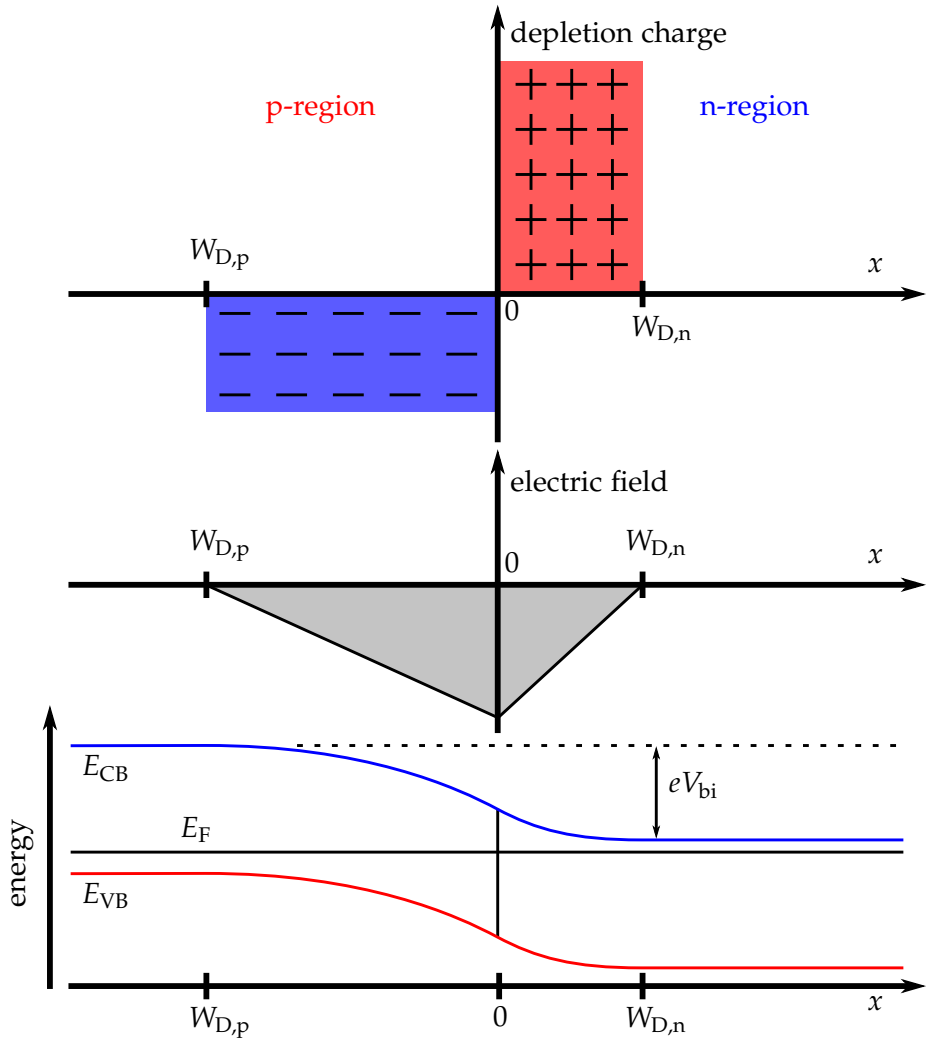

Figure 2.1: Schematic picture of space charge, electric field and band energies for a p–n junction within the depletion approximation.

where $\epsilon = \epsilon_0 \epsilon_r$ is the dielectric permittivity of the semiconductor and V an externally applied voltage. Forward bias voltage therefore decreases the space charge width, negative bias voltage increases the space charge width.
Regarding non-radiative recombination within the space charge region, Eq. (2.9) still holds. Using Eq. (2.6), assuming $E_t = E_i$ and assuming similar lifetimes for electrons and holes, the net recombination rate becomes:

$$R_t = \frac{n_i^2 \left(\exp\left(\frac{eV}{k_B T}\right) - 1\right)}{\tau \left(n + p + 2n_i\right)} = \frac{n_i^2 \left(\exp\left(\frac{eV}{k_B T}\right) - 1\right)}{\tau n_i \left(\exp\left(\frac{E_{F,e} - E_i}{k_B T}\right) + \exp\left(\frac{E_i - E_{F,h}}{k_B T}\right) + 2\right)} \tag{2.12}$$

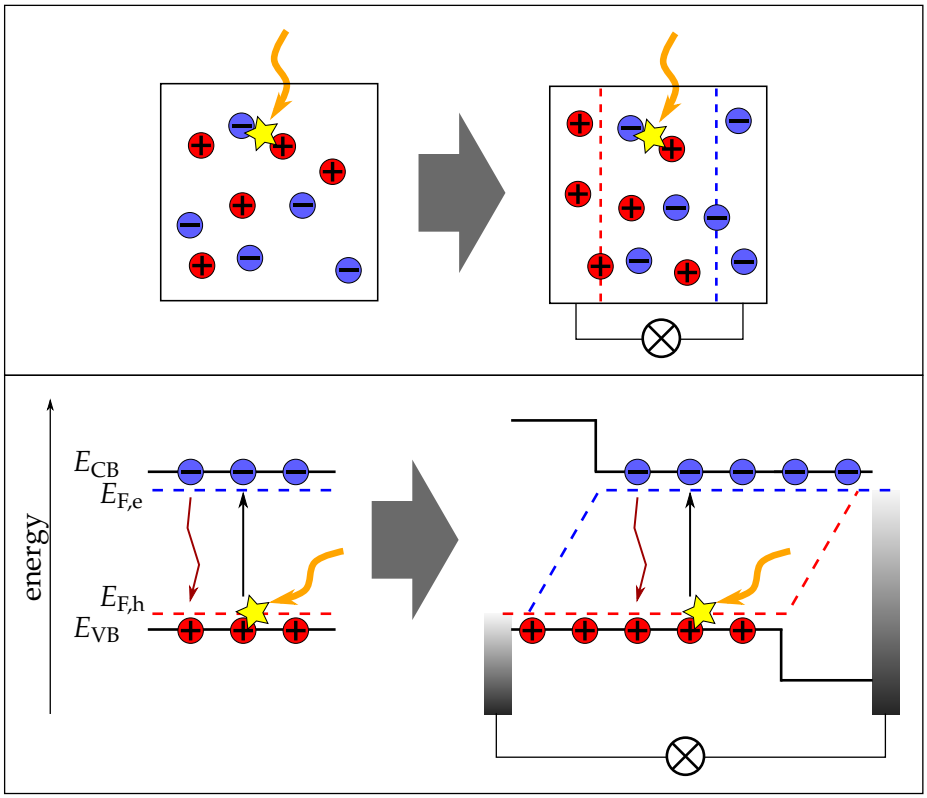

Figure 2.2: Simple picture of a solar cell as a device, where charge carriers are generated and separated (upper part) and the realization of such a concept as semiconductor heterojunction solar cell with metal contacts (lower part).

The recombination rate is maximal, when E_i is in the middle between both quasi Fermi levels, that is, where $n = p$. It can be approximated at this point as

$$R_{t,max} \approx= \frac{n_i}{2\tau} \exp\left(\frac{eV}{2k_B T}\right) \tag{2.13}$$

2.2 Solar cell principles

The physics of solar cells in general and Cu(In,Ga)(S,Se)$_2$ based thin film solar cells in particular have been described in detail in many textbooks, e.g. in [6–8]. This section will provide a brief introduction into the subject with special emphasis on the very general discussion as given by Peter Würfel in [6], while refraining from reproducing every detail.

2.2.1 Introduction to solar cells

What is a solar cell? In the context of this work, the easiest answer would be: a box, converting a flux of photons (i.e., an illumination power) into a flux of electrical charge driving a load (i.e., an electric power).

A solar cell must therefore fulfill at least two requirements: First, electrical charge carriers must be generated, second, these charge carriers must be sorted into reservoirs according to their sign, building up an electrochemical potential difference between the two reservoirs. This difference in electrochemical potential enables the solar cell to drive a load. A simple scheme is shown in the upper part of Fig. 2.2. When photons generate charge carriers, the latter will be distributed homogeneously, since the net charge is preserved, our solar cell box looks neutral from the outside. The absolute number of charge carriers is limited by recombination processes. The recombination rate can be assumed to increase with the number of carriers, in equilibrium the recombination rate equals the generation rate. Now, a mechanism to sort the charges is implemented. This mechanism can be thought of as two semipermeable membranes, letting pass only positive or negative charges. As depicted in the upper right part of Fig. 2.2, these membranes lead to a new steady-state situation, where there is a net charge of opposite signs at each side of the solar cell box. In open circuit conditions, the equilibrium density of charge carriers in between of the two membranes is still the same as before, limited by recombination processes. When the two sides of the box are connected, the maximum current is limited by the generation rate in between the membranes. In principle such a solar cell may even be generalized to the case where there is only a conversion of the photon energy to chemical energy (e.g. by splitting of water), a 'chemical solar cell' would be the result [6]. Most commonly, however, solar cells are realized with semiconductor technology. The idea of such a realization is shown in the lower part of Fig. 2.2. Photons with energy larger than the band gap energy can excite electrons from the valence band into the conduction band, in consequence, there are excess electrons in the conduction band and excess holes in the valence band. In the balance of generation and recombination, the electron and hole distributions are not described by the Fermi level any more, but by two separate quasi Fermi levels, denoted in the figure by $E_{\mathrm{F,e}}$ and $E_{\mathrm{F,h}}$. In order to realize the sorting of electrons to one side and holes to the other side, differently doped semiconductors can be used. In a heterojunction solar cell, where different materials lead to band offsets, the picture is displayed in the lower right part of Fig. 2.2. The p-type semiconductor on the one side and the n-type semiconductor on the other side are the realization of semipermeable membranes, effectively lowering the density of holes (electrons) on right (left) side, thereby limiting the recombination processes to the center region.

To describe the actual current of charge carriers in a solar cell, two special cases can be considered separately first. When the charge carriers are uniformly distributed (i.e. there is no concentration gradient), the current is solely dependent on the electric field, 'pulling' at the charge:

$$\text{field current:} \qquad J_{\mathrm{field},i} = \sigma_i \mathcal{E} = -\frac{\sigma_i}{e} \mathrm{grad}\,(e\phi)\,, \tag{2.14}$$

where σ_i is the electrical conductivity, dependent on the charge carrier type i, $\mathcal{E}$ is the electric field strength, e is the elementary charge, and ϕ is the electrostatic

potential.
In the second special case, the electrostatic potential is constant, and the current is solely the result of a gradient of the concentration n, or more generally a gradient of the chemical potential μ:

$$\text{diffusion current:} \qquad J_{\text{diffusion},i} = -\frac{\sigma_i}{z_i e}\text{grad}\left(\mu_i\right), \tag{2.15}$$

where z_i is the sign of the charge of carrier type i and μ_i is the chemical potential of carrier type i.
In the general case, both driving forces on the current have to be added, driving the total current:

$$\begin{aligned}\text{total current:} \qquad J_i &= -\frac{\sigma_i}{z_i e}\left(\text{grad}\left(\mu_i\right) + \text{grad}\left(z_i e\phi\right)\right) \\ &= -\frac{\sigma_i}{z_i e}\text{grad}\left(\mu_i + z_i e\phi\right) \\ &= -\frac{\sigma_i}{z_i e}\text{grad}\left(\eta_i\right),\end{aligned} \tag{2.16}$$

where $\eta_i = \mu_i + z_i e\phi$ is the electrochemical potential. It is essential, that the total current is not derived from an addition of currents, which would each lead to energy dissipation, but from an addition of driving forces. The electrochemical potentials for electrons and holes can be identified in the semiconductor solar cell as the quasi Fermi levels with $\eta_\text{e} = E_\text{F,e}$ and $\eta_\text{h} = -E_\text{F,h}$, taking into account the reverse sign of the energy for the holes compared to the electrons.

In order to derive the principle dependence of current and voltage, the continuity equation in steady state

$$\text{div}J = e\left(G - R\right), \tag{2.17}$$

where G is the generation rate and R is the recombination rate, is integrated over the region, where generation and recombination take place. In thermal equilibrium without illumination, the generation and recombination rate are equal, i.e. $G_0 = R_0$. The illumination adds a generation rate of ΔG and it can be generally assumed that the recombination rate will be proportional to the product of electron and hole densities and thereby proportional to $\exp\left(\left(\eta_\text{e} + \eta_\text{h}\right)/k_\text{B}T\right) = \exp\left(\left(E_\text{F,e} - E_\text{F,h}\right)/k_\text{B}T\right)$. Equation (2.17) is therefore rewritten

$$\text{div}J = e\left(R_0 + \Delta G - R_0 \exp\left(\left(E_\text{F,e} - E_\text{F,h}\right)/k_\text{B}T\right)\right) \tag{2.18}$$

The integral over ΔG is identified as the short circuit current J_sc, and for small resistance to the electrical transport, the sum $\eta_\text{e} + \eta_\text{h} = E_\text{F,e} - E_\text{F,h}$ is approximately constant and can be identified with eV, where V is the voltage between the metal contacts. The integral of Eq. (2.18) can therefore be written in the form

$$J = J_0\left(\exp\left(\frac{eV}{k_\text{B}T}\right) - 1\right) - J_\text{sc}. \tag{2.19}$$

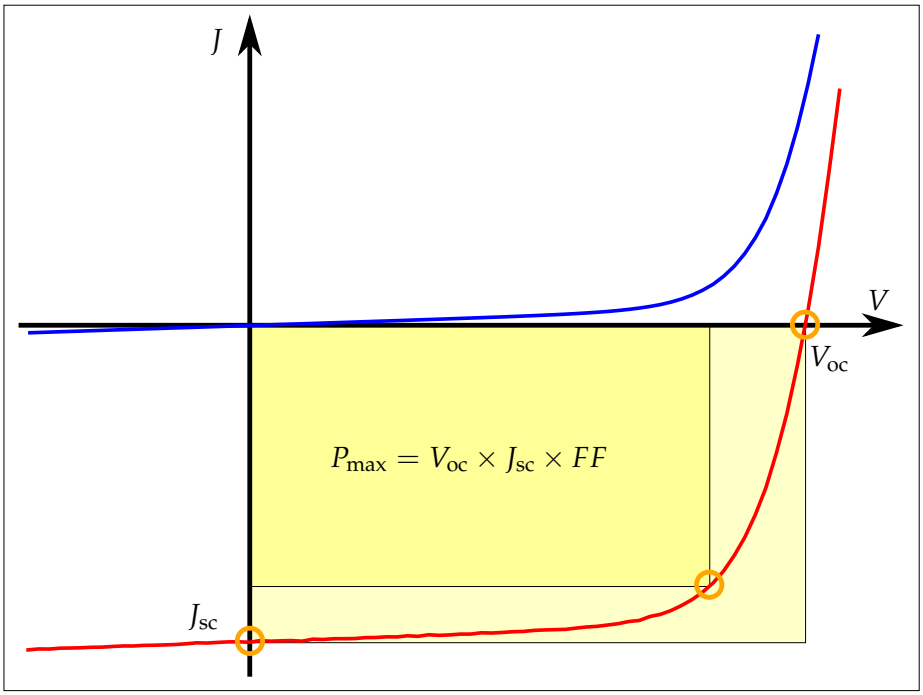

Figure 2.3: Typical JV curve for a solar cell in the dark (blue line) and under illumination (red line). The yellow rectangle indicates the maximum electrical power, that can be generated.

The reverse saturation current J_0 incorporates the recombination processes and the short circuit current density J_{sc} incorporates the integration over the generation profile. The result is a JV curve similar to the one in Fig. 2.3. A voltage dependent measurement of the current density under illumination allows for the extraction of the three parameters, determining the solar cell efficiency: short circuit current density J_{sc}, open circuit voltage V_{oc} and fill factor FF. Since it is the total current I, which is actually measured, the term IV curve will be used in the following, where the current density J is typically calculated with a known sample area. J_{sc} and V_{oc} are determined by examining where the IV curve crosses the current axis or the voltage axis. The fill factor is found by first calculating the maximum power per area from the IV curve and then calculating the quotient $FF = P_{max}/(V_{oc} \times J_{sc})$. Ideally the fill factor would be unity, which is not possible because of the non vanishing J_0. The solar cell efficiency is given by the quotient of the maximum electrical power and the power of the incoming photons $\eta = P_{max}/P_{illumination}$. The efficiency is dependent on the match of the solar cell absorption to the illumination spectrum and may be also dependent on the intensity of illumination. For better comparability solar cell efficiencies are therefore usually calculated from measurements under simulated AM1.5 global illumination ($100\,mW\,cm^{-2}$).
The maximum efficiency of a solar cell is linked to the fraction of photons from illumination spectrum, that can be converted into free charge carriers. In the case of a solar cell, built from a semiconductor material with a single band gap E_g, this fraction would be maximal at E_g approaching 0. The maximum open

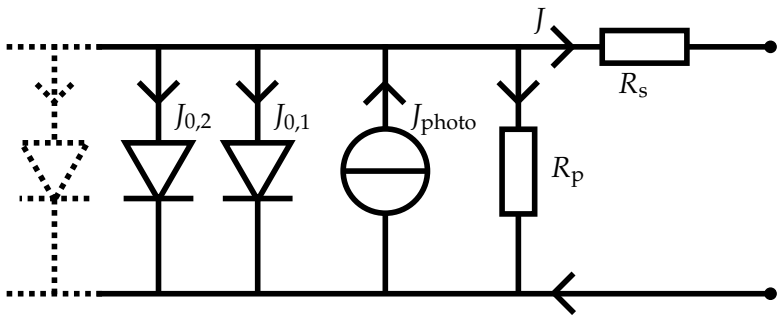

Figure 2.4: Graphical representation of the diode model of a solar cell, according to Eq. (2.20).

circuit voltage on the other hand has its upper limit at E_g. In consequence, the optimum band for such a solar cell is a compromise between maximum current and maximum voltage. A calculation by Shockley and Queisser, limited to radiative recombination in an ideal p–n junction solar cell for 6000 K black body radiation leads to the famous efficiency limit at ~30 % [10]. Adaptation for the AM1.5 spectrum shows that besides some small local maxima, there is a broad maximum for band gaps in the region between 1.1 eV and 1.5 eV. This maximum is shifted to higher band gap energies, when radiative recombination is replaced by dominant non-radiative recombination in the space charge region [8].

2.2.2 *Modeling solar cell IV curves*

While Eq. (2.19) gives a rough picture of typical solar cell IV curves, there are several adjustments to be made in order to reliably model IV curves. First, dependent on the recombination mechanism, the exponent eV/k_BT has to be replaced by eV/Ak_BT, where A is the ideality factor. A description of different recombination mechanisms and their respective ideality factors is given in the next section. Second, in a real solar cell, series resistance to the current is non negligible. Additionally, shunting has to be accorded for, generally it is assumed to be ohmic. These adjustments lead to the equation

$$J = -\sum_i \left[J_{0,i} \left(\exp\left(\frac{e\,(V - JR_s)}{A_i k_B T} \right) - 1 \right) \right] - \frac{V - JR_s}{R_p} + J_{photo}, \tag{2.20}$$

where i denotes the recombination channel, $J_{0,i}$ is the saturation current for the recombination channel i, R_s is the ohmic series resistance, and R_p is the ohmic shunt resistance. The photocurrent is denoted as J_{photo} here as it may differ from the short circuit current J_{sc}. A graphical representation of this is given in Fig. 2.4. Depending on the number of recombination pathways included in the model, it is called the 'one diode model' or 'two diode model'. More than two pathways are usually not included, even the two diode model usually involves too many free parameters to be reliable. If one recombination channel is assumed to be dominant, the model is restricted to one diode. Equation (2.20) is an implicit definition for

the current density J. A complete IV curve can be calculated numerically, e.g. with the Newton-Raphson method for approximating roots. An implementation is given in Appendix C.1. The aim of modeling in these diode models is of course the extraction of parameters from measured IV curves.
In principle, it is possible to numerically fit the model equation to the measured data. An example of an implementation used in this work is given in Appendix C.2. It is, however, still a challenge to have a fast and reliable algorithm, capable enough to be implemented in a fabrication line. Therefore, complete curve fitting is usually only done for small sets of experiments. In fabrication, it is instead more common to monitor series and shunt resistance. The shunt resistance is easily calculated from the slope of the dark IV curve in the vicinity of $V = 0$, the series resistance can be extracted from the slope of both IV curves at large currents. It is not uncommon, that a 'series resistance' is calculated from the slope around V_{oc}. This is understandable because of the difficulty of always measuring at large currents. For the Cu(In,Ga)(S,Se)$_2$ based solar cells examined in this work, this would, however, not lead to R_s in the diode model. The slope around V_{oc} is mostly determined by the diode ideality factor and, in the case of Zn(O,S) buffer layers, S-shape curve distortion. While it may still be of practical use to monitor this parameter, it should not be confused with an ohmic resistance, the denomination as 'series resistance' is misleading.
The S-shape distortion, mentioned above (a pronounced example can be found in Fig. 4.7), shows the limitation of the diode model in the form of Fig. 2.4. Other non-linear elements such as e.g. electronic barriers would have to be included in the model to account for the peculiarities of Cu(In,Ga)(S,Se)$_2$ solar cells, complicating it to the point of uselessness. The diode model is therefore only applied to cells with very diode-like characteristics, where an influence of these additional non-linear elements can be considered small.

A different approach is the actual modeling of the solar cell in terms of electronic properties of each layer and each interface. Numerical solving of the Poisson equation, relating charge and potential, and the continuity equations for holes and electrons, is necessary to calculate the current response on an applied voltage. A very useful tool, developed by Niemegeers, Burgelman and others is utilized in this work. This tool, named SCAPS (solar cell capacitance simulator) [11], allows for a large variety of parameters to be used in the simulation, including defects in he bulk and at the interfaces. In this work, SCAPS is mainly used to systematically examine model parameters regarding their probable importance for the experimentally observed effects. Due to the lack of sufficient analytical data, the cells shown in the following chapters are modeled mostly with parameters from the literature, such as the textbook by Scheer and Schock [8].

2.2.3 *Recombination processes in CIGSSe solar cells*

The recombination current (or diode current) in the solar cell is of crucial importance for the efficiency of the solar cell. This becomes clear, when the dependency of V_{oc} on the recombination current is examined according to Eq. (2.20) (one dominant recombination channel, infinite shunt resistance):

$$\begin{aligned} 0 &= J_{photo} - J_0 \left(\exp\left(\frac{eV_{oc}}{Ak_BT} \right) - 1 \right) \\ &\approx J_{photo} - J_0 \exp\left(\frac{eV_{oc}}{Ak_BT} \right) \\ \Leftrightarrow \qquad V_{oc} &\approx \frac{Ak_BT}{e} \ln\left(\frac{J_{photo}}{J_0} \right). \end{aligned} \tag{2.21}$$

The relation $V_{oc} \gg \frac{Ak_BT}{e} < 75\,\mathrm{mV}$ (for $A < 3$) is used here to simplify the equation. A large J_0 is leading to a small open circuit voltage. In order to examine the temperature dependence of the open circuit voltage, it is assumed that the saturation current J_0 is thermally activated with an activation energy u_a:

$$J_0 = J_\infty \exp\left(-\frac{u_a}{k_BT} \right), \tag{2.22}$$

where $J_\infty = J_0(T = \infty)$ is assumed to be independent of temperature. Using this relation in Eq. (2.21) results in

$$V_{oc} \approx \frac{Au_a}{e} - \frac{Ak_BT}{e} \ln\left(\frac{J_\infty}{J_{photo}} \right) = \frac{U_a}{e} - \frac{Ak_BT}{e} \ln\left(\frac{J_\infty}{J_{photo}} \right). \tag{2.23}$$

An extrapolation of V_{oc} to $T = 0$ therefore leads to the energy U_a, which is related to the activation energy of the recombination process by $U_a = Au_a$.

As mentioned before, different recombination processes lead to different ideality factors A. In the CIGSSe solar cell, due to the large band gaps of buffer layer and window layer, the large majority of photons will be absorbed in the CIGSSe absorber. A discussion of the recombination processes can therefore be limited to recombination in the CIGSSe absorber and at its interfaces. Also, due to the large number of defects present in the CIGSSe absorber, radiative recombination and Auger recombination are not of importance and therefore not discussed here. Figure 2.5 depicts a schematic CIGSSe band diagram with the four most relevant recombination channels indicated. 1: recombination at the back contact, 2: recombination in the quasi neutral region (QNR), 3: recombination in the space charge region (SCR), and 4: recombination at the interface with the buffer layer. A brief summary of the basic characteristics of each recombination channel, as found in standard textbooks [7–9], is given below:

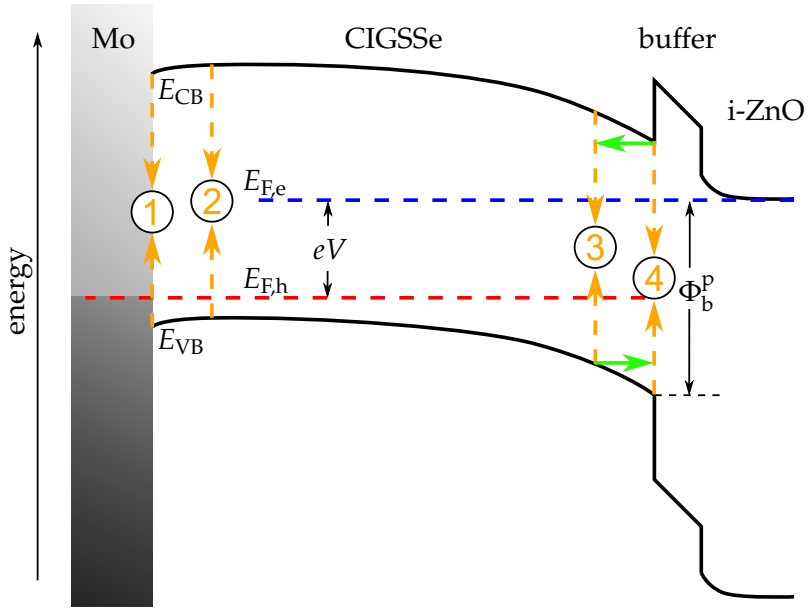

Figure 2.5: The four most prominent recombination processes in CIGSSe solar cells (adapted from [7]). 1: back surface recombination. 2: recombination in the quasi neutral region. 3: recombination in the space charge region. 4: interface recombination. Green arrows indicate a tunneling contribution, relevant only when large electric fields are present.

RECOMBINATION AT THE BACK CONTACT: Recombination of electrons at the back contact may become dominant, when there is still considerable generation near or diffusion to the back contact, that is, when the CIGSSe absorber thickness is comparable to or smaller than the light penetration depth or the electron diffusion length. Generally, an increased Ga concentration towards the back contact reduces the absorption of photons in this region and provides a 'back surface field', leading to a decrease of the electron concentration near the surface, thereby reducing the recombination rate. Therefore, back surface recombination is usually not dominant in CIGSSe solar cells, if they are thick enough. It is possible to account for a finite surface recombination velocity in J_∞ for the QNR recombination [7].

QNR RECOMBINATION: The diode current in the quasi neutral region of the CIGSSe absorber follows the Shockley diode equation for a single sided junction. The ideality factor is therefore $A = 1$ and the activation energy of the saturation current is the band gap $u_a = E_g$.

SCR RECOMBINATION: In CIGSSe solar cells, the SCR width is comparable to the absorber thickness, SCR recombination does therefore contribute considerably to the total diode current. The recombination in the SCR is maximal, at the point where the densities of holes and electrons are equal, $n = p$. For a single mid-gap defect, the ideality factor results in $A = 2$ and the activation energy of the saturation current is $u_a = E_g/2$. For an exponential trap distribution $n_t(E) = n_{t,0} \exp(-E/k_B T^*)$ with the characteristic energy $k_B T^*$, the ideality factor

and activation energy calculate as

$$\frac{1}{A} = \frac{1}{2}\left(1 + \frac{T}{T^*}\right), \qquad u_a = \frac{E_g}{A}. \tag{2.24}$$

A is therefore always smaller than 2, for values of $k_B T^*$ in the range of 100 meV to 150 meV, ideality factors of 1.6 to 1.7 would be the result [7]. In Cu(In,Ga)(S,Se)$_2$, however, values of $k_B T^*$ are reported to be in the range of $k_B T = 0.25$ meV [8]. A single defect, which is not located at mid-gap, would have a similar effect of lowering the ideality factor.

INTERFACE RECOMBINATION: In the case of an inverted interface due to the n+ doping of the window layer, it is the hole concentration, that limits the recombination process at the absorber/buffer interface:

$$J_{0,if} = e \times S_h \times p|_{if} = e \times S_p \times N_{VB} \exp\left(-\frac{\Phi_b^p - eV}{k_B T}\right), \tag{2.25}$$

with the surface recombination velocity of S_p and the density of holes at the interface $p|_{if}$. When the voltage drop over p- and n-side of the junction is assumed to be linearly divided the voltage dependent barrier to the interface recombination can be written as $\Phi_{b,0}^p + \alpha V$, leading to a diode law with activation energy and ideality factor of [7]:

$$A = \frac{1}{1-\alpha} \quad , \qquad u_a = \Phi_{b,0}^p \tag{2.26}$$

The following cases can be considered:

- $N_A \ll N_D$ at the junction: $\alpha = 0$, $A = 1$
- $N_A \sim N_D$ at the junction: $\alpha = 0.5$, $A = 2$
- $N_A \gg N_D$ at the junction: $\alpha = 0$, $A \to \infty$

TUNNELLING ENHANCED RECOMBINATION: According to Nadenau et al. [12] the ideality factors for recombination in the space charge region and interface recombination change in the presence of tunneling processes as:

$$\frac{1}{A_{SCR}} = \frac{1}{2}\left(1 + \frac{T}{T^*} - \frac{U_{00}^2}{3(k_B T)^2}\right), \quad A_{IF} = \frac{U_{00}}{k_B T}\coth\left(\frac{U_{00}}{k_B T}\right), \tag{2.27}$$

where U_{00} is the tunneling energy

$$U_{00} = \frac{e\hbar}{2}\sqrt{\frac{N_A}{m^* \epsilon}} \quad , \tag{2.28}$$

with the effective tunneling mass m^*, and the absorber's dielectric constant ϵ.

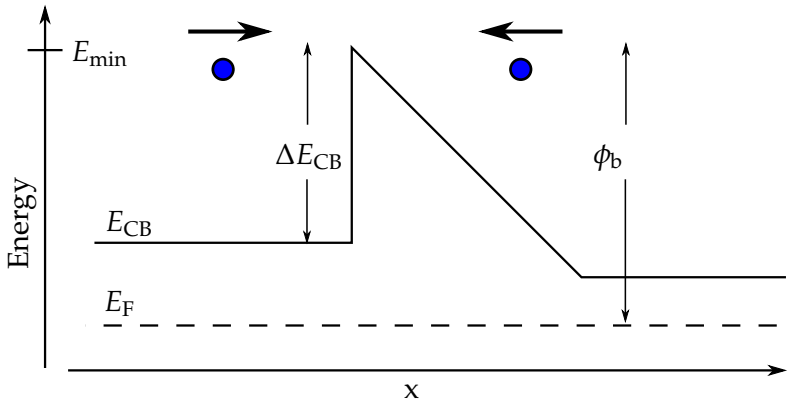

Figure 2.6: Charge transport via thermionic emission over an electronic barrier in the conduction band.

2.2.4 *Charge transport at an electronic barrier via thermionic emission*

In this work, a basic understanding of the transport of electrons across an energetic barrier at the absorber/buffer/window interfaces will be of fundamental importance for the interpretation of the presented experiments. A brief introduction is therefore given here, where a more detailed description can be found e.g. in [9] and with application to thin film solar cells in [8].
In general two fundamental processes govern the charge transport across an energetic barrier, tunneling and thermionic emission. Tunneling is a quantum mechanical effect, where charge carriers are transferred with a certain probability through rather then over the barrier. A tunnel current is only weekly temperature dependent, but largely influenced by the width of the barrier. When the barrier width is in the range of tens of nanometers or larger, the contribution to the net current is therefore nonnegligible only at low temperatures and high voltages.
Charge transport according to thermionic emission theory on the other hand is dependent on the charge carrier density at the barrier's maximum energy and therefore temperature and barrier height are the most important factors. Figure 2.6 depicts the case of a conduction band offset ΔE_{CB}, constituting the electronic barrier. Only electrons with energy larger than E_{min}, the barriers maximum energy, can transfer across the barrier. This results in a thermionic emission current $J_{te,0}$:

$$J_{te,0} = \int_{E_{min}}^{\infty} e v_x \mathrm{d}n = A^* T^2 \exp\left(-\frac{\phi_b}{k_B T}\right) \tag{2.29}$$

where v_x is the electron velocity component perpendicular to the barrier and e is the elementary charge. $\phi_b = E_{min} - E_F$ is the barrier height, where it is important to note that the barrier is not given by the conduction band offset but by the maximum distance of conduction band and Fermi energy. A^* is the effective Richardson constant and can be calculated [9] in dependence of the effective electron mass m^* as

$$A^* = \frac{4\pi e m^* k_B^2}{h^3} \tag{2.30}$$

In another approach the Maxwallian thermal particle flux to a wall with an average thermal velocity v_{th} yields a current J_{wall} of

$$J_{\mathrm{wall}} = \frac{1}{4} n e v_{\mathrm{th}} \tag{2.31}$$

With the assumption that only electrons with energy greater than the maximum conduction band energy can pass the barrier, n becomes

$$n = N_{\mathrm{CB}} \exp\left(-\frac{\phi_{\mathrm{b}}}{k_{\mathrm{B}} T}\right) \tag{2.32}$$

where N_{CB} is the effective density of states in the conduction band. This leads to a thermionic emission current of

$$J_{\mathrm{te},0} = \frac{1}{4} e v_{\mathrm{th}} N_{\mathrm{CB}} \exp\left(-\frac{\phi_b}{k_{\mathrm{B}} T}\right). \tag{2.33}$$

The square temperature dependence outside the exponential part is still preserved through the temperature dependence of v_{th} and N_{CB}.
As was pointed out e.g. in [13], for a measured short circuit current J_{sc} the maximum barrier allowing this current to be transported can then be calculated as

$$\phi_{\mathrm{max}} \approx k_{\mathrm{B}} T \ln\left(\frac{N_{\mathrm{CB}} e v_{\mathrm{th}}}{4 J_{\mathrm{sc}}}\right) \tag{2.34}$$

Concluding this excursion, an energetic barrier in the conduction band can severely limit the electron current, exponentially with the barrier height $\phi_{\mathrm{b}} = \Delta E_{\mathrm{CB}} + (E_{\mathrm{CB}} - E_{\mathrm{F}})$. Such a barrier can be reduced by choosing materials with smaller conduction band offset or by increasing the number of free charge carriers at the barrier, decreasing the distance between Fermi level and conduction band minimum.

2.3 CIGSSe AS MATERIAL FOR SOLAR CELLS

Viable materials for the use in thin film solar cells should fulfill the requirement of having a direct band gap in the range of 1.1 eV to 1.5 eV. Alloys of $CuInSe_2$, $CuGaSe_2$, and $CuInS_2$ fulfill this requirement as visible in the graph displayed in Fig. 2.7. These materials belong to the family of I-III-VI_2 semiconductors and their chalcopyrite structure can be derived from the II-VI cubic zinc blende structure (ZnS), where the atoms are tetrahedrally coordinated. The II atoms are replaced by alternating I (Cu) and III (In,Ga) atoms, so that each VI (S,Se) atom has bonds with two I atoms and two III atoms and each of the I and III atoms has four bonds to VI atoms. The resulting chalcopyrite unit cell has twice the size compared to the zinc blende unit cell. The lower band gap energy of the chalcopyrites compared to their II-VI counterparts is due to the stronger p–d repulsion of the Cu 3d orbital

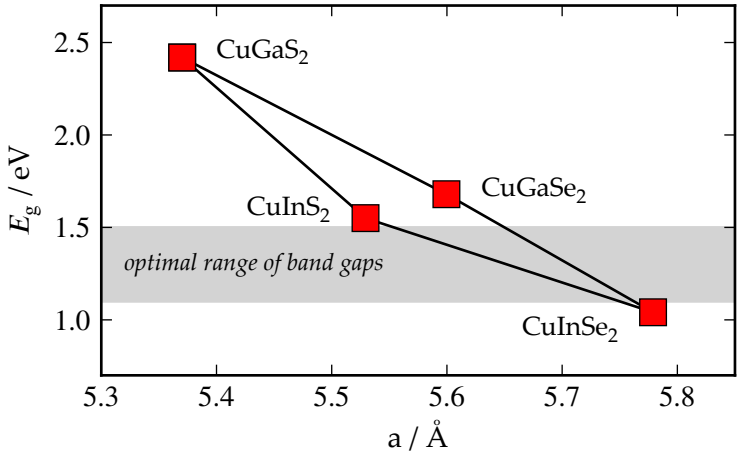

Figure 2.7: Band gap energies versus lattice constant a in the CIGSSe system. Values taken from [7].

and the anion p orbital, leading to an upshift of the valence band maximum [14]. The Cu(In,Ga)(S,Se)$_2$ system forms solid solutions with no miscibility gap, which principally makes a fine tuning of the band gap over the whole range possible and allows for elaborate band gap gradients, that are utilized to maximize record cell efficiencies [15]. The optical band gap of an alloy $A_{1-x}B_x$ is usually approximated with

$$E_g(x) = (1-x)E_g(A) + xE_g(B) - bx(1-x), \tag{2.35}$$

where b is the optical bowing parameter. Wei and Zunger [16] have calculated bowing parameters and valence band offsets ΔE_{VB} in the Cu(In,Ga)(S,Se)$_2$ system to be

$$\begin{aligned} b(\mathrm{CuInS_2}, \mathrm{CuInSe_2}) &= 0.04\,\mathrm{eV} \\ \Delta E_{VB}(\mathrm{CuInS_2}, \mathrm{CuInSe_2}) &= 0.28\,\mathrm{eV} \\ b(\mathrm{CuGaSe_2}, \mathrm{CuInSe_2}) &= 0.21\,\mathrm{eV} \\ \Delta E_{VB}(\mathrm{CuGaSe_2}, \mathrm{CuInSe_2}) &= 0.04\,\mathrm{eV} \end{aligned} \tag{2.36}$$

Experiments were published, showing bowing parameters in the range of 0.18 eV to 0.26 eV for Cu(In$_x$,Ga$_{1-x}$)Se$_2$ [17–19], and the range of values reviewed in [16] points to a negligible bowing parameter for CuIn(S$_x$,Se$_{1-x}$)$_2$.
Cu(In,Ga)(S,Se)$_2$ is grown p-type, native doping stems from Cu vacancies [20] and intentional doping is realized with alkali (mostly Na) impurities [21]. Compensating donor defects are Se vacancies and In$_{Cu}$ antisite defects [22].

2.3.1 *Band offsets at the CIGSSe/buffer interface*

While positive conduction band offsets ΔE_{CB} can be the cause for a severe limitation of the transported current as discussed in Section 2.2.4, a negative conduction band offset at the absorber/buffer interface results in a limitation of the open circuit voltage, especially in the presence of dominant interface recombination. Figure 2.8

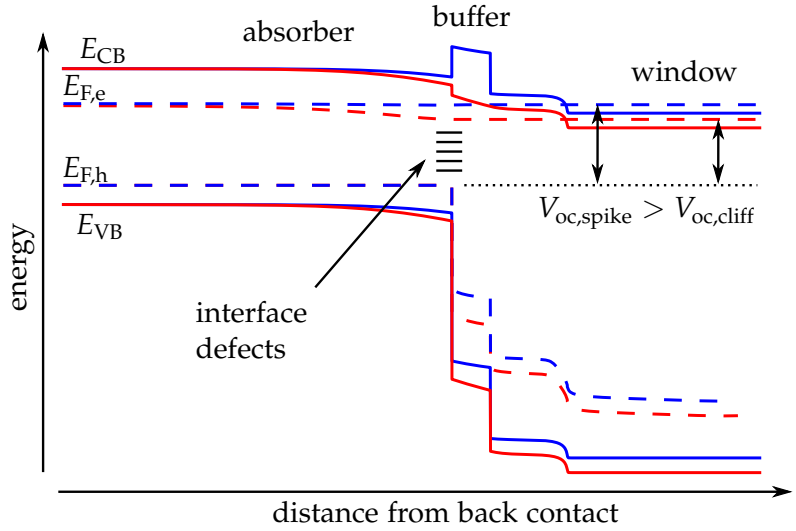

Figure 2.8: Two band diagrams under illumination in open circuit condition. The blue lines show a configuration with positive ΔE_{CB} (spike), the red lines show a configuration with negative ΔE_{CB} (cliff)

shows two band diagrams under illumination, one with positive ΔE_{CB} (spike), the other with negative ΔE_{CB} (cliff). The open circuit voltage, which is the difference between $E_{F,e}$ and $E_{F,h}$ at the right and front and back side of the cell, is visibly reduced for the cliff configuration. The reason is also visible as a gradient of $E_{F,e}$ in the absorber towards the absorber/buffer interface. Interface recombination at the interface is the dominant process limiting the open circuit voltage. It is therefore important, especially when employing wide band gap chalcopyrites, to avoid a conduction band cliff.
In [23] Andreas Klein gives a review of energy band alignments for chalcogenide solar cells. While the CIGSSe/CdS interface shows a spike configuration at low Ga content, the valence band offset ΔE_{VB} was shown to be constant ~1 eV with increasing Ga content, implying an eventual transition into the cliff configuration. For the Zn(O,S) buffer layer, the band alignment was shown to depend on the ratio [S]/([S]+[O]) of the layer. The band gaps of ZnO and ZnS are 3.2 eV and 3.6 eV respectively and the system shows significant band gap bowing with a bowing parameter of 3 eV [24]. While this large bowing allows for a tunable bandgap in the region of 2.6 eV to 3.6 eV, the valence band offset shows bowing as well. Calculations by Persson et al. [25] show an almost constant conduction band offset until [S]/([S]+[O]) $\approx$ 0.5, at which point the valence band offset stays almost constant and the conduction band offset rises with the band gap. These findings were experimentally confirmed [26, 27]. In consequence, a small positive conduction band offset at the $CuInSe_2$/Zn(O,S) interface is accompanied by the minimum band gap, which is undesirable in terms of absorption.

2.3.2 *Metastabilities in CIGSSe solar cells*

$Cu(In,Ga)(S,Se)_2$ based solar cells, are frequently reported to show metastable illumination-induced changes of the current–voltage characteristics. Light-induced metastabilities can principally be divided into two groups, one relying on the red part of the optical spectrum, the other relying on the blue part of the spectrum [28]. Red light is absorbed throughout the absorber, where an increase in net acceptor concentration is observed, which can generally be described as persistent photoconductivity [29]. When heat is applied to the solar cell or over long times of dark storage, the net acceptor concentration is reduced again, and has to be restored by illumination. Blue light on the other hand side is completely absorbed in the buffer layer and the CIGSSe region near the interface to the buffer layer. Absorption of blue light leads to a decrease of the junction capacitance, which can be explained by an increased SCR width, i.e. a reduction of the net acceptor density near the absorber/buffer interface [30].
A possible explanation for the observed effects was found by Lany and Zunger [28], who pointed out that a complex of a Se vacancy and a Cu vacancy (V_{Se}-V_{Cu}) can undergo a transition from donor to acceptor and double acceptor and vice versa, when thermal activation energy is supplied in combination with excess holes or excess electrons. Deep in the absorber, the ground state is the donor state, which explains the effect of red illumination, providing excess electrons, enabling the transition to the acceptor configuration. Near the interface to the n+ window, the Fermi level is crossing the defect levels, leading to a transition to the acceptor configuration and directly next to the inverted surface to the double acceptor configuration (p+ layer). Upon illumination with blue light, excess holes are present near the interface, leading to a partial transition of these acceptors back to the donor configuration.
Another defect leading to metastable behavior is the In_{Cu} antisite DX center. This defect, while being an intrinsic donor in $Cu(In,Ga)(S,Se)_2$ based devices, captures excess electrons near the interface, which leads to a transition into a deep neutral defect configuration which pins the Fermi level in the band gap, thereby reducing the open circuit voltage. In the presence of excess holes, these recombine at the DX center, restoring the donor configuration [31].
Aside from intrinsic defects in the $Cu(In,Ga)(S,Se)_2$ material, Eisgruber et al. proposed a model, where the buffer layer doping is initially largely compensated by deep traps, capturing most of the free electrons [32]. The reduction of the buffer doping density leads to a larger voltage drop in the n-doped part of the cell and therefore to distortions of the current–voltage characteristics. An absorber/buffer configuration with a larger conduction band spike would suffer worse from such an effect, possibly explaining the increased importance of light-soak observed for CBD-Zn(O,S) buffer layers (c.f. Chapter 4). This can on the other side also be explained by a reduction of absorption in the buffer layer, leading to less free holes near the buffer layer and therefore to a reduced transition rate of defects in the $Cu(In,Ga)(S,Se)_2$ material [30].

2.4 Measurement methods

2.4.1 *Determination of the layer thickness and composition with XRF measurements*

X-ray fluorescence (XRF) measurements are a useful tool for quick (60 s) analysis of thin film composition and thickness. For this work routine thickness measurements of the prepared Zn(O,S) based buffer layers on Cu(In,Ga)(S,Se)$_2$ substrate were carried out using a Fischerscope X-RAY XDV instrument. In this instrument, a tungsten anode is used as a source of x-ray irradiation. This irradiation leads to a release of electrons from the lower shells in the irradiated material, whereupon the free core levels are filled by electrons from higher shells, a process accompanied by element-specific X-ray fluorescence radiation. The radiation is captured by a silicon drift detector where photons can be separated by the drift time of the generated carriers and the photon energy can be calculated from the amount of generated charges.
The Fischerscope X-RAY XDV is a non-vacuum instrument, light elements like S and O can therefore not be detected with sufficient accuracy. The implemented model for composition and thickness measurements therefore consists of three layers, namely glass/Mo/Cu(In,Ga)(S,Se)$_2$/Zn, where the glass is modeled to be an infinite substrate material with a composition that was determined by a measurement on glass only. The Fischerscope software is then making a model fit to the measured spectrum, determining the thickness of the Mo layer, composition and thickness of the Cu(In,Ga)(S,Se)$_2$ layer, neglecting its sulfur content, and the thickness of the assumed Zn layer. Since in reality there is no layer of elemental zinc but a layer of Zn(O,S), the density of this layer has to be adjusted accordingly. Therefore scanning electron microscopy pictures of cross sections for two samples with different layer thickness (see Fig. 2.9) were used to calibrate the model. The result is a setup that is applied routinely for documentation purposes. With the experience growing from continuous use of the XRF thickness measurement the latter quickly becomes unnecessary for process development purposes. As displayed in Fig. 2.10 there is a distinct color change of the CIGSSe/Zn(O,S) layer stack with increasing Zn(O,S) film thickness. A rule of thumb is that a layer with first signs of turning blueish is too thick and a layer that is barely darker compared to uncoated CIGSSe is too thin. This does however only apply if there is no significant change made to the optical layer properties. A direct comparison of Zn(O,S) layers with different [S]/([S]+[O]) ratios is meaningless due to changes of the band gap (see Chapter 4 as well as a direct comparison of Zn(O,S) layers with ZnInOS layers (see Chapter 5).

For ZnInOS films the previously described XRF approach is not possible as the indium content within the buffer layer cannot be separated from the indium content within the CIGSSe, especially since the former contributes only a small fraction to the total fluorescence signal. I therefore used the same model described before. This results in an effective Zn(O,S) layer thickness d_{ZnOS}. With the knowl-

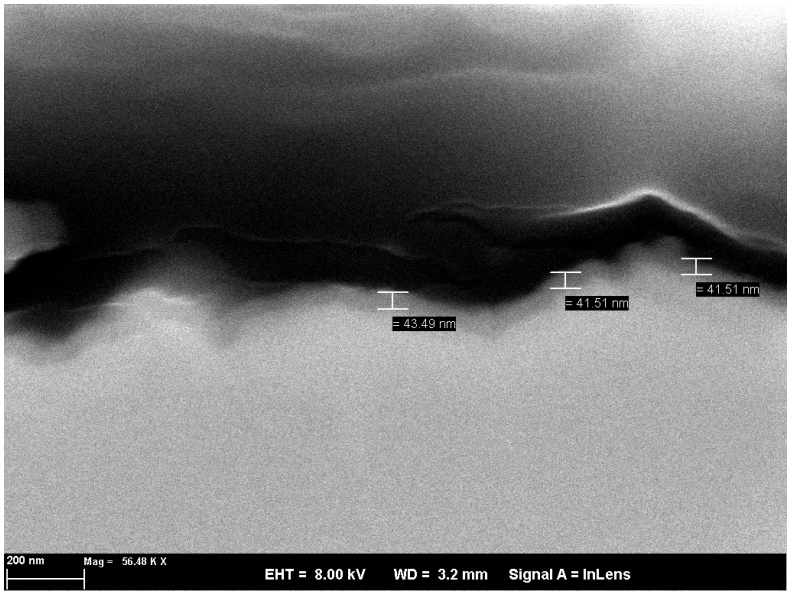

(a) SEM crosssection for CIGSSe/Zn(O,S), single deposition

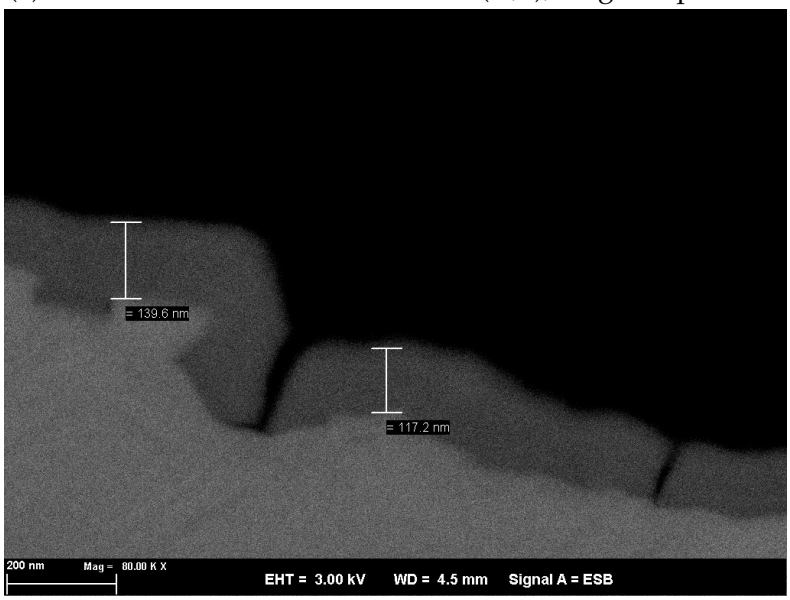

(b) SEM crosssection for CIGSSe/Zn(O,S), two consecutive depositions. Visible cracks are observed only for this sample with high layer thickness.

Figure 2.9: Examples for SEM cross section images taken for the calibration of the XRF thickness measurements. Several more similar images were taken into account.

edge or an estimation of the elemental composition (n_{In}, n_{Zn}) of the layer with respect to the standard Zn(O,S) layer, a correcting factor can be estimated. In a first approximation it is assumed that each indium atom with surrounding anions takes up the same amount of space as a zinc atom. The film thickness could then

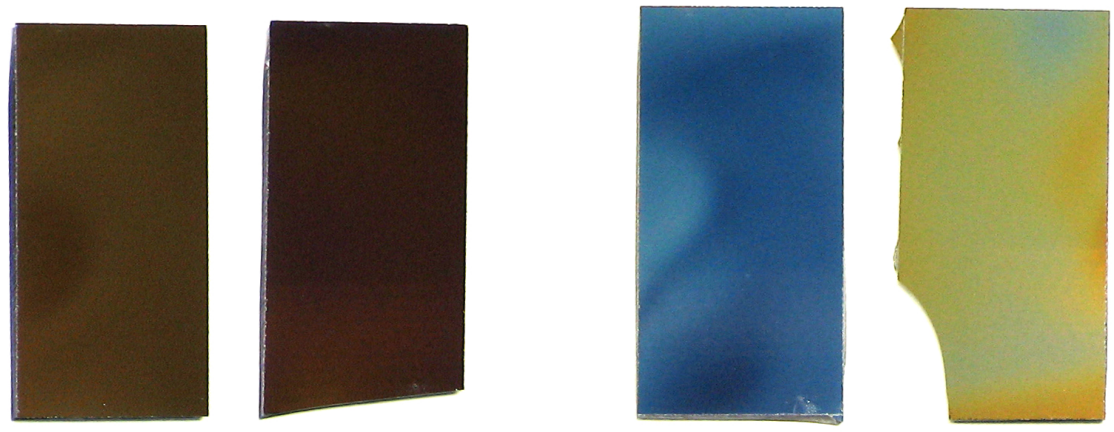

Figure 2.10: Digital images of coated substrates (3.5 cm×7 cm) for different deposition times. The films were deposited with an acidic process similar to the one described in Section 5.2.1 without and with indium sulfate in the process solution. The change of visual appearance with increasing deposition time is mainly due to the change in film thickness. The change from Zn(O,S) to ZnInOS may also result in a change in the refractive index, influencing the color scale. Some thickness inhomogeneities are clearly visible and can be attributed to inhomogeneities in the solution flow around the sample. These inhomogeneities are typical in shape and magnitude for beaker processes discussed in this work.

be calculated as

$$d_{\mathrm{ZnInOS,calc}} = d_{\mathrm{ZnOS}} \times \left(1 + \frac{n_{\mathrm{In}}}{n_{\mathrm{Zn}}}\right), \tag{2.37}$$

where n_{In} and n_{Zn} are the atomic concentrations of In and Zn respectively. This is a very rough estimate however, since it may be assumed that indium atoms take up more space. A next step is to estimate how much more space indium actually takes. The respective volume ratios $V_{\mathrm{In}}/V_{\mathrm{Zn}}$ are calculated for oxides and sulfides separately:

$$\frac{V_{\mathrm{In,In_2O_3}}}{V_{\mathrm{Zn,ZnO}}} = \frac{1}{2}\frac{m_{\mathrm{mol,In_2O_3}}}{\rho_{\mathrm{In_2O_3}}} \times \frac{\rho_{\mathrm{ZnO}}}{m_{\mathrm{mol,ZnO}}} = \frac{1}{2}\frac{277.64\,\mathrm{g}}{7.12\,\mathrm{g\,cm^{-3}}} \times \frac{5.68\,\mathrm{g\,cm^{-3}}}{81.39\,\mathrm{g}} \approx 1.36 \tag{2.38}$$

and

$$\frac{V_{\mathrm{In,In_2S_3}}}{V_{\mathrm{Zn,ZnS}}} = \frac{1}{2}\frac{m_{\mathrm{mol,In_2S_3}}}{\rho_{\mathrm{In_2S_3}}} \times \frac{\rho_{\mathrm{ZnS}}}{m_{\mathrm{mol,ZnS}}} = \frac{1}{2}\frac{325.83\,\mathrm{g}}{4.9\,\mathrm{g\,cm^{-3}}} \times \frac{4.09\,\mathrm{g\,cm^{-3}}}{97.46\,\mathrm{g}} \approx 1.40 \tag{2.39}$$

where m_{mol} designates the molar mass and ρ the density of the compounds and the factor $1/2$ stems from the two indium atoms per molecule. The material densities were taken from [8]. For film thickness calculations the average of these estimated ratios will be used:

$$\chi = \frac{1}{2}\left(\frac{V_{\mathrm{In,In_2O_3}}}{V_{\mathrm{Zn,ZnO}}} + \frac{V_{\mathrm{In,In_2S_3}}}{V_{\mathrm{Zn,ZnS}}}\right) \approx 1.38, \tag{2.40}$$

leading to

$$d_{\mathrm{ZnInOS,calc}} = d_{\mathrm{ZnOS}} \times \left(1 + \frac{n_{\mathrm{In}}}{n_{\mathrm{Zn}}}\chi\right) \approx d_{\mathrm{ZnOS}} \times \left(1 + \frac{n_{\mathrm{In}}}{n_{\mathrm{Zn}}} \times 1.38\right). \tag{2.41}$$

Films that were deposited on molybdenum coated substrates for process development purposes allow for a cross-check of this approach. On molybdenum coated substrates Zn as well as In are resolved in the XRF spectrum. Therefore it is possible to use a second model, where the measured molybdenum background is substracted from the spectrum and a single layer containing Zn and In is fitted for composition and thickness. With the assumption that the model calibration via the density of Zn is still valid, the density of In in the model is introduced as

$$\rho_{\mathrm{In,ZnInOS}} = \rho_{\mathrm{Zn,ZnOS}} \times \frac{m_{\mathrm{In}}}{m_{\mathrm{Zn}}} \times \chi^{-1} \approx \rho_{\mathrm{Zn,ZnOS}} \times 1.31 \tag{2.42}$$

Resulting layer thicknesses deviate less than 5 % when both models are compared for films deposited on molybdenum coated glass.

2.4.2 *Thin film analysis by X-ray photoelectron spectroscopy (XPS)*

In order to obtain information about the actual elemental composition of different buffer layers and the band alignment at the CIGSSe/buffer interface, X-ray photoelectron spectroscopy (XPS) measurements were employed. A more detailed description of the measurement method regarding to the investigated materials in this work can be found in [23, 33, 34]. The actual measurements were carried out by Anne Fuchs at the department for Analysis of Functional Materials and Physical Analytics in support of this work. The measurement setup consists of a Physical Electronics Quantera SXM instrument equipped with a monochromatic Al anode leading to photon energies of 1486.6 eV. These photons are irradiating the sample to be analyzed, leading to an emission of free electrons from the sample. The number and kinetic energy of these electrons is measured. Since the kinetic energy is approximately (neglecting the material work function) equal to the photon energy minus the electron binding energy of the excited core level, this measured spectrum yields information about the elemental composition. Different elements are identified by determination of the binding energy peak positions and the related amounts are determined by evaluation of the integral peak intensities. The linearity of the spectrometer is ensured by reference measurements of clean silver, copper and gold samples.
XPS is a very surface sensitive method. Emitted electrons from the bulk material undergo inelastic scattering, reducing the number of final emission at the surface, leading to complete attenuation after $\sim$ 10 nm [34]. Since the electron inelastic mean free path is increasing with increasing kinetic energy (in the relevant range above 50 eV), the surface sensitivity is less for electrons emitted from core levels with low binding energies. In a very practical example for this work, the Zn $2p_{3/2}$ peak with a binding energy of $\sim$ 1022 eV is more surface sensitive compared

to the In $3d_{5/2}$ peak with binding energy of $\sim$ 444.7 eV, the In $3d_{5/2}$ peak from the CIGSSe substrate is therefore 'shining through' thin Zn(O,S) buffer layers (thickness close to 10 nm) even if they are covering the substrate completely. In addition to surface measurements, the measurements setup allows for careful sputtering with Ar ions. Repeated cycles of measurement and sputtering lead to a depth profile of the analyzed thin film.

2.4.2.1 *Determination of film composition by analysis of the Auger Parameter*

Aside from the core level peaks, emission lines of Auger electrons are visible in the XPS spectrum for many elements. When a photoelectron is emitted from a core level, an electron from a higher energetic shell takes its place, while the difference in binding energy is directly transferred to another electron. This third electron, the Auger electron, has a kinetic energy equaling

$$E_{\text{kin}} = (E_{\text{CL}\,1} - E_{\text{CL}\,2}) - E_{\text{CL}\,3}, \tag{2.43}$$

where $E_{\text{CL}\,1/2/3}$ designate the binding energies of the electrons involved in the process. Since no intermediate photon is required, transitions that would be forbidden by the dipole selection rule do occur. The resulting spectrum is again characteristic for each element while being independent of the initial photon energy.
Since the chemical environment leads to small changes in the electron binding energies, the shift of core level peaks and Auger peaks with respect to published literature data contains information about the film composition. However, if the conductivity of the analyzed sample is low, surface charging will occur in the measurement process, leading to a shift of the whole spectrum as well. A more robust tool for the analysis of the chemical surrounding is the Auger parameter, defined as the sum of the core level binding energy and the kinetic energy of the Auger electron, where the peaks with highest intensity are chosen in both cases. The Auger emission line is identified by three letters, designating the electron shells of the same order, as described previously, with suffixes indicating subshells. In the work of Tobias Adler [27, 33], a detailed study of the Auger parameter for Zn(O,S) buffer layers, dependent on the ratio [S]/([S]+[O]) in the film is given. He empirically derived the equation

$$\alpha_{\text{Zn}} = 2010.1\,\text{eV} + x \times 1.26\,\text{eV}, \tag{2.44}$$

where α_{Zn} is the Zn Auger parameter determined from the Zn $2p_{3/2}$ and the Zn $L_3M_{4,5}M_{4,5}$ emission lines, and x is the ratio [S]/([S]+[O]) within the Zn(O,S) film. This equation is used in the following sections to determine the ratio [S]/([S]+[O]) for chemically deposited Zn(O,S) films. This method has the advantage that it is not necessary to remove influences from surface adsorbed oxygen and hydroxides from the O 1s emission line in order to get reliable results.
Another common tool is the so called Wagner plot [35], where the Auger electron kinetic energy is plotted over the core level binding energy. The previously

described Auger parameter is represented by diagonal lines in such a diagram indicating constant integer Auger parameters. If measurement results are plotted together with literature data in such a Wagner plot, this allows for an easy overview of possible chemical environments in the analyzed sample. In Section 5.3.2 such a Wagner plot is shown in Fig. 5.5(b) for indium in ZnInOS buffer layers.

2.4.2.2 *Determination of valence band maximum positions from XPS spectra*

Valence band maximum (E_{VBM}) positions are obtained from an XPS measurement by linear extrapolation of the valence band spectrum (an example can be seen in Fig. 4.27(a)) and linear extrapolation of the constant background in the band gap. The crossing of the two extrapolations is taken to be the valence band maximum energy. The spectral resolution of the spectrometer was tested by using two different analyzer pass energies, 6.5 eV (high resolution, low signal/noise ratio) and 55 eV (low resolution, high signal/noise ratio). The observed deviation of the difference between E_{VBM} and core level energies was in the range of 150 meV. The Fermi level as the origin of the binding energy axis was calibrated by determining the Fermi level position of a clean Ag surface. Since all samples are electrically connected with the spectrometer, the Fermi level position is constant and relative changes of the valence band binding maximum energies are observed in semiconductors. The measurement accuracy was also cross-checked with the dissertation work of Anne Fuchs [36] by measuring E_{VBM} and Cd $3d_{5/2}$ for a chemically deposited CdS layer on CIGSSe. The difference of these energies falls in the expected range, while the difference between Fermi level and E_{VBM} is with 1.85 eV slightly larger than observed in [36]. The latter effect can, however, be attributed to differences in the substrate material and the overall quality of surface potential measurements is rated good.

2.4.2.3 *Determination of valence band offsets from XPS sputtering depth profiles*

Since the energy of the valence band maximum as well as the Fermi level at the surface of the analyzed thin film can be determined from XPS spectra, it is possible to determine the valence band offset at the CIGSSe/buffer interface from XPS measurements [23, 27, 37, 38].
There are two inherent problems for the determination of the valence band offset. First, the electron inelastic mean free path is exceeding the thickness of an atomic layer. Since electrons emitted from the valence band have high kinetic energy, the surface sensitivity of the valence band spectrum is poor. Second, due to the multicrystalline structure of the CIGSSe the interface to the buffer layer is very rough. During sputter depth profiling this leads to the substrate being partially exposed, thereby 'smearing' the interface in sputter depth profiles. It is therefore not possible to measure both valence band spectra of the CIGSSe and the buffer layer directly at the interface. Circumventing this problem, in this work I follow the method described by Fritsche et al. [37], which is illustrated in Fig. 2.11. First,

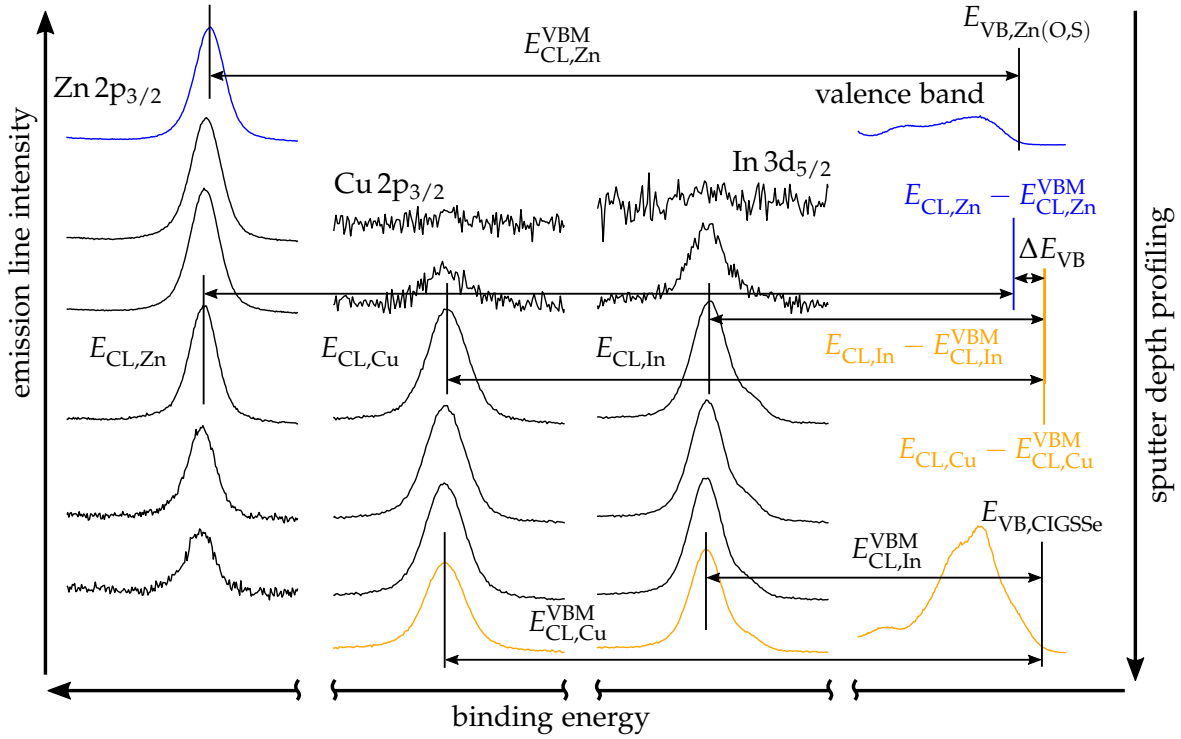

Figure 2.11: Graphic description of the measurement principle for determining the valence band offset ΔE_{VB} at the CIGSSe/buffer interface with XPS sputtering depth profiling according to [23, 27, 37, 38]. The displayed spectra stem from an actual depth profile measurement, conducted in the course of this work.

the surface is cleaned in an initial sputter step in order to reduce the surface contamination. Then, the binding energy of the valence band maximum E_{VB} and the core level binding energies with respect to the valence band maximum E^{VBM}_{CL} for the Zn $2p_{3/2}$, S $2p_{3/2}$, and In $3d_{5/2}$ (in case of indium incorporation into the buffer layer) emission lines of the buffer layer are taken at the cleaned surface. E_{VB} and E^{VBM}_{CL} for the Cu $2p_{3/2}$, In $3d_{5/2}$, and Se $3d_{5/2}$ emission lines in the CIGSSe are taken after sputtering deep into the material ensuring complete removal of the buffer layer. During the sputter depth profiling, shifts in those core level binding energies mentioned aforehand are monitored. With the assumption that the values E^{VBM}_{CL} are constant, the position of the valence band maxima of buffer layer and substrate are then calculated for each step in the depth profiling, and for each core level emission line. Under the assumption of constant E^{VBM}_{CL}, a measured change in E_{CL} directly translates into a change of the valence band position with regard to the Fermi level and band bending becomes apparent (for an example see Fig. 5.11). The valence band offset ΔE_{VB} is then taken as the difference of the calculated valence band maxima, averaging a region where elements from both buffer layer and absorber are detected in significant amounts, i.e. where the calculated atomic concentration of Cu is rising above 20 %. It is important to note that the band bending mentioned aforehand leads to potentially different shifts of the valence band signals for substrate and layer. Therefore the different valence band maximum energies would have to be carefully separated or, as in the

approach used here, taken only at the beginning and the end of the sputter profile, where only one of them can be detected (c.f. Fig. 2.11).
An alternative approach, avoiding problems arising with the sputtering procedure, such as preferential sputtering or induced sputter damages and diffusion, is to perform the same basic analysis with a step-by-step deposition of the buffer layer, where the last point is taken after complete attenuation of the substrate signal. However, this method is only really suitable for in-situ deposition processes, avoiding surface contamination after each single deposition step. Since that was not possible with the chemical bath processes employed in this work, this approach was not utilized in this work. Tobias Adler published a comparison of both approaches for Zn(O,S) buffer layers in [33], showing that there is a systematic offset in the results for high sulfur content in the buffer layer. This offset might indicate that there is a systematic error, when the sputtering depth profiling approach is used as will be discussed in Section 5.3.4.

2.4.3 *Determination of the thin film band gap from transmittance and reflectance spectra*

In this work, transmittance and reflectance spectra were measured with a setup consisting of an Ocean Optics DH-2000-BAL UV-Vis-NIR light source and an Ocean Optics Maya2000 Pro spectrometer, connected to an optical fiber with high UV transmittance. The analyzed thin films were deposited on quartz glass with constant transmittance over the whole range of the observed spectrum (200 nm to 1100 nm). The measurement of transmittance was performed by positioning the optical fibers, coming from light source and leading to the spectrometer, face to face with each other, separated by the analyzed sample. When measuring the reflectance, a bifurcated fiber was employed to separate incoming and reflected light. The sample position was adjusted in such a way, as to maximize the measurement signal.
The absorption coefficient α is calculated from the recorded transmittance and reflectance spectra. In an approximation to the real system which consists of two layers, namely the quartz substrate and the thin film, surrounded by air, an equation can be derived for a single film with the same medium on both sides, considering multiple internal reflections as displayed in Fig. 2.12. The partial reflectance from a single reflection process is denoted as R' whereas the total reflectance and transmittance are functions of this partial reflectance and the absorption coefficient $R(R', \alpha)$ and $T(R', \alpha)$. The transmittance T can be derived as a geometric series:

$$\begin{aligned} I_0 T &= I_0 (1-R')^2 e^{-\alpha d} \left(1 + R'^2 e^{-2\alpha d} + R'^4 e^{-4\alpha d} + \ldots\right) \\ &= I_0 (1-R')^2 e^{-\alpha d} \sum_{i=0}^{\infty} \left(R'^2 e^{-2\alpha d}\right)^i \\ &= I_0 \frac{(1-R')^2 e^{-\alpha d}}{1 - R'^2 e^{-2\alpha d}} \end{aligned} \tag{2.45}$$

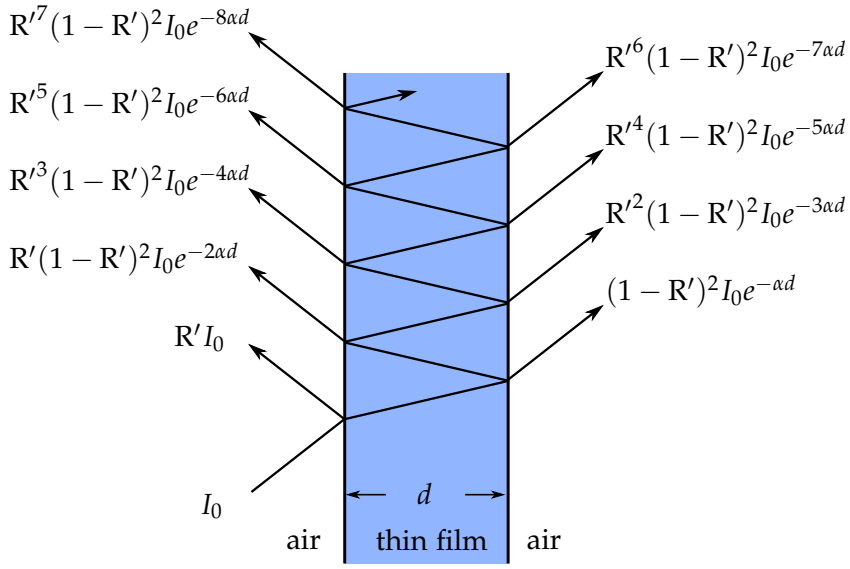

Figure 2.12: Multiple reflection processes in a thin film surrounded by air, leading to expressions for the transmittance and the reflectance, that can be derived from geometric series.

If R' can be calculated from known material properties, this expression can be solved for αd:

$$\alpha d = \ln\left(\frac{2R'^2T}{-R'^2+2R'+\sqrt{R'^4-4R'^3+4R'^2T^2+6R'^2-4R'+1}-1}\right), \tag{2.46}$$

For large absorption coefficients this relation can be further simplified:

$$T \approx (1-R')^2 e^{-\alpha d} \qquad \Rightarrow \qquad \alpha d \approx \ln\left(\frac{(1-R'^2)}{T}\right), \tag{2.47}$$

However, in most cases neither this simplification is possible, nor is R' known as only the total reflectance R is measured. In this case R can be derived as a geometric series as well:

$$\begin{aligned} I_0 R &= I_0 R' + I_0 R'(1-R')^2 e^{-2\alpha d}\left(1 + R'^2 e^{-2\alpha d} + R'^4 e^{-4\alpha d} + \ldots\right) \\ &= I_0 R' + I_0 R'(1-R')^2 e^{-2\alpha d} \sum_{i=0}^{\infty}\left(R'^2 e^{-2\alpha d}\right)^i \\ &= I_0 R' + I_0 \frac{R'(1-R')^2 e^{-2\alpha d}}{1-R'^2 e^{-2\alpha d}} = I_0 R'\left(1 + T e^{-\alpha d}\right) \end{aligned} \tag{2.48}$$

Substitution then leads to

$$T = \frac{\left(1 - \frac{R}{1+Te^{-\alpha d}}\right)^2 e^{-\alpha d}}{1 - \left(\frac{R}{1+Te^{-\alpha d}}\right)^2 e^{-2\alpha d}}. \tag{2.49}$$

Solving Eq. (2.49) for the exponent αd results in the following expression

$$\alpha d = \ln\left(\frac{2T}{-R^2+2R+T^2+\sqrt{R^4-4R^3-2R^2T^2+6R^2+4RT^2-4R+T^4+2T^2+1}-1}\right), \tag{2.50}$$

which is evaluated for the measured spectra or R and T in order to get the spectrum of the absorption coefficient.
The band gap can be determined from this spectrum of the absorption coefficient α by utilizing the following relationships for direct or indirect semiconductors [39]:

$$\begin{aligned} \text{direct gap}: \quad & \alpha\,\hbar\omega \approx \text{ const.} \times \sqrt{\hbar\omega - E_g} \\ \text{indirect gap}: \quad & \alpha\,\hbar\omega \approx \text{ const.} \times \left(\hbar\omega - E_g\right)^2 \end{aligned} \tag{2.51}$$

In case of a direct semiconductor $(\alpha\,\hbar\omega)^2$ is plotted over the photon energy $\hbar\omega$ whereas in case of an indirect semiconductor $\sqrt{\alpha\,\hbar\omega}$ is plotted over $\hbar\omega$, the so called Tauc plot [40]. In both cases a linear extrapolation of the data to $\alpha = 0$ yields the optical band gap. If the layer thickness is not known exactly and therefore a direct calculation of α is not possible, the same extrapolation can be performed when α is substituted by αd in the plotting procedure. This is just scaling the ordinate and has no influence on the derivation of the band gap.

2.5 Standard procedures

2.5.1 *CIGSSe formation and sample shipment procedure*

The CIGSSe material used as deposition substrate and as absorber material of the presented solar cells in this work has exclusively been received from the Bosch Solar CISTech GmbH, Brandenburg, Germany. There, it has been fabricated in a large area sequential process, described in the journal article by Probst et al. [41]. A molybdenum back contact is formed on float glass by DC magnetron sputtering. Metal precursors, containing Cu, In, and Ga, are DC magnetron sputtered on top of the molybdenum back contact. Subsequently, the CIGSSe absorber is formed in a forced convection process, where a batch of coated glass substrates is heated in an oven while ventilators circulate variable mixtures of inert gas, H_2Se, H_2S, Se-vapor, and S-vapor. The sulfur components are added in a last step, leading to the formation of a CIGSe/CIGSSe structure. After cooling down, the substrates are transferred to a storage chamber, containing nitrogen gas. Before shipment, some of the large-area substrates are coated with cadmium sulfide in a typical chemical bath process, for the use as reference samples later on. Subsequently, from the center of each substrate, three neighboring pieces with dimension 30 cm × 30 cm are cut out, avoiding inhomogeneities at the edges. These sub-module sized substrates are then shipped in a box containing nitrogen gas with excess pressure and transferred to a storage cabinet, constantly flooded with nitrogen gas, in our laboratory. Although the substrates stay in inert atmosphere most of the time, an

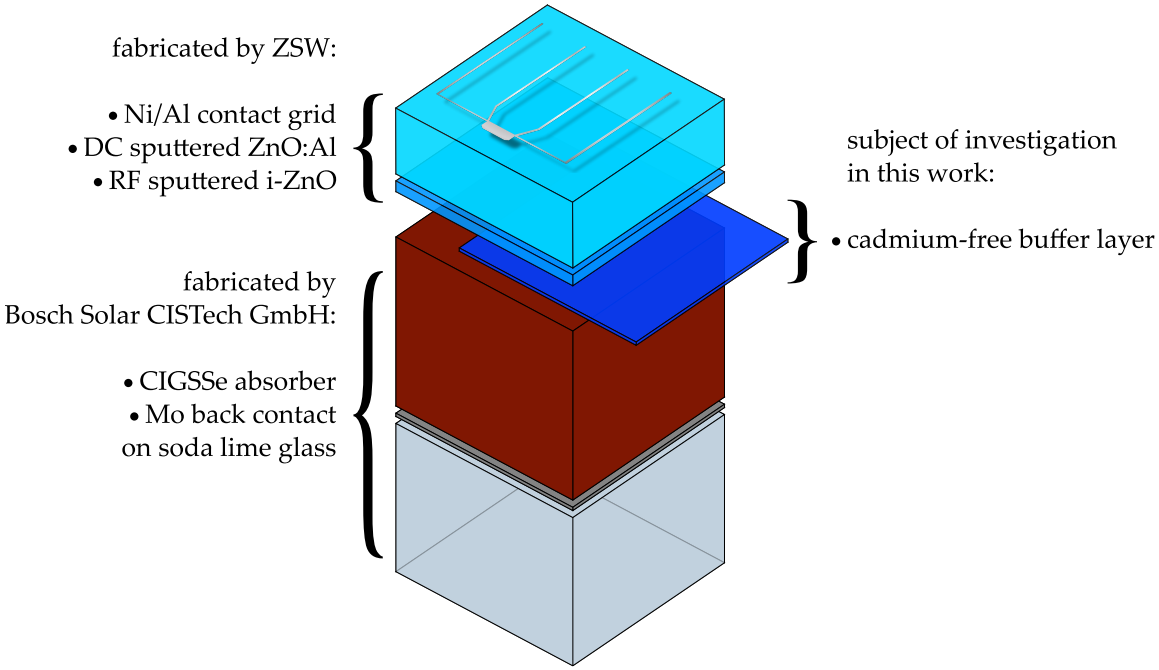

(a) CIGSSe solar cell layer stack.

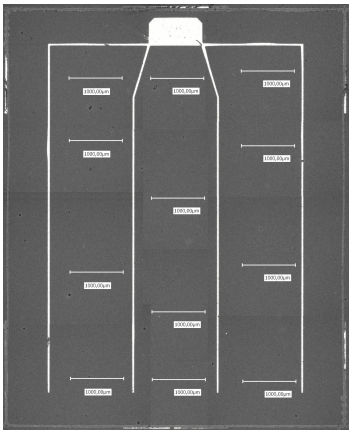

(b) Stitched microscope images of a typical cell.

Figure 2.13: (a) Schematic CIGSSe solar cell layer stack (not drawn to proportion) and (b) a stitched microscope images of a of a typical cell with clearly visible Ni/Al contact grid and mechanical scribing lines.

exposure to ambient conditions during the cutting and transferring steps in the range of a few hours, could not be avoided.

2.5.2 *Cell fabrication*

A complete CIGSSe solar cell layer stack is drawn in Fig. 2.13(a). For this work only the buffer layer was deposited in our laboratory. Sputtering of i-ZnO and aluminum doped ZnO, evaporation of Ni/Al contact grids, and mechanical cell

separation is in principle possible in our laboratory. The processes are, however, unstable at times and are therefore used only for a small set of experiments. Most of the solar cells, and in fact all of the cells shown in this work, are therefore processed at the Zentrum für Solarenergie- und Wasserstoff-Forschung Baden Württemberg (ZSW). Mostly, the substrate is cut to 3.5 cm×7 cm for a layout of two rows with each ten 0.5 cm² cells. On rare occasions a different 10 cm×10 cm layout of four rows with each six 1 cm² cells was used. The ZSW processes were not disclosed in detail, but could be slightly adjusted according to my specification as will be discussed in Section 4.5.
Estimated from SEM images, the RF sputtered i-ZnO has a thickness ranging between 60 nm and 80 nm and the DC sputtered ZnO:Al is ~400 nm thick. The contact grid layout is designed for a total cell area of 0.5 cm² and the shadowed cell area amounts to ~0.03 cm² resulting in an active cell area of 0.47 cm². An image of a typical cell, generated from stitched microscope images, is displayed in Fig. 2.13(b), where apart from contact grid damages, additional inaccuracies of the mechanical scribing are visible. These deficiencies contribute to the statistical spread of short circuit currents, measured in this work. An antireflective coating, which would further enhance the short circuit current, was not applied for cells presented in this work.

References

[6] P. Würfel, *Physics of Solar Cells: From Principles to New Concepts*, (WILEY-VCH Verlag GmbH & Co. KGaA, 2005), ISBN: 978-3-527-61854-5 (Cited on pages 5, 9, 10, 42).

[7] U. Rau and H.-W. Schock, "Cu(In,Ga)Se_2 solar cells", in *Clean Electricity from Photovoltaics*, (World Scientific, 2001), ISBN: 978-1-86094-161-0 Chap. 7, pp. 277–345 (Cited on pages 5, 9, 15–17, 20, 42).

[8] R. Scheer and H.-W. Schock, *Chalcogenide Photovoltaics*, (Wiley-VCH Verlag GmbH & Co. KGaA, 2011), ISBN: 978-3-527-63370-8 (Cited on pages 5, 9, 13–15, 17, 18, 25).

[9] S. M. Sze and K. K. Ng, *Physics of Semiconductor Devices*, (John Wiley & Sons, 2006), ISBN: 978-0-470-06832-8 (Cited on pages 5, 15, 18).

[10] W. Shockley and H. J. Queisser, "Detailed Balance Limit of Efficiency of p–n Junction Solar Cells", Journal of Applied Physics **32**, 510–519 (1961) (Cited on page 13).

[11] M. Burgelman, P. Nollet, and S. Degrave, "Modelling polycrystalline semiconductor solar cells", Thin Solid Films **361–362**, 527–532 (2000) (Cited on page 14).

[12] V. Nadenau, U. Rau, A. Jasenek, and H. W. Schock, "Electronic properties of $CuGaSe_2$-based heterojunction solar cells. Part I. Transport analysis", Journal of Applied Physics **87**, 584–593 (2000) (Cited on page 17).

[13] A. Kanevce, M. Gloeckler, A. O. Pudov, and J. R. Sites, "Conduction-Band-Offset Rule Governing J-V Distortion in CdS/CI(G)S Solar Cells", in Symposium F – Thin-Film Compound Semiconductor Photovoltaics, Vol. 865, MRS Proceedings (2005), F5.32 (Cited on page 19).

[14] J. E. Jaffe and A. Zunger, "Theory of the band-gap anomaly in ABC_2 chalcopyrite semiconductors", Phys. Rev. B **29**, 1882–1906 (1984) (Cited on pages 20, 122).

[15] P. Jackson, D. Hariskos, R. Wuerz, O. Kiowski, A. Bauer, T. M. Friedlmeier, and M. Powalla, "Properties of Cu(In,Ga)Se_2 solar cells with new record efficiencies up to 21.7%", physica status solidi (RRL) – Rapid Research Letters **9**, 28–31 (2015) (Cited on page 20).

[16] S.-H. Wei and A. Zunger, "Band offsets and optical bowings of chalcopyrites and Zn-based II-VI alloys.", Journal of Applied Physics **78**, 3846 (1995) (Cited on pages 20, 92, 126).

[17] M. I. Alonso, M. Garriga, C. D. Rincón, E. Hernández, and M. León, "Optical functions of chalcopyrite $CuGa_xIn_{1-x}Se_2$ alloys", Applied Physics A **74**, 659–664 (2002) (Cited on page 20).

[18] C. A. Durante Rincón, E. Hernández, M. I. Alonso, M. Garriga, S. M. Wasim, C. Rincón, and M. León, "Optical transitions near the band edge in bulk $CuIn_xGa_{1-x}Se_2$ from ellipsometric measurements", Materials Chemistry and Physics **70**, 300–304 (2001) (Cited on page 20).

[19] P. D. Paulson, R. W. Birkmire, and W. N. Shafarman, "Optical characterization of $CuIn_{1-x}Ga_xSe_2$ alloy thin films by spectroscopic ellipsometry", Journal of Applied Physics **94**, 879–888 (2003) (Cited on page 20).

[20] S. B. Zhang, S.-H. Wei, A. Zunger, and H. Katayama-Yoshida, "Defect physics of the$CuInSe_2$ chalcopyrite semiconductor", Phys. Rev. B **57**, 9642–9656 (1998) (Cited on page 20).

[21] P. Salomé, H. Rodriguez-Alvarez, and S. Sadewasser, "Incorporation of alkali metals in chalcogenide solar cells", Solar Energy Materials and Solar Cells **143**, 9–20 (2015) (Cited on page 20).

[22] S. Siebentritt, M. Igalson, C. Persson, and S. Lany, "The electronic structure of chalcopyrites-bands, point defects and grain boundaries", Progress in Photovoltaics: Research and Applications **18**, 390–410 (2010) (Cited on page 20).

[23] A. Klein, "Energy band alignment in chalcogenide thin film solar cells from photoelectron spectroscopy", Journal of Physics: Condensed Matter **27**, 134201 (2015) (Cited on pages 21, 26, 28, 29, 105, 107, 125).

[24] B. K. Meyer, A. Polity, B. Farangis, Y. He, D. Hasselkamp, T. Krämer, and C. Wang, "Structural properties and bandgap bowing of $ZnO_{1-x}S_x$ thin films deposited by reactive sputtering", Applied Physics Letters **85**, 4929–4931 (2004) (Cited on page 21).

[25] C. Persson, C. Platzer-Björkman, J. Malmström, T. Törndahl, and M. Edoff, "Strong valence-band offset bowing of $ZnO_{1-x}S_x$ enhances p-type nitrogen doping of ZnO-like alloys", English, Physical Review Letters **97**, 146403(4) (2006) (Cited on pages 21, 64, 106, 122).

[26] D. Kieven, A. Grimm, I. Lauermann, M. C. Lux-Steiner, J. Palm, T. Niesen, and R. Klenk, "Band alignment at sputtered ZnS_xO_{1-x}/Cu(In,Ga)$(Se,S)_2$ heterojunctions", physica status solidi (RRL) – Rapid Research Letters **6**, 294–296 (2012) (Cited on page 21).

[27] T. Adler, M. Botros, W. Witte, D. Hariskos, R. Menner, M. Powalla, and A. Klein, "Valence band offsets at Cu(In,Ga)Se_2/Zn(O,S) interfaces", physica status solidi (a) **211**, 1972–1980 (2014) (Cited on pages 21, 27–29, 69, 112, 115).

[28] S. Lany and A. Zunger, "Light-and bias-induced metastabilities in Cu(In,Ga)Se_2 based solar cells caused by the (V_{Se}-V_{Cu}) vacancy complex", Journal of Applied Physics **100**, 113725 (2006) (Cited on pages 22, 55).

[29] U. Rau, M. Schmitt, J. Parisi, W. Riedl, and F. Karg, "Persistent photoconductivity in Cu(In,Ga)Se_2 heterojunctions and thin films prepared by sequential deposition", Applied Physics Letters **73**, 223–225 (1998) (Cited on page 22).

[30] M. Igalson, A. Urbaniak, P. Zabierowski, H. A. Maksoud, M. Buffiere, N. Barreau, and S. Spiering, "Red-blue effect in Cu(In,Ga)Se_2-based devices revisited", Thin Solid Films **535**, 302–306 (2013) (Cited on pages 22, 40, 55, 63).

[31] S. Lany and A. Zunger, "Intrinsic DX Centers in Ternary Chalcopyrite Semiconductors", Physical Review Letters **100**, 016401 (2008) (Cited on pages 22, 55).

[32] I. Eisgruber, J. Granata, J. Sites, J. Hou, and J. Kessler, "Blue-photon modification of nonstandard diode barrier in $CuInSe_2$ solar cells", Solar Energy Materials and Solar Cells **53**, 367–377 (1998) (Cited on pages 22, 63, 64).

[33] T. Adler, "Zn(O,S) Puffer Eigenschaften in Cu(In,Ga)Se_2 Solarzellen", PhD thesis (Technische Universität Darmstadt, Dec. 2013) (Cited on pages 26, 27, 30, 107, 125).

[34] A. Klein, "Energy band alignment at interfaces of semiconducting oxides: A review of experimental determination using photoelectron spectroscopy and comparison with theoretical predictions by the electron affinity rule, charge neutrality levels, and the common anion rule", Thin Solid Films **520**, 3721–3728 (2012) (Cited on pages 26, 105, 107).

[35] C. D. Wagner, "Auger lines in x-ray photoelectron spectrometry", Analytical Chemistry **44**, 967–973 (1972) (Cited on page 27).

[36] A. M. H. Fuchs, "Der Frontkontakt der CdTe-Dünnschichtsolarzelle: Charakterisierung und Modifizierung von Puffer- und Fensterschichten und deren Grenzflächen", PhD thesis (Technische Universität Darmstadt, 2015) (Cited on page 28).

[37] J. Fritsche, T. Schulmeyer, D. Kraft, A. Thißen, A. Klein, and W. Jaegermann, "Utilization of sputter depth profiling for the determination of band alignment at polycrystalline CdTe/CdS heterointerfaces", Applied Physics Letters **81**, 2297–2299 (2002) (Cited on pages 28, 29).

[38] C. Platzer-Björkman, T. Törndahl, D. Abou-Ras, J. Malmström, J. Kessler, and L. Stolt, "Zn(O,S) buffer layers by atomic layer deposition in Cu(In,Ga)Se_2 based thin film solar cells: Band alignment and sulfur gradient", Journal of Applied Physics **100**, 044506 (2006) (Cited on pages 28, 29, 61, 64).

[39] P. Y. Yu and M. Cardona, *Fundamentals of Semiconductors*, 4th ed., (Springer-Verlag Berlin Heidelberg, 2010), ISBN: 978-3-642-00710-1 (Cited on page 32).

[40] J. Tauc, "Optical properties and electronic structure of amorphous Ge and Si", Materials Research Bulletin **3**, 37–46 (1968) (Cited on page 32).

[41] V. Probst, I. Koetschau, E. Novak, A. Jasenek, H. Eschrich, F. Hergert, T. Hahn, J. Feichtinger, M. Maier, B. Walther, and V. Nadenau, "A New Mass Production Technology for High-Efficiency Thin-Film CIS-Absorber Formation", IEEE Journal of Photovoltaics **4**, 687–692 (2014) (Cited on page 32).

3 Chapter 3
PVD-In_2S_3

In_2S_3 thin films, deposited by thermal evaporation, will be presented as promising buffer layers in this chapter. Most of the chapter will be concerned with the distinctive improvement of these buffer layers upon annealing of the completed solar cell and the change of this annealing behavior when the CIGSSe surface is treated with wet-chemical means prior to buffer layer deposition. The last section of this chapter will provide model simulations, leading to a two-part explanation for the observed effects.

3.1 Literature survey

Thermally evaporated indium sulfide thin films have been very successfully applied as buffer layers for CIGSSe solar cells in the recent past. The current record cell efficiency was published in early 2016 with 18.2 % by Spiering et al. [42], the record efficiency on submodule level (30 cm × 30 cm, 662 cm^2 aperture area) was set in 2016 with 17.9 % by the AVANCIS GmbH [43]. Indium sulfide is referred to in this context as In_2S_3, In_2S_x, or In_xSy, due to the fact, that different deposition conditions can lead to stoichiometries slightly deviating from the In_2S_3 formula. An extensive review of the material properties of In_2S_3 thin films with application as buffer layers, was given by Barreau [44]. For PVD-In_2S_3 thin films, band gaps close to the single crystal value of 2.0 eV are reported, together with n-type conductivity. Special attention is turned to the fact that while indium sulfide films can provide good lattice matching to the CIGSSe absorber, a prerequisite for a low concentration of defects at the interface, the spinel structure of the low temperature indium sulfide α and β phases allows thermally activated indiffusion of Na and Cu from the CIGSSe material. Especially the Cu incorporation is of concern for the solar cell efficiency. While Cu depletion at the CIGSSe surface can increase the band gap of the absorber by lowering the valence band maximum and reduce interface recombination, Cu incorporation into the In_2S_3 material leads eventually to the formation of a $CuIn_5S_8$ phase at the interface [44, 45]. This is discussed as the reason for the impact of substrate temperature during film deposition. It was found that temperatures above 230 °C are detrimental for device efficiency. [44, 46], while temperatures below 200 °C lead to the need for additional post-annealing treatments [44, 46, 47]. Such annealing treatments are shown to increase the open circuit voltage and the fill factor as well as the short circuit current. The

pronounced increase in open circuit voltage is attributed to reduced interface recombination. Changes in the short circuit current were associated with changes of the effective collection length of electrons in the absorber [48]. The optimum time of annealing is differing in the literature, probably because of different buffer layer thicknesses and absorber materials. Regarding the band alignment, Bär et al. argue from their measurements that the heavily intermixed interface leads to a small conduction band spike of 0.1 eV at the absorber/buffer interface, while the interface without intermixing would lead to a cliff configuration with increased interface recombination [45].
Paying attention to temperature dependent IV characteristics, there is also discussion about an initially large tunneling contribution to the current in cells with PVD-In_2S_3 buffer layer [42, 49]. This is explained within a model exhibiting a high p-type doping concentration at the absorber surface (p+ layer), a model also under discussion as a cause for metastabilities of the solar cell characteristics [30, 50, 51] (cf. Section 2.3.2). The direct association of this p+ layer in cells with indium sulfide buffer with metastable acceptor-like V_{Se}-V_{Cu} or In_{Cu} defects is, however, unclear. For cells with indium sulfide buffer, metastable solar cell characteristics have been reported by Spiering et al. [42], while Igalson et al. report almost no metastabilities [30] and Pistor reports their absence [48]. While no metastable effects were observed in this work, the p+ layer model fits the observations nicely and is therefore adapted here.
While the above mentioned optimization of the band alignment can reduce interface recombination, this can also be achieved by a high amount of n-type inversion of the CIGSSe surface as theoretically demonstrated by Klenk [52]. An experimental approach to this is the incorporation of donor defects at the CIGSSe surface by wet-chemical means, i.e. the partial electrolyte treatment with cadmium containing solutions [53–55]. Such a treatment will be applied in this work in the attempt to mitigate the need for interface intermixing by annealing treatments.

3.2 Process description

Indium sulfide buffer layers are deposited by thermal evaporation on top of 10 cm × 10 cm sized CIGSSe substrates, fabricated by the Bosch CISTech GmbH (c.f. Section 2.5.1). These substrates were cut from module sized samples, taking special care to use directly neighboring pieces for series experiments. Part of the CIGSSe substrates are submitted to wet chemical treatments prior to buffer layer deposition, namely a treatment in deionized water or a treatment in cadmium containing solution. The treatment in deionized water is performed by immersion of the substrate for 20 min in deionized water kept at a temperature of 80 °C and drying it in nitrogen gas flow afterwards. The treatment in cadmium containing solution is inspired by the partial electrolyte treatment by Bär et al. [54]. A solution of deionized water containing 1.5 mM cadmium acetate and 1.3 M ammonia is prepared. After immersion of the substrate in this solution, it is heated up to 70 °C in approximately 10 min, at which point the substrate is taken out, rinsed with

2.5 % ammonia solution and dried in nitrogen gas flow. This process is similar to a cadmium sulfide buffer layer deposition with the exception that a sulfur compound is omitted.
For buffer layer deposition, crystalline In_2S_3 (fabricated by heating elemental indium in sulfur containing atmosphere), ground to a fine powder, is used as source material. This In_2S_3 powder is thermally evaporated by heating in a pyrolytic boron nitride crucible in vacuum. X-Ray diffraction analysis indicates that the source material is in the pure tetragonal phase before and after heating procedures. Nevertheless, before the material is used for buffer layer deposition, it is conditioned at 750 °C for approximately one hour in order to avoid fast source material degeneration having an unexpected influence on the layer quality. Since the deposition chamber does not allow for a transfer of substrates without breaking the vacuum, the source material is tempered at 750 °C for approximately 30 min after each vacuum break, before a deposition process is started.
In_2S_3 buffer layer deposition processes are performed at chamber pressures ranging between 1×10^{-7} mbar and 3×10^{-6} mbar, where the deposition speed is controlled within limits by adjusting the crucible temperature between 720 °C and 770 °C. The substrate is not actively heated during the deposition process and is located at approximately 40 cm distance from the crucible. While the deposition speed is affected by the temperature (0.2 nm s^{-1} to 1.5 nm s^{-1}), no significant changes of the cell performance on the crucible temperature was observed within these limits. The thickness of the deposited layer is controlled by monitoring with an oscillating crystal microbalance during the deposition process. The microbalance thickness d_{mb} was cross-checked and corrected by deposition of two layers with different thickness on silicon wafers and measuring the thickness with a DEKTAK profilometer and XRF mesurements in vacuum at the CISTech facilities, a direct measurement of the thickness on top of the CIGSSe material was not possible in this work.
After In_2S_3 buffer layer deposition, the substrates are stored in nitrogen atmosphere (exposure to ambient conditions during packaging is unavoidable) and shipped to the ZSW for cell preparation. At the ZSW, an i-ZnO, a ZnO:Al layer and a Ni/Al grid are deposited as described in Section 2.5.2. The area of the finished cells, separated by mechanical scribing, is 0.5 cm^2 (~0.47 cm^2 active area).

3.3 Annealing behavior of solar cells with In_2S_3 buffer layer

IV curves in the dark and under simulated AM1.5 illumination (while actively cooling the cell to 25 °C) were measured at the ZSW. After an initial measurement, the cells with In_2S_3 buffer layer are usually annealed on a hotplate at 200 °C in air in order to increase the solar cell efficiency. The standard time for the annealing procedure was set to 40 min. However, the time needed for maximum efficiency was observed to differ for different samples from different batches.
Figure 3.1 shows IV curves for exemplary cells from similar samples with different

Table 3.1: Solar cell parameters for cells with In_2S_3 buffer layers with different thicknesses before (1) and after (2) annealing. The statistical data is represented by the median and median absolute deviation. Each ensemble consists of 20 cells.

	$d = 35\,\mathrm{nm}$		$d = 21\,\mathrm{nm}$		$d = 11\,\mathrm{nm}$	
	1	2	1	2	1	2
η / %	9.4 ± 0.3	7.5 ± 0.4	11.6 ± 0.2	13.9 ± 0.1	11.5 ± 0.2	13.8 ± 0.2
η_{max} / %	10.0	8.3	12.0	14.3	11.9	14.4
V_{oc} / mV	504 ± 5	410 ± 16	539 ± 2	564 ± 2	544 ± 1	600 ± 1
fill factor / %	52.3 ± 1.1	49.3 ± 1.1	58.9 ± 0.6	65.3 ± 0.7	57.8 ± 0.4	61.0 ± 0.8
J_{sc} / mA cm^{-2}	35.1 ± 0.1	36.7 ± 0.3	36.6 ± 0.2	37.9 ± 0.2	36.5 ± 0.2	37.7 ± 0.2

In_2S_3 buffer layer thickness (35 nm, 21 nm, and 11 nm). The cell with thick buffer layer gains short circuit current, but significantly looses open circuit voltage. This behavior was reproduced for another experiment with an In_2S_3 layer thickness in the same range, does however not always occur. More common is the annealing behavior exhibited by both cells with thinner buffer layer, where all relevant solar cell parameters are increased by the annealing step. It is noteworthy here that the amplitude if this effect seems to be larger for the thinner buffer layer, this is, however, only true for the increase in open circuit voltage. Since the fill factors are smaller for the thinner buffer layer, this is generally not translated into higher efficiencies. A table with statistical data regarding this set of experiments is displayed in Table 3.1. As mentioned in the literature survey, this increase of open circuit voltage and fill factor is commonly attributed to a decrease of recombination at the absorber/buffer interface. Generally, when the solar cell follows the diode model, the total current through the solar cell can be thought of as a superposition an exponentially increasing recombination current and a constant photocurrent. In this case it can be shown for constant series and shunt resistance that the fill factor has to increase with increasing open circuit voltage [6, 7]. The cell parameters in Table 3.1 follow this relation.

In the following I will utilize wet chemical treatments to modify the absorber surface prior to buffer layer deposition. The resultant cells show solar cell characteristics and an annealing behavior that will enable me to separate two underlying mechanisms in the previously discussed annealing behavior of cells built on untreated absorber material.
First, a comparative analysis of the temperature dependent open circuit voltage will show that the increase of V_{oc} is due to a shift of the dominant recombination path away from the interface, achieved both with annealing or wet chemical treatments. Second, the gain in J_{sc} is linked to an increased effective collection length in the absorber by analysis of external quantum efficiency measurements, an effect

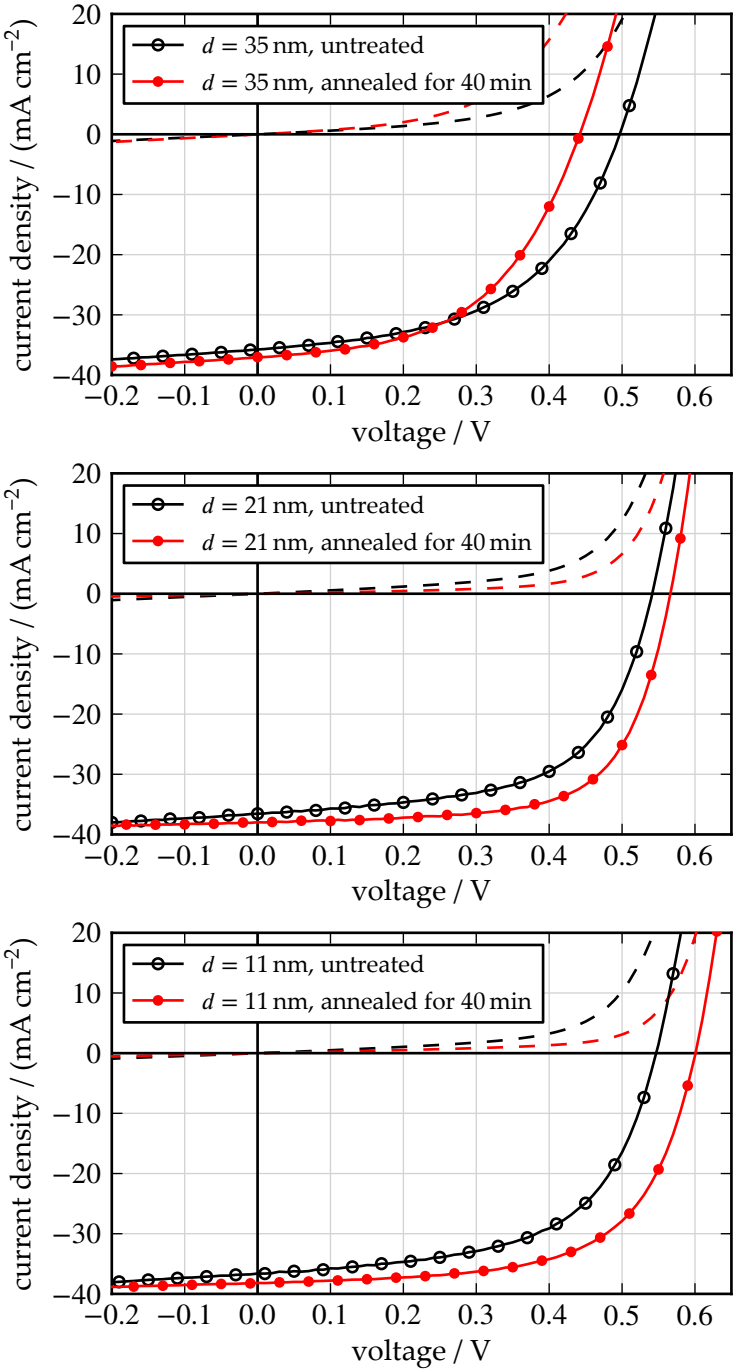

Figure 3.1: IV curves of solar cells with different corrected thicknesses of the In_2S_3 buffer layer. One measurement was performed before (black, empty symbols) and one measurement was performed after annealing the completed cell at 200 °C for 40 min in air (red, filled symbols). Measurements in the dark are displayed by dashed lines, measurements under simulated AM1.5 illumination are displayed by solid lines.

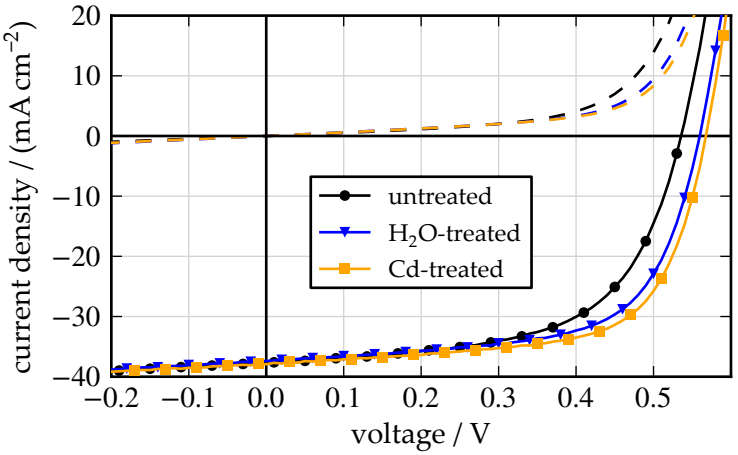

Figure 3.2: IV curves of exemplary cells (not annealed), partly submitted to wet-chemical treatments prior to In_2S_3 buffer layer deposition. Measurements in the dark are displayed by dashed lines, measurements under simulated AM1.5 illumination are displayed by solid lines.

only achieved with the annealing treatment. This effect will then be explained within a model including a p+ layer in the absorber near the interface, supported by a numerical simulation.

When the CIGSSe material is treated in water or cadmium containing solution prior to buffer layer deposition, there is an increase of the open circuit voltage and the fill factor. A comparison of exemplary IV curves is shown in Fig. 3.2. While the gain in open circuit voltage is similar to the gain upon annealing, the short circuit current is not affected and the fill factor is increasing only slightly. Figure 3.3 displays IV curves illustrating the annealing behavior of the cells built on wet-treated absorber. Statistical data can be found in Table 3.2. There is a significant difference in how these cells respond to annealing compared to the cells built on untreated absorber (c.f. Fig. 3.1). While the short circuit current and fill factor are increasing upon annealing, the open circuit voltage is decreasing, resulting in a characteristic cross-over in the figure. As mentioned before, usually a decrease in open circuit voltage would be assumed to be accompanied by a decrease in fill factor. The results shown here therefore are counter-intuitive at first and require further explanation.

In order to gain additional insight into the differences between cells with or without a wet-chemical treatment of the absorber, temperature dependent measurements of the current–voltage characteristics were performed. IV curves were measured in the dark and under illumination by a 250 W halogen light source (LOT LS0308) at 75 mW cm^{-2}. A temperature range from 225 K to 300 K was accessible by cooling the cell, mounted on a copper block inside a vacuum chamber,

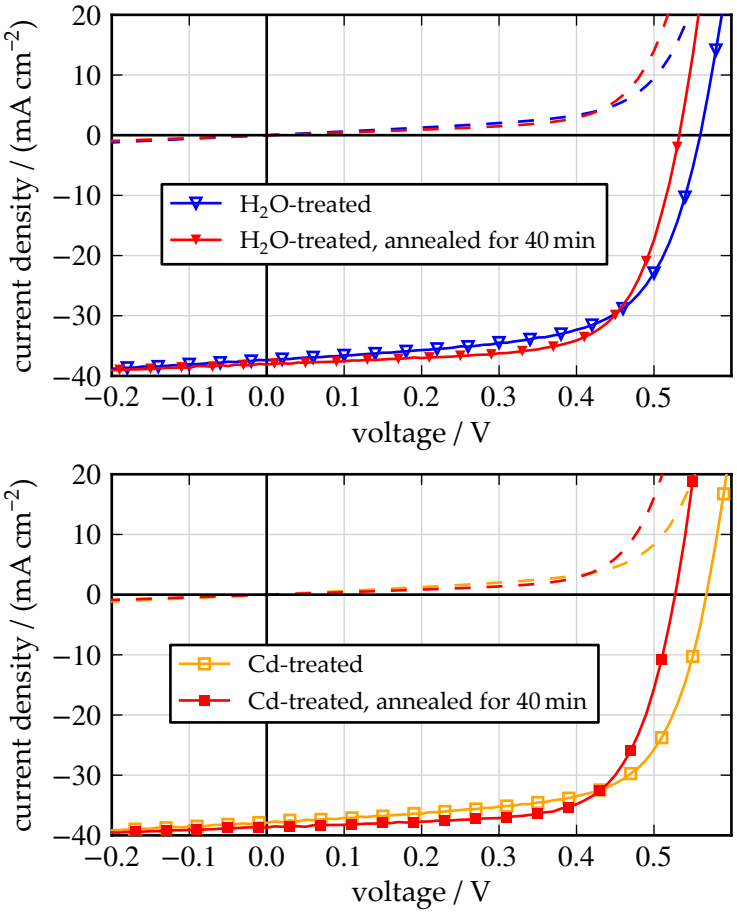

Figure 3.3: IV curves of solar cells with In_2S_3 buffer layer, deposited on water-treated and Cd-treated absorber, before and after annealing at 200 °C for 40 min. Measurements in the dark are displayed by dashed lines, measurements under simulated AM1.5 illumination are displayed by solid lines.

Table 3.2: Solar cell parameters for cells with In_2S_3 buffer layers before (1) and after (2) annealing. The substrates were submitted to two different wet-chemical treatments prior to buffer layer deposition and the buffer layer thickness is 21 nm. The statistical data is represented by the median and median absolute deviation. Each ensemble consists of 20 cells.

	H_2O-treated		Cd-treated	
	1	2	1	2
η / %	12.2 ± 0.3	13.4 ± 0.2	13.3 ± 0.2	13.1 ± 0.3
η_{max} / %	13.4	13.8	14.1	14.1
V_{oc} / mV	554 ± 2	532 ± 2	565 ± 1	513 ± 8
fill factor / %	60.0 ± 1.1	66.2 ± 0.7	63.1 ± 0.8	67.0 ± 0.5
J_{sc} / mA cm^{-2}	36.8 ± 0.2	37.9 ± 0.2	37.2 ± 0.1	38.2 ± 0.2

by means of an AIM stirling cooler. Good thermal contact between the cell and the copper block was achieved by use of vacuum grease. The cell temperature was measured indirectly with a PT100 temperature sensor, placed inside a drilled hole in the glass substrate of a similar solar cell attached next to the measured solar cell. This PT100 temperature sensor was also used inside a drilled hole in the lowest part of the copper block, testing the limits of the stirling cooler without the assembled measurement setup, measuring temperatures down to 70 K. With assembled measurement setup, there seems, however, to be too much thermal load for the cooler and temperatures below 220 K were not accessible. The measurement procedure starts with cooling the cell down in the dark until there is no further decrease in the temperature due to the limitations of the stirling cooler. At that point the cooler is shut off and IV curves are measured during warm-up every 3 K first in the dark and then under illumination. There is no active heating of the cell, a complete warm-up process therefore takes approximately half a day. The illumination is a significant source of heat, but since it is shut off most of the time, the impact on the total warm-up time is rather small. It has to be noted here that we never observed any light-soak effect on the IV curves for solar cells with In_2S_3 buffer layer, neither at room temperature nor cooled down. Otherwise such an effect would be overlaying the results presented here because of the probably low relaxation speed of possible metastable effects in the cooled state. In between measurement cycles the cells were annealed on a hotplate in air, first for 10 min and then for an additional 30 min.
Subsets (every ~15 K) of the measured IV curves of three solar cells, prepared on untreated, water-treated, and Cd-treated absorber material, before and after the cumulative 40 min of annealing, are displayed in Fig. 3.4. The cells used for this measurement are from a different batch compared to those from Figs. 3.2 and 3.3, while the overall annealing behavior is very similar, the actual solar cell parameters differ. Looking at Fig. 3.4, the annealing procedure reduces the dark current at low temperatures. For the cells prepared on treated absorber, however, the temperature dependence of the diode current is modified such that the current at room temperature is similar to or even exceeds the current before annealing. Another interesting feature is the distinct roll-over of the IV curves after annealing at low temperature for the cells prepared on treated absorber. After annealing, the cell on untreated absorber also exhibits a low dark diode current, which however does not lead to a roll-over as there is a crossing of the IV curves with and without illumination. This curve crossing even at room temperature is no common feature of the cells with In_2S_3 buffer layer, that were prepared for this work, and may well be a peculiarity of this batch. The open circuit voltages, interpolated from the measured IV curves are plotted for each cell and each annealing state over the temperature in Fig. 3.5. An extrapolation of the measured values to the temperature $T = 0\,\mathrm{K}$ yields the activation energy U_a for the dominant recombination channel (c.f. Eq. (2.23)). The extrapolated values are printed in Table 3.3 together with

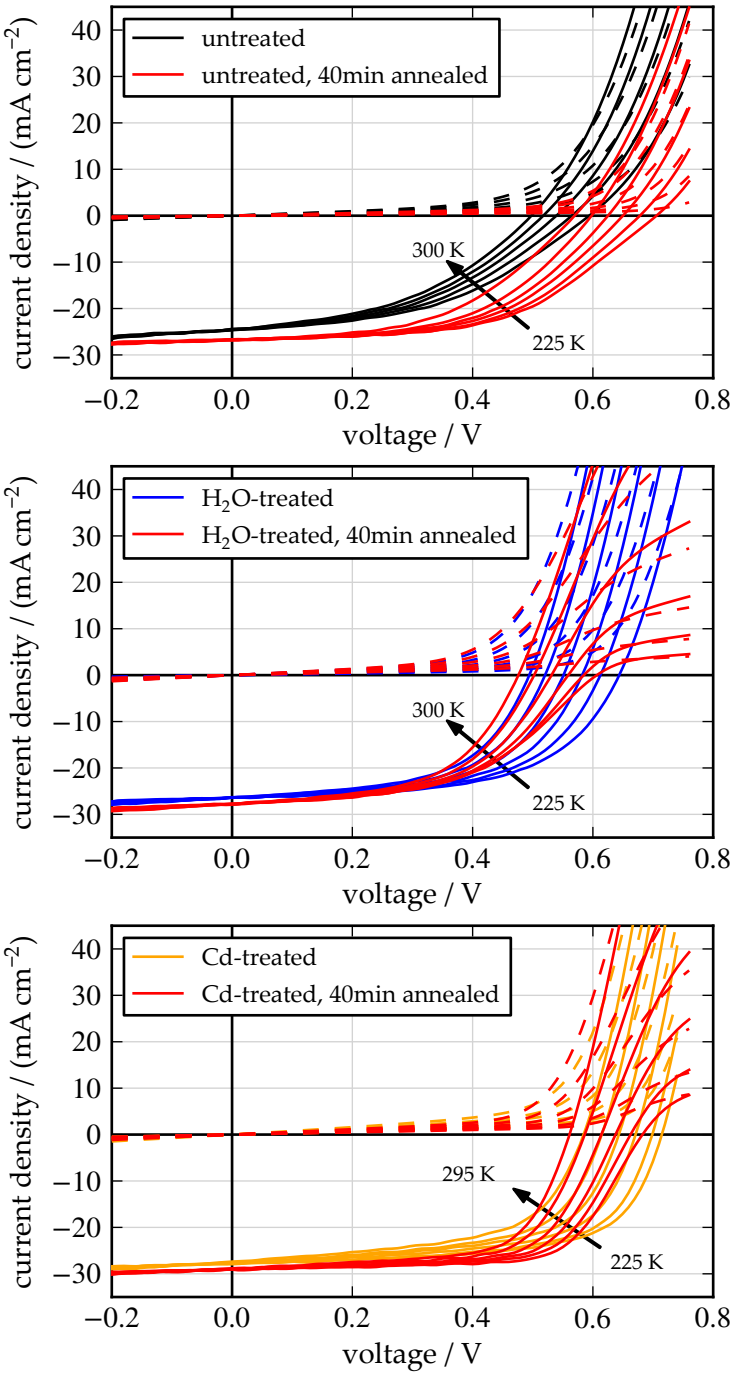

Figure 3.4: Temperature dependent IV curves of exemplary cells with In_2S_3 buffer layer, prepared on untreated, water-treated and Cd-treated absorber material, before and after 40 min of annealing at 200 °C in air. Measurements in the dark are displayed by dashed lines, measurements under simulated AM1.5 illumination are displayed by solid lines.

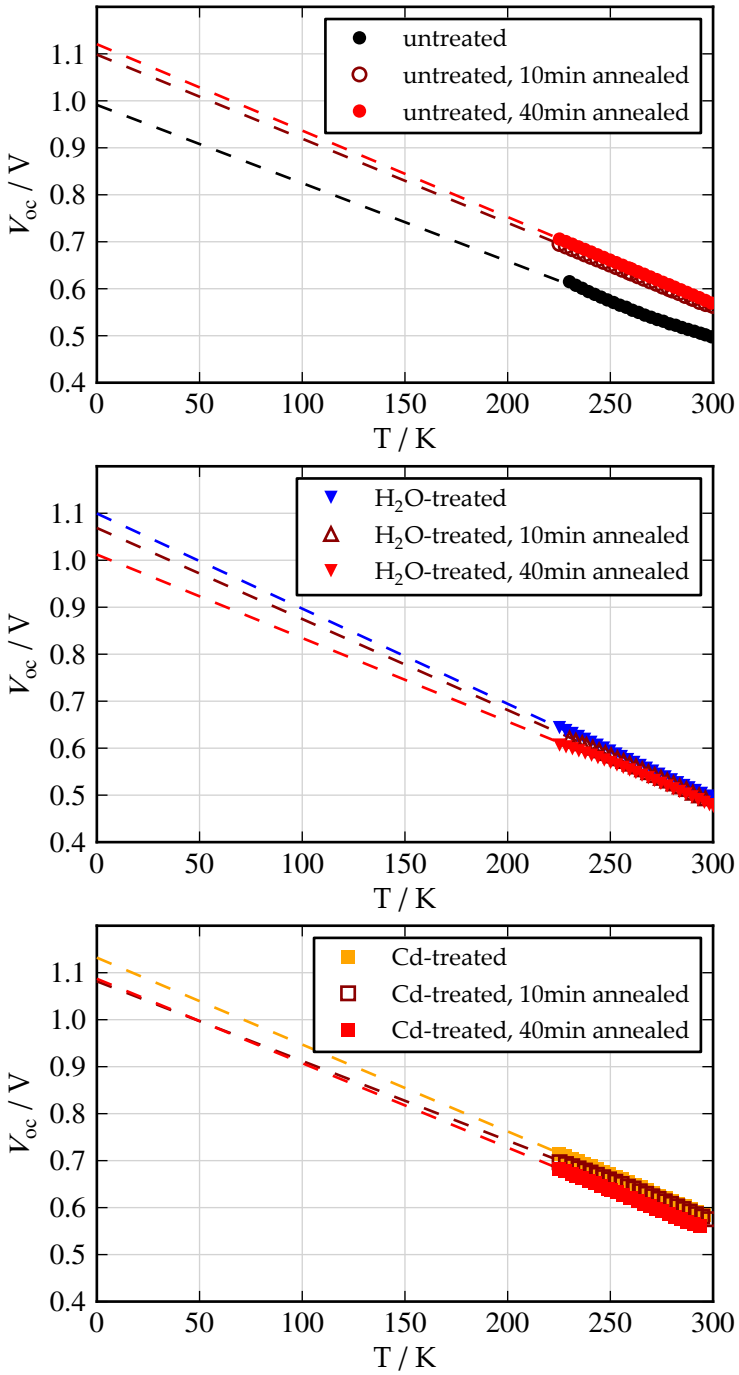

Figure 3.5: Temperature dependent open circuit voltages for cells prepared on untreated, water-treated, and Cd-treated absorber material, before and after annealing for 10 min and cumulative 40 min. Dashed lines show the extrapolation to $T = 0$ K, yielding the activation energy of the dominant recombination channel. The respective values are displayed in Table 3.3.

Table 3.3: Open circuit voltages and fill factors extracted from IV curves at $T \approx 292\,K$ and extrapolated open circuit voltages at $T = 0\,K$ for cells submitted to different wet-chemical treatments prior to buffer layer deposition.

	$V_{oc}(292\,K)$	fill factor (292 K)	$V_{oc}(0\,K)$
untreated			
not annealed	505 mV	43.5 %	991 mV
10 min annealed	572 mV	52.4 %	1101 mV
40 min annealed	581 mV	51.2 %	1117 mV
H_2O-treated			
not annealed	510 mV	56.5 %	1100 mV
10 min annealed	499 mV	58.8 %	1069 mV
40 min annealed	490 mV	54.6 %	1012 mV
Cd-treated			
not annealed	590 mV	58.6 %	1132 mV
10 min annealed	586 mV	64.4 %	1082 mV
40 min annealed	561 mV	66.0 %	1087 mV

the open circuit voltages and fill factors at room temperature. While the increase in open circuit voltage at room temperature is accompanied with an increase of activation energy from 0.99 eV to 1.12 eV for the cell prepared on untreated absorber material, the activation energy starts above 1.1 eV and slightly drops upon annealing, still staying above 1 eV, for the cells prepared on treated absorber. Each IV curve, measured in the dark, was fitted with the one diode model (Eq. (2.20)) and the resulting ideality factors A and saturation currents J_0 are displayed in Fig. 3.6. For the cell prepared on water-treated absorber, there is a significant deviation of the IV curve from the diode model after annealing, limiting the current at large voltages. This effect, visible as the roll-over in Fig. 3.4, prevents accurate curve fitting for this cell in the annealed state. Since the current-limitation has a later onset for the cell prepared on Cd-treated absorber material, it was possible to restrict the voltage range for the fitting so that fits were possible. This does, however, leave the data with an additional source of error to keep in mind. Regarding the actual data in Fig. 3.6, the wet chemical treatments have the effect of lowering the initial ideality factor. While the ideality factor for the cell on untreated absorber starts with 2.5 at room temperature and increases with decreasing temperature to 3.2 at 230 K, the ideality factor for the cells on treated absorber start with 2.0 and shows less temperature dependence. Upon annealing, the

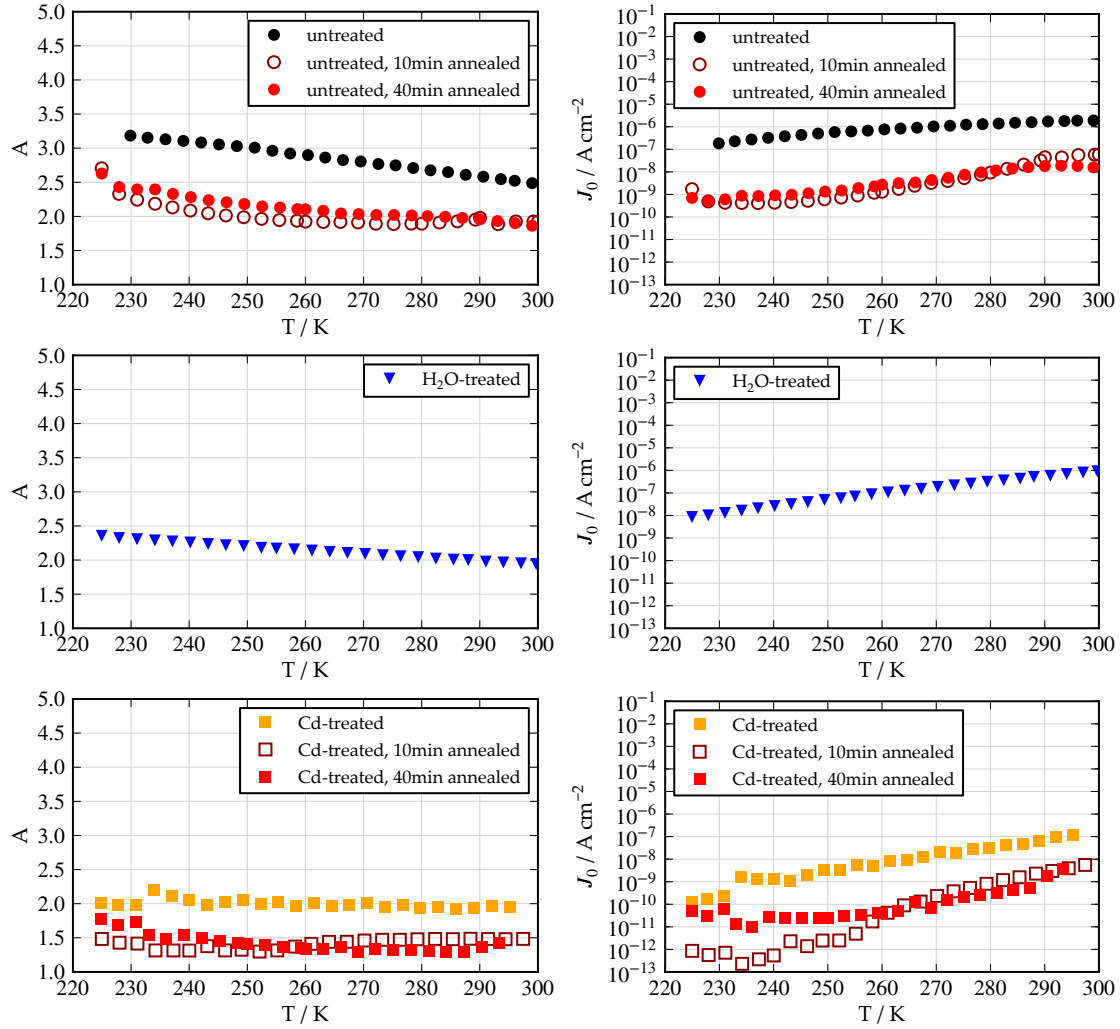

Figure 3.6: Ideality factors A and saturation currents J_0 from one diode model fits to the measured IV curves in the dark, partly displayed in Fig. 3.4. Due to characteristics differing significantly from the diode model, a curve fit was not possible for the cell prepared on water-treated absorber material. For the cell prepared on Cd-treated absorber, after annealing, the IV curves deviate from the diode model at large voltages, and though the range was limited for the fit, this is a possible source of error.

ideality factor of the cell on untreated absorber drops to 1.9 and looses most of its temperature dependency. For the cell prepared on Cd-treated absorber, annealing results in a drop of the ideality factor to ~1.5, still being largely independent of temperature.
From the discussion above, the increase of open circuit voltage for the cell prepared on untreated absorber can be understood by assuming a decrease of tunneling contribution to the interface recombination current. The high temperature dependent ideality factor shown in Fig. 3.6 indicates a tunneling contribution to the dark current. Tunneling enhanced interface recombination would lower the activation energy for recombination. The increase of U_a from 0.99 eV to 1.12 eV, accompanied by a decrease of the ideality factor to 2 therefore fits this explanation. The initially

higher U_a together with lower ideality factors for cells built on treated absorber can be interpreted as such that there is no dominant tunneling enhanced interface recombination for these cells.

Regardless of the wet-chemical absorber treatment and regardless of the batch (c.f. Figs. 3.2 to 3.4), all cells show an increased short circuit current and fill factor after annealing. Measurements of the external quantum efficiency (EQE) without bias illumination reveal that the gain in short circuit current is associated with an increase of the quantum efficiency in the red part of the spectrum. The results of the measurements are shown in Fig. 3.7. The EQE setup is calibrated with Si and Ge diodes. The Ge diode calibration, however, led to poor data quality due to its low sensitivity. The data is therefore shown here only up to wavelengths of 1100 nm with increasing uncertainty above 1050 nm. Such a gain in the red part of the spectrum can be due to reduced absorption in the window layer [56] when for example the free carrier density is reduced during annealing, leading to less free carrier absorption. This effect would be, however, voltage independent. Measurements with applied negative bias voltage show that the same gain in EQE in the red part of the spectrum could be achieved by applying $-0.5\,\mathrm{V}$ to the cell. The comparison of annealing and application of bias voltage is shown in Fig. 3.8. Such a voltage dependent gain in EQE in the red part of the spectrum can be explained by an increase of the collection length for generated electrons in the absorber. Within a simple model neglecting recombination at the back contact and losses in the space charge region [57, 58], the effective collection length L_{eff} of generated electrons is the sum of the space charge width and the diffusion length of electrons in the absorber material. The logic here is, that an electron has to reach the space charge region to be collected. The quantum efficiency can in this case be approximated by the equation [57]

$$QE \approx 1 - \exp\left(-\alpha L_{\mathrm{eff}}\right), \tag{3.1}$$

where α is the absorption coefficient of the absorber material. The number of collected photons, contributing to the QE is assumed to be the number of photons absorbed up to the point L_{eff} in the absorber. With the knowledge of the frequency dependent absorption coefficient, the effective collection length could be calculated for each measurement of the EQE. Since the absorption coefficient is, however, not known, the relation for absorption in a semiconductor with direct bandgap $\alpha = A\left(E_g - \hbar\omega\right)^{\frac{1}{2}}\left(\hbar\omega\right)^{-1}$ (c.f. Section 2.4.3) is used, combining the unknown factors to $L_{\mathrm{eff,norm}} = AL_{\mathrm{eff}}$. The equation

$$QE \approx 1 - \exp\left(-\left(E_g - \hbar\omega\right)^{\frac{1}{2}}\left(\hbar\omega\right)^{-1} L_{\mathrm{eff,norm}}\right) \tag{3.2}$$

is fitted to the red part of the spectrum for each measured and normalized set of EQE data, where the absorber band gap E_g is estimated with 1.05 eV. These

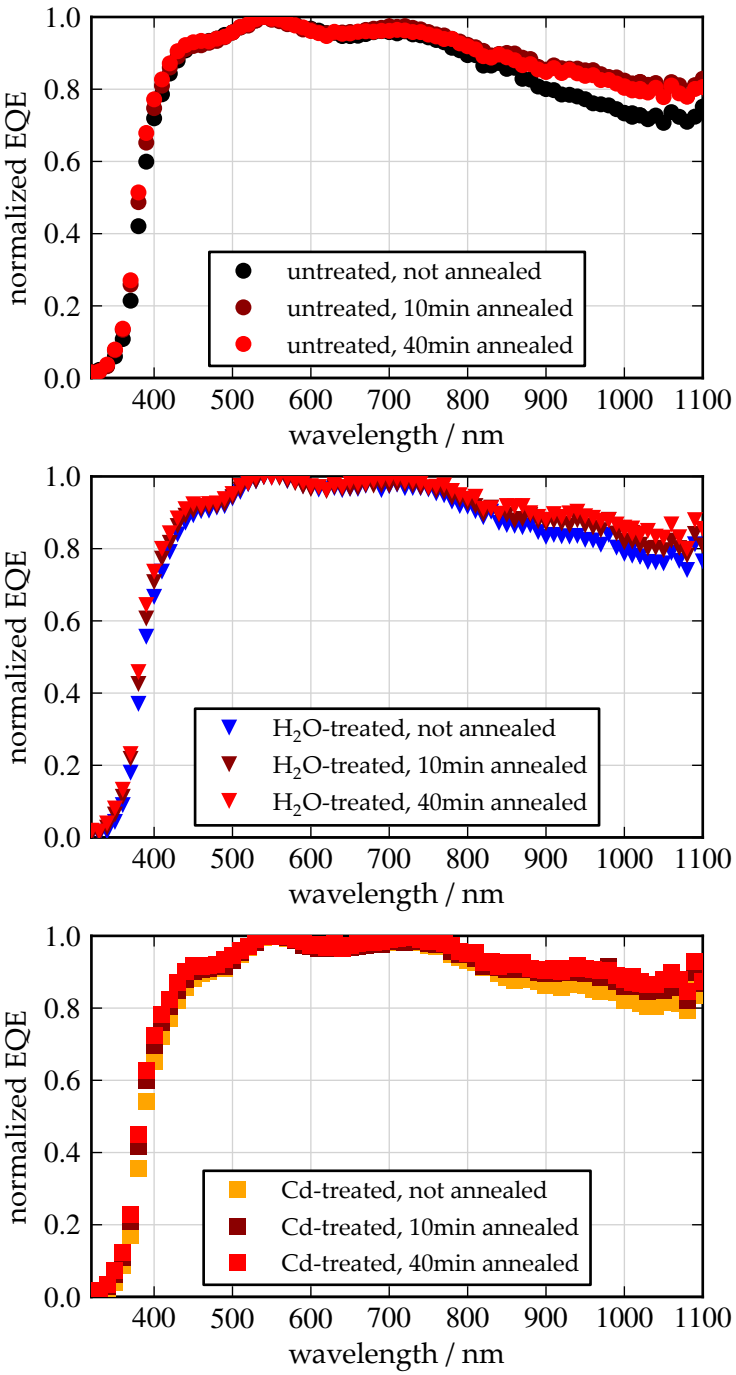

Figure 3.7: Plots of the normalized external quantum efficiencies for cells with an In_2S_3 buffer layer thickness of 21 nm, prepared on untreated, water-treated and Cd-treated absorber material. The cells were annealed at200 °C in air and an increased quantum efficiency in the red part of the spectrum is visible for all cells upon anneling.

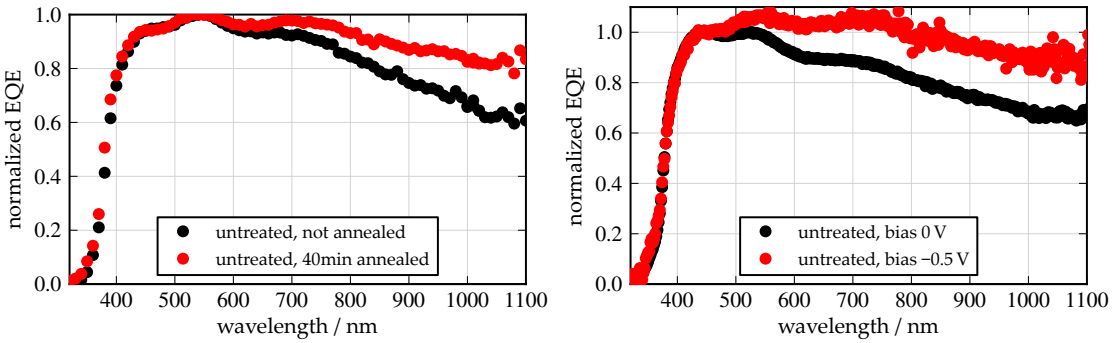

(a) Impact of annealing on the EQE.

(b) Impact of bias voltage on the EQE.

Figure 3.8: Plots of the normalized external quantum efficiencies for two similar cells with an In_2S_3 buffer layer thickness of 11 nm, prepared on untreated absorber, with and without applied negative bias voltage. The negative bias voltage leads to an increase of the external quantum efficiency in the red part of the spectrum. The normalization in the right figure (b) is done for the first hump in the EQE curve, and not for the maximum EQE, leading to values larger than 1.

Table 3.4: Relative increase of the collection length upon annealing or with applied bias voltage.

	$L_{\text{eff,norm}}(1) / L_{\text{eff,norm}}(2)$
untreated ($d = 11\,\text{nm}$), 40 min annealed	1.59
untreated ($d = 11\,\text{nm}$), $V_{\text{bias}} = -0.5\,\text{V}$	1.53
untreated ($d = 21\,\text{nm}$), 40 min annealed	1.24
H_2O-treated ($d = 21\,\text{nm}$), 40 min annealed	1.22
Cd-treated ($d = 21\,\text{nm}$), 40 min annealed	1.22

fits are displayed in Fig. 3.9 and the calculated increase of the parameter $L_{\text{eff,norm}}$ is gathered for each cell in Table 3.4. It is reasonable to assume that the optical properties of the CIGSSe material do not change significantly upon annealing at 200 °C, the calculated increase of $L_{\text{eff,norm}}$ can therefore directly translated into an increase of L_{eff}. For the case with applied bias, the increase of the effective collection length can directly be attributed to an increase of the space charge width. And while it is possible, it is probably not likely that the crystal quality of the CIGSSe material is so much improved, that the increased collection length can be attributed to a longer diffusion length of the electrons in the absorber. As a common effect for all cells, prepared on treated absorber material or not, an increased space charge width is the likely result of the annealing post-treatment.

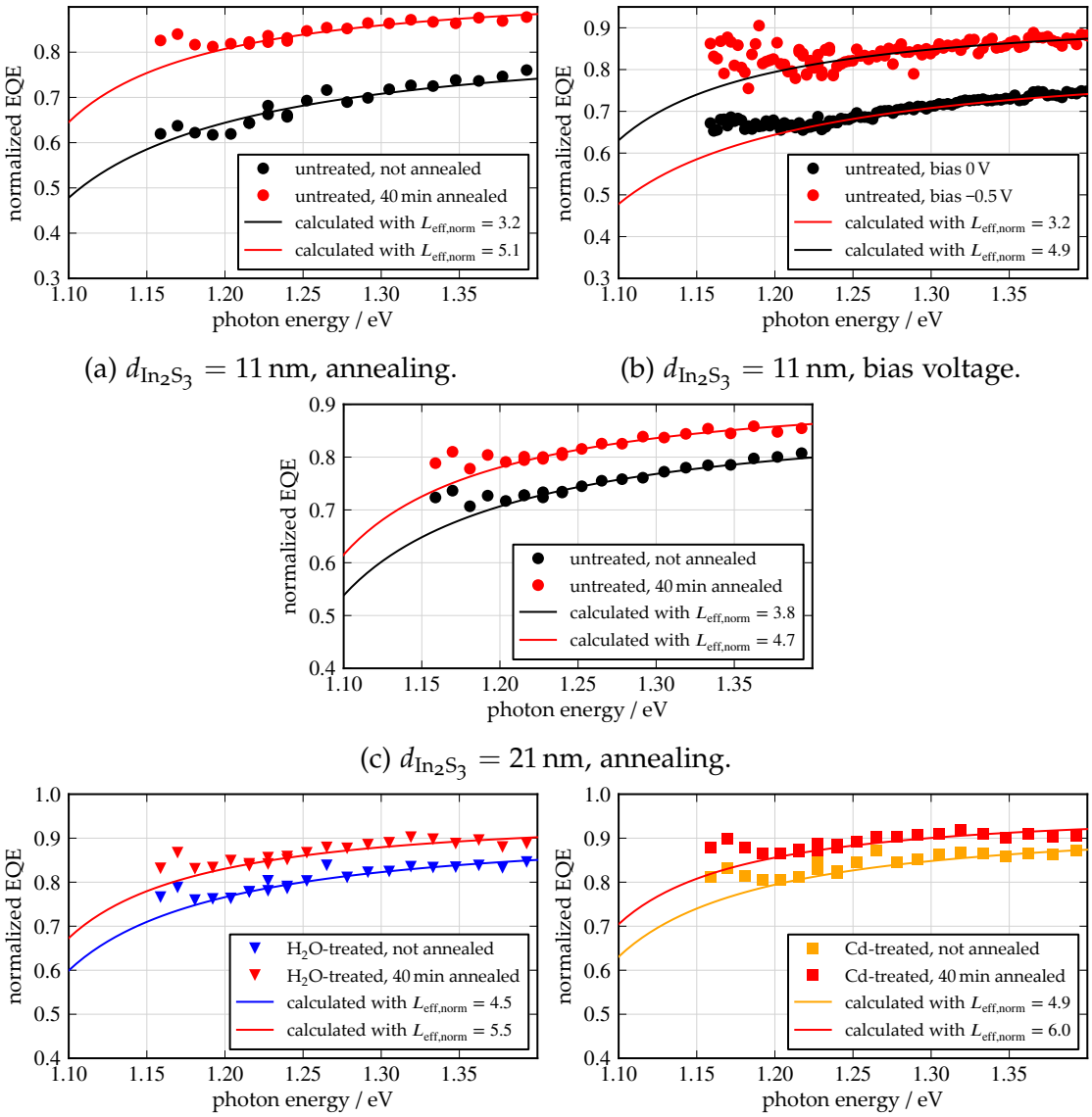

(a) $d_{In_2S_3} = 11\,nm$, annealing.

(b) $d_{In_2S_3} = 11\,nm$, bias voltage.

(c) $d_{In_2S_3} = 21\,nm$, annealing.

(d) $d_{In_2S_3} = 21\,nm$, H_2O-treated, annealing.

(e) $d_{In_2S_3} = 21\,nm$, Cd-treated, annealing.

Figure 3.9: Fitted curves for Eq. (3.2) to the sets of measured and normalized EQE data in the red part of the spectrum.

3.4 Modeling of the annealing effect

There are two effects of the annealing, to be carefully separated, regarding the annealing behavior of cells prepared on untreated, or wet-treated absorber material. The first effect, the increase of short circuit current and fill factor, observed for all cells is a attributed here to an increase in space charge width. The second effect, the increase or decrease of the open circuit voltage upon annealing, is where there is a distinct difference between cells with and without wet chemical treatment.
From the discussion above, the annealing procedure reduces an initially large contribution of tunneling to the recombination current. Possibly the total defect

density at the interface is lowered such that interface recombination is not dominant any more. Otherwise annealing would have to reduce the electric field near the interface, for this explanation to hold. A reason for this lower field could be a lower absorber doping, accompanied by an increased space charge region width in the absorber, possibly caused by elemental diffusion. A higher degree of n-type inversion directly at the interface, caused by the introduction of donor defects, would also lead to a larger SCR width due to the reduction of the voltage drop in buffer and window layer. However, the combination with the p+ layer would lead to an even higher electric field directly at the interface. The reduction of interface recombination might also be attributed to a diffusion of Cu from the absorber into the buffer layer, leading to a Cu depleted absorber surface with lower valence band maximum, thereby increasing the barrier for hole recombination at the absorber/buffer interface [44, 46, 48]. This type of explanation is, however, mostly valid for CIGSe type absorber. Since the sulfur content in the absorber used for this work, should lower the valence band maximum energy in the first place, the effect of the valence band lowering should be less important.
The cells prepared on wet-treated absorber, especially for the Cd treatment, show an initially higher effective collection length, a higher initial open circuit voltage and a higher activation energy of the recombination current above 1.1 eV. Together with the initially lower ideality factors, this indicates that the tunneling enhanced interface recombination is not dominant in these cells even in the state before annealing. A higher degree of n-type interface inversion might be expected for the Cd treatment, as Cd, incorporated at the CIGSSe surface would act as donor impurity [59]. The same effect, albeit less reproducible and less intense, can be achieved with the treatment in deionized water. The reason for this is unclear with possible contributions of the sodium concentration at the absorber surface and surface oxygenation. Surface oxygenation would passivate interface donor defects, leading to less band bending and a decrease of recombination centers. Additionally, Cu could be driven by oxygenation to diffuse into the absorber, reducing the p-type doping, thereby increasing the space charge region width [60]. These effects were detrimental if the cell was not initially limited by interface recombination, which, however, seems to be the case here.
In an attempt to explain the unusual open circuit voltage loss of the cells prepared on treated absorber material due to annealing, the attention is turned here to the observed increase of the effective collection length. A low collection length due to a high amount of p-type doping next to the absorber/buffer interface is a key feature of the p+ layer model [30, 50, 51]. The high p-type doping density near the interface, relative to the absorber bulk doping density, can possibly be explained by In_{Cu} antisites being in their neutral state near the interface or $V_{Se/S}$–V_{Cu} divacancies being in their acceptor state near the interface [28, 31]. The density of sulfur vacancies might be reduced by diffusion of sulfur from the buffer layer into the absorber, reducing the acceptor density. SCAPS simulations conducted to examine the influence of such a p+ layer and its reduction, fit the observed characteristics quite nicely. The results of simulations for two configurations of the p+ layer are depicted in Fig. 3.10. The width of the p+ layer was set constant to 60 nm

and the density of shallow acceptors was changed from $N_{A,p+} = 8 \times 10^{16}\,cm^{-3}$ to $N_{A,p+} = 3 \times 10^{16}\,cm^{-3}$ as indicated in the legend. A complete set of the simulation parameters can be found in Appendix A.2. The band diagrams in Fig. 3.10(a) are shown in equilibrium conditions without illumination, where the difference in space charge width is apparent. Another effect of the p+ layer is the overall energetic upshift of the absorber/buffer junction (in other terms: the decrease of electron concentration at the interface), leading to a barrier for the electron current, as described in Section 2.2.4. The model relies on a low concentration of donor impurities at the interface, leading to a configuration, where the density of holes is larger than the density of electrons at the interface. The electron concentration then is the limiting factor for recombination processes. In consequence, the band upshift effectively impedes the recombination current, leading to a lower dark current and a higher open circuit voltage under illumination in Fig. 3.10(b). Also, the loss in open circuit voltage upon removing this barrier is therefore directly correlated with the amount of interface defects assumed in the simulation. The gain in short circuit current and fill factor is reproduced here, the collection is not as voltage dependent without the p+ doping. Simulated quantum efficiencies shown in Fig. 3.10(c) show that, the effect of negative bias and removal of the high p+ doping is similar in the simulation, mirroring the experimental results as expected.

3.5 Conclusion for the PVD-In_2S_3 buffer layer

In this chapter, In_2S_3 thin films were introduced as a good choice for application as buffer layer in CIGSSe based solar cells. Final efficiencies above 14 % as well as no observed metastable behavior are promising with regard to industrial application. However, the characteristic annealing behavior, with no indication of a constant ideal annealing time, is a problem, that has to be addressed. It was here found that an increase in open circuit voltage can be achieved by wet-chemical treatments prior to buffer layer deposition, yielding efficient solar cells without annealing. Still, a deficient short circuit current and fill factor can only be increased by an annealing procedure, that proves to be detrimental for cells prepared on wet-treated absorber. Therefore there was no gain in the maximum efficiency.
The employ of wet chemical treatments allowed for a separation of two effects occurring during annealing. A two-part explanation for this annealing behavior is therefore offered here. First, the interface quality can be improved by either annealing or wet-chemical treatments, leading to less tunneling enhanced interface recombination. Second, the initially small collection length due to a p+ layer is only improved by annealing, removing an energetic barrier at the same time. Because of the low electron density at the interface, a removal of the barrier (increasing the electron density) leads to potential voltage losses if the defect density at the interface is high. Due to this effect, a careful balancing of the annealing time is needed in order to reach maximum efficiencies.

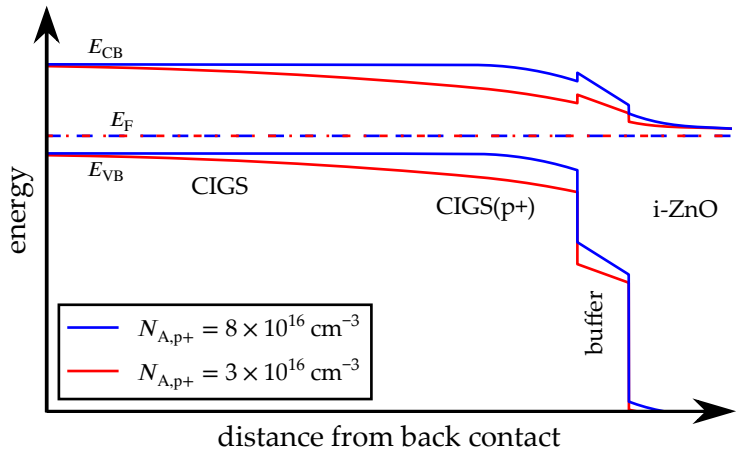

(a) Simulated band diagrams in equilibrium without illumination. The Fermi level is given by a dashed line.

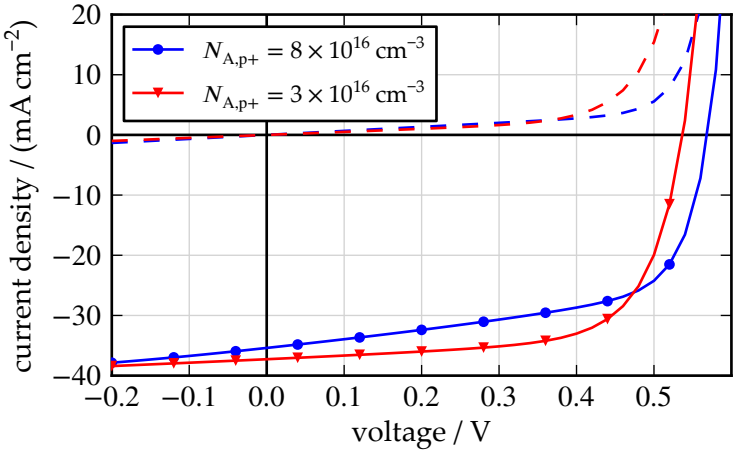

(b) Simulated IV curves.

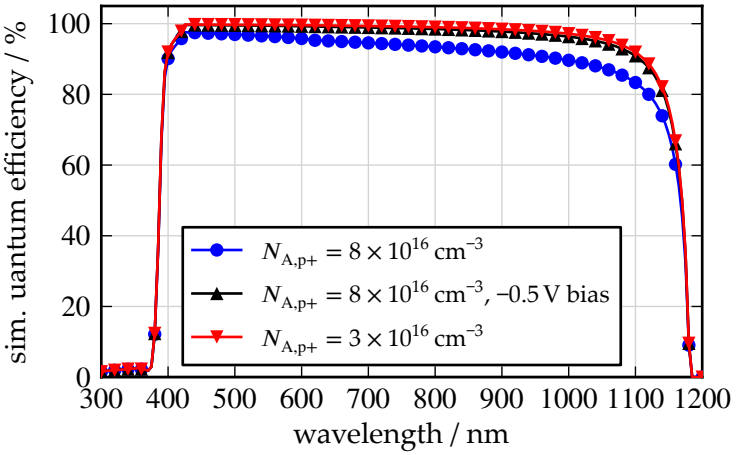

(c) Simulated quantum efficiencies without bias illumination and with/without negative bias voltage.

Figure 3.10: Results of the SCAPS simulations for the p+ layer model with parameters from Appendix A.2.

Some of the observed effects in this chapter have not been addressed with the amount they might deserve. It was noted, that In_2S_3 buffer layer thickness has an influence on the annealing behavior. It was also shown that the cells prepared on treated absorber show an impeded current at low temperatures. Additional analysis of the elemental composition of absorber surface and buffer layer, before and after annealing, would give further insights. However, due to decisions within the Robert Bosch GmbH and the publicly funded NeuMas project, the investigations of the PVD-In_2S_3 buffer layer ceased at this point and the focus switched to Zn(O,S) based layers instead. The main issues were efficiencies of cells with In_2S_3 buffer layer being reproducibly lower compared to other materials and growing uncertainty about the reliability and cost of an up-scaled evaporation process. The second and larger part of this work will therefore be concerned with chemically deposited Zn(O,S) buffer layers.

References

[6] P. Würfel, *Physics of Solar Cells: From Principles to New Concepts*, (WILEY-VCH Verlag GmbH & Co. KGaA, 2005), ISBN: 978-3-527-61854-5 (Cited on pages 5, 9, 10, 42).

[7] U. Rau and H.-W. Schock, "Cu(In,Ga)Se_2 solar cells", in *Clean Electricity from Photovoltaics*, (World Scientific, 2001), ISBN: 978-1-86094-161-0 Chap. 7, pp. 277–345 (Cited on pages 5, 9, 15–17, 20, 42).

[28] S. Lany and A. Zunger, "Light-and bias-induced metastabilities in Cu(In,Ga)Se_2 based solar cells caused by the (V_{Se}-V_{Cu}) vacancy complex", Journal of Applied Physics **100**, 113725 (2006) (Cited on pages 22, 55).

[30] M. Igalson, A. Urbaniak, P. Zabierowski, H. A. Maksoud, M. Buffiere, N. Barreau, and S. Spiering, "Red-blue effect in Cu(In,Ga)Se_2-based devices revisited", Thin Solid Films **535**, 302–306 (2013) (Cited on pages 22, 40, 55, 63).

[31] S. Lany and A. Zunger, "Intrinsic DX Centers in Ternary Chalcopyrite Semiconductors", Physical Review Letters **100**, 016401 (2008) (Cited on pages 22, 55).

[42] S. Spiering, A. Nowitzki, F. Kessler, M. Igalson, and H. A. Maksoud, "Optimization of buffer-window layer system for CIGS thin film devices with indium sulphide buffer by in-line evaporation ", Solar Energy Materials and Solar Cells **144**, 544–550 (2016) (Cited on pages 39, 40).

[43] AVANCIS GmbH, *Module with record efficiency from AVANCIS: Fraunhofer ISE certifies CIGS solar module with an efficiency of 17.9%*. online press release, May 2016, http://www.avancis.de/en/press/news/article/avancis-erzielt-erneuten-wirkungsgradrekord-fraunhofer-ise-zertifiziert-cigs-solarmodul-mit-wirkungsgrad-von-179/ (visited on 05/16/2016) (Cited on page 39).

[44] N. Barreau, "Indium sulfide and relatives in the world of photovoltaics", Solar Energy **83**, 363–371 (2009) (Cited on pages 39, 55).

[45] M. Bär, N. Barreau, F. Couzinié-Devy, L. Weinhardt, R. G. Wilks, J. Kessler, and C. Heske, "Impact of Annealing-Induced Intermixing on the Electronic Level Alignment at the In_2S_3/Cu(In,Ga)Se_2 Thin-Film Solar Cell Interface", ACS Applied Materials & Interfaces **8**, 2120–2124 (2016) (Cited on pages 39, 40).

[46] S. Spiering, S. Chowdhury, A. Drese, D. Hariskos, A. Eicke, and M. Powalla, "Evaporated indium sulphide as buffer layer in Cu(In,Ga)Se_2-based solar cells", in 21st European Photovoltaic Solar Energy Conference (Sept. 2006), pp. 1847–1852 (Cited on pages 39, 55).

[47] P. Pistor, A. Grimm, D. Kieven, F. Hergert, A. Jasenek, and R. Klenk, "Dry vacuum buffers for industrial chalcopyrite absorbers from a sequential absorber process route", in Photovoltaic Specialists Conference (PVSC), 2011 37th IEEE (June 2011), pp. 002808–002812 (Cited on page 39).

[48] P. Pistor, "Formation and Electronic Properties of In_2S_3/Cu(In,Ga)Se_2 Junctions and Related Thin Film Solar Cells", PhD thesis (Freie Universität Berlin, 2009) (Cited on pages 40, 55).

[49] H. A. Maksoud, M. Igalson, and S. Spiering, "Influence of post-deposition heat treatment on electrical transport properties of In_2S_3-buffered Cu(In,Ga)Se_2 cells", Thin Solid Films **535**, 158–161 (2013) (Cited on page 40).

[50] M. Topič, F. Smole, J. Furlan, and M. A. Contreras, "Examination of CdS/-CIGS Solar Cell Temperature Dependence", in 14th European Photovoltaic Solar Energy Conference (June 1997), pp. 2139–2142 (Cited on pages 40, 55).

[51] A. Niemegeers, M. Burgelman, R. Herberholz, U. Rau, D. Hariskos, and H.-W. Schock, "Model for electronic transport in Cu(In,Ga)Se_2 solar cells", Progress in Photovoltaics: Research and Applications **6**, 407–421 (1998) (Cited on pages 40, 55).

[52] R. Klenk, "Characterisation and modelling of chalcopyrite solar cells", Thin Solid Films **387**, 135–140 (2001) (Cited on page 40).

[53] K. Ramanathan, F. Hasoon, S. Smith, A. Mascarenhas, H. Al-Thani, J. Alleman, H. Ullal, J. Keane, P. Johnson, and J. Sites, "Properties of Cd and Zn partial electrolyte treated CIGS solar cells", in Photovoltaic Specialists Conference, 2002. Conference Record of the Twenty-Ninth IEEE (May 2002), pp. 523–526 (Cited on page 40).

[54] M. Bär, L. Weinhardt, C. Heske, H.-J. Muffler, M. C. Lux-Steiner, E. Umbach, and C. Fischer, "Cd^{2+}/NH_3 treatment of Cu(In,Ga)$(S,Se)_2$ thin-film solar cell absorbers: a model for the performance-enhancing processes in the partial electrolyte", Progress in Photovoltaics: Research and Applications **13**, 571–577 (2005) (Cited on page 40).

[55] M. Bär, U. Bloeck, H.-J. Muffler, M. Lux-Steiner, C.-H. Fischer, M. Giersig, T. Niesen, and F. Karg, "Cd^{2+}/ NH_3-treatment of Cu(In,Ga)(S,Se)$_2$: Impact on the properties of ZnO layers deposited by the ion layer gas reaction method", Journal of Applied Physics **97**, 014905 (2005) (Cited on page 40).

[56] S. Siebentritt, "What limits the efficiency of chalcopyrite solar cells?", Solar Energy Materials and Solar Cells **95**, 1471–1476 (2011) (Cited on page 51).

[57] R. Klenk, H.-W. Schock, and W. H. Bloss, "Photocurrent collection in thin film solar cells-calculation and characterization for CuGaSe2/(Zn,Cd)S", in 12th European Photovoltaic Solar Energy Conference (Apr. 1994), pp. 1588–1591 (Cited on page 51).

[58] S. S. Hegedus and W. N. Shafarman, "Thin-film solar cells: device measurements and analysis", Progress in Photovoltaics: Research and Applications **12**, 155–176 (2004) (Cited on page 51).

[59] C. Persson, Y.-J. Zhao, S. Lany, and A. Zunger, "*n*-type doping of $CuInSe_2$ and $CuGaSe_2$", Phys. Rev. B **72**, 035211 (2005) (Cited on page 55).

[60] L. Kronik, U. Rau, J.-F. Guillemoles, D. Braunger, H.-W. Schock, and D. Cahen, "Interface redox engineering of Cu(In,Ga)Se_2–based solar cells: oxygen, sodium, and chemical bath effects", Thin Solid Films **361–362**, 353–359 (2000) (Cited on page 55).

4 Chapter 4 CBD-Zn(O,S)

A novel, fast process for the deposition of Zn(O,S) buffer layers on submodule sized substrates is presented in this chapter. The resulting solar cell characteristics (effects of annealing and prolonged illumination) are discussed within the framework of theoretical considerations involving an electronic barrier for generated charge carriers. Countermeasures such as an improved window layer deposition process, absorber optimization, and intentional buffer layer doping, all with the aim of reducing the necessity for post-treatments, are presented as well.

4.1 Literature survey

Zn(O,S) based thin films are one of the most frequently employed choices as cadmium-free buffer layers for chalcopyrite solar cells. Reviews of the progress in developing these layers with application as buffer layers can be found in [61], [62] and [63]. A wide range of chemical bath deposition routes is given in [64]. The current record efficiency for a CIGSe based solar cell with Zn(O,S) buffer layer is 21 % on cell level [65] and the record on submodule level was increased to 17.9 % [66]. These results are close to the records set with CdS buffered cells usually compensating a reduced open circuit voltage with increased short circuit currents due to the larger band gap of Zn(O,S) compared to CdS. While there is an increasing interest in alternative deposition methods such as atomic layer deposition [38, 67] and RF sputtering from mixed ZnO/ZnS compound targets [68, 69], the most commonly utilized method for the deposition of Zn(O,S) buffer layers remains the chemical bath deposition (CBD). Mostly, the basic process chemistry is inspired by standard alkaline CBD processes that were established for the deposition of CdS buffer layers, using solution formulations with ammonia as complexing agent and pH buffer and thiourea as sulfur source. While there is little oxide or hydroxide formation in CdS deposition processes, due to the more similar solubility products of zinc sulfide, oxide, and hydroxide, there is always a formation of Zn(S,O,OH) compounds [70]. In aqueous solutions, the solubility product of the cadmium or zinc sulfide compounds is generally lower compared to the oxide or hydroxide compounds, meaning that a formation of sulfide is preferred in the whole pH range. At pH larger than 10, the solubility products of the oxide and hydroxide compounds are decreasing and the probability of oxide

or hydroxide formation is increasing. Additional dependencies on the chemical bath composition and temperature exist as described by Hubert et al. [71]. For the sake of simplicity, I will stick with the nomenclature of Zn(O,S), while it has to be kept in mind that chemically deposited films will most likely contain hydroxides. Regarding the film formation, there are two general types of processes occurring in the chemical bath. Heterogeneous reactions, catalyzed at the CIGSSe surface, lead to crystal growth directly on the substrate (ion-by-ion process). Homogeneous reactions lead to particle formation in the bulk of the process solution, whereupon particles may be adsorbed at the substrate surface and form a layer there (cluster-by-cluster process). A detailed discussion of these mechanisms can be found in [72]. Generally, the first few atomic layers are considered to grow from a heterogeneous reaction while the majority of the Zn(O,S) layer is assumed to grow from precipitating nanoparticles [73, 74].
Usually CBD processes for Zn(O,S) deposition are slow, taking up to 20 min for a deposition of 30 nm [66, 75–79]. There are several approaches to reduce this deposition time: reducing the ammonia concentration [73], working with preheated reagents [79], adding H_2O_2 to the process solution [80, 81], or by replacing thiourea with the faster decomposing thioacetamide (TAA) [78]. The main idea is to increase the amount of free Zn^{2+} and S^{-} ions in the process solution. This can, however, lead to a shift towards a more homogeneous reaction, altering the layer properties or even inhibit layer formation [74, 78]. The addition of stronger complexing agents in addition to ammonia is therefore employed to balance this effect. Complexing agents found in the literature include hydracine [82], nitrilotriacetatic acid [78, 83], citrate [84–86], ethanolamine [85], triethanolamine [87], methylamine [87], dimethylamine [87], ethylenediamine [88], and ethylenediaminetetraacetatic acid [89]. Generally, improved deposition times of 5 min to 8 min for 30 nm could be achieved by these means [78, 79, 81]. The process utilized in this work uses N-(2-hydroxyethyl)ethylenediaminetriacetic acid (HEEDTA) as complexing agent, completely replacing ammonia, while the pH is adjusted by addition of NaOH. Ammonia-free processes have been reported before at moderate pH [83, 89]. In this work the deposition will take place at high pH > 13, theoretically shifting the process in the direction of increasing oxide/hydroxide precipitation [70]. The original idea and the initial development of this process is attributed to Jürgen Hackenberg and Rolf Keller at the Corporate Research of the Robert Bosch GmbH.
Solar cells prepared with buffer layers from this new CBD process initially show low efficiencies due to large S-shape distortions of the IV curve. Therefore, in the following chapters, there will be extensive coverage of the effect of post-treatments on the solar cell efficiencies after cell fabrication. There are many reports in the literature, showing that chalcopyrite based solar cells with CBD-Zn(O,S) buffer layer are affected by annealing treatments, by prolonged illumination (light-soak) and by a combination of both (hot light-soak). The effect of annealing post-treatments is acknowledged by others to reduce the initial S-shape distortion of the IV curve [90–93]. Witte et al. observed an increase of doping concentration and shorter depletion width in the CIGSe after the annealing, which they attribute

to Na, observed to diffuse towards the buffer layer. They also observe diffusion of Zn and S from the buffer layer into the CIGSe and a slight decrease of the [S]/([S]+[O]) ratio and the band gap of the buffer layer. Further, a decrease of hydroxide, sulfate and carbon concentration was observed upon annealing. All these effects were rather small at an annealing temperature of 200 °C, commonly used for the post-treatment, and larger at 300 °C. Kobayashi et al. on the other hand, did not observe any change of [S]/([S]+[O]) upon annealing in the dark [92]. Naghavi et al. noticed that the annealing treatment can to some extent substitute further light-soaking treatments, both having a similar effect [91, 93]. They also observed that there is a significant lowering of the initial S-shape distortion of the IV curve, when the standard i-ZnO window layer is replaced by $Zn_{0.74}Mg_{0.26}O$. They ascribe this to the formation of magnesium hydroxide, dehydrating the buffer layer. Further, they observe an improvement, when the first few nanometers of the window layer are sputtered without the presence of oxygen in the sputter gas, and ascribe this to an increase in buffer layer doping due to the release of oxygen from the buffer layer. In addition, it is observed, that there is a larger effect of annealing and light-soaking due to initially larger IV curve distortions, when the buffer layer thickness is increased.

The role of the light-soak post-treatment is discussed in the literature to an even greater extend. There are three main threads in the discussion, all acknowledging that light in the blue or ultraviolet part of the spectrum plays a crucial role. First, chalcogenide buffer layers, including CdS, are argued to have a high amount of compensating acceptor traps, that are neutralized when charge carriers are generated in the buffer layer [32, 94]. Light-soaking then would mainly increase the effective net doping concentration of the buffer layer. Along the same line, it is argued that acceptor-like defects at the interfaces play the same role, on the base of experimental evidence that the buffer/window interface is critical [95]. Second, it is argued by Igalson et al. that the presence of metastable defect configurations in the CIGSe absorber is the cause for the light-soaking behavior [30, 96]. Possible candidates are the V_{Se}-V_{Cu} vacancy complex or the In_{Cu} antisite DX center as introduced in Section 2.3.2. These defects undergo a transition from acceptor into a metastable donor configuration, when free holes are captured. Illumination with blue light then leads to a decrease of a highly p-doped layer in the absorber near the interface. While CdS supplies free holes to the absorber near the interface, larger band gap materials do not generate a sufficient amount of free holes, thereby increasing the light-soak time. At last, there is the observation by Kobayashi et al. that prolonged illumination of CIGSSe/Zn(O,S) layer stacks leads to a significant diffusion of sulfur from the buffer layer into the absorber, thereby reducing [S]/([S]+[O]) in the buffer layer [92]. This effect is facilitated by additional application of heat, leading to the heat light-soaking treatment usually employed in their group. In contrast to Witte et al. [90] they also observe that the concentration of hydroxides is not affected by annealing or light-soaking.

Summarizing, without exception all experimental evidence points to a lowering of an electronic barrier upon annealing or light-soaking [30, 32, 90–97] and it is undisputed that one key factor for this barrier is the conduction band offset be-

tween CIGSe and Zn(O,S) (cf. Sections 2.2.4 and 2.3.1). It has been shown in theory and experiment that this offset is large for pure ZnS and reduced with increasing oxygen content in the layer [25, 38]. Thus, the inevitable incorporation of oxygen into CBD-Zn(O,S) is actually advantageous and should even be increased in case of observed S-shape distortions of the IV curve. However, there has been no report of successfully depositing Zn(O,S) with [S]/([S]+[O]) less than 60 % on CIGSe. In the literature cited above, the reported range is between 60 % and 80 %. The inability to lower the sulfur content within the framework of CBD is one reason for the increased interest in atomic layer deposition and sputtering as alternative deposition methods.

As mentioned, it was already observed by others [32, 93, 94] that an increase in buffer layer doping would be beneficial for the solar cell performance. In the case of pure ZnS, intentional doping is difficult because both n-type and p-type pinning energies lie inside the band gap, making degenerate doping impossible due to Fermi-level-induced compensation effects [98]. When the Fermi level approaches either conduction band or valence band, the formation energy of intrinsic defects (e.g. vacancies and interstitials) is lowered until, at the pinning energies, spontaneous formation of these defects occurs. Nevertheless it has been shown possible to achieve n-type doping for ZnS and Zn(O,S) with aluminum [86, 99]. P-type doping has been demonstrated with Cu [100]. CdS and CdZn(O,S) layers have been doped with indium [101], aluminum [102] and boron in the form of boric acid [103, 104]. Aluminum can be introduced into the CBD process in the form of aluminum sulfate [86, 102]. In this work aluminum potassium sulfate and boric acid will be added to the CBD process for Zn(O,S), inspired by the literature cited above.

In this chapter there will also be a discussion of the influence of the Zn(O,S) interface with the window layer on the solar cell characteristics. As mentioned above, key experiments on this topic have already been published by Naghavi et al. [93]. Other groups also report the omission of oxygen in the sputter gas during i-ZnO deposition [97] or the usage of ZnMgO instead of i-ZnO [69]. A systematic simulation of the conduction band offset at the buffer/window interface, the buffer layer doping, and buffer layer thickness was published by Sozzi et al., showing that the S-shape IV curve distortion can be reduced, when a window layer with lower electron affinity than i-ZnO is employed or the buffer layer doping is significantly increased [105].

Partly contrary to our findings, Buffière et al. recently reported that they achieved devices with less pronounced light-soaking effect by employing thick buffer layers ($d \sim 100\,\mathrm{nm}$), increasing the resistivity of the i-ZnO window layer, and working on CIGSe close to stoichiometry ([Cu]/([Ga]+[In]) ~ 1) [97].

Experiment and simulation are therefore revisited together in this work.

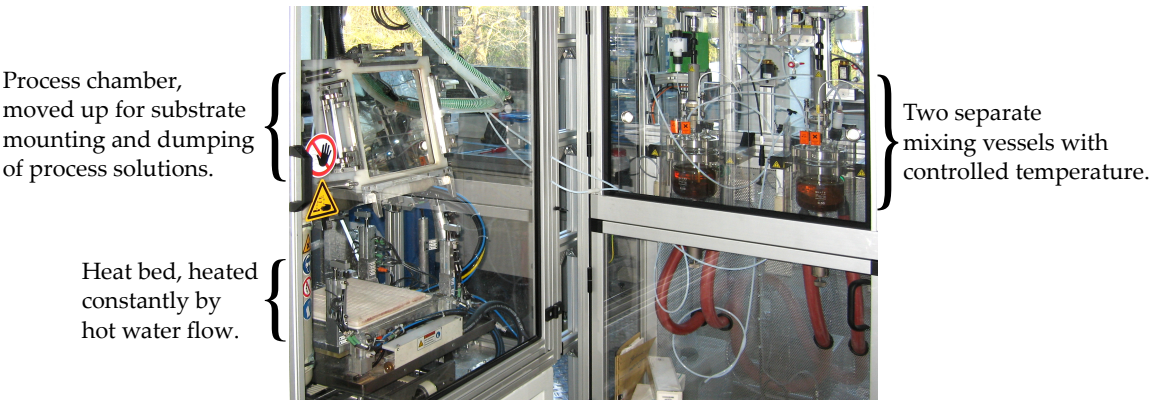

Figure 4.1: Photograph of the equipment used for Zn(O,S) depositions on 30 cm × 30 cm sized substrates in this work.

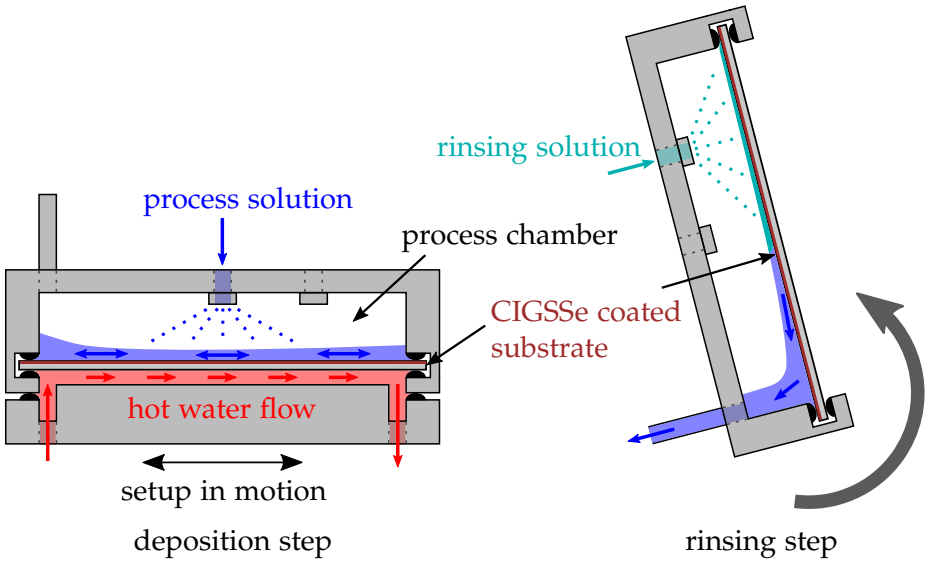

Figure 4.2: Sketch of the process chamber during the deposition step and the rinsing step. Heating during the deposition step is accomplished by a hot water flow on the glass side of the substrate. The process solution and the rinsing solution are sprayed on the CIGSSe coated side of the substrate. During rinsing, the process chamber is lifted and rotated in order to drain the solutions inside.

4.2 Process description

Zn(O,S) layers were chemically deposited with a novel and fast alkaline process on 30 cm × 30 cm sub-module sized CIGSSe substrates, fabricated by the Bosch Solar CISTech GmbH as described in Section 2.5.1.

The equipment utilized for the deposition process is depicted in the photograph in Fig. 4.1. It consists of a process chamber, that can be lowered to a heat bed, heating the glass side of the substrate with constant hot water flow, while the CIGSSe side of the substrate is exposed to the process solution, sprayed into the process

chamber. A sketch of process chamber and heat bed are given in Fig. 4.2. During the deposition process, the whole setup, heat bed and process chamber, is set in periodic motion, ensuring a constant mixing of the solution in the process chamber. The homogeneity of deposited films was found in our group to depend on the amplitude and pattern of this motion. The second part of the equipment consists of two temperature controlled mixing vessels, where automatic gravimetric dosing of pre-defined amounts of stock solution can be combined with manual volumetric dosing of solutions. Since the vessel openings are small, the process solutions are mixed using stock solutions, rather than adding chemicals in solid form. When a process is started, the content of a mixing vessel can be transferred to the process chamber by pressure of additional nitrogen gas flow, spraying the solution onto the substrate.
The sample processing procedure consists of three separate steps, a pre-treatment step, the actual Zn(O,S) deposition, and a rinsing step. During the pre-treatment step, the substrate is heated up to 75 °C. This is taking roughly the 5 min that are used as a standard time. Additional chemicals can be used in order to modify the CIGSSe surface prior to Zn(O,S) deposition. In addition to having a potential influence on the final cell efficiencies, this surface modification can also have an influence on the deposition rate. As a standard, 2.5 % ammonia solution containing 15 mM HEEDTA trisodium salt is used, ensuring very reproducible deposition rates and efficiencies. The pre-treatment solution is dumped and the substrate is rinsed with deionized water before the deposition process is started by transferring the pre-heated process solution to the process chamber. This solution contains 5 mM $ZnSO_4$ heptahydrate, 15 mM HEEDTA trisodium salt, 0.56 M NaOH and 10 mM TAA, dissolved in deionized water. Solutions with 20 mM $ZnSO_4$ heptahydrate (100 mL), 100 mM HEEDTA trisodium salt (60 mL), 2.5 M NaOH (90 mL), and 133 mM TAA (30 mL) dissolved in deionized water were used as stock solutions. Adding 120 mL deionized water, the resulting 400 mL were found to be sufficient for homogeneous deposition processes on 30 cm × 30 cm sized substrates. The TAA stock solution is added after heating the process solution to 75 °C and directly before transferring to the process chamber to prevent precipitation of Zn(O,S) in the mixing vessel. During deposition, the substrate temperature kept at 75 °C. The deposition time is usually set to be between 3 min and 4.5 min for a target layer thickness of ~30 nm and has to be adjusted sometimes, accounting for different surface conditions of the CIGSSe substrate. The deposition time has to be lowered to 2 min when an adapter mask is used for deposition on 10 cm × 10 cm sized substrates. The process solution is dumped after the process and the substrate is washed with 2.5 % ammonia solution in the rinsing step in order to remove loosely attached precipitates and dissolve hydroxides. After drying the substrate in nitrogen gas flow, it is then submitted to a heat treatment at 190 °C for 10 min in an oven with hot air circulation in order to dehydrate the deposited layer.

4.3 Film properties

The described CBD process leads to a fast Zn(O,S) thin film formation, starting before the process solution is becoming turbid. This indicates a fast heterogeneous reaction at the CIGSSe surface. The homogeneous reaction in the bulk of the solution, leading to Zn(O,S) precipitation, is also contributing to the layer formation at a later point. The fast heterogeneous reaction might be facilitated in this process by the single hydroxyl group of the HEEDTA, which not being used for the complexation might attach itself to the substrate surface. A look at the SEM pictures displayed in Fig. 4.3, especially in Fig. 4.3(b), shows a flowerlike surface morphology. The film exhibits good edge coverage and a low density of uncovered pinholes. The large feature visible in Fig. 4.3(a) stems from the absorber substrate and not from the CBD process. In addition to the flowerlike Zn(O,S) thin film, there are a number of small agglomerates visible in the SEM pictures. These agglomerates consist of spherical particles bound together in chains and clusters. From Fig. 4.3(c) it is apparent, that these agglomerates may be partly connected to the thin film, explaining why they are not removed with the rinsing procedure. From Fig. 4.3(a), although the number of clearly visible agglomerates is large, they are evenly distributed and the density is by far too low to cover the substrate surface. They are probably precipitating from the homogeneous reaction in the bulk of the solution, where they grow to their size larger than 100 nm, while the thin film is formed by a heterogeneous reaction and smaller particles from a homogeneous reaction closer to the substrate. A cross section image of a thicker layer, deposited in two deposition steps, shown in Fig. 4.3(d), shows that the Zn(O,S) layer itself is not crystalline but seems to be formed as an amorphous layer. Looking at Figs. 4.3(e) and 4.3(f), displaying SEM images of the same thicker film, many cracks in the layer are apparent. While the thinner layer is crack-free, the thick layer shows these cracks on the whole investigated area. In the cross section, it is visible that these cracks are restricted to the Zn(O,S) layer and are accompanied by slight delamination. Possibly the layer cracking is happening during the annealing process, leading to a densification of the layer, whereupon it cracks at a weak spot, i.e. near substrate grain boundaries. The thinner layer is more tolerant towards strain and therefore does not crack. Similar cracking of thick Zn(O,S) layers was observed by Buffière et al. [97]. In principle this seems to limit the maximum film thickness, however, working solar cells could be prepared from the substrate with cracked buffer layer, showing that the small amount of exposed substrate surface in narrow cracks does not significantly harm the final cell.

In Table 4.1 results from an XPS analysis of at typical Zn(O,S) buffer layer on CIGSSe substrate are presented before and after a sputter step for 1 min at 1 kV in order to remove surface contamination. Atomic concentrations are determined from integral peak intensities. Before sputtering the substrate does not 'shine through' the buffer layer, however, the extracted [S]/([S]+[O]) ratio may be influenced by surface-adsorbed oxygen and is indeed rather low with

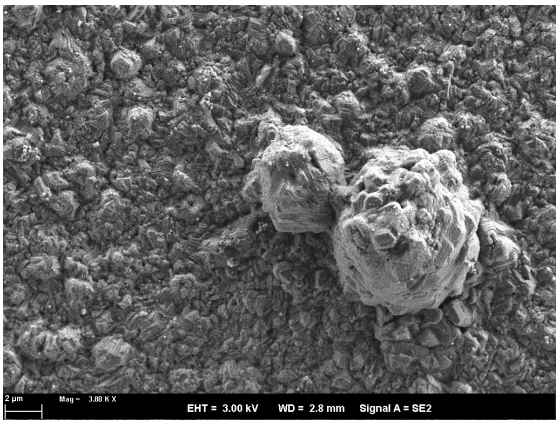

(a) Sample A: $d_{\mathrm{ZnOS}} \approx 50\,\mathrm{nm}$

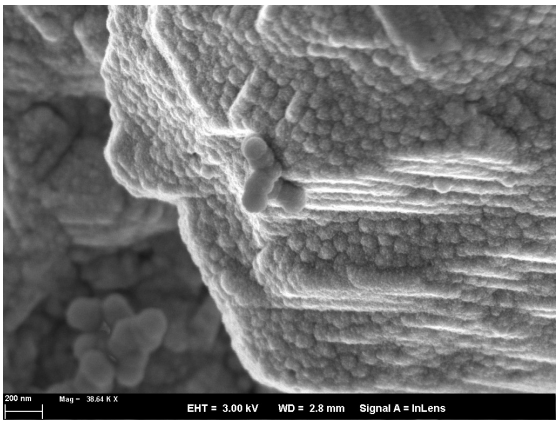

(b) Sample A: $d_{\mathrm{ZnOS}} \approx 50\,\mathrm{nm}$

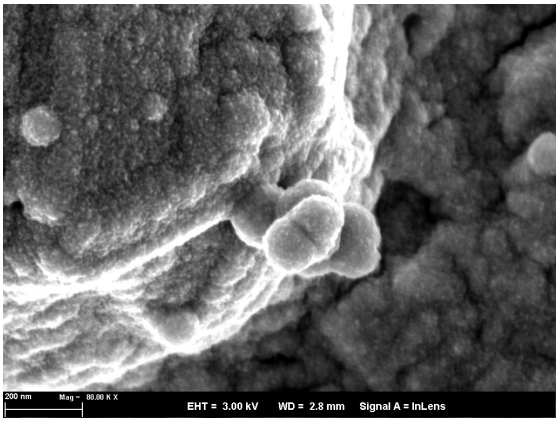

(c) Sample A: $d_{\mathrm{ZnOS}} \approx 50\,\mathrm{nm}$

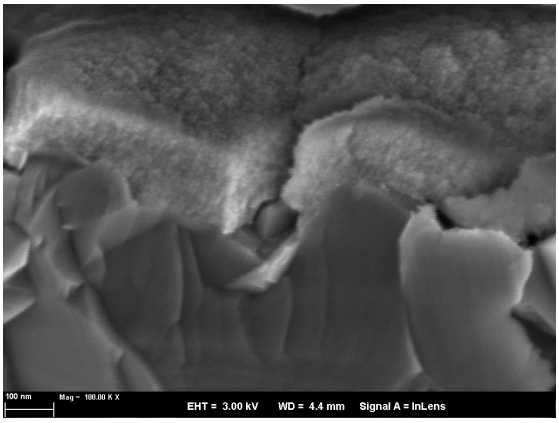

(d) Sample B: $d_{\mathrm{ZnOS}} \approx 130\,\mathrm{nm}$

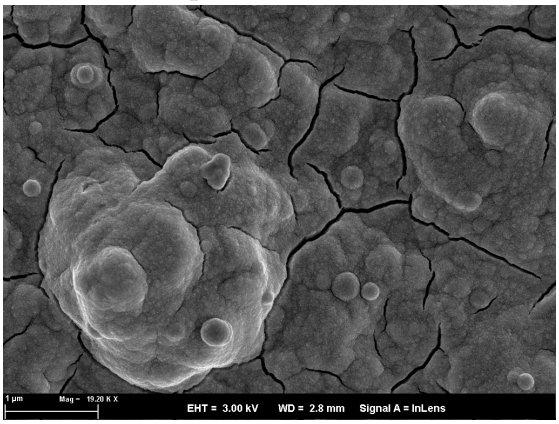

(e) Sample B: $d_{\mathrm{ZnOS}} \approx 130\,\mathrm{nm}$

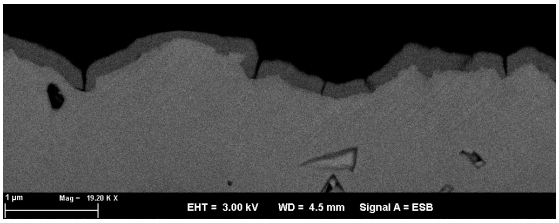

(f) Sample B: $d_{\mathrm{ZnOS}} \approx 130\,\mathrm{nm}$

Figure 4.3: Scanning electron microscopy (SEM) images of two Zn(O,S) layers with different thickness, deposited on CIGSSe and annealed at 190 °C in air.

[S]/([S]+[O]) = 0.45. Indeed, after sputtering, together with the adventitious carbon, the amount of detected oxygen is reduced and the ratio increased to [S]/([S]+[O]) = 0.66, which is in the typical range for CBD-Zn(O,S) as was discussed in the literature survey. In addition to the expected elements, Na and Cl were detected. The occurrence of Na might be explained by diffusion from the CIGSSe material. Due to the addition of NaOH and HEEDTA trisodium salt, a significant amount of Na is also present in the process solution, an incorporation during film formation is therefore a possibility as well. The chlorine might be explained by impurities in the used chemicals.
In addition to calculating the ratio [S]/([S]+[O]) from atomic concentrations, it is also calculated from the Auger parameter for zinc (α_{Zn}) according to Eq. (2.44) derived by Adler et al. [27] before and after sputtering. The calculated values of 0.61 and 0.62 respectively are in the expected range and no change upon sputtering is observed. This is expected, as the majority of zinc atoms contributing to the Auger spectrum are not in contact with the surface adsorbates. The calculation of the [S]/([S]+[O]) ratio from the Auger parameter is therefore preferred to the calculation from atomic concentrations because preferential sputtering cannot be excluded in the latter case. From comparison of both methods, it may, however, also be concluded, that the influence of preferential sputtering on the result is rather small.
Regarding the suitability of the process for large area deposition, Fig. 4.4 shows maps of the Zn(O,S) layer thicknesses, measured by XRF on a 30 cm × 30 cm substrates. Although a small gradient is observed for all layer thicknesses, the overall homogeneity is good with a relative standard deviation usually below 5 %. This is a prerequisite for the fabrication of 30 cm × 30 cm submodules. Such modules were produced and the process was even successfully transferred to module level at the Bosch Solar CISTech GmbH. This work, however, is only concerned with the results on cell level.

4.4 Solar cell performance

After buffer layer deposition, solar cells are fabricated from the coated substrates at ZSW, as described in Section 2.5.2. A first measurement of IV curves is then also performed at the ZSW with simulated AM1.5 illumination, where the sample is actively cooled to 25 °C. Any further annealing steps are done on a hotplate at 200 °C in air and any light-soaking involves continuous simulated AM1.5 illumination while actively cooling the substrate. The same procedures are also performed in our laboratory with the exception that an active cooling is not possible, a rise of typically up to 60–70 °C is observed during light-soaking procedures as long as several hours.
An example of measured IV curves in the dark and under illumination for a solar

Table 4.1: XPS elemental analysis for a Zn(O,S) buffer layer on top of CIGSSe at the untreated surface and after a sputtering step in order to remove surface contaminations. Ratios [S]/([S]+[O]) are calculated from the atomic concentrations and from the Auger parameter for zinc α_{Zn}.

	atomic concentrations / %									
	C	O	Na	S	Cl	Cu	Zn	Se	In	[S]/([S]+[O])
before sputtering	31.5	20.8	0.7	16.9	0.4	–	29.8	–	–	0.45
after sputtering	5.0	14.3	1.3	26.0	0.2	0.2	52.8	0.2	< 0.2	0.66

	energies from XPS spectrum / eV			
	E_{CL}(Zn $2p_{3/2}$)	E_{kin}(Zn LMM)	α_{Zn}	[S]/([S]+[O])
before sputtering	1021.99	988.87	2010.86	0.61
after sputtering	1021.95	988.93	2010.88	0.62

cell with Zn(O,S) buffer layer in comparison to a cell with CdS buffer layer is displayed in Fig. 4.5. Clearly the device shows the typical annealing and light-soaking behavior mentioned beforehand. Before any post-treatment there is no photocurrent collection under forward nor at small negative voltage bias. This is improved significantly by the annealing step at 200 °C in air. The IV curve now shows that there is photocurrent collection at forward bias voltages, still there is a large S-shape distortion of the curve with insufficient current collection at larger forward bias voltages, reducing the fill factor and open circuit voltage. The reduction of open circuit voltage is in this case the consequence of the low collection efficiency at forward bias voltage. The dark diode current is small, it is the linear shunt current, which is approximately equal to the photocurrent at the open circuit voltage. After light-soaking under simulated AM1.5 illumination for typically 30 min to 120 min the S-shape distortion is removed from the IV curve. The current collection under forward voltages does not seem to be inhibited up to the open circuit voltage, ensuring fill factors above 60 %. The dark current is increased as well and there is typically no crossing of IV curves in the dark and under illumination observed after light-soaking. A look at the the IV curves in Fig. 4.6, measured continuously during the light-soak, shows that the current limitation at large positive voltages and the inhibited photocurrent collection are

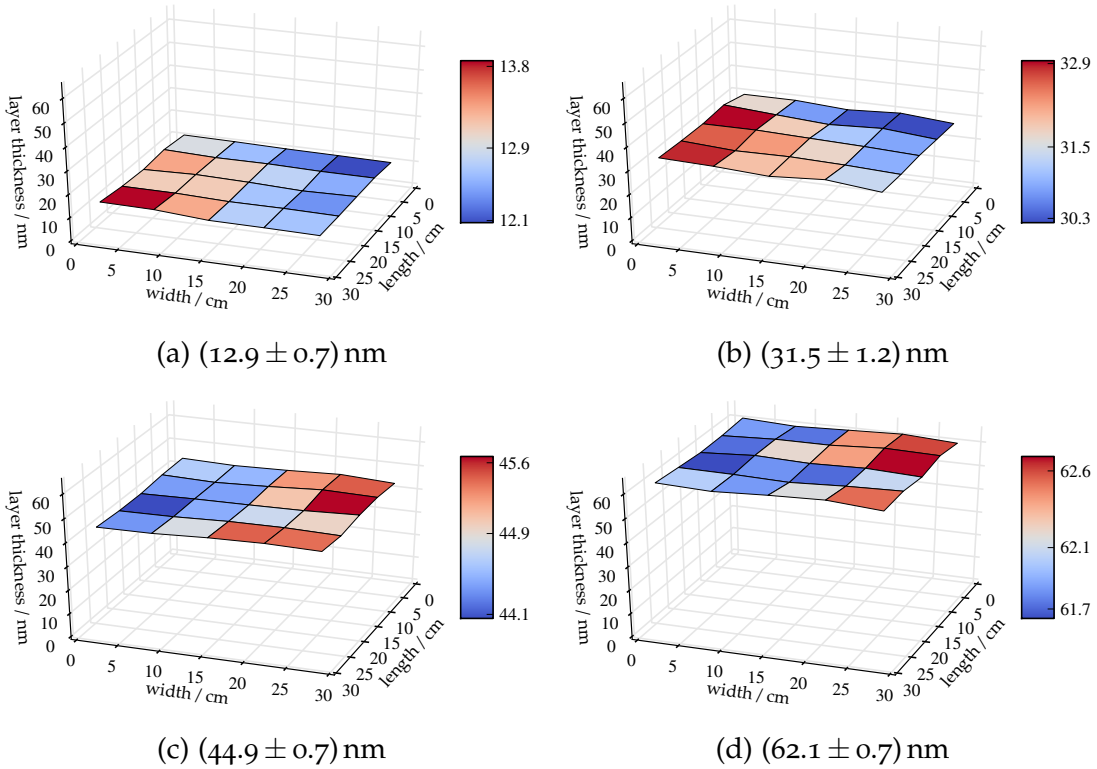

(a) (12.9 ± 0.7) nm

(b) (31.5 ± 1.2) nm

(c) (44.9 ± 0.7) nm

(d) (62.1 ± 0.7) nm

Figure 4.4: XRF maps for d_{ZnOS} on 30 cm × 30 cm substrates for four processes with different deposition parameters, showing the possibility to adjust the layer thickness over a wide range. Colors are used as indicator for average thicknesses of each area and subcaptions give the average thickness with standard deviation.

linked and removed at the same pace with continuing illumination. Figure 4.6 also shows that this effect is saturating as longer and longer intervals are needed in order to see a change of the IV curve. While the change induced by annealing was observed to be stable, the change induced by light-soak was observed to revert within days to weeks in dark storage with different speeds for different samples. An immediate reversal was observed, when the cells were annealed at 200 °C in air.

The comparison with the CdS-buffered reference cell shows that the short circuit current is increased with the Zn(O,S) buffer layer, and the open circuit voltage is reduced, which is typical for chemically deposited buffer layers as mentioned in the literature survey.

Acknowledging that both annealing and light-soak increase the photocurrent collection under forward bias, both treatments are interchangeable as to their impact of lowering an electronic barrier for this current. While there may be different effects amounting to the electronic barrier (see Section 4.5.1), resolved independently by each treatment, in the end both treatments have the same effect, justifying a closer look. Figure 4.7 shows IV curves under illumination for a set of 24 cells, measured in quick succession, where the whole measurement is taking approximately 5 min, during which all cells are exposed to the illumination. There

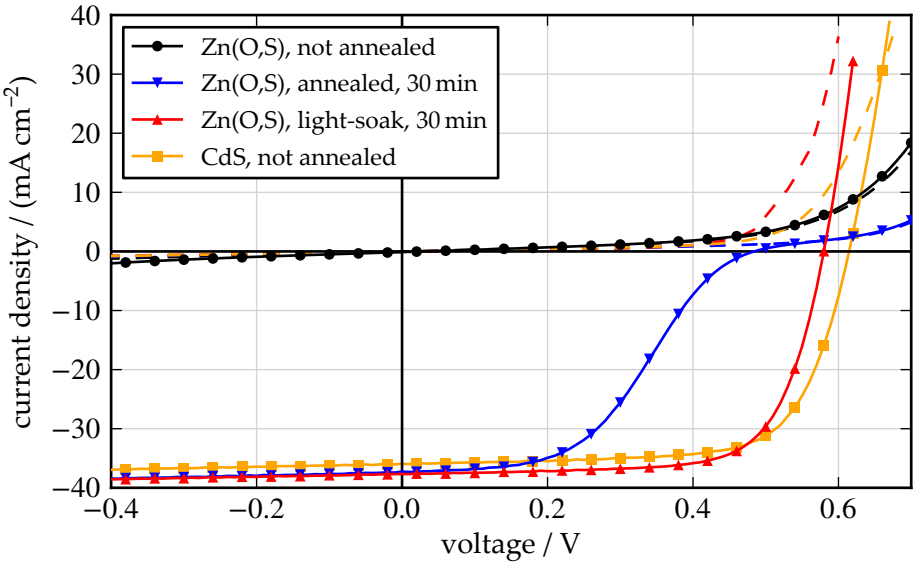

Figure 4.5: IV curves for an exemplary cell with Zn(O,S) buffer layer before any post-treatments, after annealing at 200 °C, and after light-soaking under simulated AM1.5 illumination, while being actively cooled to 25 °C. For comparison a IV curve of the best reference device with CdS buffer layer is shown as well. Measurements in the dark are given with dashed lines, measurements under simulated AM1.5 illumination are given with solid lines.

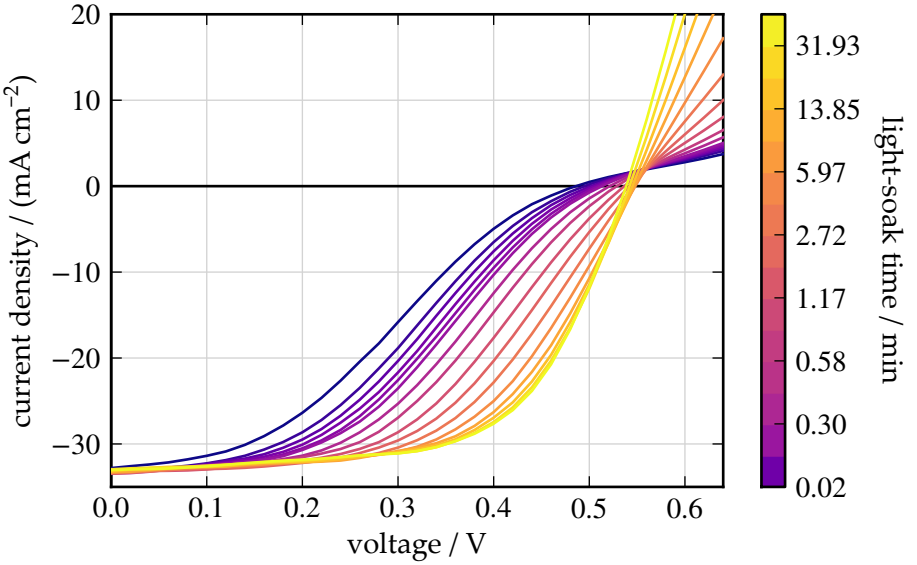

Figure 4.6: IV curves for a cell with Zn(O,S) buffer layer continuously measured while illuminating the cell with a halogen light source at 75 mW cm^{-2}. A subset of these measurements, logarithmic in time, is shown in the figure and the accumulated light-soak time is indicated by a colorbar in logarithmic scale.

are no curves displayed for the case before any thermal post-treamtents, because there is no significant effect of the light-soaking treatment within 5 min. After 5 min of annealing (Fig. 4.7(a)), all cells still show largely inhibited current collection, but there is already a clear trend evolving, towards better characteristics for the cells measured last. This trend is due to the light-soaking, occuring during the measurement time, which is larger for the later cells. This is also the explanation for the sometimes large spread of efficiencies in boxplots shown in later parts of this work. After further annealing, the cells are always observed to relax again to a state with more inhibited current collection, the inflection point of the S-shape distortion is, however, shifted to higher voltages each time and as can be seen in the succession of Figs. 4.7(a) to 4.7(d), the light-soak time needed for reaching high efficiencies is decreasing with each step. A closer look at the shift of IV curves with increasing annealing time, as displayed in Fig. 4.8, shows that the shift of the S-shape distortion is large at first, but limited at larger annealing times. In Fig. 4.8(b), the interpolated voltages at fixed current densities of $-10\,\mathrm{mA\,cm^{-2}}$, $-20\,\mathrm{mA\,cm^{-2}}$, and $-30\,\mathrm{mA\,cm^{-2}}$ are plotted over the annealing time with exponential curves as a guide to the eye. Visibly, the annealing post-treatment is most effective until a time of ~30 min is reached with only small increases after that. Therefore, the standard annealing time for cells with Zn(O,S) buffer layer was chosen to be 30 min, bearing in mind though, that this might not be an optimum any more when the absorber, the Zn(O,S) properties, or the window layer change.

The actual solar cell performance will of course largely depend on the CIGSSe absorber quality. Since the CIGSSe coated substrates used in this work were received from experimental runs at Bosch Solar CISTech, no constant absorber properties could be ensured, making comparison between batches complicated. A more detailed discussion will be given in the next section. There were however, a few shipments with larger quantities of very comparable substrates. Statistical data for one of these substrate batches is shown in Fig. 4.9 and Table 4.2. This data includes six substrates, coated with Zn(O,S) in separate deposition processes, and three substrates, coated with CdS in the same deposition process at Bosch Solar CISTech. Each substrate contains 20 cells, where only 10 are measured before light-soaking. The total number of included cells is given with each table column and boxplot. While the spread of efficiencies before light-soaking is large due to partial light-soaking during the measurement, the median absolute deviations after light-soaking are smaller even compared to the CdS-buffered reference cells. It is also apparent, that the process presented here results in Zn(O,S) buffer layers, that are able to match or even surpass the efficiency of reference cells on median level. The maximum efficiency of a Zn(O,S) buffer layer from the standard process is reported here with 15.5 % on total cell area and 16.1 % on calculated active area. While median and maximum efficiencies on cell level are very promising, the light-soaking that is needed for all cells is a hindrance for large scale industrial application. The annealing process can reduce the time needed for light-soaking and is much easier to apply as a large scale process. However, it would be much pre-

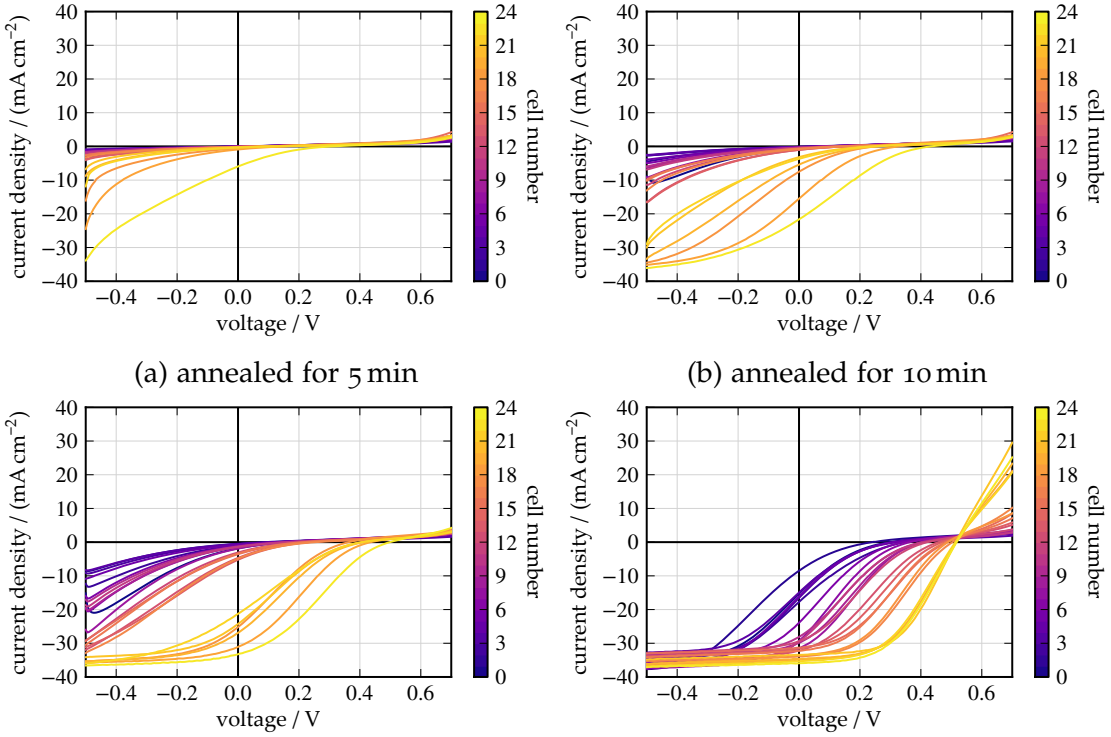

(a) annealed for 5 min

(b) annealed for 10 min

(c) annealed for 15 min

(d) annealed for 30 min

Figure 4.7: IV curves for 24 cells with Zn(O,S) buffer on the same substrate, sequentially measured while illuminating the whole substrate with simulated AM1.5 illumination. In between the measurements, the substrate was submitted to annealing treatments on a hotplate at 200 °C in air. The subcaptions give the cumulative annealing time.

ferred if the barrier that is supposedly reduced with annealing and light-soaking treatments would be lower from the beginning, rendering one or both treatments unnecessary. This will be the starting point for the discussion in the following sections.

4.5 Window layer adaptations

The previous section was concerned with the CBD-deposition of an Zn(O,S) buffer layer. The resulting solar cells, while having promising final efficiencies, are severely limited with regard to industrial application because of the need for annealing and light-soak post-treatments.
Since the process itself is very reliable, the question arises, if it is possible to resolve this limitation within the means easily accessible to the Bosch CISTech fabrication. In this section, the experimentally accessible parameters at the CIGSSe/buffer-/window interfaces are therefore first evaluated with regard to their importance for an electronic barrier formation in systematic simulations. Then, experiments

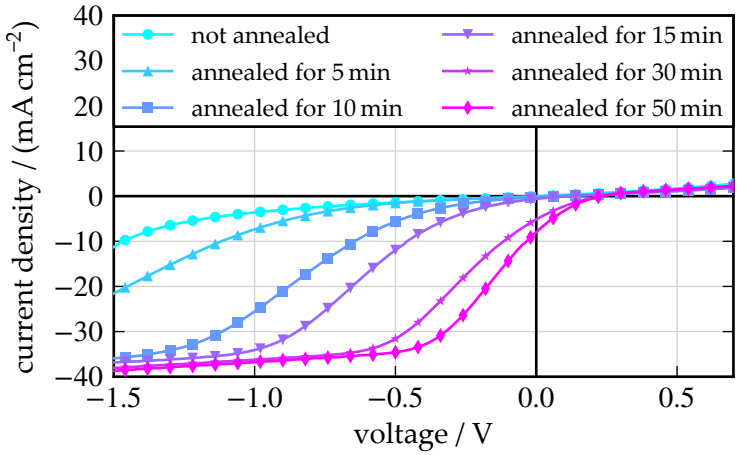

(a) IV curves

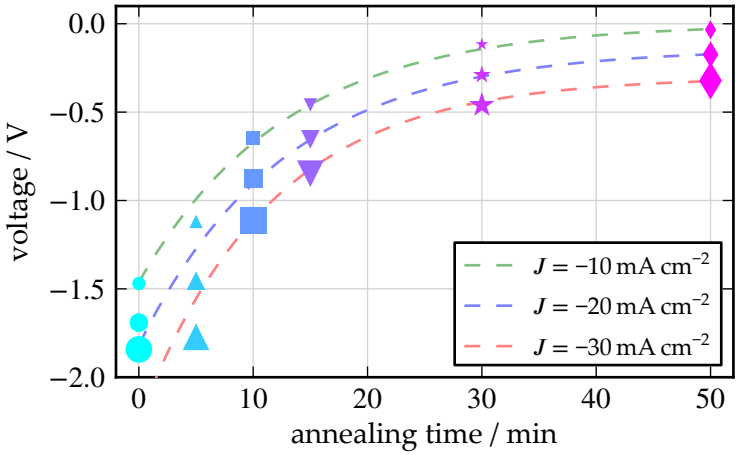

(b) voltages at fixed currents

Figure 4.8: (a) IV curves for one cell with Zn(O,S) buffer layer, as they evolve with progressing cumulative annealing time. The effect of light-soaking is assumed to be removed with each annealing step. (a) A plot of interpolated voltages at three fixed currents over the cumulative annealing time. Exponential curves are given with dashed lines as a guide to the eye.

will be presented with the direct aim to reduce the initial electronic barrier by altering the window layer deposition process.

4.5.1 SCAPS simulations

As was discussed in the introductory section to thermionic emission (Section 2.2.4), a positive conduction band offset ΔE_{CB} (spike) is a common cause for a barrier to the electron transport. The actual barrier height consists of the sum of ΔE_{CB} and the distance between Fermi level and conduction band minimum. Simulated band diagrams regarding the impact of $\Delta E_{CB,ab}$, the offset at the absorber/buffer interface, together with resulting IV curves are shown in Fig. 4.10. While small

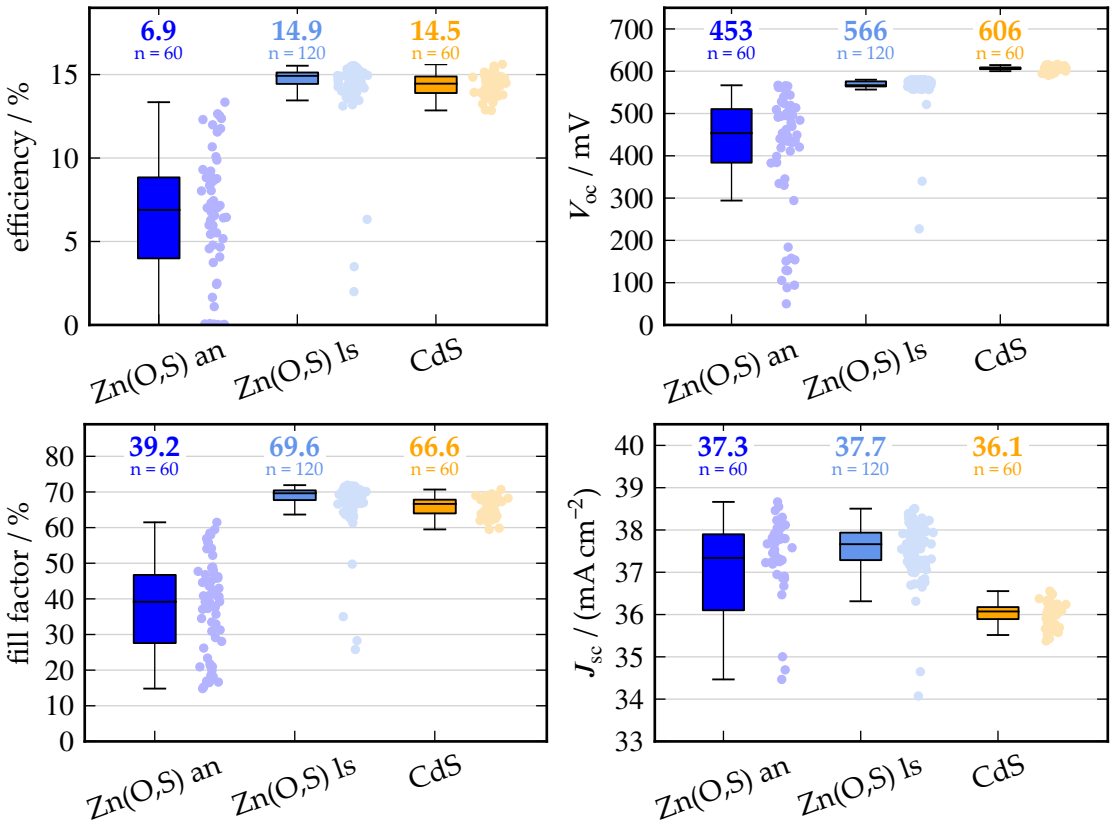

Figure 4.9: Boxplots and scatter plots of solar cell parameters for cells with Zn(O,S) buffer layer after the annealing post-treatment (an) and after light-soaking (ls) in comparison to cells with CdS buffer layer. Median values are given above each boxplot together with the number of cells in the dataset.

Table 4.2: Solar cell parameters for cells with Zn(O,S) buffer layer after annealing and after light-soaking in comparison to cells with CdS buffer layer. The statistical data is represented by the median and median absolute deviation.

	buffer layer		
parameter	Zn(O,S) annealed	Zn(O,S) light-soaked	CdS
$n_{samples}$	60	120	60
η / %	6.89 ± 2.32	14.92 ± 0.29	14.45 ± 0.48
η_{max} / %	13.3	15.5	15.6
V_{oc} / mV	453 ± 63	567 ± 6	607 ± 2
fill factor / %	39.2 ± 8.7	69.6 ± 0.9	66.6 ± 1.6
J_{sc} / mA cm^{-2}	37.3 ± 0.6	37.7 ± 0.3	36.1 ± 0.1

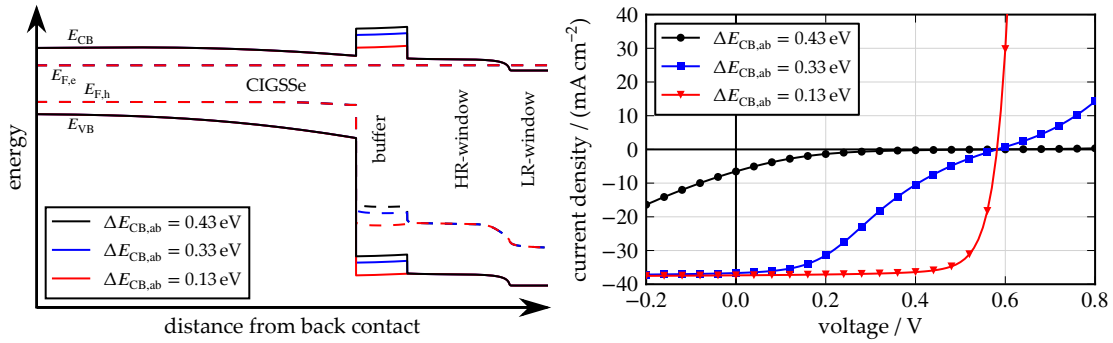

(a) Simulated band diagrams.

(b) Simulated IV curves.

Figure 4.10: Simulated band diagrams and IV curves for different absorber/buffer spike configurations. In order to obtain different values of $\Delta E_{CB,ab}$, the electron affinity of the buffer layer was changed.

positive conduction band offsets do not deteriorate the IV curve within the used model, offsets in the range of 0.3 eV and larger lead to the S-shape distortions that were observed experimentally in the last section. It is also apparent that, due to the exponential dependency of the current on the barrier height, small changes at large barrier heights have large influence on the transported current.

The model parameters for all simulations in this section can be found in Appendices A.1 and A.3 with variations indicated in the respective captions. In order to visually compare influences on the barrier height, band diagrams in open circuit condition are most useful because the differences in band diagrams become more apparent the flatter the bands are. Therefore all band diagrams shown in this section are calculated under illumination at 0.58 V, which is close to open circuit conditions for the base model, as indicated by the flat quasi Fermi levels. To underline the generality of the discussion, the terms HR-window (high resistive window layer) and LR-window (low resistive window layer) will be used in this section instead of specific material names such as i-ZnO and ZnO:Al.

For a buffer layer with low n-type doping a moderate spike of 0.33 eV leads to a distortion of the IV curve, this can however be resolved by increasing the buffer layer doping. Figure 4.11 shows simulations from virtually no doping to a doping level of $5 \times 10^{17}\,\mathrm{cm}^{-3}$, comparable to a HR-window layer. The IV curve distortion is visibly resolved. In this case, it is the charge concentration that is effectively decreasing the barrier height, as the Fermi level approaches the conduction band minimum. It is noteworthy at this point, that the change in IV characteristics, observed in the previous section, would involve a change of doping concentrations in the order of several orders of magnitude.

Another factor influencing the charge concentration next to the buffer layer's interfaces is the concentration of charged defects at these interfaces. Positively charged defects increase the free electron concentration, whereas negatively charged defects

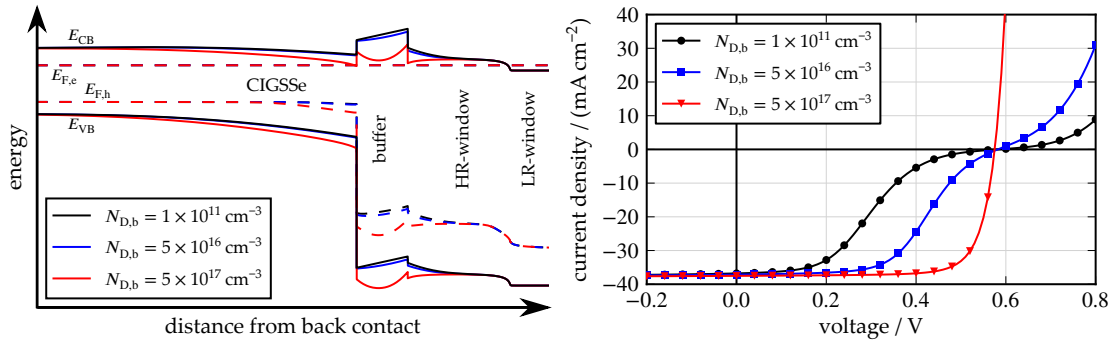

(a) Simulated band diagrams.

(b) Simulated IV curves.

Figure 4.11: Simulated band diagrams and IV curves for different buffer layer doping levels, adjusted by the shallow donor concentration $N_{D,b}$ within the model. A moderate spike was chosen with $\Delta E_{CB,ab} = 0.33$ eV.

decrease the free electron concentration. When the number of defect states is very large, the Fermi level is pinned to the defect energy. Figure 4.12 shows simulations illustrating the influence of interface defect concentrations on the energetic barrier. The parameter, changed in each simulation is the acceptor concentration at the buffer/window interface. Negative charged defects decrease the electron concentration at this interface and therefore the conduction band is shifted upwards, increasing the barrier and distorting the IV curve significantly. There are three sets of such simulations shown in the figure. In the first set, there is no defect concentration at the absorber/buffer interface, the Fermi level is therefore not pinned and the conduction band upshift is extending into the absorber. In the second set of simulations, a large amount of donor defects is set at the absorber/buffer interface 0.2 eV below the absorber conduction band. The overall barrier is reduced and the conduction band upshift at the absorber surface is only slight. In the next set, a larger amount of donor defects is set close to the conduction band of the absorber, pinning the Fermi level at this position. The electronic barrier is reduced further and the impact of acceptor defects at the buffer/window interface is lowered significantly. It can therefore be concluded that, while acceptor defects at the buffer/window interface are harmful in distorting the IV curve, an effective inversion of the CIGSSe surface significantly lowers the susceptibility to IV curve distortions. A case with a significant density of acceptor defects at the absorber/buffer interface is not shown here. A lowering of the Fermi level at the interface would be the consequence, leading to an increased barrier height.
The next important parameter is the n-type doping density of the HR-window layer. Ideally a heterojunction solar cell would comprise a p/n+ junction, where there is almost no voltage drop in the n-doped side of the junction. However, the high resistive window layer does provide protection against accidental shunting, leading to higher efficiencies in module production. Figure 4.13 shows simulations with a moderate conduction band spike, where the doping density of the HR-window is varied over several orders of magnitude. The increase in doping density increases the electron concentration next to the buffer layer, thereby reducing

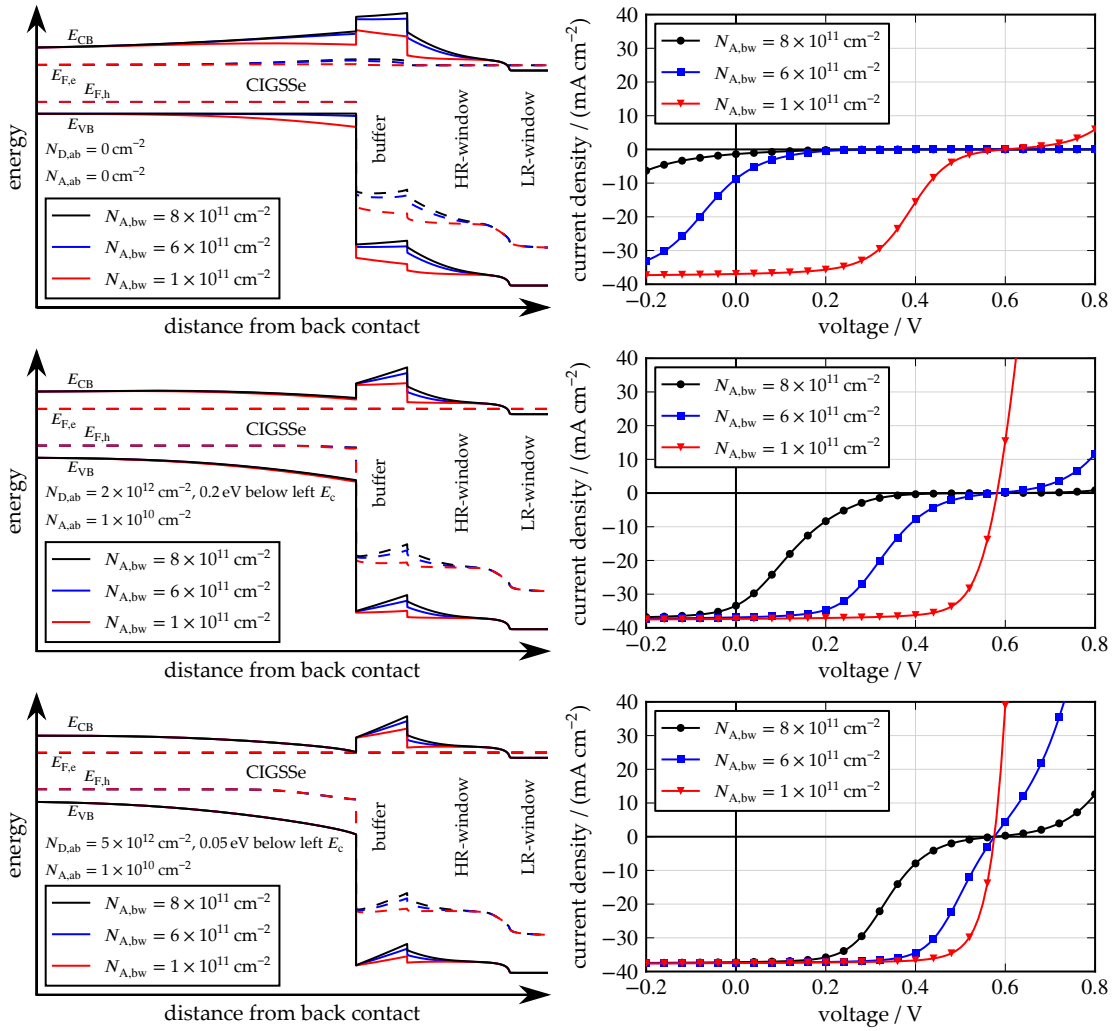

Figure 4.12: Simulated band diagrams and IV curves for different defect concentrations at the absorber/buffer and buffer/window interfaces. The first set of simulations constitute the case without pinning at the absorber/buffer interface, the second set has a moderate pinning and the third case a strong pinning next to the conduction band minimum.

the barrier. With a degenerately doped window layer, the IV curve distortion is almost resolved. In the case of medium to large conduction band spikes it may therefore be necessary to remove the HR-window layer in order to resolve issues with S-shape IV curve distortions. Another possibility to increase the electron concentration near the buffer layer, while still using a high resistive window layer, is to adjust the band alignment at the buffer/window interface. Since the commonly used i-ZnO is considered to have a large negative conduction band offset with the buffer layer, this was the standard configuration in the model so far. The impact of reducing this negative conduction band offset is shown in Fig. 4.14. In this set of simulations only the electron affinity of the HR-window material was set to different values, with the result, that the IV curve distortion can be removed

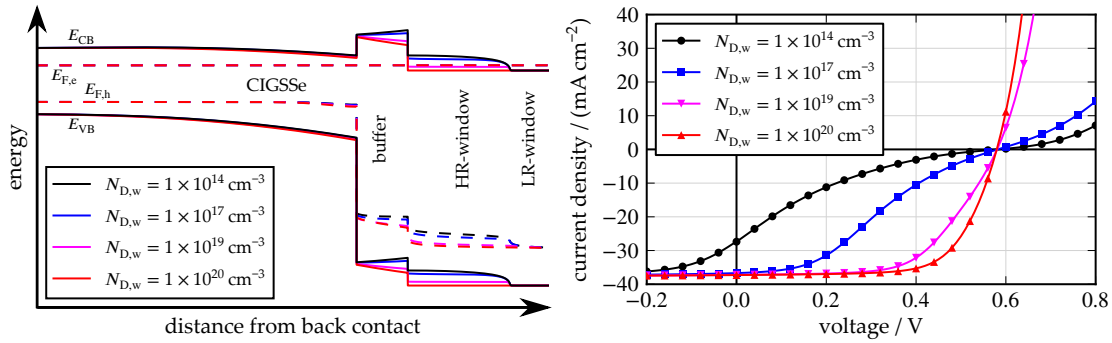

(a) Simulated band diagrams. (b) Simulated IV curves.

Figure 4.13: Simulated band diagrams and IV curves for several concentrations of shallow donors in the HR-window layer from almost non-existing doping to degenerate doping. The compensating acceptor defect, normally included in the model, is omitted here and a conduction band spike of $\Delta E_{CB,ab} = 0.33\,eV$ was chosen.

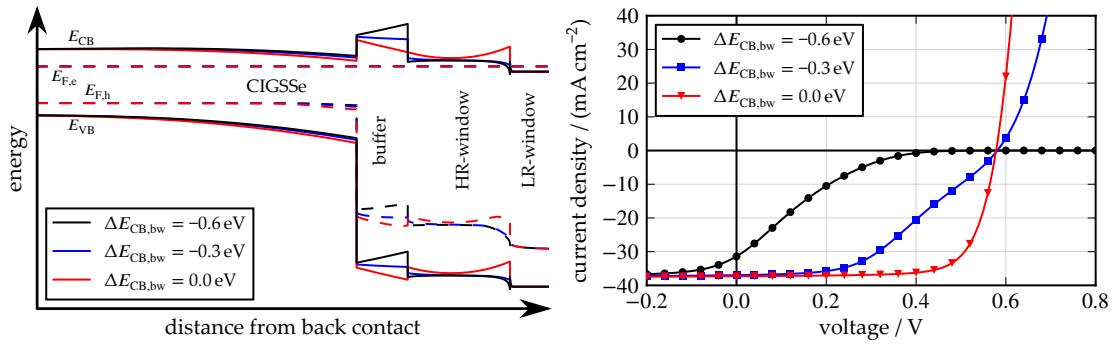

(a) Simulated band diagrams. (b) Simulated IV curves.

Figure 4.14: Simulated band diagrams and IV curves for a fixed absorber/buffer conduction band offset $\Delta E_{CB,ab} = 0.33\,eV$ and varied negative buffer/window conduction band offsets $\Delta E_{CB,bw}$.

completely just by removing the negative conduction band offset at the buffer-/window interface. It has to be noted here, that the doping concentration in the high resistive window layer still is considered to be an order of magnitude larger compared to the buffer layer. Using a window layer with good band alignment but with lower doping concentration would essentially have the same effect as increasing the buffer layer thickness, leading to an increase of the electronic barrier with decreasing doping density.

4.5.2 *Experiments*

The simulations demonstrate, that while a large conduction band spike can severely deteriorate the solar cell efficiency, there are other factors having similar effect, especially at the buffer/window interface. As explained in Section 2.5, the window

layers were deposited by commission at the ZSW without disclosure of process details. Within some limits, adaptations of the deposition parameters could be discussed and adjusted as will be presented here with the aim to separate the model parameters that were discussed before. The following paragraphs will contain discussions on a qualitative level, actual solar cell parameters for each IV curve can be found in Appendix B.

OMITTING O_2 IN THE SPUTTER GAS AT THE BEGINNING OF THE I-ZNO DEPOSITION – INCREASE OF $N_{D,b}$, REDUCTION OF $N_{A,bw}$: As was mentioned in the literature survey, there are reports of the beneficial effect on initial cell efficiencies, when oxygen gas is omitted from the sputter gas during the first few nm of i-ZnO deposition [93, 97]. Generally, a mixture of oxygen and argon is used as a sputter gas, where the oxygen concentration can be used to tune the i-ZnO doping level. Sputtered ZnO will show n-type conductivity due to oxygen vacancies, the number of the latter can be reduced when oxygen gas is included in the process [106]. Omission of oxygen in the first few nm of the deposition process will, however, not increase the doping level of the whole i-ZnO layer by orders of magnitude. Therefore Naghavi et al. discuss that it might rather be the buffer layer doping that is increased by release of oxygen from the buffer layer during the deposition process [93]. As they show in their publication and as can be seen in Fig. 4.11, an increase of the buffer doping level of several orders of magnitude would be necessary to have a significant influence on the S-shape IV curve distortion. In the last section, it was also shown that the concentration of charged defects at the buffer/window interface can significantly distort the IV curve. Negatively charged defects might be introduced during sputter deposition of i-ZnO, when oxygen is included in the sputter gas, or there might be a compensation effect as the mechanism discussed by Naghavi et al. adds positively charged defects with a higher concentration at the surface, when oxygen is omitted.
The standard i-ZnO layer deposition process at the ZSW includes 4 % oxygen in the sputter gas. Experiments were therefore commissioned, where an i-ZnO bilayer was deposited instead of a monolayer. In the first deposition step, with a target thickness of about 20 nm, oxygen was omitted in the sputter gas. The resulting IV curves are presented in Fig. 4.15. There is visibly a large impact on the solar cell performance. While Fig. 4.15(a) is very similar to Fig. 4.5, showing no current collection before the annealing treatment and an S-shape distortion before light-soaking, Fig. 4.15(b) does not show any S-shape distortions at all. The largest difference obviously is achieved for the case before any post-treatment. And while there is still some impact of the post-treatments registered, these cells reached their final efficiency during one measurement cycle (~5 min light-soak), significantly reducing the time needed for post-treatments.

REDUCTION OF O_2 IN THE SPUTTER GAS DURING THE WHOLE I-ZNO DEPOSITION – INCREASE OF $N_{D,w}$: The omission of oxygen in the first of two i-ZnO layers did increase the initial solar cell efficiencies significantly. While the magnitude of

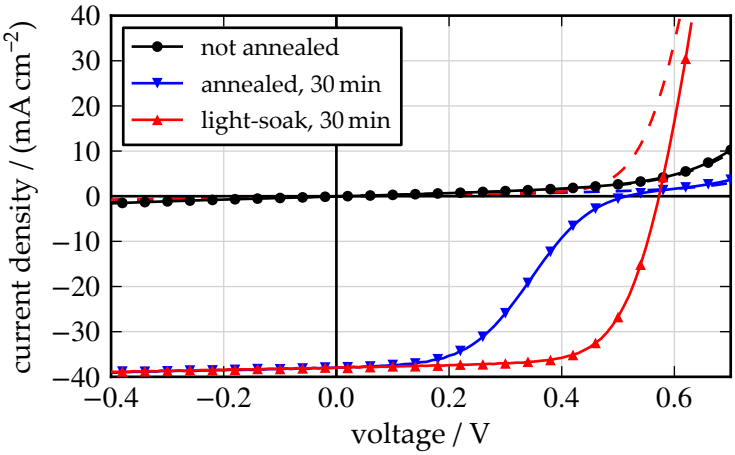

(a) i-ZnO monolayer, 4% O_2 (sputter gas)

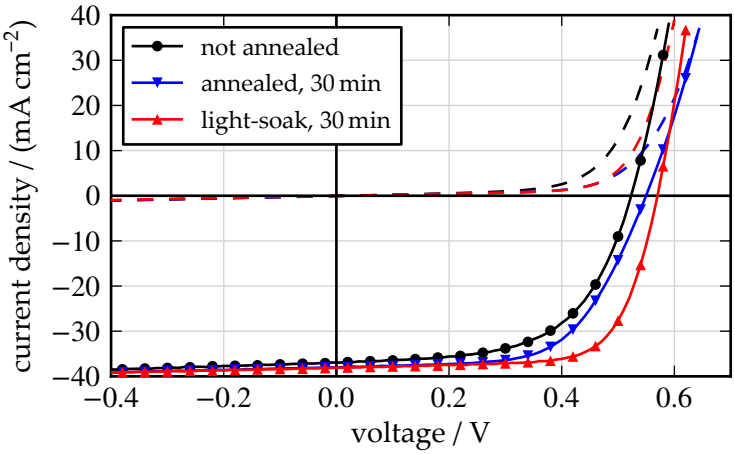

(b) i-ZnO bilayer, 0%/4% O_2 (sputter gas)

Figure 4.15: Measured IV curves for exemplary cells with different i-ZnO layer before any post-treatments, after annealing at 200 °C, and after light-soaking under simulated AM1.5 illumination. (a) shows a cell with standard i-ZnO monolayer, including oxygen gas in the deposition process, (b) shows a cell with bilayer i-ZnO, omitting oxygen from the sputter gas for the first layer. Measurements in the dark are given with dashed lines, measurements under simulated AM1.5 illumination are given with solid lines.

change does point to an effect related to the interface, it was mentioned before that the omission of oxygen from the sputter gas will inevitably also increase the i-ZnO conductivity. As was demonstrated with the simulations shown in Fig. 4.13, increasing the i-ZnO conductivity will also have the effect of lowering the barrier. Therefore, in the next set of experiments the second i-ZnO layer was deposited with different concentrations of oxygen in the sputter gas, reducing it from 4 % to complete omission. The resulting IV curves are displayed in Fig. 4.16. Visibly, there is a continuous improvement of the solar cell characteristics with decreasing content of oxygen in the sputter gas. It has to be noted here that the cells shown

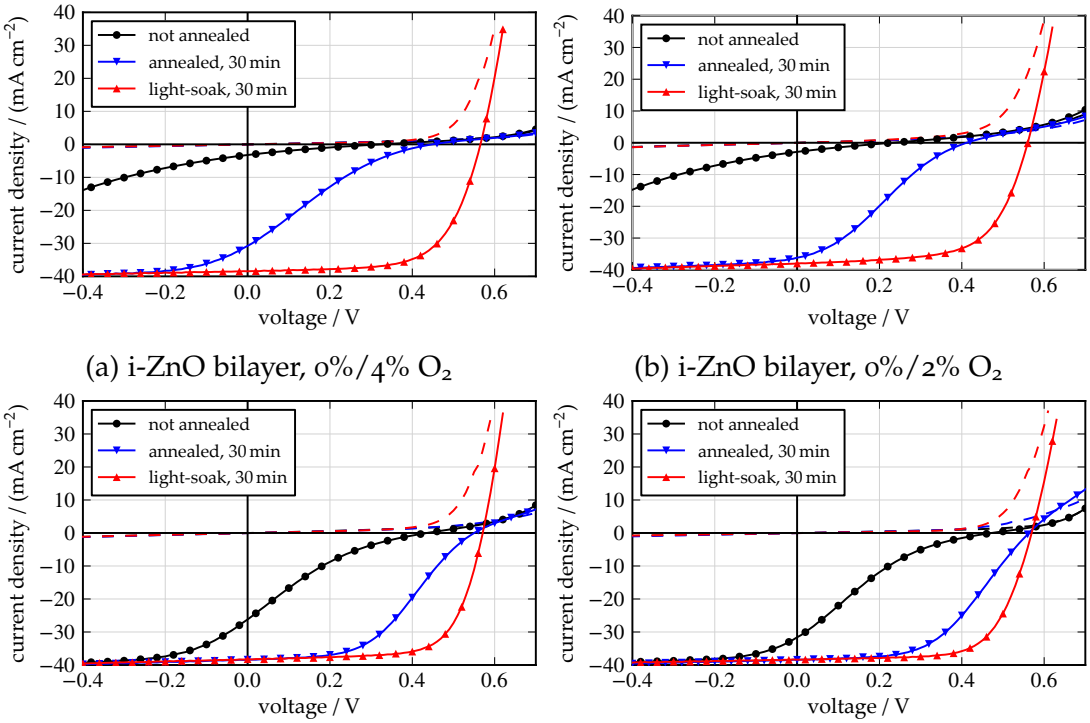

(a) i-ZnO bilayer, 0%/4% O_2

(b) i-ZnO bilayer, 0%/2% O_2

(c) i-ZnO bilayer, 0%/1% O_2

(d) i-ZnO bilayer, 0%/0% O_2

Figure 4.16: Measured IV curves for exemplary cells with i-ZnO bilayers and adjusted oxygen content during sputtering of the second i-ZnO layer before any post-treatments, after annealing at 200 °C, and after light-soaking under simulated AM1.5 illumination. (a) to (d) show cells with decreasing oxygen content in the sputter process up to a complete omission. Measurements in the dark are given with dashed lines, measurements under simulated AM1.5 illumination are given with solid lines.

in Fig. 4.16 have worse characteristics compared to the cell shown in Fig. 4.15(b), which is at first glance surprising as buffer and window layer deposition processes are very similar. This can, however, be attributed to two different CIGSSe batches and will be discussed in more detail in Section 4.6. No significant decrease of the shunt resistance was detected with the increased i-ZnO conductivity. This is probably due to the good coverage of the Zn(O,S) buffer on the CIGSSe. Therefore from this point on, most of the cells presented in this work will comprise the 'optimized' i-ZnO layer, a monolayer deposited without oxygen in the sputter gas.

OMITTING THE I-ZNO LAYER – INCREASE OF $N_{D,W}$: The next step of increasing the window layer conductivity is to omit the i-ZnO layer completely. As was shown in the simulation, a degenerate doping of the window layer might be necessary to remove the electronic barrier. This essentially means a removal of the conceptual HR-window layer. Figure 4.17 shows a comparison of IV curves for exemplary cells with two different buffer layer thicknesses, with and without i-ZnO layer. While there is no significant advantage of i-ZnO omission for the thin Zn(O,S) buffer layer (Figs. 4.17(a) and 4.17(b)), there is a notable decrease in the shunt resistance

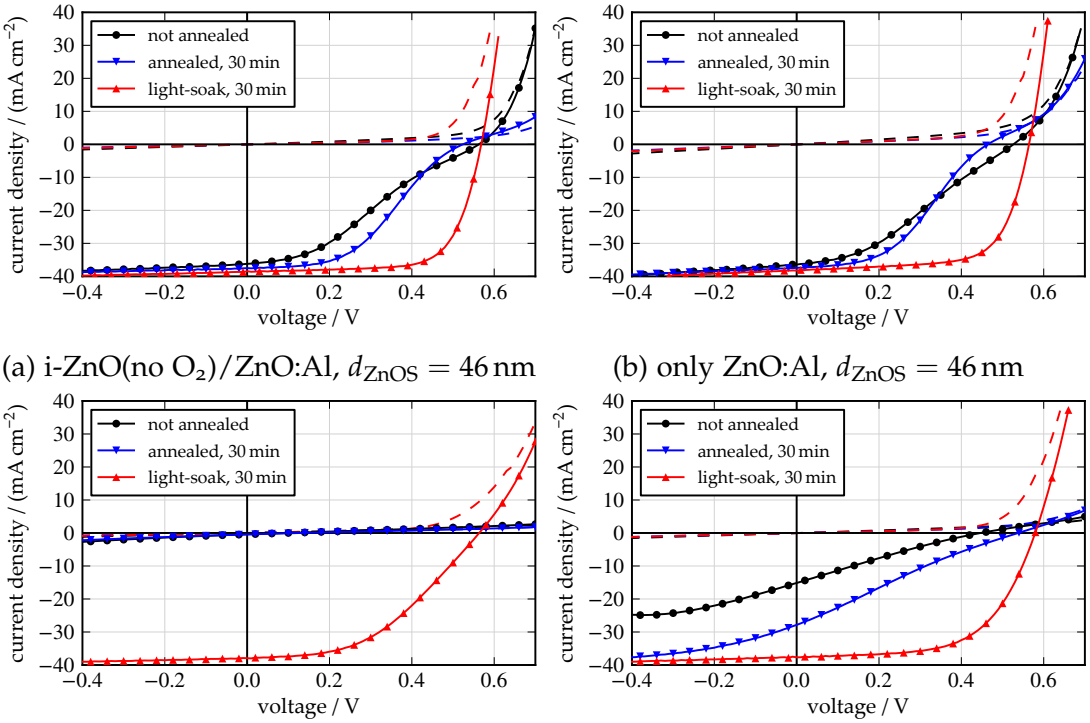

(a) i-ZnO(no O_2)/ZnO:Al, $d_{ZnOS} = 46\,nm$

(b) only ZnO:Al, $d_{ZnOS} = 46\,nm$

(c) i-ZnO(no O_2)/ZnO:Al, $d_{ZnOS} = 127\,nm$

(d) only ZnO:Al, $d_{ZnOS} = 127\,nm$

Figure 4.17: Measured IV curves for exemplary cells with and without optimized i-ZnO layers, exhibiting two different Zn(O,S) buffer layer thicknesses. Measurements in the dark are given with dashed lines, measurements under simulated AM1.5 illumination are given with solid lines.

(lower in Fig. 4.17(b) compared to Fig. 4.17(a)), deteriorating the fill factor slightly. In the case of the thick buffer layer in Figs. 4.17(c) and 4.17(d) on the other hand, there is a significant improvement of the solar cell characteristics upon removal of the i-ZnO layer. First, the thick highly resistive buffer layer provides enough protection against accidental shunting that there is no difference in shunt currents visible. Second, the high buffer layer thickness diminishes the positive effect of the optimized i-ZnO layer as it prevents an increase of charge concentration near the absorber/buffer interface. This leads to a deteriorated IV curves in Fig. 4.17(c) and leaves room for improvement by removal of the i-ZnO layer. If the Zn(O,S) buffer layer thickness were to be optimized, it is possible that an optimum could be found, where there is no disadvantage of omitting the i-ZnO layer.

Replacing i-ZnO by sputtered $Zn(O_{0.72},S_{0.25})$ or $Zn(O,S)/Zn_{0.74}Mg_{0.26}O$ – Reduction of $|\Delta E_{CB,bw}|$: Lastly, there is the possibility to replace the i-ZnO layer by another material. While the combination of CdS and i-ZnO is well established, the simulation shown in Fig. 4.14 does indicate that a material with optimized band alignment would decrease the impact of an initially harmful conduction band spike at the CIGSSe/Zn(O,S) interface.

Within the publicly funded NeuMaS project, $Zn(O_{0.75},S_{0.25})$ layers, sputtered from a mixed ZnO/ZnS target were in the focus of investigation. As described in Section 2.3.1, the [S]/([S]+[O]) ratio directly influences the conduction band minimum position, lowering it with increasing oxygen concentration in the film. The conduction band minimum of $Zn(O_{0.75},S_{0.25})$ can be assumed to lie in between the conduction band minima of i-ZnO and CBD-$Zn(O_{0.4},S_{0.6})$. According to the simulations shown, a decrease of S-shape IV curve distortions would therefore be expected upon replacing i-ZnO with sputtered $Zn(O_{0.75},S_{0.25})$. A comparison of IV curves for exemplary cells comprising an optimized i-ZnO window layer or a sputtered $Zn(O_{0.75},S_{0.25})$ layer (deposited at the CISTech facilities) is shown in Fig. 4.18. Regarding the solar cell efficiencies after annealing and light-soak, the i-ZnO layer is better. The cell with sputtered $Zn(O_{0.75},S_{0.25})$ shows significantly smaller short circuit current and fill factor. The former can be partly attributed to the $Zn(O_{0.75},S_{0.25})$ layer, a decreased transmission was often observed in our lab during the development of these layers. In addition, the current is limited due to the larger ZnO:Al thickness, used at the CISTech facilities to match cell development more closely with module development, where the higher thickness is needed to sustain larger lateral currents. Still, a fill factor limitation with fairly linear IV curves at large forward voltages is observed, pointing to an increased series resistance. While these deficiencies make the cell in Fig. 4.18(b) the less efficient device, the impact of post-treatments is significantly reduced. As the $Zn(O_{0.75},S_{0.25})$ layer is also sputtered with pure argon sputter gas, an increased current collection could be expected in the untreated state, but both states before light-soaking also show less IV curve distortion in comparison to the cell with optimized i-ZnO, indicating the potential of a better conduction band alignment.

While sputtered Zn(O,S) was available for this work, the actually established choice is a replacement of i-ZnO with ZnMgO. Minemoto et al. have shown that the incorporation of Mg increases the band gap of the material mainly by raising the conduction band minimum, resulting in a less pronounced negative conduction band offset at the buffer/window interface [107]. Indeed the ZSW [69] as well as Naghavi et al. [93] have established a Zn(O,S)/$Zn_{0.74}Mg_{0.26}O$ buffer/HR-window combination that yields higher efficiencies and less distorted IV curves compared to the Zn(O,S)/i-ZnO combination. And again it is found that the oxygen content in the sputter gas during $Zn_{0.74}Mg_{0.26}O$ deposition influences the initial solar cell characteristics [93].

The ZSW did not disclose the details of their ZnMgO deposition process, nevertheless, a few samples were fabricated with ZnMgO instead of i-ZnO as the HR-window layer. I therefore conducted a comparative experiment with samples cut from the same Zn(O,S) deposition experiment. The resulting IV curves for two exemplary cells from this experiment are shown in Fig. 4.19. The cell with optimized i-ZnO layer (Fig. 4.19(a)) shows characteristics well comparable to Fig. 4.15(b), where in this case there is still an impact of the annealing post-treatment, but light-soaking is not necessary any more. The cell with ZnMgO layer

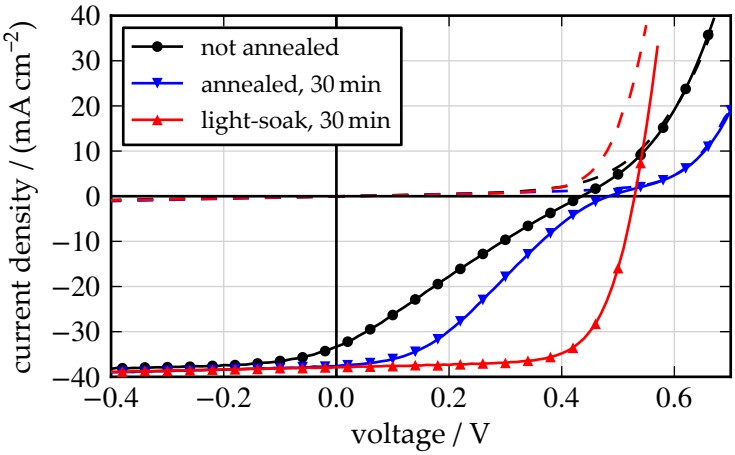

(a) i-ZnO monolayer (no O_2)

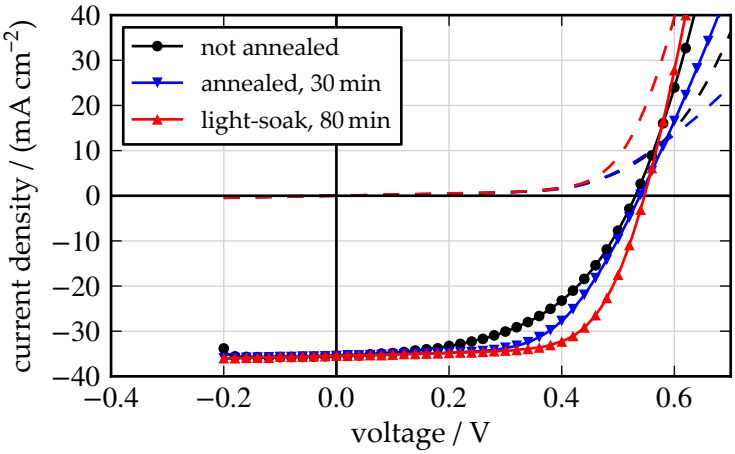

(b) sputtered $Zn(O_{0.75},S_{0.25})$

Figure 4.18: Measured IV curves for exemplary cells with (a) optimized i-ZnO layer and (b) sputtered $Zn(O_{0.75},S_{0.25})$ layer. Measurements in the dark are given with dashed lines, measurements under simulated AM1.5 illumination are given with solid lines.

(Fig. 4.19(b)) on the other hand side shows S-shape IV curve distortions before light-soaking. Compared to the cell with optimized i-ZnO this ZnMgO layer is therefore a step backwards. However, especially regarding the IV curve before any post-treatments, there is a significant improvement in comparison to the standard i-ZnO layer (c.f. Fig. 4.15(a)). Since the process details for the sputtering of the ZnMgO layer were not disclosed, it is possible, that this positive effects stems from the omission of oxygen in the sputter gas. As Naghavi et al. [93] did not observe any light-soaking effect with their cells comprising a ZnMgO layer when oxygen is omitted from the sputter gas, this might mean that oxygen was not omitted from the sputter gas for the cells presented here. If that was the case, the exchange of i-ZnO for ZnMgO would indeed provide a significant improvement and further improvement would be possible by adjusting the process. Along the same line, it is worth mentioning, that the few cells prepared with ZnMgO layer showed slightly

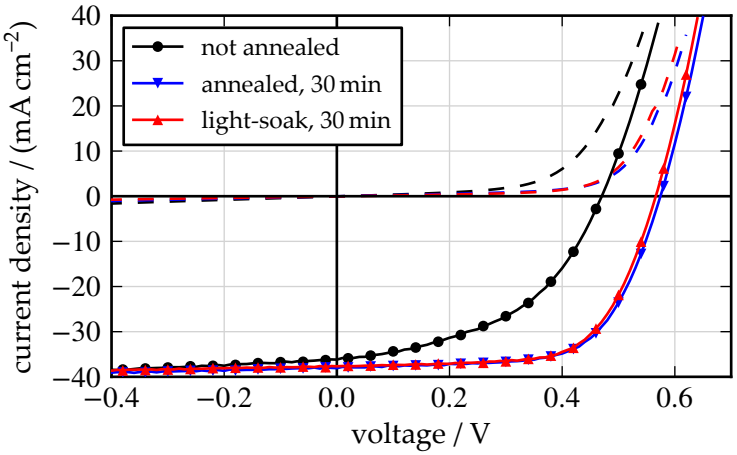

(a) i-ZnO monolayer (no O_2)

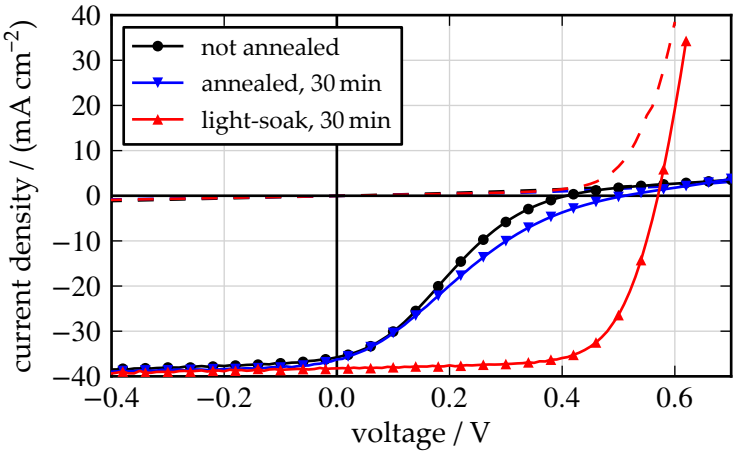

(b) ZnMgO layer (ZSW)

Figure 4.19: Measured IV curves for exemplary cells with (a) optimized i-ZnO layer and (b) ZnMgO layer. Measurements in the dark are given with dashed lines, measurements under simulated AM1.5 illumination are given with solid lines.

above average open circuit voltage and fill factor after light-soaking. Although no in-house record cell was among them, the pathway of exchanging i-ZnO with other materials is most promising.

4.6 Solar cell performance in relation to CIGSSe composition

In the last section, it was shown that while the CBD-Zn(O,S) buffer layer initially leads to poor solar cell efficiency and the need for post-treatments arises, this effect can be significantly reduced by adjusting the window layer deposition parameters. But while it can therefore be concluded that the buffer/window interface plays an important role in determining the height of the electronic barrier, it is initially the conduction band spike at the absorber/buffer interface that is giving rise to this

barrier and it was also shown with simulations in the last section that an effective inversion of CIGSSe surface can have a positive effect on the current collection. Additionally it was presented, that the impact of optimizing the window layer deposition seemed to be different for different batches of CIGSSe absorber I received from the CISTech facilities. In this section, the interplay of CIGSSe composition and solar cell performance will be discussed in more detail.
Figure 4.20 shows the systematic difference of solar cell characteristics between two groups of absorber material that were predominant during the period of developing the CBD-Zn(O,S) buffer and adapting the window layer deposition for this work. They will be denoted as 'Group A' and 'Group B' in the following. The apparent difference between both CIGSSe batches is that with the standard i-ZnO layer deposition (Figs. 4.20(a) and 4.20(b)) there is a significant improvement of current collection for Group A upon annealing, while for Group B it is still largely limited. After light-soaking, both absorber batches result in decent solar cells. Changing to the i-ZnO bilayer with omitted oxygen from the sputter gas while depositing the first layer results in a significant improvement before light-soaking for both absorber batches, while Group A still shows the larger current collection at forward bias. This difference disappears when the buffer layer thickness is reduced and the optimized i-ZnO layer deposition is applied.
While both Group A and Group B are susceptible for improvement of the window layer deposition process, it is clear that Group A absorber and the CBD-Zn(O,S) buffer layer fit better as the initial electronic barrier can be inferred to be smaller. A systematic look at the differences between Group A and Group B absorber show that the most striking one is the amount of incorporated sulfur. Figure 4.21 shows scatter plots of routinely generated XRF data, where 25 measurements are taken on the 30 cm × 30 cm sized substrate before window layer deposition. Sulfur cannot be detected within the non-vacuum XRF measurement. Se, Cu, In, and Ga concentration in the absorber material are, however, monitored. The calculation of [Se]/([Cu]+[In]+[Ga]) gives an indication of the sulfur content in the absorber as missing Se can be expected to be replaced with S. The data shown in Fig. 4.21 clearly falls into five different groups with different [Se]/([Cu]+[In]+[Ga]) ratio and different [Cu]/([Ga]+[In]) ratio. The previously mentioned Group A and Group B are indicated within the figure. The colors indicate median and maximum for the efficiencies and open circuit voltages of each sample, showing that Group A outperforms all other batches. Since the statistical ensemble includes a lot of different adjustments of buffer and window layer deposition parameters and the two groups with low Ga concentration were used in a more early stage of development, the comparison may be afflicted with some uncertainties. To lower these uncertainties, excluding experiments with detrimental character falling far short of the absorber's potential, all samples with median efficiencies below 12 % were removed from the statistical ensemble.
There are some systematic trends visible in Fig. 4.21. First of all, there is a close relation of median and maximum values. The samples with higher median open

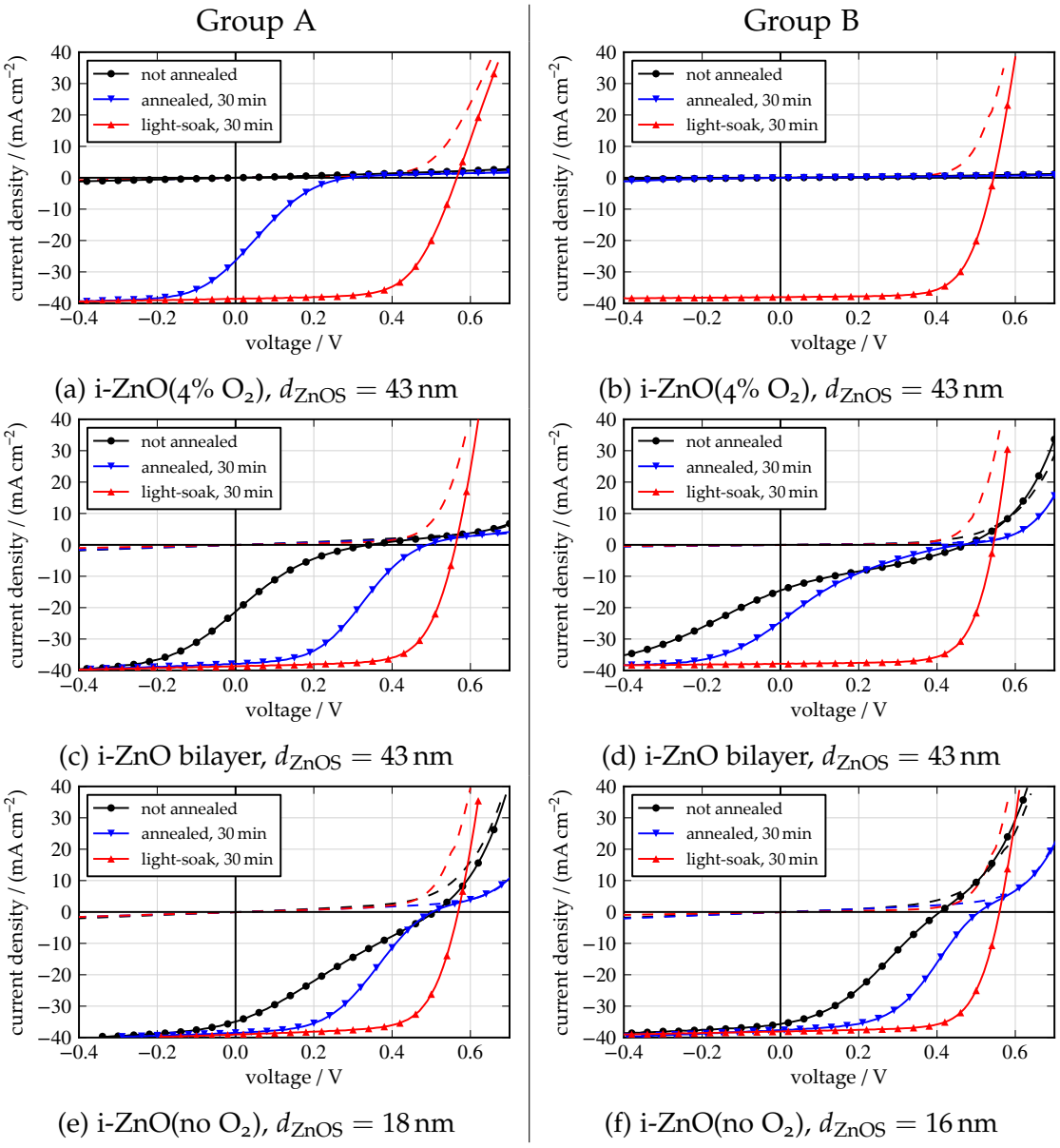

(a) i-ZnO(4% O_2), $d_{ZnOS} = 43\,nm$

(b) i-ZnO(4% O_2), $d_{ZnOS} = 43\,nm$

(c) i-ZnO bilayer, $d_{ZnOS} = 43\,nm$

(d) i-ZnO bilayer, $d_{ZnOS} = 43\,nm$

(e) i-ZnO(no O_2), $d_{ZnOS} = 18\,nm$

(f) i-ZnO(no O_2), $d_{ZnOS} = 16\,nm$

Figure 4.20: Measured IV curves for exemplary cells from two systematically different CIGSSe batches (columns). In rows there are three variations of i-ZnO layer depositions (c.f. Section 4.5.2) with the last row also having a thinner buffer layer. Measurements in the dark are given with dashed lines, measurements under simulated AM1.5 illumination are given with solid lines.

circuit voltages, generally show higher maximum voltages as well, and this is true for the efficiencies as well, if somewhat less pronounced. Then there is a distinct relation between Se concentration (and inferred S concentration) and median open circuit voltage. This is expected because of the larger band gap and the lower valence band maximum position at the CIGSSe surface compared to the CIGSe surface, reducing recombination at the CIGSSe/buffer interface. The Ga concentration on the other hand seems to have less influence on the open circuit

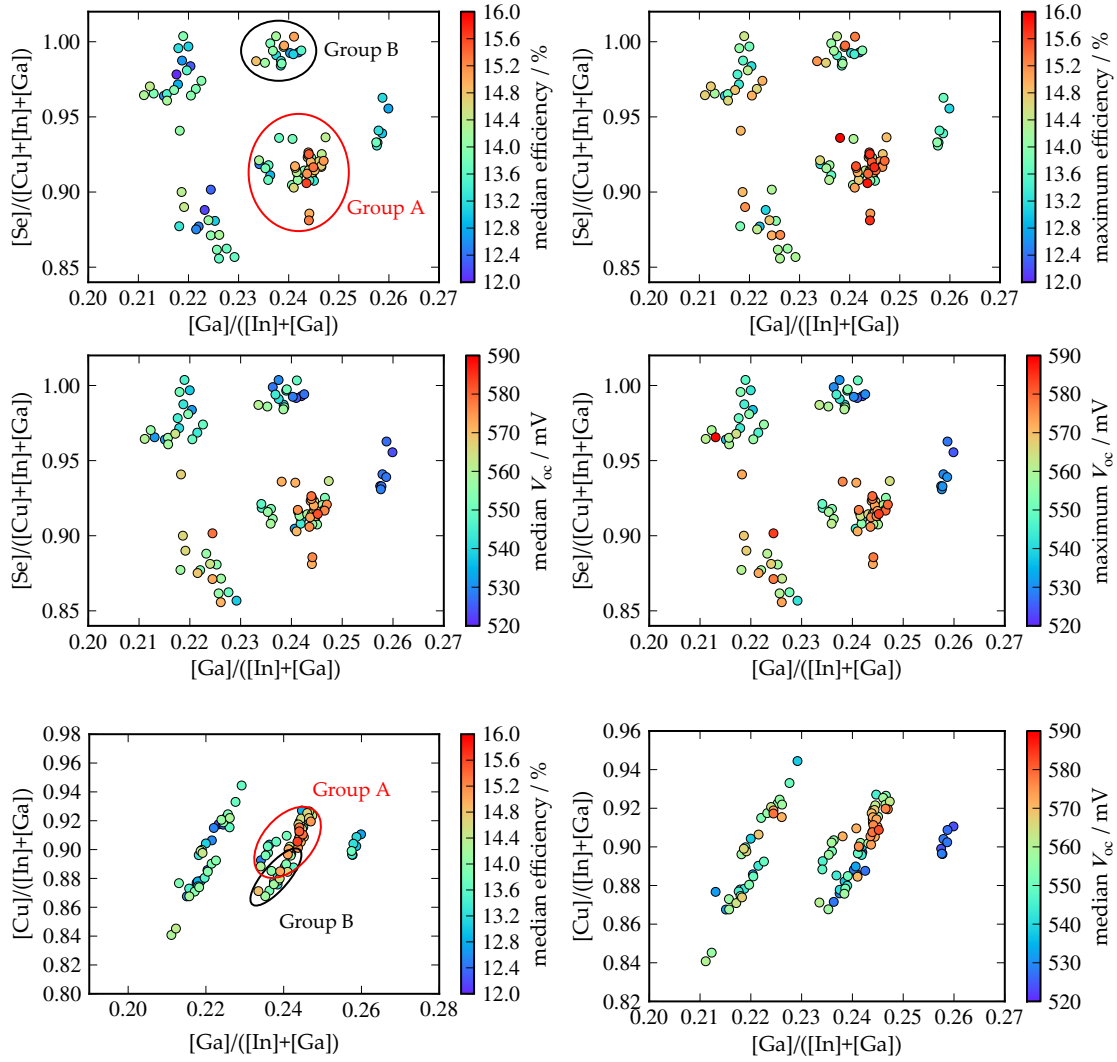

Figure 4.21: Plots of XRF data, averaged over 25 measurements on 30 cm × 30 cm sized substrates (c.f. Section 2.4.1), routinely generated before window layer deposition. The color indicates the solar cell parameters of the finished cells after light-soaking as defined by the label of each colorbar. All plots are generated from the same statistical ensemble, containing various buffer/window combinations.

voltage in this statistical ensemble. Regarding the Cu concentration, the influence on the solar cell characteristics cannot easily be separated from the influence of the Ga concentration as both elements are sputtered from a mixed target (hence the two linear shapes in the scatter plot).
In order to confirm the difference in sulfur concentration for Group A and Group B, Raman spectroscopy measurements were conducted on a piece of substrate for each group with a frequency-doubled Nd:YAG laser (532 nm, 60 mW) used as light source. Both spectra exhibit modes for $CuInSe_2$ and $CuInS_2$. The intensity difference between the two is, however, smaller for the sample from Group A as shown in Fig. 4.22(a). This difference is a good indicator for the change of [S]/([S]+[Se]) in the film [108], showing that Group A indeed has a higher concentration of sulfur at

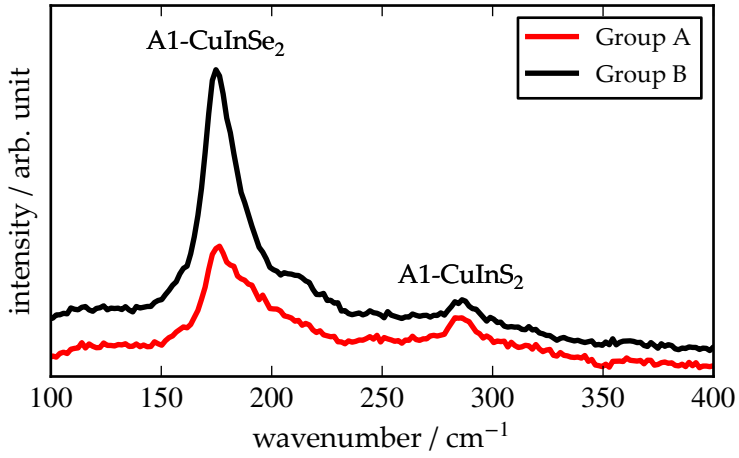

(a) Raman spectroscopy measurement

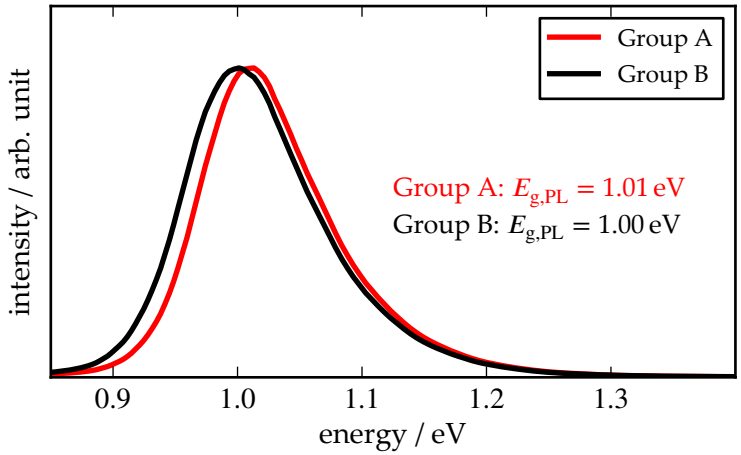

(b) Photoluminescence measurement

Figure 4.22: Raman spectroscopy and photoluminescence measurements on two samples from the Group A (red) and Group B (black) absorber batches. The Raman spectra are corrected for a linear background, extracted at large wavenumbers, and shifted to be displayed on top of each other. The photoluminescence spectra are normalized to the maximum intensity.

the surface compared to Group B. An additionally performed measurement of the photoluminescence spectrum, excited with an IR laser ($\lambda = 830\,\mathrm{nm}$), shows little difference between the two samples as visible in Fig. 4.22(b). Although the peak is indeed shifted to lower energies for the samples from Group B, the change is small. The position of the peak maximum ($E_{g,PL}$) is shifted by only 0.01 eV. While the Raman spectroscopy measurement is rather surface sensitive due to the higher absorption of the 532 nm light, the photoluminescence measurement penetrates the absorber, thereby showing that the incorporation of sulfur mainly affects the absorber surface.

While the effect of sulfurizing the absorber surface on the open circuit voltage is commonly known, the beneficial effect on the electronic barrier at the ab-

sorber/Zn(O,S) interface is not discussed in the literature. Apart from directly raising the conduction band minimum [16], thereby decreasing the absorber/buffer conduction band spike, the possibility cannot be excluded that the introduction of sulfur at the surface leads to a higher degree of surface inversion.
Altogether, it is clear that while the CdS buffer layer usually performs well with only minor deviations on different absorber configurations, the combination of absorber and CBD-Zn(O,S) is rather important, not only in terms of median and maximum efficiencies but also in terms of metastabilities and the need for post-treatments. Concluding this section, in the light of the presented results, a general recommendation of the combination with high sulfur concentration at the surface and high overall gallium concentration seems to be justified.

4.7 Doping CBD-Zn(O,S) with Al and B

While Section 4.5.2 and Section 4.6 were concerned with optimizations of the absorber/buffer/window system without actually changing the buffer layer deposition process, it was discussed in Section 4.5.1 that an increase in n-type doping of the buffer layer can lead to a barrier lowering. In this section the intentional doping by addition of aluminum and boron into the deposition process is attempted. Both aluminum and boron are added to the process described in Section 4.2 without further changes, as the deposition speed is not affected by the addition. Aluminum is added in the form of $AlK(SO_4)_2 \cdot 12H_2O$ and boron is added in the form of boric acid ($B(OH)_3$), both with varying concentrations up to 4 mM and 12.5 mM respectively.
Comparing solar cells with buffer layers produced from these changed solution formulations to solar cells with standard Zn(O,S) buffer layer, a distinct change in the characteristics is visible. Boxplots of solar cell parameters for layers doped with aluminum and boron are shown in Figs. 4.23 and 4.25. In the case of addition of aluminum it is visible in Fig. 4.23 that the initial cell efficiencies and the efficiencies after annealing are slightly higher compared to the standard layer. This is due to partial removal of the S-shape distortion of the IV curve.

It has to be noted though that this effect is only visible for some batches and sometimes only before annealing. In Fig. 4.24 IV curves for exemplary cells after annealing are shown for four different batches with varying absorber material composition and with varying i-ZnO deposition processes. The observed positive tendency is only present in the first batch. In the second batch there even is a negative impact and the third and forth batch do not show any impact at all. Also, only in the first batch there is a visible impact on diode current in the dark.
The addition of boric acid on the other hand, leads to a larger increase in efficiency, which is also observed repeatedly. Figure 4.26 shows IV curves of exemplary cells from four different batches after annealing. All concentrations of boric acid lead to a reduction of the S-shape distortion and thereby increased efficiencies before light-soaking. As visible in Fig. 4.25, in these cases with bilayer i-ZnO, the cells

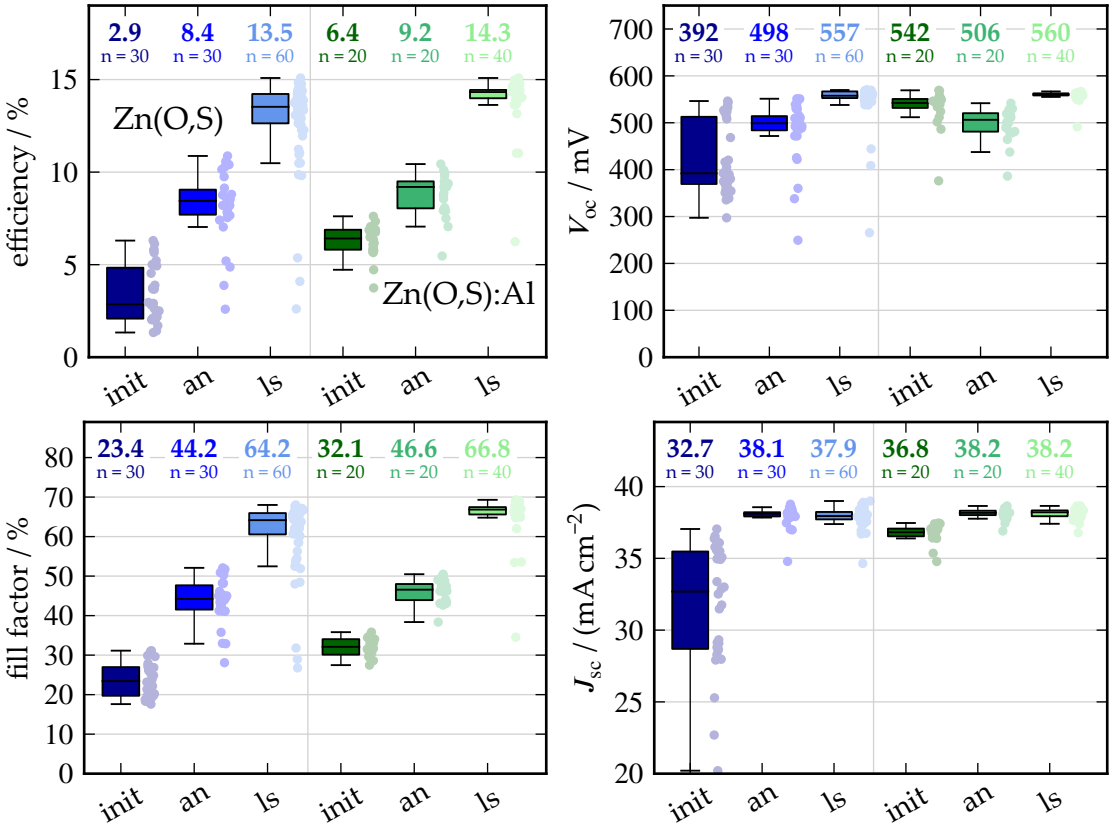

Figure 4.23: Boxplots and scatter plots of solar cell parameters for cells with Zn(O,S) buffer layer before any post-treatment (init), after the annealing post-treatment (an) and after light-soaking (ls). Intentional doping with aluminum is attempted by addition of 1 mM $AlK(SO_4)_2 \cdot 12H_2O$ to the process solution. Median values are given above each boxplot together with the number of cells in the dataset.

do not need to be light-soaked any more. The initial electronic barrier is reduced enough by the annealing post-treatment. The maximum efficiency of a cell with Zn(O,S):B buffer layer was measured to be 15.9 % (16.9 % on active area), which is the highest efficiency for cells with Zn(O,S) based buffer layer from our laboratory. Detailed statistics of solar cell parameters are therefore given for this sample in Table 4.3.

An XPS analysis of samples processed from solutions containing 2 mM aluminum salt and 12.5 mmol dm^{-3} boric acid did not show traces of aluminum or boron in the buffer layer. Regarding the sensitivity of the measurement, the upper limit for the atomic concentration therefore is estimated to be below the range of a few percent. A closer look at the valence band spectra (cf. Section 2.4.2.2) of the layers under investigation, shows a significant trend towards larger energetic distances between Fermi level and valence band maximum position with

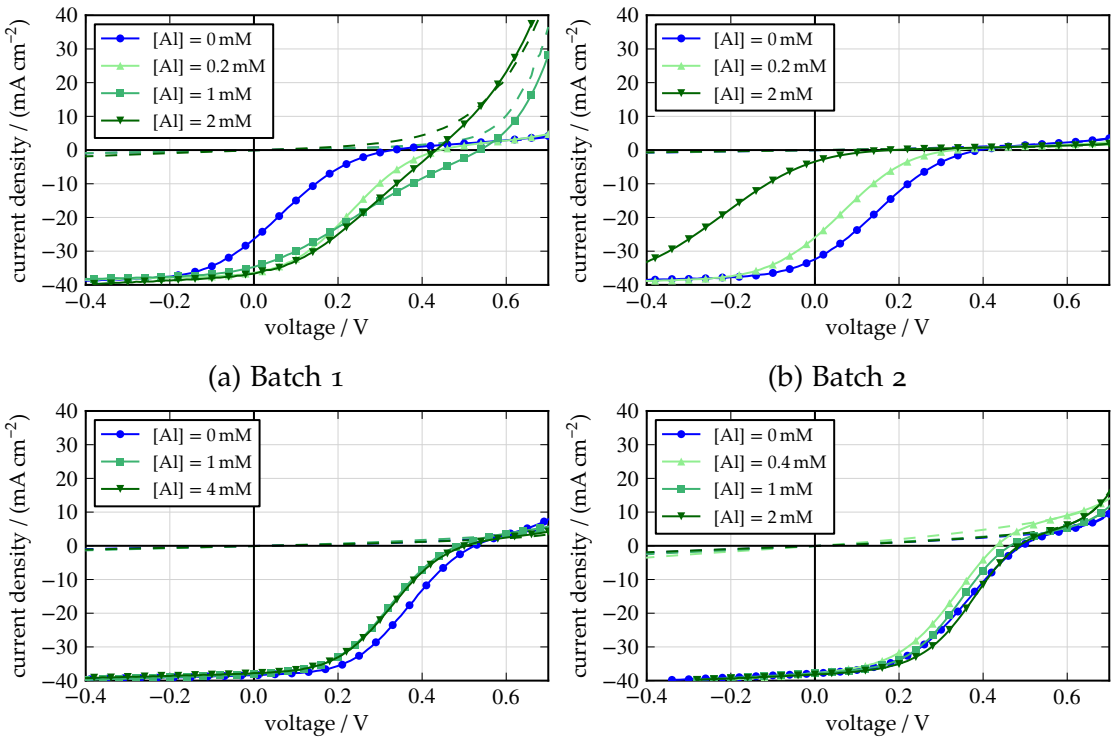

(a) Batch 1

(b) Batch 2

(c) Batch 3

(d) Batch 4

Figure 4.24: IV curves for exemplary cells from different batches, where the concentration of aluminum in the process solution was varied. Data for the complete Batch 1 was shown in Fig. 4.23. All measurements are after annealing and before light-soaking. The absorber composition and the window layer varies between batches.

Table 4.3: Solar cell parameters for the champion sample with Zn(O,S):B buffer layer. The statistical data is represented by the median and median absolute deviation.

	Zn(O,S):B buffer layer		
parameter	not annealed	annealed	light-soaked
n_{samples}	20	20	20
η / %	9.14 ± 0.36	15.26 ± 0.46	14.88 ± 0.47
η_{max} / %	9.6	15.8	15.9
V_{oc} / mV	592 ± 5	579 ± 1	573 ± 2
fill factor / %	42.2 ± 0.9	68.9 ± 2.1	68.8 ± 1.8
J_{sc} / mA cm^{-2}	36.9 ± 0.3	38.1 ± 0.1	37.8 ± 0.1

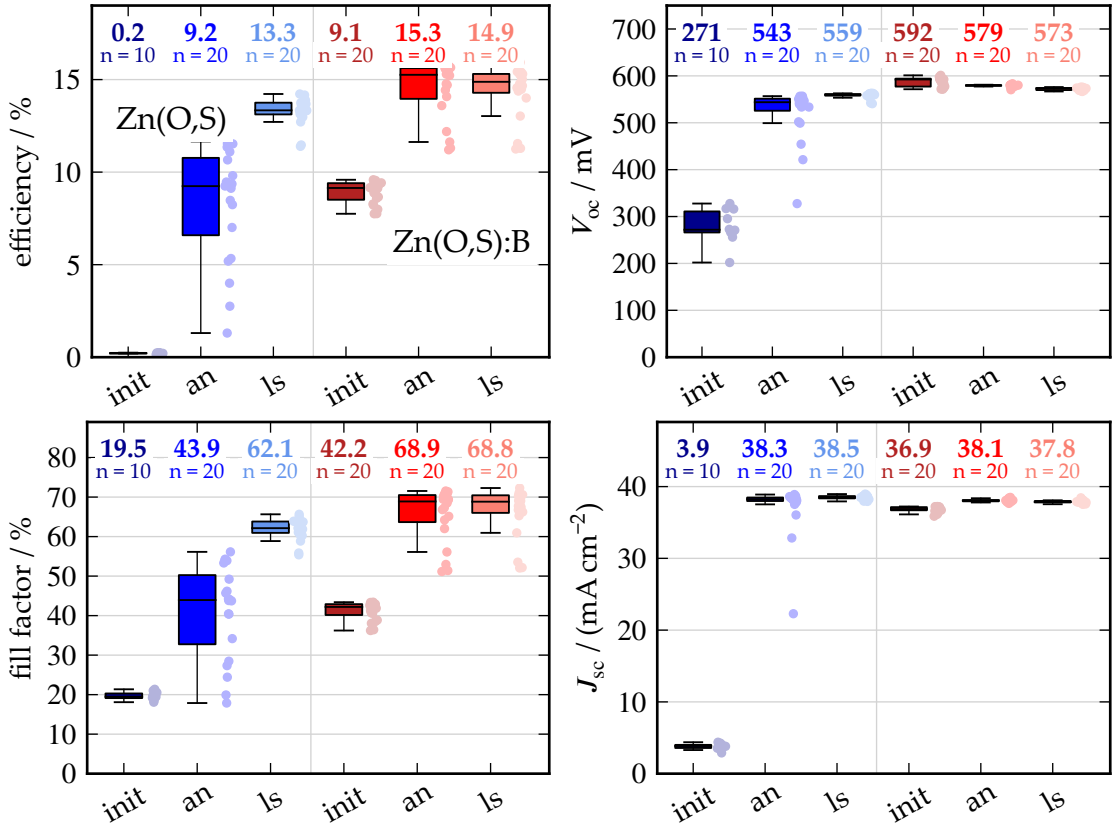

Figure 4.25: Boxplots and scatter plots of solar cell parameters for cells with Zn(O,S) buffer layer and bilayer i-ZnO before any post-treatment (init), after the annealing post-treatment (an) and after light-soaking (ls). Intentional doping with boron is attempted by addition of 12.5 mM boric acid to the process solution. Median values are given above each boxplot together with the number of cells in the dataset.

aluminum and boron addition. This is displayed in Fig. 4.27 where the spectra are shown for the three layers in Fig. 4.27(a) and the extrapolated valence band maximum energies with respect to the Fermi level for six measurements at three locations on each sample in Fig. 4.27(b). Due to the missing n-type window layer, the thin buffer layers in contact with the p-type CIGSSe can be expected to be largely depleted, leading to a lowering of the Fermi level, dependent on the p-type doping concentration in the CIGSSe absorber. Nevertheless, a shift of the Fermi level with respect to the valence band maximum may still be an indicator for an increase in n-type doping density.
Besides the intended doping, the change of the process solution formulation may also have an influence on the ratio [S]/([S]+[O]) in the film. To exclude this possibility, the ratios [S]/([S]+[O]) for all three layers are calculated from atomic concentrations after a short sputter step (1 min at 1 kV) as well as from the zinc Auger parameter and listed in Table 4.4. The calculated values are very similar for all samples, showing that there is no significant change of the layer stoichiometry.

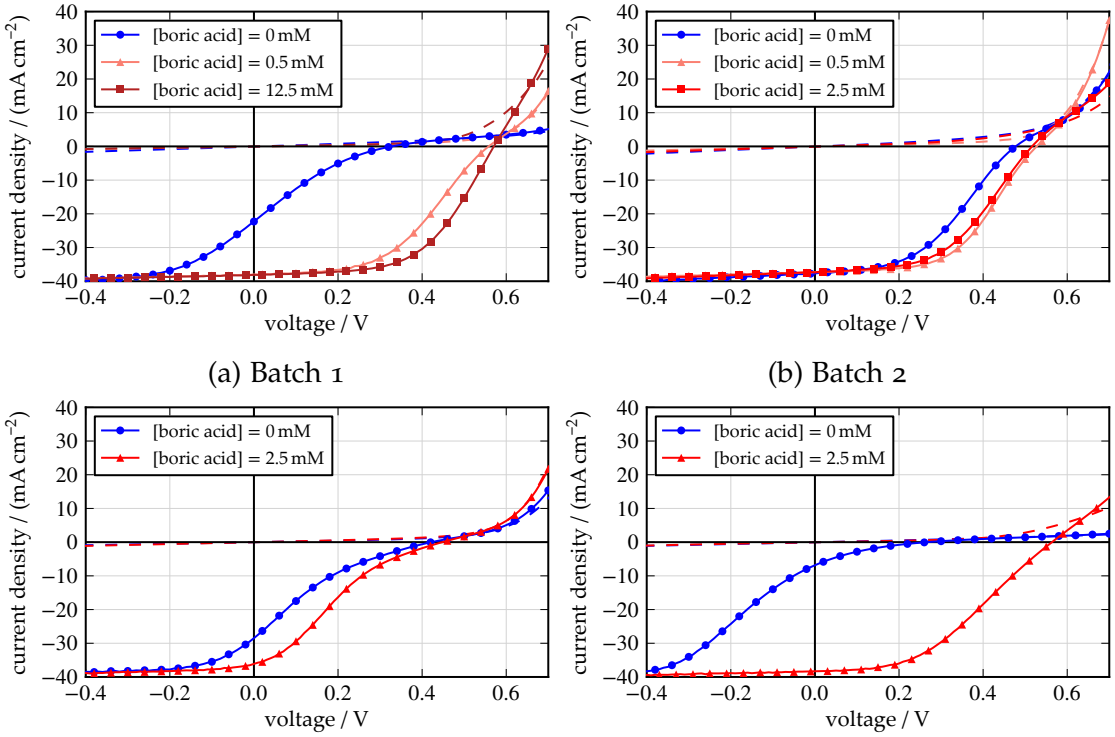

(a) Batch 1

(b) Batch 2

(c) Batch 3

(d) Batch 4

Figure 4.26: IV curves for exemplary cells from different batches, where the concentration of boric acid in the process solution was varied. All measurements are after annealing and before light-soaking. The absorber composition and the window layer varies between batches.

Table 4.4: Layer properties derived from XPS measurements.

	buffer layer		
parameter	Zn(O,S)	Zn(O,S):Al	Zn(O,S):B
[S]/([S+O]) (atomic concentration)	0.65	0.66	0.66
[S]/([S+O]) (Auger parameter)	0.62	0.65	0.67
$\lvert E_{\mathrm{VBM}} - E_{\mathrm{F}} \rvert$ / eV	1.63	1.80	1.90

An unintentional alteration of the conduction band offset is therefore unlikely.

In order to obtain a higher resolution analysis of aluminum or boron traces, additional secondary ion mass spectroscopy (SIMS) measurements for the same samples were commissioned at the Luxembourg Institute of Science and Technology, Materials Research and Technology Department, and carried out on a CAMECA SC-ULTRA instrument using oxygen ion sputtering. In the case of intentional doping with aluminum, an increased aluminum concentration is indeed observed in comparison to the other samples. This increase is, however, not

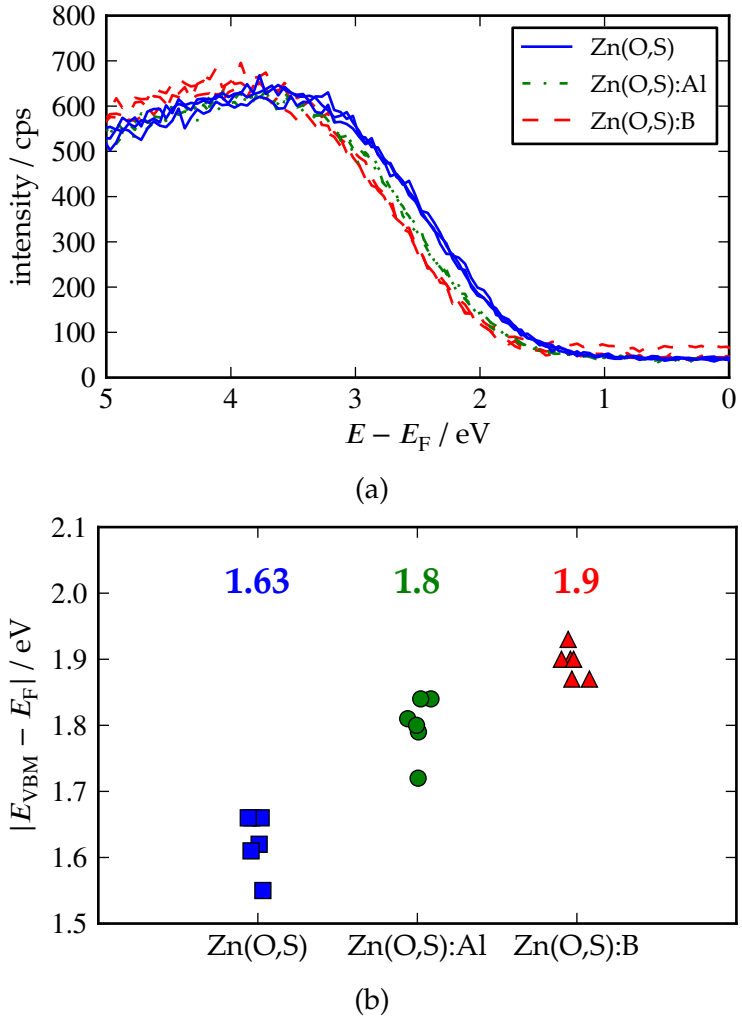

Figure 4.27: Results from XPS surface measurements on CIGSSe/Zn(O,S) layer stacks without and with addition of aluminum or boron compound to the process solution. (a) shows measured spectra and (b) shows extrapolated valence band maximum energies with respect to the Fermi level. Mean values are given above the respective markers.

restricted to the buffer layer region, but instead mainly observed in the CIGSSe material, indicating diffusion of aluminum during the process or during annealing from the buffer layer into the CIGSSe surface. In the case of boron, the detected traces are clearly limited to the buffer layer region. The intentionally doped sample shows the highest amount of detected boron, the differences between the three samples are, however, rather small. Altogether, the performed SIMS measurements are inconclusive and would have to be repeated to support future work.

In the light of these analyses, it may seem doubtful if the Zn(O,S) layers are actually doped with aluminum or boron. In the case of the addition of aluminum salt, this might explain the low impact and poor reproducibility, especially if the diffusion rate of aluminum into the absorber is affected by the CIGSSe composition.

In the case of added boric acid, the results presented here seem to be insufficient to explain the observed larger increase in efficiencies with good reproducibility. On the other hand, the observed shift of the surface potential is an indicator that the electronic properties of the device really are changed by the addition of aluminum or boron towards better type inversion at the CIGSSe/buffer interface. In addition, the reproducibly improved solar cell efficiencies upon addition of boric acid to the process justifies a clear recommendation to further advance this modification of existing Zn(O,S) buffer layer technologies in future work.

4.8 Conclusion for the CBD-Zn(O,S) buffer layer

A novel chemical bath deposition process for Zn(O,S) buffer layers was presented in this chapter. While deposition rate and film quality are good, the resulting solar cells show severely distorted IV curves. This was explained here within a model including an energetic barrier to the electron current. While the IV curve distortion can be resolved with annealing and light-soaking post-treatments, these treatments would complicate large-scale fabrication. Therefore, the remainder of this chapter was dedicated to reduce or even eliminate the need for such post-treatments. In conclusion, here is a guideline to improve CIGSSe cells (absorber from a two-step process) with CBD-Zn(O,S) buffer layer:

- Keep the Zn(O,S) buffer layer as thin as possible.
  - Thick buffer layers with low doping concentration lead to large unwanted voltage drops in the n-side of the junction.
- Incorporate boron as dopant into the CBD process.
  - Higher n-type doping of the buffer layer leads to an effective barrier lowering and ideally results in a p/n+ junction at the absorber/buffer interface.
- Do not sputter-deposit layers on top of Zn(O,S) with oxygen present in the sputter gas.
  - Oxygen present in the sputter gas may induce acceptor type defects at the buffer/window interface or result in lower n-type doping of the buffer layer. Both leading to a higher effective barrier to the current due to a larger voltage drop in the n-side of the junction.
- Do not use a high resistive window layer or keep its conductivity as high as possible while still preventing shunts.
  - Ideally a p/n+ junction will lead to no voltage drop in the n-side of the junction, a large amount of electrons injected into the buffer layer will reduce the effective barrier to the current.
- If a high resistive window layer has to be used, use a material with good conduction band alignment to the Zn(O,S).

  - The better the conduction band alignment, the more electrons will be injected into the buffer layer, lowering the effective barrier to the current.

- Adapt the absorber material. A high sulfur content at the surface is favorable.
  - Apart from typical open circuit voltage gains upon sulfurization, the improved conduction band alignment to the Zn(O,S) buffer layer reduces the conduction band spike and thereby the effective barrier to the current.

If these factors are taken into account, judging from the progress that was made during this work, it should be possible to realize a CIGSSe solar cell with Zn(O,S) buffer layer, deposited in a fast chemical bath process, showing no necessity for annealing or light-soaking post-treatments. Especially the adaptation of the absorber material can, however, pose a serious problem for an existing fabrication. Therefore the more direct approach to lower the electronic barrier by adjusting the conduction band minimum of the chemically deposited buffer layer will be in the focus of the next chapter.

References

[16] S.-H. Wei and A. Zunger, "Band offsets and optical bowings of chalcopyrites and Zn-based II-VI alloys.", Journal of Applied Physics **78**, 3846 (1995) (Cited on pages 20, 92, 126).

[25] C. Persson, C. Platzer-Björkman, J. Malmström, T. Törndahl, and M. Edoff, "Strong valence-band offset bowing of $ZnO_{1-x}S_x$ enhances p-type nitrogen doping of ZnO-like alloys", English, Physical Review Letters **97**, 146403(4) (2006) (Cited on pages 21, 64, 106, 122).

[27] T. Adler, M. Botros, W. Witte, D. Hariskos, R. Menner, M. Powalla, and A. Klein, "Valence band offsets at Cu(In,Ga)Se_2/Zn(O,S) interfaces", physica status solidi (a) **211**, 1972–1980 (2014) (Cited on pages 21, 27–29, 69, 112, 115).

[30] M. Igalson, A. Urbaniak, P. Zabierowski, H. A. Maksoud, M. Buffiere, N. Barreau, and S. Spiering, "Red-blue effect in Cu(In,Ga)Se_2-based devices revisited", Thin Solid Films **535**, 302–306 (2013) (Cited on pages 22, 40, 55, 63).

[32] I. Eisgruber, J. Granata, J. Sites, J. Hou, and J. Kessler, "Blue-photon modification of nonstandard diode barrier in $CuInSe_2$ solar cells", Solar Energy Materials and Solar Cells **53**, 367–377 (1998) (Cited on pages 22, 63, 64).

[38] C. Platzer-Björkman, T. Törndahl, D. Abou-Ras, J. Malmström, J. Kessler, and L. Stolt, "Zn(O,S) buffer layers by atomic layer deposition in Cu(In,Ga)Se_2 based thin film solar cells: Band alignment and sulfur gradient", Journal of Applied Physics **100**, 044506 (2006) (Cited on pages 28, 29, 61, 64).

[61] S. Siebentritt, "Alternative buffers for chalcopyrite solar cells", Solar Energy **77**, 767–775 (2004) (Cited on page 61).

[62] D. Hariskos, S. Spiering, and M. Powalla, "Buffer layers in Cu(In,Ga)Se_2 solar cells and modules", Thin Solid Films **480–481**, 99–109 (2005) (Cited on page 61).

[63] N. Naghavi, D. Abou-Ras, N. Allsop, N. Barreau, S. Bücheler, A. Ennaoui, C.-H. Fischer, C. Guillen, D. Hariskos, J. Herrero, et al., "Buffer layers and transparent conducting oxides for chalcopyrite Cu(In,Ga)$(S,Se)_2$ based thin film photovoltaics: present status and current developments", Progress in Photovoltaics: Research and Applications **18**, 411–433 (2010) (Cited on page 61).

[64] S. Pawar, B. Pawar, J. Kim, O.-S. Joo, and C. Lokhande, "Recent status of chemical bath deposited metal chalcogenide and metal oxide thin films", Current Applied Physics **11**, 117–161 (2011) (Cited on page 61).

[65] T. M. Friedlmeier, P. Jackson, A. Bauer, D. Hariskos, O. Kiowski, R. Wuerz, and M. Powalla, "Improved Photocurrent in Cu(In,Ga)Se_2 Solar Cells: From 20.8% to 21.7% Efficiency with CdS Buffer and 21.0% Cd-Free", IEEE Journal of Photovoltaics **5**, 1487–1491 (2015) (Cited on page 61).

[66] J. Nam, Y. Kang, D. Lee, J. Yang, Y.-S. Kim, C. B. Mo, S. Park, and D. Kim, "Achievement of 17.9% efficiency in 30×30 cm^2 Cu(In,Ga)$(Se,S)_2$ solar cell sub-module by sulfurization after selenization with Cd-free buffer", Progress in Photovoltaics: Research and Applications **24**, 175–182 (2015) (Cited on pages 61, 62).

[67] S. Merdes, V. Malinen, F. Ziem, I. Lauermann, M. Schüle, F. Stober, F. Hergert, N. Papathanasiou, and R. Schlatmann, "Zn(O,S) buffer prepared by atomic layer deposition for sequentially grown Cu(In,Ga)$(Se,S)_2$ solar cells and modules", Solar Energy Materials and Solar Cells **126**, 120–124 (2014) (Cited on page 61).

[68] R. Klenk, A. Steigert, T. Rissom, D. Greiner, C. A. Kaufmann, T. Unold, and M. C. Lux-Steiner, "Junction formation by Zn(O,S) sputtering yields CIGSe-based cells with efficiencies exceeding 18%", Progress in Photovoltaics: Research and Applications **22**, 161–165 (2014) (Cited on page 61).

[69] M. Powalla, W. Witte, P. Jackson, S. Paetel, E. Lotter, R. Wuerz, F. Kessler, C. Tschamber, W. Hempel, D. Hariskos, R. Menner, A. Bauer, S. Spiering, E. Ahlswede, T. Friedlmeier, D. Blázquez-Sánchez, I. Klugius, and W. Wischmann, "CIGS cells and modules with high efficiency on glass and flexible substrates", IEEE Journal of Photovoltaics **4**, 440–446 (2014) (Cited on pages 61, 64, 85).

[70] C. Hubert, N. Naghavi, A. Etcheberry, O. Roussel, D. Hariskos, M. Powalla, O. Kerrec, and D. Lincot, "A better understanding of the growth mechanism of Zn(S,O,OH) chemical bath deposited buffer layers for high efficiency Cu(In,Ga)(S,Se)$_2$ solar cells", physica status solidi (a) **205**, 2335–2339 (2008) (Cited on pages 61, 62).

[71] C. Hubert, N. Naghavi, B. Canava, A. Etcheberry, and D. Lincot, "Thermodynamic and experimental study of chemical bath deposition of Zn(S,O,OH) buffer layers in basic aqueous ammonia solutions. Cell results with electrodeposited CuIn(S Se)$_2$ absorbers", Thin Solid Films **515**, 6032–6035 (2007) (Cited on page 62).

[72] P. O'Brien and J. McAleese, "Developing an understanding of the processes controlling the chemical bath deposition of ZnS and CdS", Journal of Materials Chemistry **8**, 2309–2314 (1998) (Cited on page 62).

[73] R. Sáez-Araoz, D. Abou-Ras, T. Niesen, A. Neisser, K. Wilchelmi, M. Lux-Steiner, and A. Ennaoui, "In situ monitoring the growth of thin-film Zn-S/Zn(S,O) bilayer on Cu-chalcopyrite for high performance thin film solar cells", Thin Solid Films **517**, 2300–2304 (2009) (Cited on page 62).

[74] M. Buffière, E. Gautron, T. Hildebrandt, S. Harel, C. Guillot-Deudon, L. Arzel, N. Naghavi, N. Barreau, and J. Kessler, "Composition and structural study of solution-processed Zn(S,O,OH) thin films grown using H_2O_2 based deposition route", Thin Solid Films **535**, 171–174 (2013) (Cited on page 62).

[75] T. Nakada and M. Mizutani, "18% Efficiency Cd-Free Cu(In, Ga)Se$_2$ Thin-Film Solar Cells Fabricated Using Chemical Bath Deposition (CBD)-ZnS Buffer Layers", Japanese Journal of Applied Physics **41**, L165–L167 (2002) (Cited on page 62).

[76] T. Kobayashi and T. Nakada, "Efficient Cu(In,Ga)Se$_2$ thin film solar cells with reduced thickness of ZnS(O,OH) Buffer Layer", Solar Energy Materials and Solar Cells **117**, 526–530 (2013) (Cited on page 62).

[77] A. Ennaoui, M. Bär, J. Klaer, T. Kropp, R. Sáez-Araoz, and M. C. Lux-Steiner, "Highly-efficient Cd-free CuInS$_2$ thin-film solar cells and mini-modules with Zn(S,O) buffer layers prepared by an alternative chemical bath process", Progress in Photovoltaics: Research and Applications **14**, 499–511 (2006) (Cited on page 62).

[78] D. Hariskos, R. Menner, P. Jackson, S. Paetel, W. Witte, W. Wischmann, M. Powalla, L. Bürkert, T. Kolb, M. Oertel, et al., "New reaction kinetics for a high-rate chemical bath deposition of the Zn(S,O) buffer layer for Cu(In,Ga)Se$_2$-based solar cells", Progress in Photovoltaics: Research and Applications **20**, 534–542 (2012) (Cited on pages 62, 112).

[79] C. Hubert, N. Naghavi, O. Roussel, A. Etcheberry, D. Hariskos, R. Menner, M. Powalla, O. Kerrec, and D. Lincot, "The Zn(S,O,OH)/ZnMgO buffer in thin film Cu (In,Ga)(S,Se)$_2$-based solar cells part I: Fast chemical bath deposition of Zn(S,O,OH) buffer layers for industrial application on Co-evaporated Cu(In,Ga)Se$_2$ and electrodeposited CuIn(S,Se)$_2$ solar cells", Progress in Photovoltaics: Research and Applications **17**, 470–478 (2009) (Cited on page 62).

[80] A. Ennaoui, T. Kropp, M. C. Lux-Steiner, and R. Saéz-Araoz, "Method for applying zinc sulfide and zinc oxide buffer layer on semiconductor substrate, involves dissolving certain amount of zinc salt and thiocarbamide in distilled water", WO 2010108480 A2 (2010) (Cited on page 62).

[81] M. Buffière, S. Harel, L. Arzel, C. Deudon, N. Barreau, and J. Kessler, "Fast chemical bath deposition of Zn(O,S) buffer layers for Cu(In,Ga)Se$_2$ solar cells", Thin Solid Films **519**, 7575–7578 (2011) (Cited on page 62).

[82] J. M. Doña and J. Herrero, "Process and Film Characterization of Chemical-Bath-Deposited ZnS Thin Films", Journal of The Electrochemical Society **141**, 205–210 (1994) (Cited on page 62).

[83] P. Němec, I. Němec, P. Nahalkova, Y. Němcová, F. Trojanek, and P. Malý, "Ammonia-free method for preparation of CdS nanocrystalline films by chemical bath deposition technique", Thin Solid Films **403**, 9–12 (2002) (Cited on page 62).

[84] G. Agawane, S. W. Shin, A. Moholkar, K. Gurav, J. H. Yun, J. Y. Lee, and J. H. Kim, "Non-toxic complexing agent Tri-sodium citrate's effect on chemical bath deposited ZnS thin films and its growth mechanism", Journal of Alloys and Compounds **535**, 53–61 (2012) (Cited on pages 62, 106).

[85] T. Hildebrandt, N. Loones, M. Bouttemy, J. Vigneron, A. Etcheberry, D. Lincot, and N. Naghavi, "Search for new bath formulations of Zn(S, O, OH) buffer layer to outperform record performances of CdS-based CIGSe solar cells", in Photovoltaic Specialists Conference (PVSC), 2013 IEEE 39th (June 2013), pp. 1114–1119 (Cited on pages 62, 106).

[86] J. Liao, S. Cheng, H. Zhou, and B. Long, "Al-doped ZnS thin films for buffer layers of solar cells prepared by chemical bath deposition", IET Micro Nano Letters **8**, 211–214 (2013) (Cited on pages 62, 64, 106).

[87] H. Khallaf, G. Chai, O. Lupan, H. Heinrich, S. Park, A. Schulte, and L. Chow, "Investigation of chemical bath deposition of ZnO thin films using six different complexing agents", Journal of Physics D: Applied Physics **42**, 135304 (2009) (Cited on page 62).

[88] A. Yamada, H. Miyazaki, Y. Chiba, and M. Konagai, "High-efficiency Cu(InGa)Se$_2$ solar cells with a zinc-based buffer layer", Thin Solid Films **480**, 503–508 (2005) (Cited on page 62).

[89] A. Goudarzi, G. M. Aval, R. Sahraei, and H. Ahmadpoor, "Ammonia-free chemical bath deposition of nanocrystalline ZnS thin film buffer layer for solar cells", Thin Solid Films **516**, 4953–4957 (2008) (Cited on page 62).

[90] W. Witte, D. Hariskos, A. Eicke, R. Menner, O. Kiowski, and M. Powalla, "Impact of annealing on Cu(In,Ga)Se_2 solar cells with Zn(O,S)/(Zn,Mg)O buffers", Thin Solid Films **535**, 180–183 (2012) (Cited on pages 62, 63).

[91] N. Naghavi, C. Hubert, A. Darga, G. Renou, C. Ruiz, A. Etcheberry, D. Hariskos, M. Powalla, and J. Guillemoles, "On a Better Understanding of Post-Treatment Effects on CI(G)S/Zn(S,O,OH)/ZnMgO Based Solar Cells", in 23rd European Photovoltaic Solar Energy Conference and Exhibition (Sept. 2008), pp. 2160–2164 (Cited on pages 62, 63).

[92] T. Kobayashi, T. Kumazawa, Z. Jehl Li Kao, and T. Nakada, "Post-treatment effects on ZnS(O,OH)/Cu(In,Ga)Se_2 solar cells deposited using thioacetamide-ammonia based solution", Solar Energy Materials and Solar Cells **123**, 197–202 (2014) (Cited on pages 62, 63).

[93] N. Naghavi, S. Temgoua, T. Hildebrandt, J. F. Guillemoles, and D. Lincot, "Impact of oxygen concentration during the deposition of window layers on lowering the metastability effects in Cu(In,Ga)Se_2/CBD Zn(S,O) based solar cell", Progress in Photovoltaics: Research and Applications **23**, 1820–1827 (2015) (Cited on pages 62–64, 81, 85, 86).

[94] A. Pudov, J. Sites, M. Contreras, T. Nakada, and H.-W. Schock, "CIGS J–V distortion in the absence of blue photons", Thin Solid Films **480**, 273–278 (2005) (Cited on pages 63, 64).

[95] Q. Nguyen, K. Orgassa, I. Koetschau, U. Rau, and H. Schock, "Influence of heterointerfaces on the performance of Cu(In,Ga)Se_2 solar cells with CdS and In(OH_x,S_y) buffer layers", Thin Solid Films **431–432**, 330–334 (2003) (Cited on page 63).

[96] M. Igalson and C. Platzer-Björkman, "The influence of buffer layer on the transient behavior of thin film chalcopyrite devices", Solar Energy Materials and Solar Cells **84**, 93–103 (2004) (Cited on page 63).

[97] M. Buffière, N. Barreau, L. Arzel, P. Zabierowski, and J. Kessler, "Minimizing metastabilities in Cu(In,Ga)Se_2/(CBD)Zn(S,O,OH)/i-ZnO-based solar cells", Progress in Photovoltaics: Research and Applications **23**, 462–469 (2015) (Cited on pages 63, 64, 67, 81).

[98] A. Zunger, "Practical doping principles", Applied Physics Letters **83**, 57–59 (2003) (Cited on page 64).

[99] P. Prathap, N. Revathi, Y. Subbaiah, K. R. Reddy, and R. Miles, "Preparation and characterization of transparent conducting ZnS:Al films", Solid State Sciences **11**, 224–232 (2009) (Cited on page 64).

[100] D. E. Ortíz-Ramos, L. A. González, and R. Ramirez-Bon, "p-Type transparent Cu doped ZnS thin films by the chemical bath deposition method", Materials Letters **124**, 267–270 (2014) (Cited on page 64).

[101] J.-H. Lee, W.-C. Song, J.-S. Yi, and Y.-S. Yoo, "Characteristics of the CdZnS thin film doped by thermal diffusion of vacuum evaporated indium films", Solar Energy Materials and Solar Cells **75**, 227–234 (2003) (Cited on page 64).

[102] H. Khallaf, G. Chai, O. Lupan, L. Chow, S. Park, and A. Schulte, "Investigation of aluminium and indium in situ doping of chemical bath deposited cds thin films", Journal of Physics D: Applied Physics **41**, 185304 (2008) (Cited on pages 64, 106).

[103] S. A. Al Kuhaimi and Z. Tulbah, "Structural, Compositional, Optical, and Electrical Properties of Solution-Grown $Zn_xCd_{1-x}S$ Films", Journal of The Electrochemical Society **147**, 214–218 (2000) (Cited on pages 64, 105).

[104] H. Khallaf, G. Chai, O. Lupan, L. Chow, H. Heinrich, S. Park, and A. Schulte, "In-situ boron doping of chemical-bath deposited CdS thin films", physica status solidi (a) **206**, 256–262 (2009) (Cited on page 64).

[105] G. Sozzi, F. Troni, and R. Menozzi, "On the combined effects of window/buffer and buffer/absorber conduction-band offsets, buffer thickness and doping on thin-film solar cell performance", Solar Energy Materials and Solar Cells **121**, 126–136 (2014) (Cited on page 64).

[106] K. Ellmer, A. Klein, and B. Rech, *Transparent Conductive Zinc Oxide*, (Springer Berlin Heidelberg, 2008), ISBN: 978-3-540-73612-7 (Cited on page 81).

[107] T. Minemoto, Y. Hashimoto, T. Satoh, T. Negami, H. Takakura, and Y. Hamakawa, "Cu(In,Ga)Se_2 solar cells with controlled conduction band offset of window/Cu(In,Ga)Se_2 layers", Journal of Applied Physics **89**, 8327–8330 (2001) (Cited on page 85).

[108] J. Palm, S. Jost, R. Hock, and V. Probst, "Raman spectroscopy for quality control and process optimization of chalcopyrite thin films and devices", Thin Solid Films **515**, 5913–5916 (2007) (Cited on page 90).

5 Chapter 5
The CBD-ZnInOS buffer

In this chapter the incorporation of indium as an additional cation into Zn(O,S) buffer layers will be presented. In Chapter 2 it was discussed that the band alignment at the CIGSSe/buffer interface is critical for device performance, and as we saw in Chapter 4, within the framework of chemical bath deposition it is virtually impossible to adjust the band alignment by modification of the [S]/([S]+[O]) ratio. Instead, effective interface engineering with chemically deposited materials is possible, when Zn(O,S) is alloyed with a different oxide or sulfide with a smaller band gap and lower conduction band minimum as will be shown in the following sections.

5.1 Literature survey

A replacement of the cation in Zn(O,S) based thin films is mainly motivated by an adjustment of the conduction band minimum energy E_{VB} while leaving the valence band maximum energy E_{CB} unaltered, thereby retaining the high band gap. For chalcogenides and oxides this approach is valid in most cases due to the common anion rule, stating that E_{VB} is rather unaffected by changes of the cation for materials with large anionic contribution to the valence band states [23].
From the periodic table Cd is an easy choice as a replacement for Zn, being the next larger element in the same group. Indeed early on in the development of Cu(In,Ga)Se_2 solar cells, evaporated CdZnS layers were used as window layer [109] and later CBD-(Zn,Cd)S thin films with tunable band gap were described in literature [103] as well as CBD-(Zn,Cd)(O,OH,S) buffer layers for the use in efficient Cu(In,Ga)Se_2 solar cells [110]. However, even if these thin films prove to be advantageous with respect to reduced absorption and better band alignment at high [Ga]/([Ga]+[In]) ratios at the absorber surface, the requirement to be a nontoxic cadmium free buffer layer is obviously not satisfied.
Indium sulfide and indium oxide thin films on the other hand also are reported to have lower band gaps compared to the respective zinc compounds, with 1.9 eV to 2.8 eV for In_2S_3 and 2.8 eV for In_2O_3 compared to 3.6 eV for ZnS and 3.2 eV for ZnO [23]. The common anion rule was experimentally confirmed for ZnO and In_2O_3, both exhibiting the same valence band positions [34]. For ZnS and In_2S_3 on the other hand, the data reviewed by A. Klein [23] is rather ambiguous. Following transitivity considerations it may be concluded that the difference in E_{VB} is small.

The constant valence band energies combined with reduced band gaps then lead to a reduction of conduction band energies for the shift from Zn compound to the In compound. There is no indication in the literature as to if the situation is that simple for solid solutions of all four compounds ZnS, ZnO, In_2S_3, and In_2O_3 (ZnInOS), as there might occur additional band gap bowing for $In_2(O,S)_3$ compounds similar to the bowing observed for the transition from ZnO to ZnS [25], affecting both valence band and conduction band. If the solid solution is restricted to a constant sulfide to oxide ratio, the common anion rule may however still be valid.

ZnInS compounds with different stoichiometry have been prepared by furnace annealing of ZnS/In_2S_3 mixtures, and various different phases have been identified by Boorman and Sutherland [111], demonstrating the possibility of compound formation for a variety of [In]/([In]+[Zn]) ratios, where different phases coexist for most of these ratios. ZnInOS compounds prepared by chemical bath deposition are usually fabricated in acidic processes. Due to their photocatalytic properties in the visible range of the optical spectrum there are some activities in the preparation of $ZnIn_2S_4$ nanocrystals [112, 113] and chemically deposited ZnInS thin films, showing a shift from $Zn_3In_2S_6$ to $ZnIn_2S_4$ and In_2S_3 phases as the [In]/[Zn] ratio in the process solution is increased [114]. In addition, with decreasing Zn content in the film, a decrease of the band gap was observed.
There are also some reports of applying similar films as buffer layer on chalcopyrite based solar cells [115–117], where the acidic CBD processes are all similar to the fabrication process for $In_x(OH,S)_y$ buffer layers, initially proposed by Hariskos et al. [118], utilizing the fact that ZnS can be deposited under similar conditions. Tokita et al. show that the addition of ZnCl to an acidic process can lead to $In(OH)_3$ based buffer layers that show no light-soaking effect in the finished cell [119]. This is attributed to a doping effect of the Zn in the $In(OH)_3$ material without further clarification.

The only existing claim of an alkaline process for ZnInOS-like films is a patent by Hashimoto et al. where a simple ammonia based process is describe with an indium salt added to the process solution [120]. It is however not likely that this process actually yields the wanted result. The main reason for this is that in neutral to alkaline aqueous solutions indium hydroxide will precipitate [121] and indium will not be incorporated into the layer. Similar problems seem to occur when indium chloride is added to a standard cadmium sulfide deposition process [102]. There is however a report by Asabe et al. of growing an indium selenide thin film from an alkaline aqueous solution [122]. The key to this is using tartaric acid as complexing agent as the indium tartrate complex is stable enough to prevent fast hydroxide precipitation. In Section 5.3 it will be shown that tartaric acid is not an ideal complexing agent for the fabrication of ZnInOS films, whereas the citric acid fulfills this requirement. The use of citrate complexes in the deposition of Zn(O,S) films has already been reported by others [84–86]. The novelty here is to use citric acid to simultaneously stabilize both indium and zinc in the process solution.
In Section 5.3 an XPS analysis of the fabricated ZnInOS films will be presented. A

detailed study of Zn(O,S) buffer layers by means of XPS analysis is already given in the dissertations of T. Adler [33] and a review of band alignments determined from XPS measurements can be found in the publications of A. Klein [23, 34]. The results obtained in this work will be evaluated in the context of these references.

5.2 An acidic CBD-process for ZnInOS buffer layers

5.2.1 *Process description*

Before film deposition the glass/Mo/CIGSSe substrate to be coated is placed in 2.5 % ammonia solution (1.5 M) at room temperature. The time for this pre-treatment is not fixed and usually done during the heating process for the chemical bath solution, ranging up to 15 min. Stock solutions for the chemicals involved in the CBD process were prepared with deionized water, namely a solution of 0.5 M $ZnSO_4$, a solution of 133 mM thioacetamide (TAA), a 5 % solution of sulfuric acid (0.9 M) and a solution of 40 mM $In_2(SO_4)_3$. Sulfates and sulfuric acid are used in order to minimize the influence of the anion on the process. The process solution is then prepared from these stock solutions using concentrations similar to processes cited in the literature survey. First, 102 mL of deionized water are put into a beaker with maximum volume of 600 mL, then 48 mL of the $ZnSO_4$ solution and 0.5 mL of the sulfuric acid solution are added. In a second beaker 300 mL of the TAA solution are prepared. Both solutions are then heated under stirring up to 75 °C, at which point they are put together and, after rinsing it with deionized water, the substrate is placed into the chemical bath. After around 10 min the solution becomes slightly turbid and the turbidity increases until the chemical bath becomes completely white in appearance, indicating precipitation of zinc sulfide. After a deposition time of 15 to 20 min the sample is removed from the chemical bath, rinsed in 2.5 % ammonia solution and deionized water, and finally dried in nitrogen gas flow. Before solar cell fabrication a heat treatment in an oven at 190 °C in air is performed in order to remove any residual water and hydroxides. In order to introduce indium into the buffer layer, at the beginning some volume of water is replaced by the same volume of $In_2(SO_4)_3$ stock solution. At 50 mL of the $In_2(SO_4)_3$ stock solution the solution is getting turbid already after 2 min and the color undergoes a fast shift from white to yellow, indicating a precipitation of In_2S_3 in the solution. With lower indium sulfate concentrations this happens on a longer timescale. Since all films were prepared on top of CIGSSe the exact amount of incorporated indium could not be determined by XRF measurements at this point. However, as described in Section 2.4.1 and visible in Fig. 2.10, the film color gives a rough indicator of the film thickness. A comparison of the film color with samples containing no indium while calculating the effective Zn(O,S) film thickness of these samples from XRF measurements, displayed in Fig. 5.1, indicates an incorporation of indium into these samples.

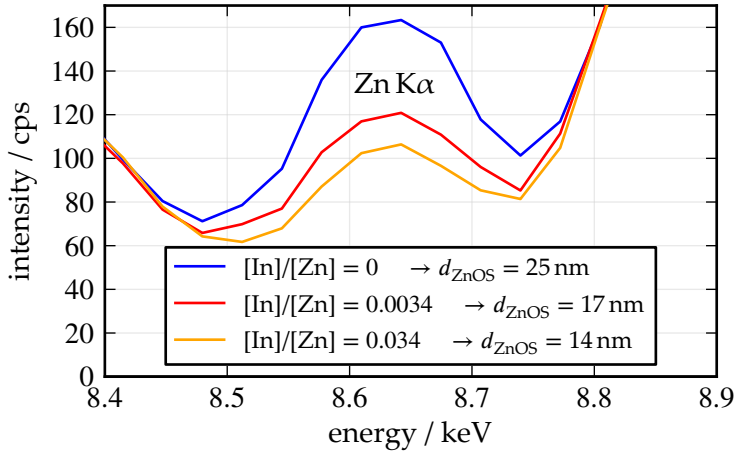

Figure 5.1: Zn Kα emission line from XPS measurements for buffer layers on CIGSSe produced from the described acidic CBD process with three different amounts of indium in the process solution. With increasing amount of indium the Zn Kα emission line intensity is decreasing, leading to decreasing effective Zn(O,S) thicknesses d_{ZnOS} while the samples have a thicker visual appearance, showing blue and yellow colors.

5.2.2 *Solar cells*

Several working solar cells were fabricated with buffer layers deposited from the described acidic CBD process. In Fig. 5.2 solar cell characteristics of two examples are shown in detail. Sample 1 was prepared with the described process without addition of indium sulfate. For Sample 2 1 mL of the $In_2(SO_4)_3$ stock solution was added. The visual appearance of the deposited layer on Sample 2 was slightly darker, normally indicating a higher film thickness. Effective Zn(O,S) film thicknesses measured with XRF however were 25 nm and 17 nm indicating a significant incorporation of indium into the buffer layer even at the ratio of [In]/[Zn] = 0.0034 in the process solution. Both samples received a sputtered i-ZnO/ZnO:Al window layer, a Ni/Al contact grid and cell separation at the ZSW. Cells with Zn(O,S) buffer layer from the acidic process clearly underperform in comparison to cells with Zn(O,S) buffer layer from the standard alkaline process described in Section 4.2. Upon incorporation of indium in sample 2 on the other hand, the solar cell performance is remarkably enhanced. Even though current collection is largely inhibited before any post-treatment, there is at least some collection at negative bias of −0.4 V. These cells did not receive an optimized i-ZnO layer as described in Section 4.5. Thus, it can be concluded that the initial electronic barrier in a heterojunction with this ZnInOS buffer layer is lower compared to the Zn(O,S) buffer from the standard alkaline process since almost complete current blocking is observed in the latter case up to a negative bias voltage of −1.5 V (c.f. Section 4.4 and Fig. 4.8). After annealing and light-soak post-treatments of the completed cells, the cells with ZnInOS buffer have a median efficiency of 14.48 % with very little deviation. As to why the electronic barrier is reduced by the incorporation of indium in acidic process, this in not known at this point. As

was pointed out in Section 2.2.4 likely causes are either a reduction of ΔE_{CB} at the absorber/buffer interface or an increase in buffer layer conductivity.

5.2.3 *Conclusion for the acidic CBD process*

It was possible do devise a simple acidic process with Zn(O,S) and In_2S_3 precipitation and film formation in parallel, as was expected from the literature survey. While the original intention was to introduce indium into a deposition process for Zn(O,S) the actual process seems to be largely dominated by In_2S_3 formation. This leads to difficulties when trying to incorporate only little amounts of indium. Nevertheless working solar cells with Zn(O,S) buffer layer as well as cells with ZnInOS could be prepared and the letter showed enhanced behavior with respect to the necessity for annealing and light-soak. Final efficiencies were comparable to CdS references shown in Section 4.4.
Although the solar cell results demonstrated in this section are very promising at the least, there are several shortcomings of the acidic process described here. Three main problems severely restrict the potential application in industry. First, the chemical consumption is very high. The amount of $ZnSO_4$ and TAA needed is higher by roughly a factor of 10 compared to the alkaline process described in Section 4.2. Second, the process is very sensitive to pH changes. There is no pH stabilization and the amount of sulfuric acid and also the amount of $In_2(SO_4)_3$ affect the pH. At pH larger than 4 precipitation of sulfides was observed, but no film formed on top of the substrate. Below a pH of 1 there was no precipitation nor film formation. The speed of film formation and also the onset of precipitation between pH 1 and pH 4 was not easily controlled as well. The last problem is the high emission rate of toxic hydrogen sulfide at low pH. This made work in the lab rather complicated and would also need to be taken care of in an industrial application. In conclusion, an alkaline process with stabilized pH, yielding the same capacity for indium integration, is highly desirable.

5.3 An alkaline CBD-process for ZnInOS buffer layers

As was discussed in the last section, an alkaline CBD process for the fabrication of mixed zinc indium oxysulfide buffer layers is desirable. Such a process is not described in literature. As mentioned in the literature survey, the key to keeping indium hydroxide from precipitating is the use of the right complexing agent. Trials with tartaric acid under common process conditions showed indeed that indium can be stabilized in the solution by this complexing agent. Only at very high pH > 13 indium hydroxide formation was precipitating slowly. When zinc sulfate is added to the solution, however, the solution becomes turbid very fast. The most probable reason is that zinc tartrate is also a very stable complex with very low solubility. The same problem occurs with oxalic acid as complexing agent with the addition that the indium complex is not stable enough and slow indium

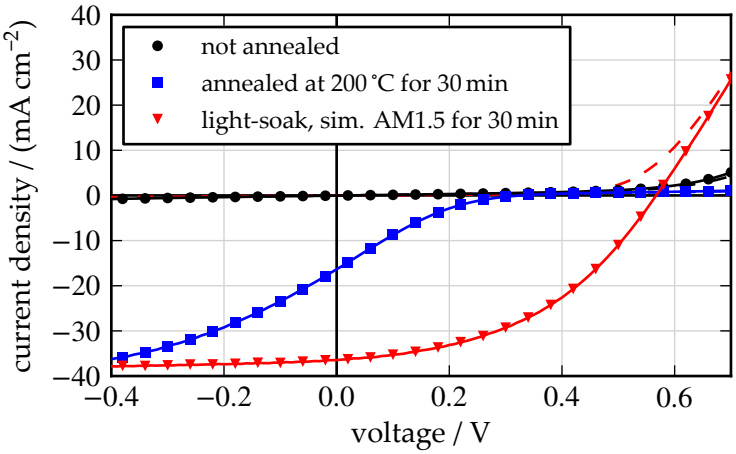

(a) Sample 1: Zn(O,S) buffer from the acidic process.

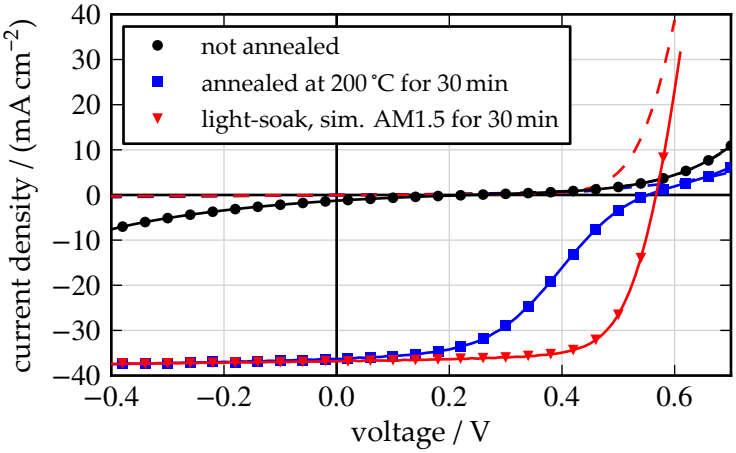

(b) Sample 2: ZnInOS buffer from the acidic process.

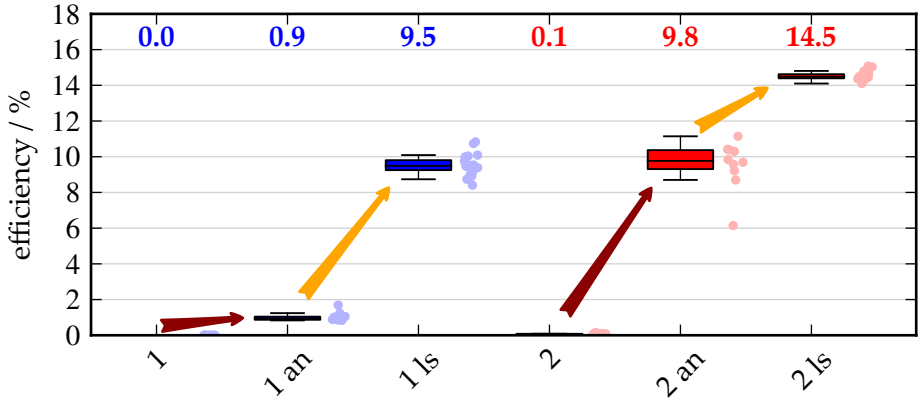

(c)

Figure 5.2: Figure (a) and (b) show IV curves for representative solar cells with buffer layers produced in an acidic chemical bath process as described in Section 5.2.1. The indium concentration in the chemical bath for sample 2 was [In]/[Zn] = 0.0034. Figure (c) shows a boxplot for the impact of annealing (an) and light-soak post-treatment (ls) for the whole ensembles. Median efficiencies are given with colored numbers above each box.

hydroxide precipitation occurs. Citric acid on the other hand yielded the wanted solution properties. No precipitation of indium or zinc compounds were observed under common process conditions as long as no sulfur source was added to the solution.

5.3.1 *Process description*

Before film deposition the substrate to be coated is placed in 2.5 % ammonia solution (1.5 M) at room temperature. The time for this pre-treatment is not fixed and usually done during the heating process for the chemical bath solution, ranging up to 15 min. For this process, stock solutions were only used for $In_2(SO_4)_3$ and TAA, namely a solution of 40 mM $In_2(SO_4)_3$ in deionized water and a solution of 133 mM TAA in deionized water. The process solution is prepared by adding $ZnSO_4$ and citric acid to constantly stirred deionized water with concentrations of 45 mM and 147 mM respectively. The amount of citric acid was chosen to have an excess of citrate anions over indium cations under the assumption that one indium cation is coordinated with 3 citrate anions. In principle it is possible to have this zinc citrate solution as a stock solution since the concentration is not altered throughout the experiments. However such a solution was repeatedly observed to turn yellowish over time (days to weeks) and although such a yellowish solution proved no worse in the CBD process, it was not employed for the experiments shown here in order to prevent unwanted effects. To the stirred solution varying amounts of the $In_2(SO_4)_3$ stock solution were added in order to adjust the ratio of zinc and indium cations in the solution [In]/[Zn] from 0 to 0.4. The resulting solution is heated up to 60 °C under constant stirring. At this point 25 % ammonia solution and the TAA stock solution are added, leading to final substance concentrations of 33 mM $ZnSO_4$, 108 mM citric acid, 2.23 M ammonia, and 13.3 mM TAA in the solution. The pH of the solution, having been below 1 before the addition of ammonia, is measured to be approximately 10.5 after the addition of ammonia regardless of the indium concentration.
Directly after the addition of ammonia and TAA, the substrate to be coated is taken out of the ammonia pre-treatment and placed in the stirred process solution, which is then heated further until it reaches a temperature of 80 °C. The process solution becomes turbid after one minute, which is before a film with significant thickness was formed. After 20 minutes the coated substrate is taken out of the solution, rinsed with 2.5 % ammonia solution and dried in nitrogen gas flow.

5.3.2 *Film properties*

For films deposited on molybdenum coated glass, the ratio [In]/([In]+[Zn]) in the film can be determined with XRF measurements. In addition the film thickness can be calculated using the formalism described in Section 2.4.1. Therefore these molybdenum coated substrates were employed for process development. Films

Table 5.1: Average ZnInOS film thickness on CIGSSe determined from XRF measurements. n_{In}/n_{Zn} ratios are determined from XPS surface measurements shown in Fig. 5.3 (interpolated values in brackets). Values $d_{ZnInS,calc}$ are calculated according to equation (2.41).

[In]/[Zn] (solution)	n_{In}/n_{Zn} (film)	d_{ZnOS}	$d_{ZnInOS,calc}$
0.00	0	41.9	
0.02	[0.015]	35.0	35.7
0.04	0.03	31.2	32.5
0.08	0.11	24.3	28.0
0.16	0.47	21.1	34.8
0.40	0.69	26.1	51.0

deposited on Cu(In,Ga)(S,Se)$_2$ substrates yield an effective Zn(O,S) thickness d_{ZnOS} from which, with knowledge of the amount of incorporated indium, the true film thicknesses can be estimated and are displayed in Table 5.1. In order to obtain information on the ratio [In]/([In]+[Zn]) and on the ratio [S]/([S]+[O]) in the produced film, XPS measurements were employed. The results for films deposited on Mo and on Cu(In,Ga)(S,Se)$_2$ are displayed in Figs. 5.3 and 5.4. In Fig. 5.3 it is clearly visible that the amount of incorporated indium can be tuned by the amount of indium salt added to the solution. A close look also reveals that the ratio of indium in the film is larger than the ratio of indium in the solution, but it is in the same order of magnitude. This shows that the process chemistry is rather stable, resulting in a good reproducibility for low to medium indium concentrations. At high amounts of indium added to the solution ([In]/[Zn] $>$ 0.4) the layer formation becomes inhibited. The deposited films have only approximately half the target thickness and two consecutive deposition processes have to be employed. Also, a small amount of loosely attached white powder, which can be dissolved with ammonia solution, is observed, indicating beginning hydroxide precipitation. The reproducibility is probably suffering from this and therefore a second dataset was included into the XPS measurements shown in Figs. 5.3 and 5.4.

The ratio [S]/([S]+[O]) in Fig. 5.4 stays fairly constant at 0.8 for the different amounts of incorporated indium. The values were determined from evaluation of the integral peak intensities of the O 1s and the S 2s emission lines and from evaluation of the Auger parameter for Zn as described in Section 2.4.2. In comparison to other published results [27, 78] and to the results shown in Section 4.2 the ratios [S]/([S]+[O]) for the samples investigated here are rather high. This indicates that the presented citrate process leads to ZnInOS films with high sulfur content, without indium hydroxide formation adding significantly to the film formation. This is affirmed further by examination of the Wagner plots (c.f. Section 2.4.2.1) in

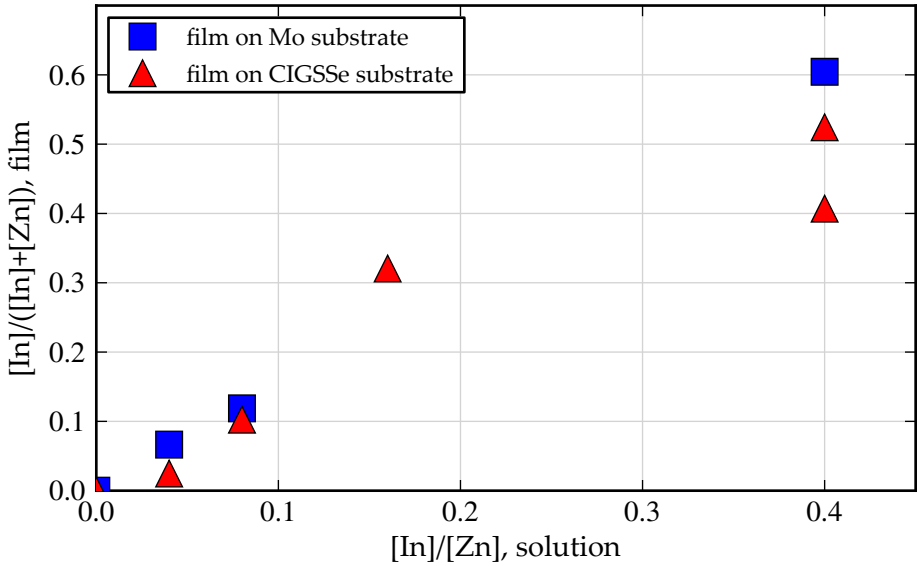

Figure 5.3: [In]/([In]+[Zn]) ratio in the ZnInOS layer determined from XPS measurements on CIGSSe as well as on Mo substrates for different amounts of indium sulfate in the chemical bath solution.

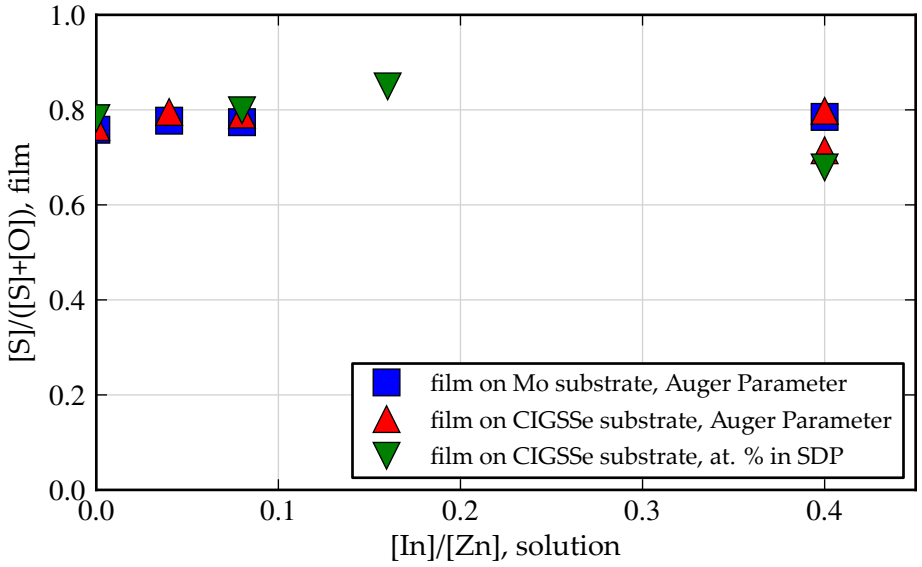

Figure 5.4: [S]/([S]+[O]) ratio in the ZnInOS layer determined from XPS measurements by evaluation of the Auger parameter for Zn and by evaluation of the integral peak intensities in sputtering depth profiles (SDP).

Fig. 5.5. The Wagner plot for zinc shows fairly constant Auger parameters between the literature values for ZnO and ZnS. In the Wagner plot for indium the spread of values is larger. All samples fit into the oxide range and only for the highest indium content, the Auger parameter fits to a mixture of oxide and hydroxide. There is a large deviation in the Zn $2p_{3/2}$ emission line binding energy, matched by a spread of In $3d_{5/2}$ bidning energies in the Wagner plot for In. To correct for

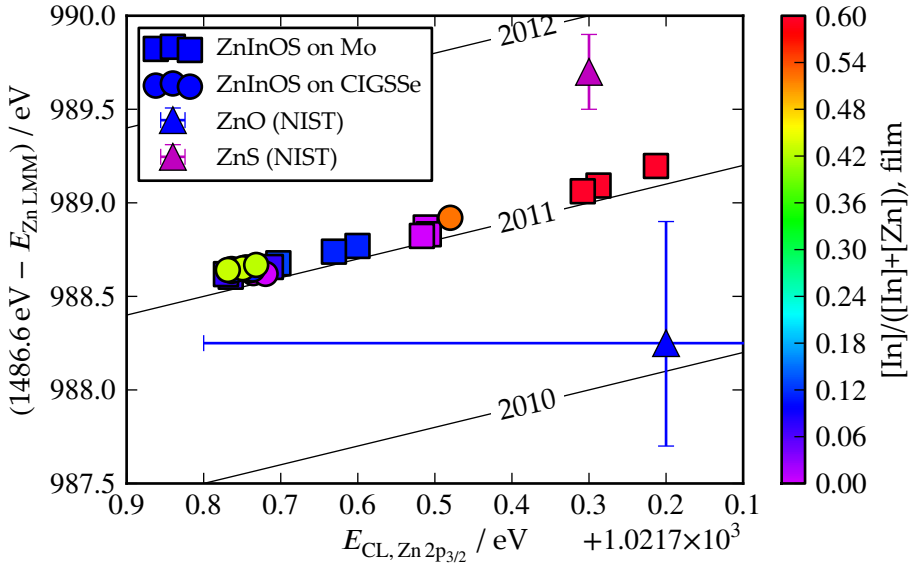

(a) Zn Wagner plot

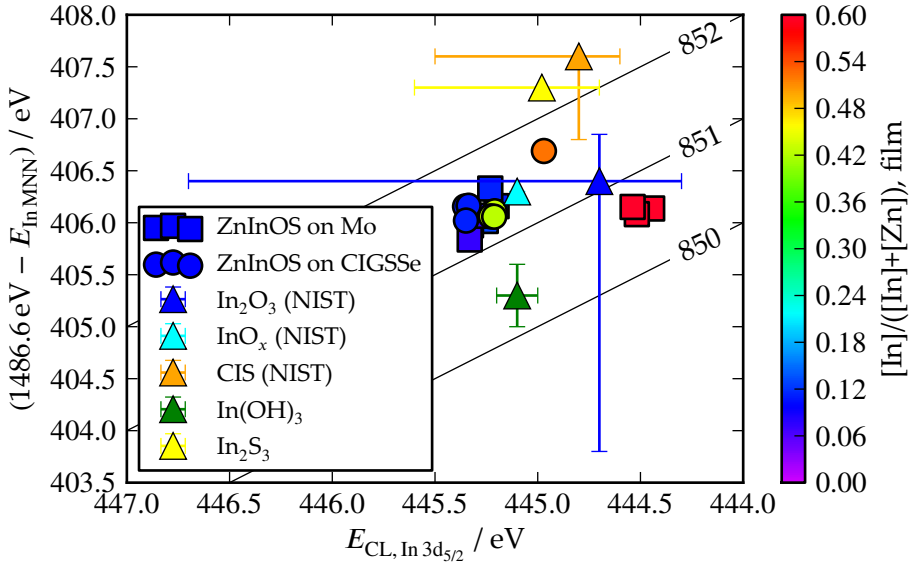

(b) In Wagner plot

Figure 5.5: In and Zn Wagner plots for the deposited ZnInOS layers. A comparison with data from the NIST X-ray Photoelectron Spectroscopy Database [123] shows that the chemical surrounding of Zn and In is largely unaffected upon increasing incorporation of indium into the film and that there is no significant contribution of hydroxides.

potential surface charging, all spectra were corrected with adventitious carbon as a reference. The still large deviation in binding energies is an indicator for additional errors, showing that only the Auger parameter is a good measure for the chemical surrounding in this case. For three layers produced from different indium concentration in the buffer layer, in addition to surface concentration measurements,

XPS sputtering depth profiles were measured. The resulting atomic concentrations are presented in Fig. 5.6. The indium concentration is fairly homogeneous for all three layers with no obvious gradients. Although, due to the comparatively large measurement area, a phase separation on a small scale cannot be excluded, these results are promising in terms of the wanted homogeneity necessary for successful interface engineering. Also noticeable is the fairly constant amount of carbon detected throughout the layer. A large amount of carbon at the surface is easily understood, since surface adsorbed organic molecules are common in samples that were stored in air, leading to a typical adventitious carbon spectrum. The carbon in the buffer layer might be understood as a consequence of the high surface roughness, leading to traces of adventitious carbon even after sputtering. Another cause might be residues from the citrate complex incorporated in the buffer layer. It is not possible to separate the small amount of carbon from the Se spectrum, therefore the amount of carbon in the CIGSSe is unclear. Another point arising from this is the possible link of carbon and oxygen in the material. At the surface the binding energy of O 1s is shifted due to binding of oxygen and carbon in the surface adsorbed species. Commonly a similar shift of the O 1s binding energy is used for the separation of ZnO and $Zn(OH)_2$ [27]. This procedure is not possible here with certainty because of the detected amount of carbon. Therefore the total broadened peak at the O 1s binding energy is used in the integration for the calculation of atomic concentrations. Additionally it has to be mentioned, that traces of Zn are found after sputtering deep into the absorber. Besides thermally induced diffusion during the dehydration step, sputter-induced diffusion during the measurement may be a reason. However, it is also reasonable to assume that the three dimensional structure of the substrate surface includes areas, which can be reached during buffer layer deposition, but which are not directly exposed during sputtering, thereby leading to traces of Zn only seemingly deep inside the absorber material.

5.3.3 Solar Cells

Solar cells were prepared from the same samples that were discussed before with respect to their elemental composition, film thicknesses are reported in Table 5.1. All cells received the standard post-treatments and IV curves were measured at the ZSW in the same procedure that was discussed in the previous sections. In this case, all cells were prepared with the adapted i-ZnO window layer, where no oxygen gas was used in the sputter gas, which is discussed in Fig. 5.7. A comparison of the IV curves before any post-treatments, after an annealing step at 200 °C and after 30 minutes of light-soak under simulated AM1.5 illumination is shown in Fig. 5.7. In addition, box plots for the efficiencies of the solar cells with buffer layers produced from different indium contents in the chemical bath are displayed in Fig. 5.9. Accompanying statistics for the final cell efficiencies after the light-soaking post-treatment are presented in Table 5.2. Each set of data consists

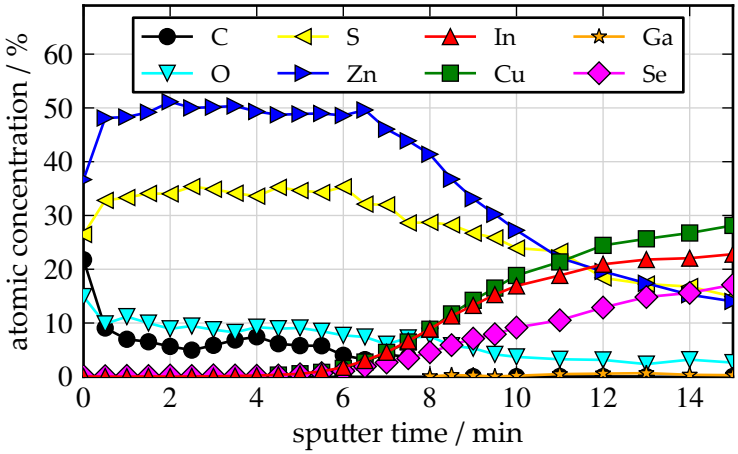

(a) [In]/[Zn] = 0

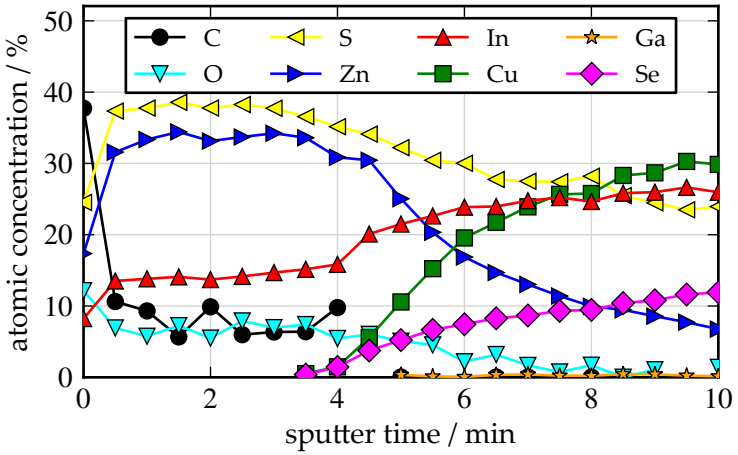

(b) [In]/[Zn] = 0.16

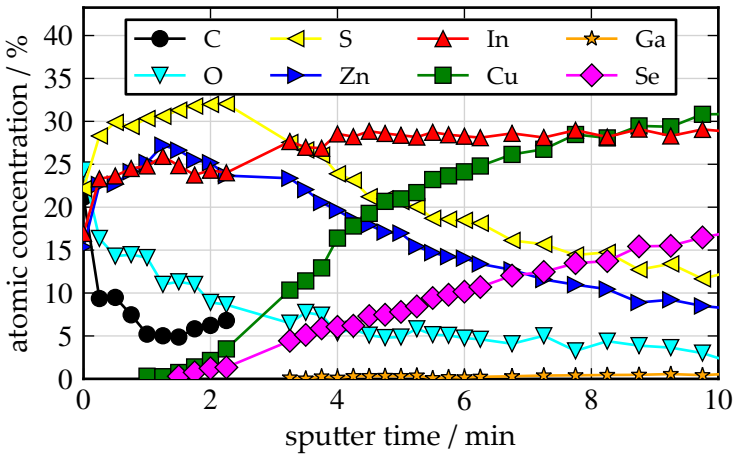

(c) [In]/[Zn] = 0.4

Figure 5.6: XPS sputter depth profiles for ZnInOS buffer layers produced from different amounts of indium in the solution on Cu(In,Ga)(S,Se)$_2$ substrates. Due to changes in the measurement setup the sputter rate in (c) is not comparable to the rates in (a) and (b). Some points in (c) were excluded because they showed a sudden offset, probably due to charge accumulation.

Table 5.2: Solar cell parameters after annealing and 30 minutes of light-soaking, the parameter distributions are represented by their median and median absolute deviation. The ratios [In]/[Zn] and [In]/([In]+[Zn]) are given for the process solution and the film (from XPS measurement) respectively.

[In]/[Zn] (solution)	0	0.08	0.16	0.4
[In]/([In]+[Zn]) (film)	0	0.102	0.321	0.407
η / %	12.65 ± 1.09	14.72 ± 0.24	13.68 ± 0.62	13.37 ± 0.63
η_{max} / %	14.2	15.4	14.8	14.5
V_{oc} / mV	559 ± 2	586 ± 2	583 ± 2	587 ± 1
FF / %	60.1 ± 4.7	66.1 ± 1.0	62.3 ± 2.7	61.3 ± 2.9
J_{sc} / (mA cm^{-2})	37.8 ± 0.3	37.8 ± 0.3	37.6 ± 0.2	37.1 ± 0.3

of 40 cells on two samples stemming from two separate deposition processes, with the exception of the highest indium concentration of [In]/[Zn] = 0.4, where there are only 20 cells on a single sample. Since the latter concentration leads to thinner films, two consecutive process steps on the same substrate were employed. In Fig. 5.7 a clear trend is visible. Regardless of indium concentration, all cells show inhibited current collection under forward bias, leading to S-shaped IV curves, before an annealing post-treatment. This S-shape is shifted to higher voltages with increasing indium content. The trend is still visible after the annealing post-treatment, where the cells with no or little indium in the buffer layer still show a very distinct S-shape and cells with sufficient indium show no S-shape any more. As a result the latter cells do not need to be light-soaked any more while the former cells still gain significantly in the light-soaking post-treatment. After light-soaking the efficiencies of all cells are at a decent level, comparable to results shown in Sections 4.5 and 5.2 for Zn(O,S) buffer layers as well as CdS buffer layers. The short circuit currents benefit from reduced absorption in the blue part of the spectrum, as visible in the EQE measurements displayed in Fig. 5.8, comparable to the cells with standard Zn(O,S) buffer layer.
With regard to the speed of the light-soak effect, a larger spread of efficiencies after the annealing post-treatment is visible in Fig. 5.9(b). Since the cells are not blanketed until they are measured this is a result of longer illumination time for the cell measured last. The larger spread for medium indium concentrations then shows an increased light-soaking speed compared to the low concentrations since the total illumination time is approximately the same for all samples. The same is

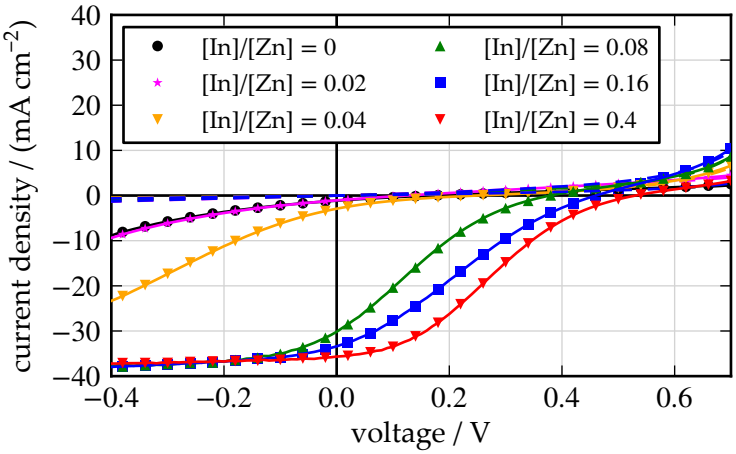

(a) not annealed

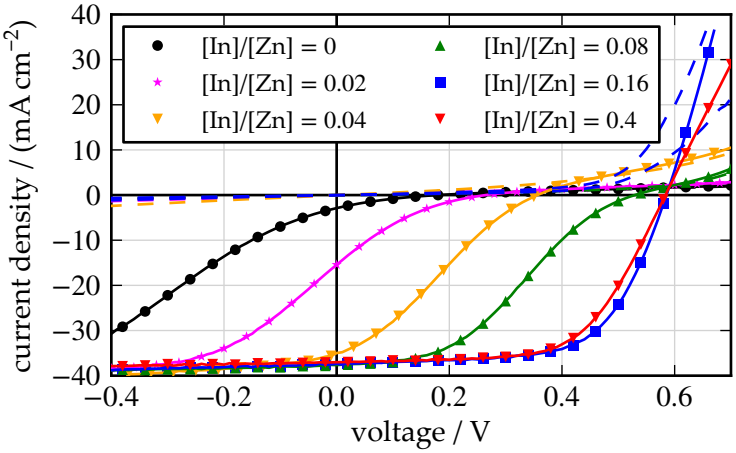

(b) annealed at 200 °C for 30 minutes

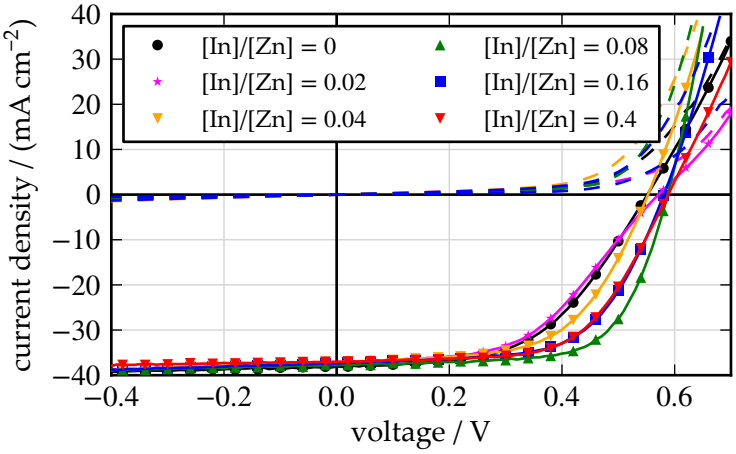

(c) light-soak under sim. AM1.5 illumination for 30 minutes

Figure 5.7: IV curves measured under simulated AM1.5 illumination (solid lines with symbols) and in the dark (dashed lines) of exemplary cells with varying amounts of indium in the chemical bath.

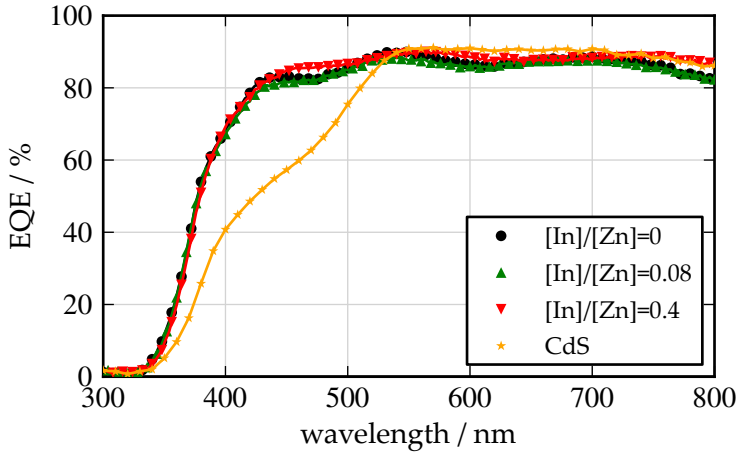

Figure 5.8: Comparison of external quantum efficiency measurements for exemplary cells with varying amounts of indium in the chemical bath and for an exemplary cell with cadmium sulfide buffer layer.

still true after an initial light-soaking post-treament and prolonged dark-storage. Fig. 5.10 shows the evolution of solar cell parameters during light-soak for the same cells discussed before after months of dark-storage. After storage in the dark all cells show some amount of relaxation with reduced fill factor and open circuit voltage. The maximum efficiency is recovered with a sufficient amount of light-soaking. Again, there is a clear trend. Cells with buffer layers produced from solutions containing more indium show less relaxation and are improving faster. From Fig. 5.10 the time needed for light-soaking until the maximum efficiency is reached can be cut by approximately a factor of 10 by incorporation of indium into the buffer layer.

5.3.4 *Band alignment at CIGSSe/ZnInOS interfaces*

Valence band offsets (ΔE_{VB}) were investigated for buffer layers with different concentrations of indium salt in the process solution, namely [In]/[Zn] = 0, [In]/[Zn] = 0.16, and [In]/[Zn] = 0.4. The samples used for this investigation are cut away from the same material used for preparation of the solar cells described earlier. They did not receive a ZnO window layer, nor any additional post-treatment. The method of determining valence band offsets from XPS sputter depth profiles is utilized here as described in Section 2.4.2.3. The resulting plots of the difference $E_{CL} - E_{CL}^{VBM}$ for all considered binding energies is shown in Fig. 5.11. For averaging, only data from Zn $2p_{3/2}$, In $3d_{5/2}$, and Cu $2p_{3/2}$ emission lines were used as they did not overlap with other lines in the spectra and were estimated to be most reliable. The averages taken are shown as dotted lines and an arrow indicates the estimated position of the interface (compare also Fig. 5.6). Also displayed in Fig. 5.11 as well as in Table 5.3 are the determined valence band maximum offsets ΔE_{VB}. A small but systematic trend of lowering ΔE_{VB} from

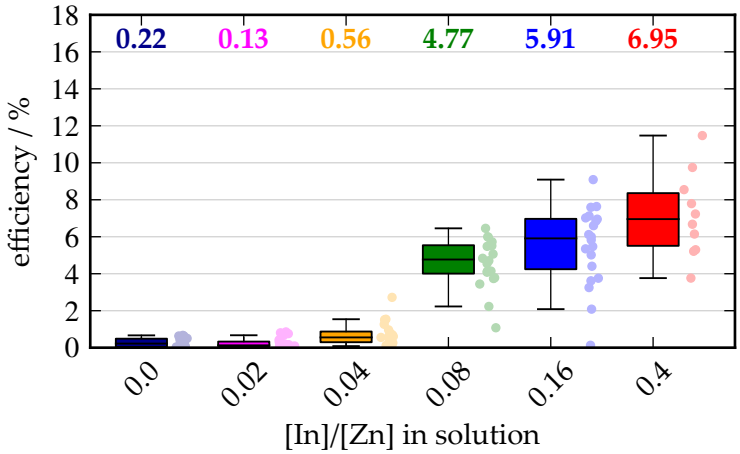

(a) not annealed

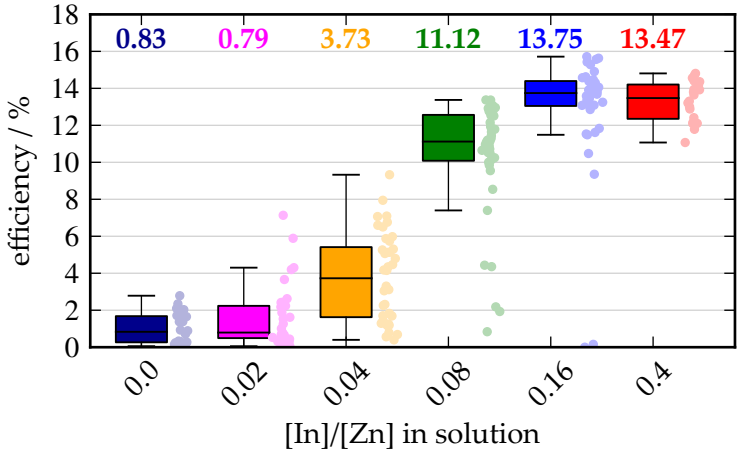

(b) annealed at 200 °C for 30 minutes

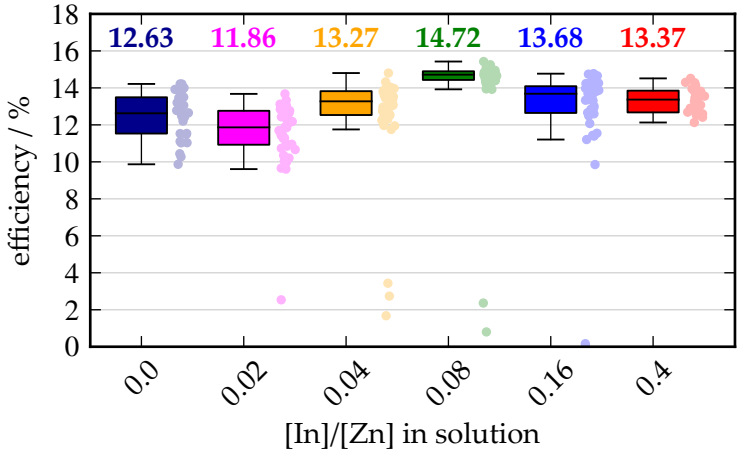

(c) light-soak under sim. AM1.5 illumination for 30 minutes

Figure 5.9: Aperture area efficiencies of solar cells measured under simulated AM1.5 illumination with varying amounts of indium in the chemical bath before and after the annealing and light-soak post-treatment. Median efficiencies are given with colored numbers above each box.

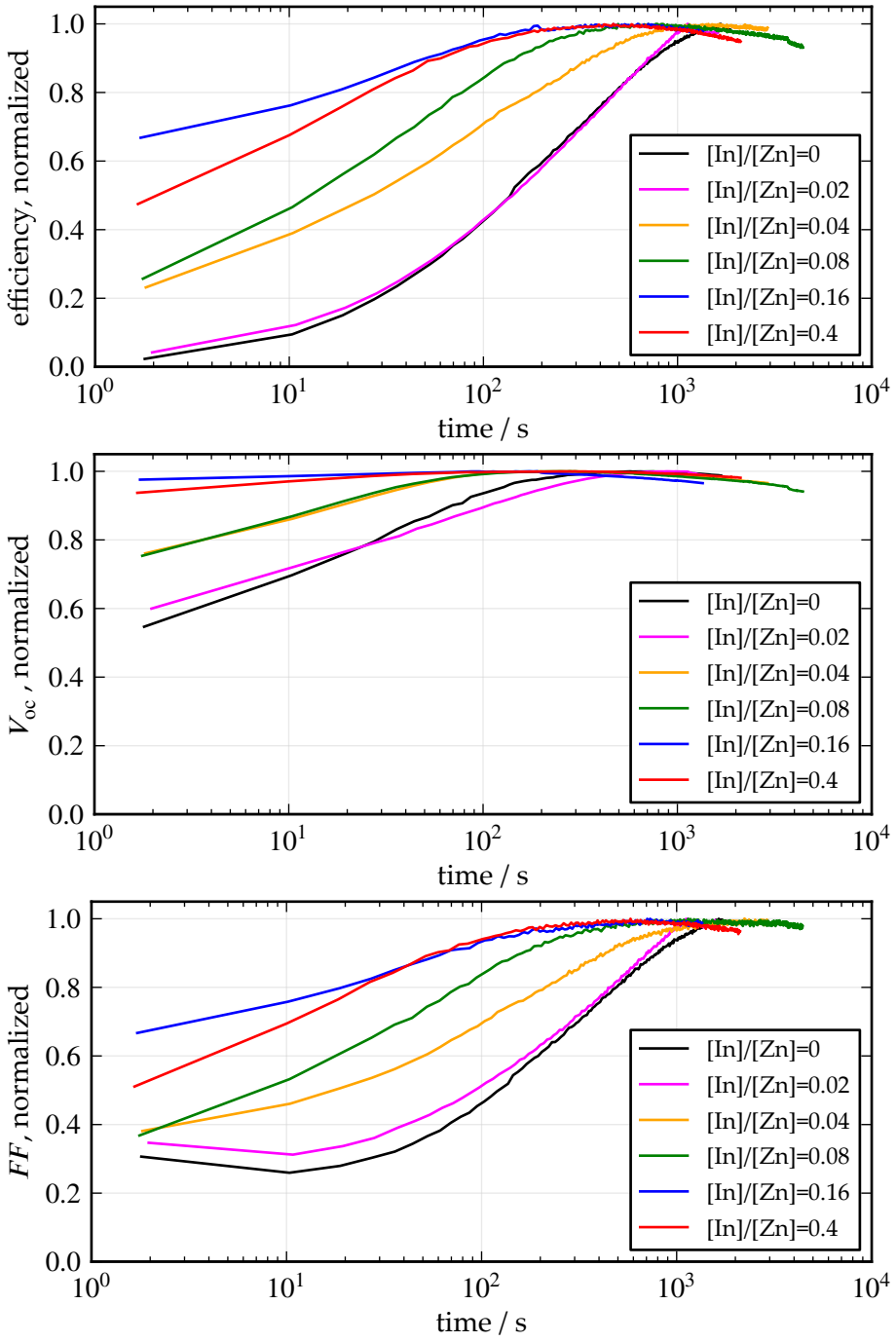

Figure 5.10: Evolution of solar cell parameters under illumination with a halogen light source at 75 mW cm^{-2} for cells with ZnInOS buffer layer fabricated with chemical bath deposition and varying amount of indium in the process solution. The cells were not actively cooled and temperatures rise to ~70 °C during light-soaking.

1.35 eV to 1.15 eV with increasing indium content in the layer is apparent. This difference is larger than the estimated uncertainty of the method of 0.1 eV.

The full band diagram at the interface can be determined with additional knowledge of the buffer layer and CIGSSe band gap when the relation $E_{CB} = E_{VB} + E_g$ is used for the calculation of the conduction band minima. The buffer layer band gaps are determined from evaluation of reflectance and transmittance measurements as introduced in Section 2.4.3. The Tauc plot, calculated accordingly, is shown in Fig. 5.12 with the assumption of a direct optical transition. This assumption is based on pure ZnS and ZnO having direct band gaps [25] and is confirmed by the straight lines obtained in Fig. 5.12. A Tauc plot with the assumption of an indirect transition did in comparison not lead to satisfactory results. The extrapolated band gaps, shown in Table 5.3, are decreasing from 3.65 eV to 3.07 eV with increasing indium concentration. These values are rather high and may be partly attributed to the large sulfur content in the films, and partly to neglecting the low energy tail in the spectrum of the absorption coefficient. The latter is a feature of Zn(O,S) based films that was also observed and explained by others [25]. Derived conduction band minimum offsets ΔE_{CB} are shown in Table 5.3. The combination of a small increase in ΔE_{VB} and a large decrease in E_g lead to a decrease in ΔE_{CB} of up to 0.38 eV. The band gap of the CIGSSe at the interface is not directly accessible here. Therefore an estimation was made from knowledge of the atomic concentrations measured in the XPS sputtering depth profiles. A ratio of [S]/([S]+[Se]) $\approx$ 0.65 was calculated near the interface and interpolation of the experimentally derived data shown by Turcu et al. [124] leads to an expected band gap of 1.3 eV. Additional band gap widening due to an ordered vacancy compound cannot completely ruled out here. Schulmeyer showed, that the core level energies are not significantly shifted in a copper poor environment, but the difference Δ_{CL}^{VBM} is reduced by ~0.5 eV [125]. This is due to the fact, that the removal of Cu lowers the valence band maximum energy because of less p–d repulsion [14]. The valence band maximum energy is therefore possibly overestimated in the measurement by 0.5 eV at the interface. Such a copper poor surface would, however, lead to some amount of surface inversion (E_F close to E_{VB}), even without n^+ doped window layer [126], which is not observed in Fig. 5.11, even when adding 0.5 eV. In any case, the surface band gap widening would primarily lead to a lowering of ΔE_{VB}, while leaving ΔE_{CB} constant, the error of not considering it it therefore probably small. The resulting band diagrams at the CIGSSe/ZnInOS interface are shown in Fig. 5.13. Space charge regions lead to band bending, visible as shifts of the valence band maximum position with respect to the Fermi level in Fig. 5.11. However, since the analyzed layer stacks did not include a highly n-doped window layer, the actual band bending in a complete device will differ from the one observed here. Therefore Fig. 5.13 is only drawn for the immediate proximity of the interface, neglecting space charge regions.

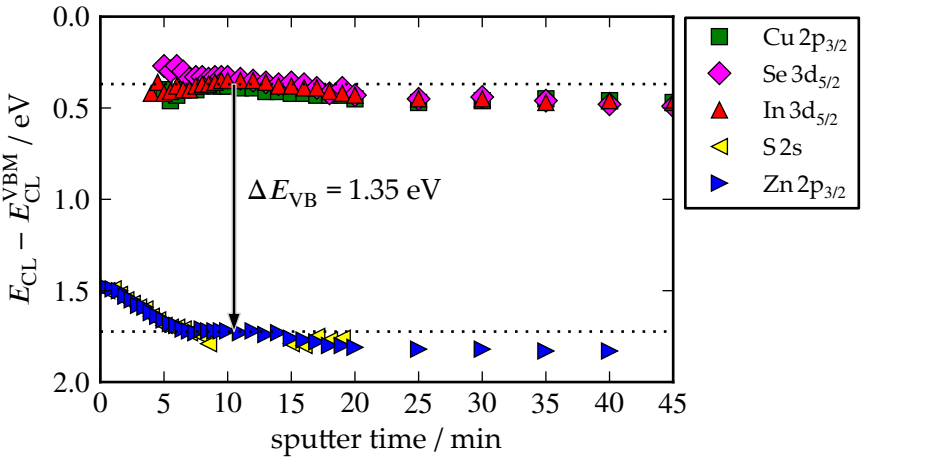

(a) [In]/[Zn] = 0

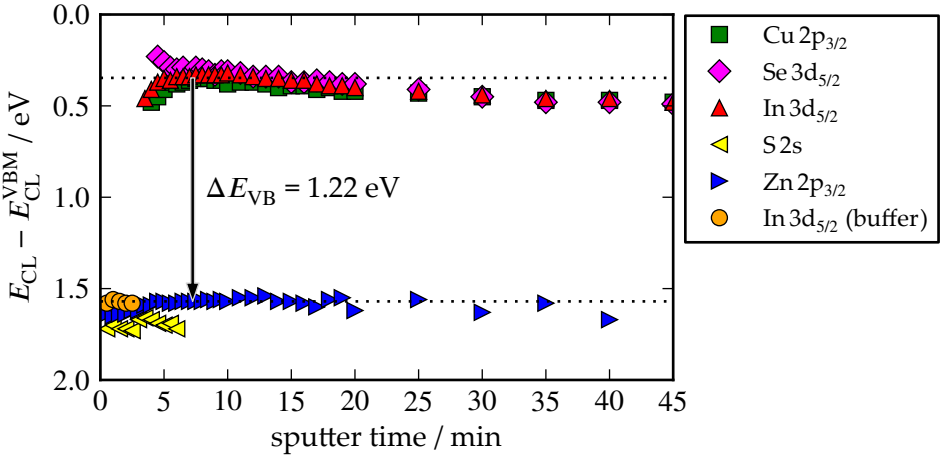

(b) [In]/[Zn] = 0.16

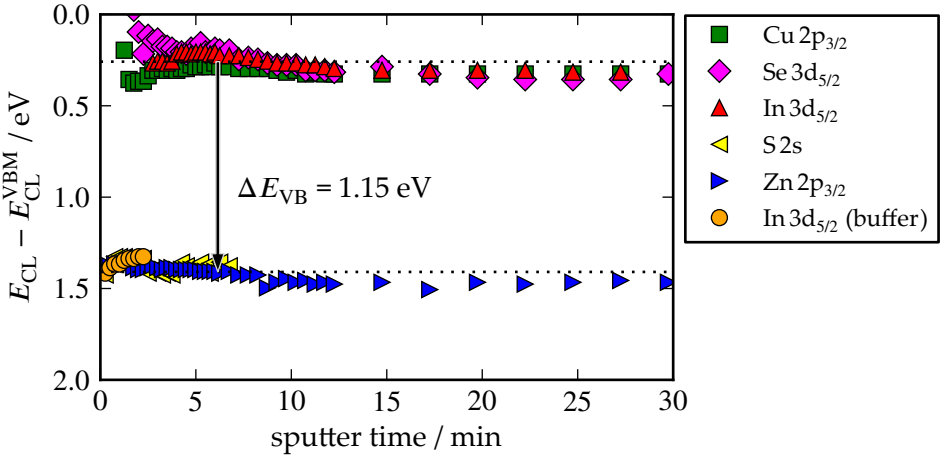

(c) [In]/[Zn] = 0.4

Figure 5.11: Determination of valence band maximum offsets ΔE_{VB} between buffer layers (different amounts of indium in the process solution) and Cu(In,Ga)(S,Se)$_2$ substrates, derived from XPS sputter depth profiles shown in Fig. 5.6. Markers represent calculated valence band maximum positions from different core levels, the dotted lines give the average taken for determining the offset.

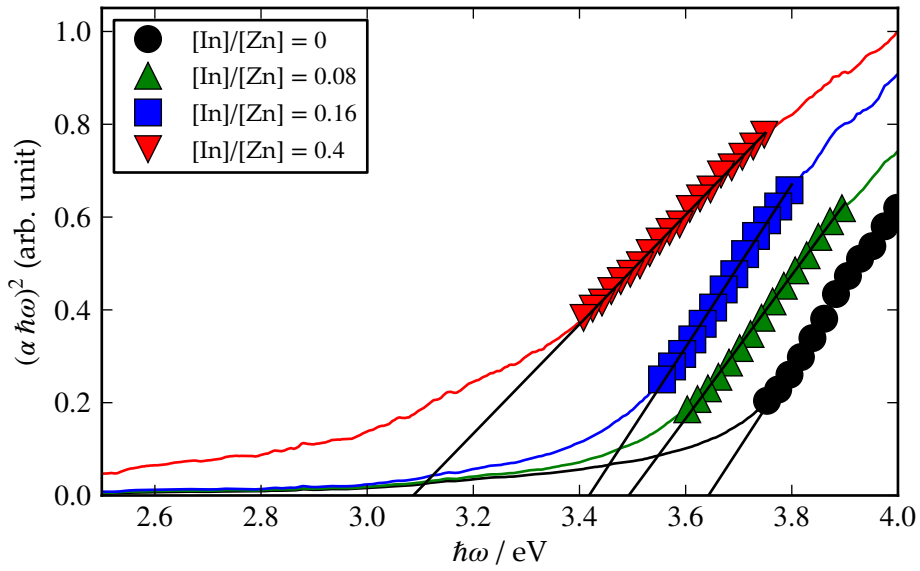

Figure 5.12: Tauc plots for ZnInOS buffer layers on quartz glass. A linear regression was applied to the marked parts of the curves, and extrapolated band gaps are shown in Table 5.3.

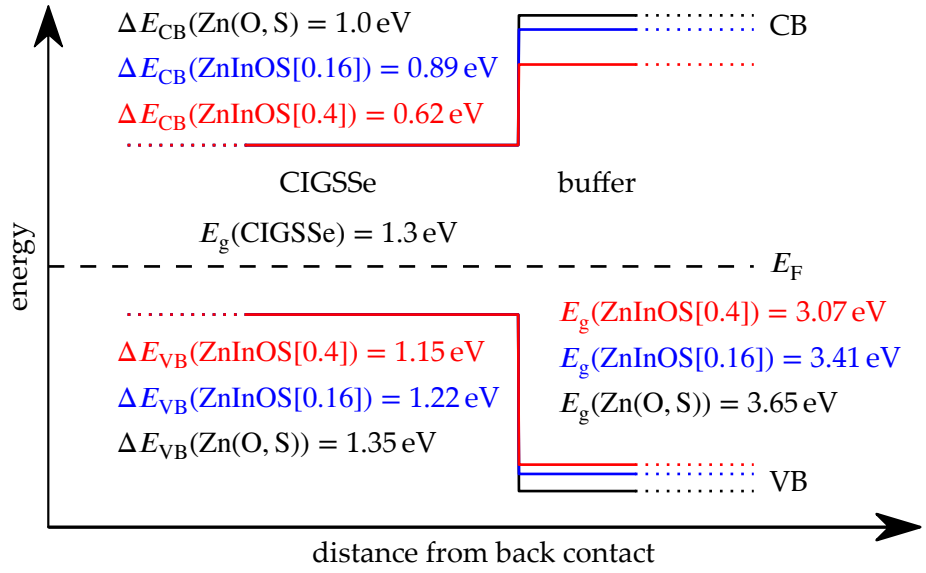

Figure 5.13: Derived band diagrams for the interface between the CIGSSe and ZnInOS buffer layers with different amounts of indium in the process solution as indicated within the figure. The band alignment was determined before any post-treatments. The valence band offsets were taken from Fig. 5.11, the band gaps for the different buffer layers were taken from Table 5.3 and the band gap of the absorber was estimated by interpolation of data in [124] with [S]/([S]+[Se]) = 0.65 from the XPS data in Fig. 5.6 to be 1.3 eV.

Table 5.3: Valence band maximum offsets from XPS measurements (Fig. 5.11) and extrapolated band gaps from optical measurements (Fig. 5.12) for ZnInOS films with different amounts of indium in the process solution. Conduction band minimum offsets are determined from the measured quantities as shown in Fig. 5.13.

[In]/[Zn]	0	0.08	0.16	0.4
ΔE_{VB} / eV	1.35	–	1.22	1.15
E_g / eV	3.65	3.50	3.41	3.07
ΔE_{CB} / eV	1.0	–	0.89	0.62

5.3.4.1 *Discussion of the results*

Summarizing, with increasing the indium content in the layer, the finding was a small decrease of ΔE_{VB} (0.2 eV) and a larger decrease of E_g (0.58 eV). The decrease in ΔE_{VB} was expected to be small, considering the largely unaffected anion ratio in the films. The common anion rule, introduced in Section 5.1, predicts no change of the valence band maximum position in this case. The magnitudes of ΔE_{VB} lie slightly below the values of 1.46 eV to 1.56 eV for CBD-Zn(O,S) buffer layers, as published by T. Adler [33]. In Adler's investigations the RF-sputtered $ZnO_{0.45}S_{0.55}$ and $ZnO_{0.5}S_{0.5}$ with ΔE_{VB} from 1.2 eV to 1.31 eV are closer to the results presented here. However, in [33], there is an indication of a systematic offset between valence band maximum offsets determined from sputter depth profiles compared to those determined from step-by-step film deposition experiments. The former constitute an underestimation with differences up to 0.3 eV, smaller differences are observed for low sulfur content in the film.
The determined band gaps are also within the ranges of literature data, namely 3.6 eV for ZnS and 1.9 eV to 2.8 eV for In_2S_3 [23].
The calculated conduction band offsets are, on the other hand, much larger than expected and cannot be brought into agreement with the observed solar cell performance in Section 5.3.3. As introduced in Section 2.2.4, the thermionic emission theory predicts a maximum barrier ϕ_{max} of approximately 0.5 eV if a non-negligible short circuit current flows through the device. In Fig. 5.7(a) cells with buffer layers produced from solutions with [In]/[Zn] $\geq$ 0.08 show visibly higher J_{sc} than possible with an electronic barrier larger than 0.5 eV. But even the smaller currents for the buffer layers with lower indium concentration would require the barrier to be significantly lower than 1 eV.
One possible error was already discussed before to be a systematic offset of up to 0.3 eV, attributed to the method of sputter depth profiling. Another source of error is the neglect of the low energy tail in the absorption coefficient spectrum when determining the band gaps. This error is hard to quantify, but it may easily be in the range of 0.2 eV, especially since the band gap for carrier transport may be smaller than the optical band gap if trap states below the conduction band may be accessed for charge carrier transport. A third source of error is the calculation of the $Cu(In,Ga)(S,Se)_2$ band gap at the interface from the atomic concentrations

measured with sputtering depth profiles. Since virtually no gallium is detected at the absorber surface, the band gap is expected to lie in between 1.04 eV for $CuInSe_2$ and 1.53 eV for $CuInS_2$ [16]. With the theoretical bowing parameter of 0.04 (see equation (2.35)) a band gap of 1.35 eV is calculated, and a range of [S]/([S]+[Se]) from 0.5 to 0.8 would result in a range of band gaps of 1.28 eV to 1.43 eV, leading to a possible error in the range of 0.15 eV.
At last, it has to be kept in mind that the i-ZnO sputtering step may alter the buffer layer to some extend. Fig. 5.7(b) shows that the electronic barrier is reduced by an annealing treatment as was also observed for cells with standard Zn(O,S) buffer layer. Such an annealing might also partly happen in the window sputtering process.
Despite all these possible errors, which are of systematic nature, the relative decrease in calculated ΔE_{CB} is correlated with the apparent decrease of an electronic barrier inhibiting the initial solar cell performance. The observed trend is therefore believed to be valid. A SCAPS simulation after systematically subtracting 0.5 eV to the values ΔE_{VB} in Table 5.3, displayed in Fig. 5.14, shows the same basic trend as observed in Fig. 5.7. The IV curve associated with the lowest conduction band offset, however, shows no S-shape, whereas in Fig. 5.7(a) there is a large S-shape visible for all buffer layers. This is an indication for either an underestimation of ΔE_{CB} in this case, or another influence on the electronic barrier. A complete set of the simulation parameters can be found in Appendix A.4.

5.3.5 *Conclusion for the alkaline CBD process*

A novel process for the preparation of ZnInOS buffer layers was presented in this section. Aside from being better applicable in a standard surrounding for buffer layer development and production due to alkaline conditions in the solution, there are two other upsides to this new process. Citric acid as an additional complexing agent is inexpensive and non-toxic and it allows for a good control of the amount of indium up to [In]/([In]+[Zn]) = 0.5 incorporated in the film dependent on the amount of indium salt in the process solution. In terms of toxicity, trials to replace thioacetamide with thiourea dioxide were successful and further work could be done here. Ammonia on the other side proved to be not replaceable so far, it is probably needed as a complexing agent for Zn in the solution. Another downside of the process is the high amount of chemicals needed in comparison to the process introduced in Section 4.2. Also, the film formation is comparably slow. In terms of a possible transfer to production, the use of an indium salt in a CBD process is not desirable as well, since indium is an expensive resource and the yield in CBD processes is low. Nevertheless, solar cells prepared with these novel ZnInOS buffer layers proved to be efficient ($\eta > 14\,\%$) and a clear trend towards cells without any light-soaking effect was observed with increasing indium content in the buffer layer. This effect was attributed to improved band alignment at the CIGSSe/buffer interface as suggested by the presented XPS and optical measurements.

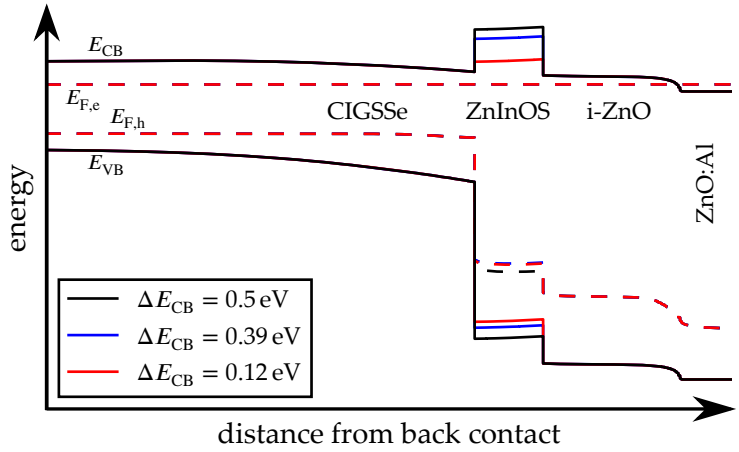

(a) Simulated band diagrams.

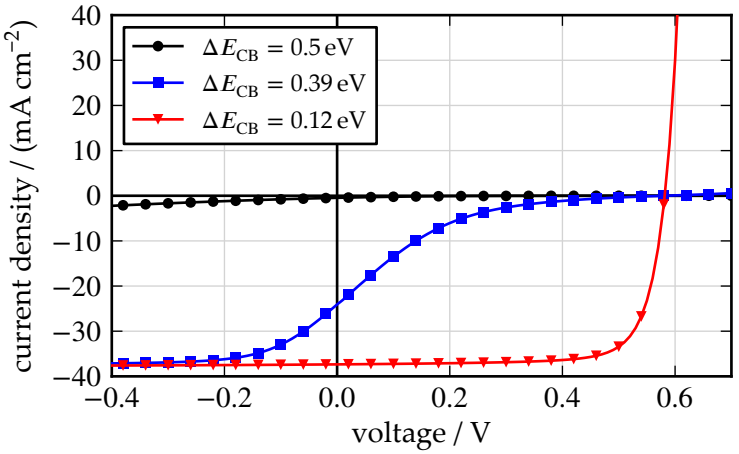

(b) Simulated IV curves.

Figure 5.14: SCAPS simulation of (a) and band diagrams in open circuit conditions and (b) IV curves for the ZnInOS buffer layers presented in Fig. 5.13 after subtracting 0.5 eV from ΔE_{VB}.

The presented results underline the need for effective interface engineering when Zn(O,S) based buffer layers are to be employed. The alloying with indium compounds is a promising way, where preparation techniques with higher yield would enable utilization in industrial production.

References

[14] J. E. Jaffe and A. Zunger, "Theory of the band-gap anomaly in ABC_2 chalcopyrite semiconductors", Phys. Rev. B **29**, 1882–1906 (1984) (Cited on pages 20, 122).

[16] S.-H. Wei and A. Zunger, "Band offsets and optical bowings of chalcopyrites and Zn-based II-VI alloys.", Journal of Applied Physics **78**, 3846 (1995) (Cited on pages 20, 92, 126).

[23] A. Klein, "Energy band alignment in chalcogenide thin film solar cells from photoelectron spectroscopy", Journal of Physics: Condensed Matter **27**, 134201 (2015) (Cited on pages 21, 26, 28, 29, 105, 107, 125).

[25] C. Persson, C. Platzer-Björkman, J. Malmström, T. Törndahl, and M. Edoff, "Strong valence-band offset bowing of $ZnO_{1-x}S_x$ enhances p-type nitrogen doping of ZnO-like alloys", English, Physical Review Letters **97**, 146403(4) (2006) (Cited on pages 21, 64, 106, 122).

[27] T. Adler, M. Botros, W. Witte, D. Hariskos, R. Menner, M. Powalla, and A. Klein, "Valence band offsets at Cu(In,Ga)Se_2/Zn(O,S) interfaces", physica status solidi (a) **211**, 1972–1980 (2014) (Cited on pages 21, 27–29, 69, 112, 115).

[33] T. Adler, "Zn(O,S) Puffer Eigenschaften in Cu(In,Ga)Se_2 Solarzellen", PhD thesis (Technische Universität Darmstadt, Dec. 2013) (Cited on pages 26, 27, 30, 107, 125).

[34] A. Klein, "Energy band alignment at interfaces of semiconducting oxides: A review of experimental determination using photoelectron spectroscopy and comparison with theoretical predictions by the electron affinity rule, charge neutrality levels, and the common anion rule", Thin Solid Films **520**, 3721–3728 (2012) (Cited on pages 26, 105, 107).

[78] D. Hariskos, R. Menner, P. Jackson, S. Paetel, W. Witte, W. Wischmann, M. Powalla, L. Bürkert, T. Kolb, M. Oertel, et al., "New reaction kinetics for a high-rate chemical bath deposition of the Zn(S,O) buffer layer for Cu(In,Ga)Se_2-based solar cells", Progress in Photovoltaics: Research and Applications **20**, 534–542 (2012) (Cited on pages 62, 112).

[84] G. Agawane, S. W. Shin, A. Moholkar, K. Gurav, J. H. Yun, J. Y. Lee, and J. H. Kim, "Non-toxic complexing agent Tri-sodium citrate's effect on chemical bath deposited ZnS thin films and its growth mechanism", Journal of Alloys and Compounds **535**, 53–61 (2012) (Cited on pages 62, 106).

[85] T. Hildebrandt, N. Loones, M. Bouttemy, J. Vigneron, A. Etcheberry, D. Lincot, and N. Naghavi, "Search for new bath formulations of Zn(S, O, OH) buffer layer to outperform record performances of CdS-based CIGSe solar cells", in Photovoltaic Specialists Conference (PVSC), 2013 IEEE 39th (June 2013), pp. 1114–1119 (Cited on pages 62, 106).

[86] J. Liao, S. Cheng, H. Zhou, and B. Long, "Al-doped ZnS thin films for buffer layers of solar cells prepared by chemical bath deposition", IET Micro Nano Letters **8**, 211–214 (2013) (Cited on pages 62, 64, 106).

[102] H. Khallaf, G. Chai, O. Lupan, L. Chow, S. Park, and A. Schulte, "Investigation of aluminium and indium in situ doping of chemical bath deposited cds thin films", Journal of Physics D: Applied Physics **41**, 185304 (2008) (Cited on pages 64, 106).

[103] S. A. Al Kuhaimi and Z. Tulbah, "Structural, Compositional, Optical, and Electrical Properties of Solution-Grown $Zn_xCd_{1-x}S$ Films", Journal of The Electrochemical Society **147**, 214–218 (2000) (Cited on pages 64, 105).

[109] R. Menner, B. Dimmler, R. Mauch, and H. Schock, "II–VI compound thin films for windows in heterojunction solar cells", Journal of Crystal Growth **86**, 906–911 (1988) (Cited on page 105).

[110] N. Naghavi, C. Hubert, A. Etcheberry, V. Bermudez, D. Hariskos, M. Powalla, and D. Lincot, "Compositional engineering of chemical bath deposited (Zn,Cd)S buffer layers for electrodeposited $CuIn(S,Se)_2$ and coevaporated $Cu(In,Ga)Se_2$ solar cells", Progress in Photovoltaics: Research and Applications **17**, 1–9 (2009) (Cited on page 105).

[111] R. Boorman and J. Sutherland, "Subsolidus phase relations in the ZnS-In_2S_3 system: 600 to 1080°C", Journal of Materials Science **4**, 658–671 (1969) (Cited on page 106).

[112] Y. Chen, S. Hu, W. Liu, X. Chen, L. Wu, X. Wang, P. Liu, and Z. Li, "Controlled syntheses of cubic and hexagonal $ZnIn_2S_4$ nanostructures with different visible-light photocatalytic performance", Dalton Transactions **40**, 2607–2613 (2011) (Cited on page 106).

[113] S. Peng, L. Li, Y. Wu, L. Jia, L. Tian, M. Srinivasan, S. Ramakrishna, Q. Yan, and S. G. Mhaisalkar, "Size-and shape-controlled synthesis of $ZnIn_2S_4$ nanocrystals with high photocatalytic performance", CrystEngComm **15**, 1922–1930 (2013) (Cited on page 106).

[114] K.-W. Cheng and C.-J. Liang, "Preparation of Zn–In–S film electrodes using chemical bath deposition for photoelectrochemical applications", Solar Energy Materials and Solar Cells **94**, 1137–1145 (2010) (Cited on page 106).

[115] R. Bayon, J. Herrero, and J. Klaer, "Optical Properties of CBD-$InZn_x$(OH, S) Buffer Thin Films for Photovoltaic Applications", in 16th European Photovoltaic Solar Energy Conference (May 2000) (Cited on page 106).

[116] K. Govender, D. S. Boyle, and P. O'Brien, "Developing cadmium-free window layers for solar cell applications: some factors controlling the growth and morphology of β-indium sulfide thin films and related (In,Zn)S ternaries", Journal of Materials Chemistry **13**, 2242–2247 (2003) (Cited on page 106).

[117] B. Asenjo, A. Chaparro, M. Gutiérrez, J. Herrero, and J. Klaer, "Study of $CuInS_2$/buffer/ZnO solar cells, with chemically deposited ZnS-In_2S_3 buffer layers", Thin Solid Films **515**, 6036–6040 (2007) (Cited on page 106).

[118] D. Hariskos, M. Ruckh, U. Rühle, T. Walter, H. W. Schock, J. Hedström, and L. Stolt, "A novel cadmium free buffer layer for $Cu(In,Ga)Se_2$ based solar cells", Solar Energy Materials and Solar Cells **41–42**, 345–353 (1996) (Cited on page 106).

[119] Y. Tokita, S. Chaisitsak, A. Yamada, and M. Konagai, "High-efficiency Cu(In,Ga)Se_2 thin-film solar cells with a novel $In(OH)_3$:Zn^{2+} buffer layer", Solar Energy Materials and Solar Cells **75**, 9–15 (2003) (Cited on page 106).

[120] Y. Hashimoto, T. Satoh, and T. Negami, "COMPOUND SEMICONDUCTOR FILM, SOLAR CELL, AND METHODS FOR PRODUCING THOSE", EP 1 662 580 A1 (2005) (Cited on page 106).

[121] C. Vanleugenhaghe and M. Pourbaix, "Indium", in *Atlas of electrochemical equilibria in aqueous solutions*, Translated from the French by James A. Franklin, (Pergamon Press, 1966), ISBN: 978-0-08-010985-5 Chap. 16.2, pp. 436–442 (Cited on page 106).

[122] M. Asabe, P. Chate, S. Delekar, K. Garadkar, I. Mulla, and P. Hankare, "Synthesis, characterization of chemically deposited indium selenide thin films at room temperature", Journal of Physics and Chemistry of Solids **69**, 249–254 (2008) (Cited on page 106).

[123] A. V. Naumkin, A. Kraut-Vass, S. W. Gaarenstroom, and C. J. Powell, *NIST X-ray Photoelectron Spectroscopy Database*, http://srdata.nist.gov/xps/ (visited on 10/14/2015) (Cited on page 114).

[124] M. Turcu, I. M. Kötschau, and U. Rau, "Composition dependence of defect energies and band alignments in the Cu($In_{1-x}Ga_x$)($Se_{1-y}S_y$) alloy system", Journal of Applied Physics **91**, 1391–1399 (2002) (Cited on pages 122, 124).

[125] T. Schulmeyer, "Mechanismen der Grenzflächenausbildung des Cu(In,Ga)Se_2-Systems", PhD thesis (Technische Universität Darmstadt, Apr. 2005) (Cited on page 122).

[126] D. Schmid, M. Ruckh, F. Grunwald, and H. W. Schock, "Chalcopyrite/defect chalcopyrite heterojunctions on the basis of $CuInSe_2$", Journal of Applied Physics **73**, 2902–2909 (1993) (Cited on page 122).

Chapter 6

6 Summary & Conclusion

This work offers insights into the physical background of problems, occurring when the Cd-free materials In_2S_3 and Zn(O,S) are employed as buffer layer for $Cu(In,Ga)(S,Se)_2$ solar cells, while also offering partial solutions to these problems.

In Chapter 3, the annealing post-treatment, leading to maximum efficiencies of cells with thermally evaporated In_2S_3 buffer layer was investigated. It was shown with temperature dependent IV curve measurements, that the open circuit voltage gain can be attributed to a decrease of recombination at the absorber/buffer interface. The reduction of the ideality factor in the one diode model suggests a decrease of an initially large tunneling contribution to the current. In a comparative study, it was shown that wet-chemical treatments (Cd-treatment or water-treatment) have a similar effect on the interface recombination, increasing the open circuit voltage and decreasing the ideality factor. The initially poor efficiencies of cells with In_2S_3 buffer layer can therefore be directly attributed to a poor absorber/buffer interface quality and wet-chemical treatments are a promising way to solve this problem. It was additionally discussed in detail, that these cells shown an increase of the effective collection length upon annealing. This was explained within the p+ layer model, where it is assumed that there is a decrease in CIGSSe surface layer doping upon annealing. Model and experiments on wet-treated absorber show a decrease of the open circuit voltage upon annealing, while fill factor and short circuit current are increased due to better collection.
The wet chemical treatments therefore enabled me to identify a two-fold explanation for the impact of annealing: the improvement of interface quality and the reduction of the p+ doping concentration near the interface. The latter effect was not achieved by the wet chemical treatments. In order to reach maximum efficiencies, a carefully balanced annealing treatment is therefore still necessary, showing the need for further improvements of this system, possibly by adjusting the CIGSSe fabrication process.

Chapter 4 introduced a new CBD process for the deposition of Zn(O,S) buffer layers. In contrast to the previously discussed In_2S_3 layer, the Zn(O,S) layers initially led to severely limited solar cell performance before any post-treatment. The beneficial influence of an annealing and a light-soaking post-treatment on the S-shape distortion of the IV curve were discussed within the model of an

energetic barrier to the electron current, together with means to reduce the need for these treatments by lowering the barrier in the first place. In Section 4.5.1, there is a systematic survey of possibly accessible parameters in the absorber/buffer-/window system, all with impact on the energetic barrier. It was calculated, that the buffer/window interface has a significant influence on the barrier height, the most important parameters being the acceptor-type defect concentration at this interface, the window layer doping concentration and the conduction band offset of the buffer layer and window layer materials. High acceptor concentrations and low window layer doping lead to an upshift of the conduction band, raising the effective barrier to the current. The same effect arises large negative conduction band offsets at the buffer/window interface. Matched conduction bands lead a higher density of electrons in the buffer layer, reducing the effective barrier to the current.
These simulations were confirmed with experiments in Section 4.5.2, by adjusting the i-ZnO deposition process and by changing the HR-window layer material to sputtered Zn(O,S) and ZnMgO, leading to a large reduction of the need for post-treatments.

Additionally, since a higher n-type doping density of the buffer layer is found be beneficial in simulations, ideally realizing a p/n+ junction without voltage drop in the n-doped side of the junction, an intentional doping with aluminum and boron was attempted by incorporating these elements into the CBD process. While the results of adding aluminum were inconclusive, an addition of boron to the process resulted in a significant improvement of solar cell efficiencies before any light-soaking, leading to the record cell for this work with 16.9 % on active area. Although XPS measurements show an increasing difference between Fermi level and valence band maximum, suggesting an increased doping, in this work neither aluminum, nor boron could be unambiguously traced in the buffer layer.
The improvements mentioned above were achieved solely by adjusting the buffer and window deposition processes. It was, however, also shown in 4.6, that the performance of cells with Zn(O,S) buffer layer is closely correlated to the quality of the absorber material. It was found that CIGSSe with more sulfur at the surface leads to higher efficiencies and to less need for post-treatments, an effect that might be explained by a lowering of the conduction band offset at the absorber/buffer interface, reducing the effective barrier to the current.
Summarizing the findings of this chapter, a guideline for efficient Zn(O,S) buffered cells was proposed in Section 4.8. Although this guideline was initially aimed at the fabrication at the Bosch CISTech GmbH, I hope, it will prove useful to other groups working on similar material combinations as well.

While the measures reported in Chapter 4 are all successful to some degree, the core problem, namely the conduction band spike at the interface between CIGSSe and CBD-Zn(O,S), remained unsolved. In Chapter 5, a potential solution to this problem is presented with the successful and controlled incorporation of indium into a new alkaline CBD process, leading to a new ZnInOS buffer

layer. It was shown, that the incorporation of indium can significantly reduce the need for post-treatments, up to the point where they are not necessary any more. An XPS study of the valence band alignment in combination with transmittance measurements shows that the incorporation of indium leads to a lowering of the conduction band spike, suggesting that this is the reason for the improved solar cell characteristics. While there are several shortcomings of the newly developed CBD process (as discussed in Section 5.3.5), the ZnInOS buffer layer presented here is a good example for successful interface engineering leading to efficient CIGSSe solar cells with Cd-free buffer layer.

Concluding, while the high potential for Cd-free buffer layers was affirmed within this work, the need for interface engineering was shown to be of crucial importance, when these buffer layers are to be employed in industrial fabrication, that is, when post-treatments are to be avoided. The need for such post-treatments was shown to arise from combinations of high defect concentrations at the interfaces, deviations from the ideal p/n+ junction, and large conduction band offsets, leading to an electronic barrier to the electron current from the absorber to the front contact. Thus, it was shown that it is not likely that CdS can be replaced as a buffer layer while leaving CIGSSe and window layer deposition processes unaltered. A thorough optimization of the CIGSSe surface, Cd-free buffer layer, and window layer, on the other hand, will lead to highly efficient and more environmentally friendly thin film solar cells.

Appendix A

A Simulation parameters

A.1 General parameters

Table A.1: General SCAPS settings.

temperature	300 K
illuminated from	right side
illumination spectrum	AM1.5G
neutral density filter	0.0605
generation profile	calculated by SCAPS
tunnel settings	not allowed

Table A.2: SCAPS contact definition.

parameter	left contact	right contact
S_e / (cm/s)	1×10^4	1×10^7
S_h / (cm/s)	1×10^7	1×10^7
metal work function	flat bands	flat bands
reflectivity	0.6	–

A.2 Cells with In_2S_3 buffer

Table A.3: SCAPS layer definitions.

	layer				
parameter	CIGS	CIGS(p+)	buffer	i-ZnO	ZnO:Al
thickness / nm	1500	60	30	80	200
graded	yes	no	no	no	no
power law exponent	3	–	–	–	–
band gap / eV	A: 1.05 B: 1.34	1.05	2.0	3.4	3.4
electron affinity / eV	4.5	4.5	4.4	4.5	4.5
ϵ_r	13.6	13.6	5.4	9	9
N_{CB} / cm^{-3}	6.8×10^{17}	6.8×10^{17}	2×10^{18}	4×10^{18}	4×10^{18}
N_{VB} / cm^{-3}	1.5×10^{19}	1.5×10^{19}	1.5×10^{19}	9×10^{18}	9×10^{18}
$v_{th,e}$ / (cm/s)	1×10^{7}	1×10^{7}	1×10^{7}	1×10^{7}	1×10^{7}
$v_{th,h}$ / (cm/s)	1×10^{7}	1×10^{7}	1×10^{7}	1×10^{7}	1×10^{7}
μ_e / (cm^2/Vs)	50	50	72	20	20
μ_h / (cm^2/Vs)	12.5	12.5	20	20	20
shallow N_D / cm^{-3}	–	–	1×10^{14}	1.1×10^{18}	1×10^{20}
shallow N_A / cm^{-3}	5×10^{15}	8×10^{16}	–	–	–

Table A.4: SCAPS layer defects.

	layer containing defect			
parameter	CIGS	CIGS(p+)	i-ZnO	ZnO:Al
defect type	acceptor	acceptor	acceptor	acceptor
σ_e / cm^{-2}	1×10^{-13}	1×10^{-13}	1×10^{-15}	1×10^{-15}
σ_h / cm^{-2}	1×10^{-13}	1×10^{-13}	1×10^{-12}	1×10^{-12}
position	E_i	E_i	E_i	E_i
total density / cm^{-3}	2×10^{14}	2×10^{14}	1×10^{18}	1×10^{16}

Table A.5: SCAPS interface defects.

	CIGS/buffer	
parameter	defect 1	defect 2
defect type	donor	neutral
σ_e / cm^{-2}	1×10^{-15}	1×10^{-15}
σ_h / cm^{-2}	1×10^{-15}	1×10^{-15}
position	0.2 eV below $E_{CB,CIGSSe}$	E_i
total density	1×10^{11}	1×10^{11}

A.3 Cells with Zn(O,S) buffer

Table A.6: SCAPS layer definitions.

	layer				
parameter	CIGSe	CISSe	buffer	HR-window	LR-window
thickness / nm	1200	300	40	80	200
graded	yes	yes	no	no	no
power law exponent	3	2	–	–	–
band gap / eV	A: 1.04 B: 1.34	A: 1.04 B: 1.3	3.6	3.4	3.4
electron affinity / eV	4.5	A: 4.5 B: 4.33	4.0	4.4	4.4
ϵ_r	13.6	13.6	8.3	9	9
N_{CB} / cm^{-3}	6.8×10^{17}	6.8×10^{17}	2×10^{18}	4×10^{18}	4×10^{18}
N_{VB} / cm^{-3}	1.5×10^{19}	1.5×10^{19}	1.5×10^{19}	9×10^{18}	9×10^{18}
$v_{th,e}$ / (cm/s)	1×10^{7}	1×10^{7}	1×10^{7}	1×10^{7}	1×10^{7}
$v_{th,h}$ / (cm/s)	1×10^{7}	1×10^{7}	1×10^{7}	1×10^{7}	1×10^{7}
μ_e / (cm^2/Vs)	50	50	107	20	20
μ_h / (cm^2/Vs)	12.5	12.5	72	20	20
shallow N_D / cm^{-3}	–	–	1×10^{16}	1.1×10^{18}	1×10^{20}
shallow N_A / cm^{-3}	1×10^{16}	1×10^{16}	–	–	–

Table A.7: SCAPS layer defects.

	layer containing defect			
parameter	CIGSe	CISSe	HR-window	LR-window
defect type	acceptor	acceptor	acceptor	acceptor
σ_e / cm^{-2}	1×10^{-13}	1×10^{-13}	1×10^{-15}	1×10^{-15}
σ_h / cm^{-2}	1×10^{-13}	1×10^{-13}	1×10^{-12}	1×10^{-12}
position	E_i	E_i	E_i	E_i
total density / cm^{-3}	2×10^{14}	2×10^{14}	1×10^{18}	1×10^{16}

Table A.8: SCAPS interface defects.

	CIGSSe/buffer		buffer/HR-window
parameter	defect 1	defect 2	defect 1
defect type	donor	acceptor	acceptor
σ_e / cm^{-2}	1×10^{-12}	1×10^{-15}	1×10^{-15}
σ_h / cm^{-2}	1×10^{-15}	1×10^{-12}	1×10^{-12}
position	0.2 eV below $E_{CB,CIGSSe}$	$E_{i,CIGSSe}$	$E_{i,buffer}$
total density	2×10^{12}	1×10^{10}	1×10^{11}

A.4 Cells with ZnInOS buffer

Table A.9: SCAPS layer definitions.

	layer				
parameter	CIGSe	CISSe	buffer	i-ZnO	n-ZnO
thickness / nm	1200	300	40	80	200
graded	yes	yes	no	no	no
power law exponent	3	2	–	–	–
band gap / eV	A: 1.04 B: 1.34	A: 1.04 B: 1.3	varied	3.4	3.4
electron affinity / eV	4.5	A: 4.5 B: 4.33	varied	4.4	4.4
ϵ_r	13.6	13.6	8.3	9	9
N_{CB} / cm^{-3}	6.8×10^{17}	6.8×10^{17}	2×10^{18}	4×10^{18}	4×10^{18}
N_{VB} / cm^{-3}	1.5×10^{19}	1.5×10^{19}	1.5×10^{19}	9×10^{18}	9×10^{18}
$v_{th,e}$ / (cm/s)	1×10^{7}	1×10^{7}	1×10^{7}	1×10^{7}	1×10^{7}
$v_{th,h}$ / (cm/s)	1×10^{7}	1×10^{7}	1×10^{7}	1×10^{7}	1×10^{7}
μ_e / (cm^2/Vs)	50	50	107	20	20
μ_h / (cm^2/Vs)	12.5	12.5	72	20	20
shallow N_D / cm^{-3}	–	–	1×10^{16}	1.1×10^{18}	1×10^{20}
shallow N_A / cm^{-3}	1×10^{16}	1×10^{16}	–	–	–

Table A.10: SCAPS layer defects.

	layer containing defect			
parameter	CIGSe	CISSe	i-ZnO	n-ZnO
defect type	acceptor	acceptor	acceptor	acceptor
σ_e / cm^{-2}	1×10^{-13}	1×10^{-13}	1×10^{-15}	1×10^{-15}
σ_h / cm^{-2}	1×10^{-13}	1×10^{-13}	1×10^{-12}	1×10^{-12}
position	E_i	E_i	E_i	E_i
total density / cm^{-3}	2×10^{14}	2×10^{14}	1×10^{18}	1×10^{16}

Table A.11: SCAPS interface defects.

	CIGSSe/buffer		buffer/i-ZnO
parameter	defect 1	defect 2	defect 1
defect type	donor	acceptor	acceptor
σ_e / cm^{-2}	1×10^{-12}	1×10^{-15}	1×10^{-15}
σ_h / cm^{-2}	1×10^{-15}	1×10^{-12}	1×10^{-12}
position	0.2 eV below $E_{CB,CIGSSe}$	$E_{i,CIGSSe}$	$E_{i,buffer}$
total density	2×10^{12}	1×10^{10}	1×10^{11}

B Appendix B
Solar cell parameters

Solar cell parameters, calculated from measured IV curves, as displayed in the figures in the main body of this thesis. Abbreviations are used for the state before annealing at 200 °C in air (n.ann.), the state after annealing for n minutes (ann. (n)) and the state after light-soak for m minutes (ls. (m)).

Table B.1: Solar cell parameters for Fig. 4.6

	buffer layer			
parameter	Zn(O,S) n.ann.	Zn(O,S) ann. (30)	Zn(O,S) ls. (30)	CdS n.ann.
η / %	0.0	8.0	15.5	15.6
V_{oc} / mV	28	484	580	615
fill factor / %	22.4	44.6	71.1	70.7
J_{sc} / mA cm^{-2}	0.1	37.3	37.7	36.0

Table B.2: Solar cell parameters for Fig. 4.15(a)

	i-ZnO monolayer		
parameter	n.ann.	ann. (30)	ls. (30)
η / %	0.0	8.1	15.0
V_{oc} / mV	16	516	573
fill factor / %	23.0	41.3	69.2
J_{sc} / mA cm^{-2}	0.1	38.0	37.9

Table B.3: Solar cell parameters for Fig. 4.15(b)

	i-ZnO bilayer		
parameter	n.ann.	ann. (30)	ls. (30)
η / %	11.4	12.7	15.3
V_{oc} / mV	523	550	570
fill factor / %	58.8	60.9	70.7
J_{sc} / mA cm^{-2}	37.0	38.1	38.1

Table B.4: Solar cell parameters for Fig. 4.16(a)

	bilayer, 0%/4% O_2		
parameter	n.ann.	ann. (30)	ls. (30)
η / %	0.2	2.6	14.2
V_{oc} / mV	323	449	565
fill factor / %	20.4	19.1	65.3
J_{sc} / mA cm^{-2}	3.2	30.8	38.5

Table B.5: Solar cell parameters for Fig. 4.16(b)

	bilayer, 0%/2% O_2		
parameter	n.ann.	ann. (30)	ls. (30)
η / %	0.1	4.0	13.5
V_{oc} / mV	231	412	560
fill factor / %	22.2	27.1	63.5
J_{sc} / mA cm^{-2}	2.9	36.2	38.0

Table B.6: Solar cell parameters for Fig. 4.16(c)

	bilayer, 0%/1% O_2		
parameter	n.ann.	ann. (30)	ls. (30)
η / %	1.9	9.9	15.2
V_{oc} / mV	436	550	571
fill factor / %	16.3	46.6	69.5
J_{sc} / mA cm^{-2}	26.2	38.4	38.2

Table B.7: Solar cell parameters for Fig. 4.16(d)

	bilayer, 0%/0% O_2		
parameter	n.ann.	ann. (30)	ls. (30)
η / %	2.5	10.9	14.7
V_{oc} / mV	473	563	570
fill factor / %	16.8	50.4	67.4
J_{sc} / mA cm^{-2}	31.6	38.4	38.4

Table B.8: Solar cell parameters for Fig. 4.17(a)

	i-ZnO/ZnO:Al, $d_{ZnOS} = 46$ nm		
parameter	n.ann.	ann. (30)	ls. (30)
η / %	6.3	8.4	15.4
V_{oc} / mV	563	524	568
fill factor / %	31.0	42.9	70.5
J_{sc} / mA cm^{-2}	36.2	37.5	38.4

Table B.9: Solar cell parameters for Fig. 4.17(b)

	ZnO:Al, $d_{ZnOS} = 46$ nm		
parameter	n.ann.	ann. (30)	ls. (30)
η / %	6.4	7.4	14.7
V_{oc} / mV	526	464	564
fill factor / %	33.4	42.7	68.2
J_{sc} / mA cm^{-2}	36.4	37.4	38.2

Table B.10: Solar cell parameters for Fig. 4.17(c)

	i-ZnO/ZnO:Al, $d_{ZnOS} = 127$ nm		
parameter	n.ann.	ann. (30)	ls. (30)
η / %	0.0	0.0	9.7
V_{oc} / mV	96	129	563
fill factor / %	24.5	24.1	45.1
J_{sc} / mA cm^{-2}	0.4	0.4	37.9

Table B.11: Solar cell parameters for Fig. 4.17(d)

	ZnO:Al, $d_{ZnOS} = 127\,nm$		
parameter	n.ann.	ann. (30)	ls. (30)
η / %	1.5	3.4	13.1
V_{oc} / mV	447	538	579
fill factor / %	22.6	22.7	60.0
J_{sc} / mA cm^{-2}	15.1	27.9	37.7

Table B.12: Solar cell parameters for Fig. 4.18(a)

	i-ZnO		
parameter	n.ann.	ann. (30)	ls. (30)
η / %	3.6	6.1	14.1
V_{oc} / mV	436	484	529
fill factor / %	24.5	33.6	70.3
J_{sc} / mA cm^{-2}	33.3	37.7	37.9

Table B.13: Solar cell parameters for Fig. 4.18(b)

	sputtered $Zn(O_{0.75},S_{0.25})$		
parameter	n.ann.	ann. (30)	ls. (80)
η / %	9.6	11.3	13.0
V_{oc} / mV	531	539	547
fill factor / %	51.0	59.2	67.4
J_{sc} / mA cm^{-2}	35.4	35.5	35.4

Table B.14: Solar cell parameters for Fig. 4.19(a)

	i-ZnO		
parameter	n.ann.	ann. (30)	ls. (30)
η / %	8.1	14.3	14.1
V_{oc} / mV	470	574	566
fill factor / %	47.4	65.4	66.1
J_{sc} / mA cm^{-2}	36.2	38.1	37.7

Table B.15: Solar cell parameters for Fig. 4.19(b)

	ZnMgO (ZSW)		
parameter	n.ann.	ann. (30)	ls. (30)
η / %	3.7	4.0	15.0
V_{oc} / mV	408	511	570
fill factor / %	25.0	21.5	69.0
J_{sc} / mA cm^{-2}	35.8	36.2	38.2

Table B.16: Solar cell parameters for Fig. 4.20(a)

	i-ZnO(4% O_2), $d_{ZnOS} = 43$ nm		
parameter	n.ann.	ann. (30)	ls. (30)
η / %	0.0	1.3	14.0
V_{oc} / mV	3	291	565
fill factor / %	0.0	16.8	63.9
J_{sc} / mA cm^{-2}	0.0	26.4	38.6

Table B.17: Solar cell parameters for Fig. 4.20(b)

	i-ZnO(4% O_2), $d_{ZnOS} = 43$ nm		
parameter	n.ann.	ann. (30)	ls. (30)
η / %	0.0	0.0	14.5
V_{oc} / mV	3	33	545
fill factor / %	0.0	24.0	70.0
J_{sc} / mA cm^{-2}	0.0	0.0	38.0

Table B.18: Solar cell parameters for Fig. 4.20(c)

	i-ZnO bilayer, $d_{ZnOS} = 43$ nm		
parameter	n.ann.	ann. (30)	ls. (30)
η / %	1.1	7.3	14.9
V_{oc} / mV	342	490	563
fill factor / %	15.6	39.5	68.3
J_{sc} / mA cm^{-2}	21.3	37.9	38.7

Table B.19: Solar cell parameters for Fig. 4.20(d)

	i-ZnO bilayer, $d_{ZnOS} = 43\,nm$		
parameter	n.ann.	ann. (30)	ls. (30)
η / %	1.9	1.8	14.6
V_{oc} / mV	473	461	544
fill factor / %	27.1	16.0	71.1
J_{sc} / mA cm^{-2}	14.5	24.6	37.9

Table B.20: Solar cell parameters for Fig. 4.20(e)

	i-ZnO(no O_2), $d_{ZnOS} = 18\,nm$		
parameter	n.ann.	ann. (30)	ls. (30)
η / %	4.5	8.2	15.1
V_{oc} / mV	508	503	569
fill factor / %	25.5	42.4	68.0
J_{sc} / mA cm^{-2}	34.9	38.5	39.0

Table B.21: Solar cell parameters for Fig. 4.20(f)

	i-ZnO(no O_2), $d_{ZnOS} = 16\,nm$		
parameter	n.ann.	ann. (30)	ls. (30)
η / %	4.9	9.1	14.9
V_{oc} / mV	408	508	560
fill factor / %	33.6	47.9	70.0
J_{sc} / mA cm^{-2}	35.7	37.7	38.1

Table B.22: Solar cell parameters for Fig. 4.24(a)

	Al doping, [Al] in solution, batch 1, ann. (30)			
parameter	[Al] = 0 mM	[Al] = 0.2 mM	[Al] = 1 mM	[Al] = 2 mM
η / %	1.5	4.5	4.8	5.0
V_{oc} / mV	330	443	537	433
fill factor / %	17.5	27.7	25.6	31.8
J_{sc} / mA cm^{-2}	26.4	36.4	34.7	36.7

Table B.23: Solar cell parameters for Fig. 4.24(b)

	Al doping, [Al] in solution, batch 2, ann. (30)		
parameter	[Al] = 0 mM	[Al] = 0.2 mM	[Al] = 2 mM
η / %	2.7	1.4	0.1
V_{oc} / mV	393	331	185
fill factor / %	21.2	16.8	15.1
J_{sc} / mA cm^{-2}	32.4	26.0	3.4

Table B.24: Solar cell parameters for Fig. 4.24(c)

	Al doping, [Al] in solution, batch 3, ann. (30)		
parameter	[Al] = 0 mM	[Al] = 1 mM	[Al] = 4 mM
η / %	8.4	7.1	7.1
V_{oc} / mV	525	485	503
fill factor / %	41.5	38.2	37.6
J_{sc} / mA cm^{-2}	38.4	38.1	37.8

Table B.25: Solar cell parameters for Fig. 4.24(d)

	Al doping, [Al] in solution, batch 4, ann. (30)			
parameter	[Al] = 0 mM	[Al] = 0.4 mM	[Al] = 1 mM	[Al] = 2 mM
η / %	7.7	6.8	7.5	8.3
V_{oc} / mV	492	431	464	485
fill factor / %	41.1	41.4	42.7	44.9
J_{sc} / mA cm^{-2}	37.8	37.8	37.9	38.2

Table B.26: Solar cell parameters for Fig. 4.26(a)

	B doping, [B(OH)$_3$] in solution, batch 1, ann. (30)		
parameter	[B(OH)$_3$] = 0 mM	[B(OH)$_3$] = 0.5 mM	[B(OH)$_3$] = 12.5 mM
η / %	1.3	10.2	12.2
V_{oc} / mV	328	558	570
fill factor / %	17.9	48.2	56.1
J_{sc} / mA cm^{-2}	22.3	38.0	38.1

Table B.27: Solar cell parameters for Fig. 4.26(b)

	B doping, $[B(OH)_3]$ in solution, batch 2, ann. (30)		
parameter	$[B(OH)_3] = 0\,mM$	$[B(OH)_3] = 0.5\,mM$	$[B(OH)_3] = 2.5\,mM$
η / %	7.9	10.3	9.5
V_{oc} / mV	477	527	516
fill factor / %	44.0	52.3	49.4
J_{sc} / mA cm^{-2}	37.7	37.3	37.4

Table B.28: Solar cell parameters for Fig. 4.26(c)

	B doping, $[B(OH)_3]$ in solution, batch 3, ann. (30)	
parameter	$[B(OH)_3] = 0\,mM$	$[B(OH)_3] = 2.5\,mM$
η / %	1.9	3.5
V_{oc} / mV	422	448
fill factor / %	15.8	21.5
J_{sc} / mA cm^{-2}	28.5	36.1

Table B.29: Solar cell parameters for Fig. 4.26(d)

	B doping, $[B(OH)_3]$ in solution, batch 4, ann. (30)	
parameter	$[B(OH)_3] = 0\,mM$	$[B(OH)_3] = 2.5\,mM$
η / %	0.3	8.9
V_{oc} / mV	267	564
fill factor / %	15.5	41.2
J_{sc} / mA cm^{-2}	6.9	38.3

Table B.30: Solar cell parameters for Fig. 5.2(a)

	Zn(O,S), acidic process		
parameter	n.ann.	ann. (30)	ls. (30)
η / %	0.0	0.9	9.3
V_{oc} / mV	21	328	567
fill factor / %	26.1	16.5	44.9
J_{sc} / mA cm^{-2}	0.0	16.3	36.5

Table B.31: Solar cell parameters for Fig. 5.2(b)

	ZnInOS, acidic process		
parameter	n.ann.	ann. (30)	ls. (30)
η / %	0.1	8.7	14.8
V_{oc} / mV	237	553	567
fill factor / %	20.8	43.4	70.9
J_{sc} / mA cm^{-2}	1.3	36.3	36.8

Table B.32: Solar cell parameters for Fig. 5.7(a)

parameter	ZnInOS, alkaline process, n.ann.					
[In]/[Zn] (solution)	0	0.02	0.04	0.08	0.16	0.4
η / %	0.0	0.0	0.1	2.2	3.8	5.3
V_{oc} / mV	168	124	249	379	460	531
fill factor / %	21.8	23.6	16.1	19.5	24.4	28.0
J_{sc} / mA cm^{-2}	1.1	1.1	2.9	30.2	33.4	35.7

Table B.33: Solar cell parameters for Fig. 5.7(b)

parameter	ZnInOS, alkaline process, ann. (30)					
[In]/[Zn] (solution)	0	0.02	0.04	0.08	0.16	0.4
η / %	0.1	0.6	3.3	7.4	14.1	13.3
V_{oc} / mV	180	265	357	529	585	584
fill factor / %	17.3	15.9	26.5	37.1	64.3	61.6
J_{sc} / mA cm^{-2}	2.9	15.4	35.0	37.7	37.4	37.0

Table B.34: Solar cell parameters for Fig. 5.7(c)

parameter	ZnInOS, alkaline process, ls. (30)					
[In]/[Zn] (solution)	0	0.02	0.04	0.08	0.16	0.4
η / %	11.0	10.7	12.0	14.9	13.3	13.3
V_{oc} / mV	552	572	553	588	581	589
fill factor / %	52.5	50.2	58.3	67.1	61.4	61.0
J_{sc} / mA cm^{-2}	38.1	37.2	37.2	37.8	37.4	37.0

Appendix C

C Algorithms

C.1 Newton-Raphson method for the calculation of IV curves within the one diode model

In this work, an implementation of the Newton-Raphson method in Python [127] was used to calculate the current density for a given array of voltages and given parameters for the one diode model:

```
import numpy as np
from math import expm1

def onediode_calc(beta,V):
    J0 = beta[0]          # saturation current
    Jph = beta[1]         # photocurrent
    Rs = beta[2]          # series resistance
    Rp = beta[3]          # shunt resistance
    A = beta[4]           # ideality factor
    Vt = 1/beta[5]        # 1/(thermal voltage) = q/kT
    J = 1e-10*np.ones(len(V))
    for i in range(len(V)):
        J1 = 1+J[i];
        while (abs(J[i]-J1)>1e-8):
            J1 = J[i];
            J[i] = J[i] - (-J[i] + Jph - J0*expm1((V[i]+J[i]*Rs)/(A*
                Vt))-(V[i]+J[i]*Rs)/Rp)/(-1-J0*Rs/(A*Vt)*exp((V[i]+J[
                i]*Rs)/(A*Vt))-Rs/Rp);
    return J
```

C.2 Implementation of a fitting routine for IV curves

In order to fit IV curves from the one diode model or with the two diode model, to experimental data, a Python routine for orthogonal distance regression fitting, using the `odrpack` package, was implemented. The functions `onediode_odrfit` and `twodiode_odrfit` are called with experimental data and an initial set of model parameters as arguments. The diode models are implicitly defined with the functions `onediode` and `twodiode`, used as models for `odrpack`.

```
import numpy as np
```

```
from math import expm1
import scipy.odr.odrpack as odrpack

def onediode(beta, x):
    # x = [V,J]
    # beta = [J0,Jph,Rs,Rp,A,q/kT]
    calc = beta[1] - (x[0]+x[1]*beta[2])/beta[3] - x[1]
    for i in range(len(x[0])):
        calc[i] = calc[i] - beta[0]*expm1(beta[5]/beta[4]*(x[0][i]+x
            [1][i]*beta[2]))
    return calc

def twodiode(beta, x):
    # x = [V,J]
    # beta = [J01,J02,Jph,Rs,Rp,A1,A2,q/kT]
    calc = beta[2] - (x[0]+x[1]*beta[3])/beta[4] - x[1]
    for i in range(len(x[0])):
        calc[i] = calc[i] - beta[0]*expm1(beta[7]/beta[5]*(x[0][i]+x
            [1][i]*beta[3])) - beta[1]*expm1(beta[7]/beta[6]*(x[0][i
            ]+x[1][i]*beta[3]))
    return calc

def onediode_odrfit(V,J,beta0):
    weights = np.sqrt(np.abs(J))
    mydata = odrpack.Data(np.row_stack([V, J]), y=1, we=weights)
    mymodel = odrpack.Model(self.onediode, implicit=True)
    myodr = odrpack.ODR(mydata, mymodel, beta0)
    myodr.ifixb = [1,1,1,1,1,0]          # only temperature is fixed
    myoutput = myodr.run()
    return myoutput.beta

def twodiode_odrfit(V,J,beta0):
    weights = np.sqrt(np.abs(J))
    mydata = odrpack.Data(np.row_stack([V, J]), y=1, we=weights)
    mymodel = odrpack.Model(self.twodiode, implicit=True)
    myodr = odrpack.ODR(mydata, mymodel, beta0)
    myodr.ifixb = [1,1,1,1,1,1,1,0]      # only temperature is fixed
    myoutput = myodr.run()
    return myoutput.beta
```

This implementation is reasonably fast and can easily be used to write scripts, performing batch processed fits to sets of experimental data. `beta0` has to be adapted from time to time though. Also, since no boundaries are implemented, the fit sometimes converges on a negative series resistance. When this was the case, the series resistance could not be manually extracted from the experimental data, because it was either too small or the voltage range was too limited. Therefore, the parameter was intentionally set to a small value and fixed in the fitting routine.

C.3 Generation of graphs in this work

The large majority of graphs in this work was generated with Python utilizing the excellent matplotlib package [128]. An example to generate a graph similar to Fig. 2.7 is given here:

```
x = [5.37,5.53,5.78,5.60,5.37]
y = [2.42,1.55,1.04,1.68,2.42]
from math import sqrt
import matplotlib as mpl
mpl.use("pgf")
pgf_with_custom_preamble = {
    "font.family": "serif",
    "text.usetex": True,
    "pgf.rcfonts": False,
    "pgf.preamble": [
            r'\usepackage{amsmath}',
            r'\usepackage{siunitx}',
            r'\sisetup{mode=text}',
            r'\usepackage{unicode-math}',
            r'\setmathfont{xits-math.otf}',
            r'\setmainfont{Palatino␣Linotype}',
            ],
    'font.size': 10.95
}
mpl.rcParams.update(pgf_with_custom_preamble)
texpt = 1/72.27
golden_ratio = (1+sqrt(5))/2
textwidth_pt = 432.48195
textwidth_inch = textwidth_pt*texpt
pwidth = 0.643*textwidth_inch
pheight = pwidth/golden_ratio
import matplotlib.pyplot as plt
f1,ax1 = plt.subplots(1, 1,figsize = [pwidth,pheight])
ax1.plot(x,y,'ks-',markerfacecolor='red',markersize=10,zorder=5)
xfill = [5.3,5.85]
yfill1 = [1.1,1.1]
yfill2 = [1.5,1.5]
plt.fill_between(xfill,yfill1,yfill2,color='lightgrey',zorder=0)
ax1.text(5.4,2.45,r'CuGaS\textsubscript{2}')
ax1.text(5.63,1.7,r'CuGaSe\textsubscript{2}')
ax1.text(5.65,0.95,r'CuInSe\textsubscript{2}')
ax1.text(5.4,1.6,r'CuInS\textsubscript{2}')
ax1.text(5.32,1.27,r'\textit{optimal␣range␣of␣band␣gaps}',fontsize
   =9)
ax1.set_xlim((5.3,5.85))
ax1.set_ylim((0.7,2.7))
ax1.set_ylabel(r'$E_\mathrm{g}$␣/␣\si{\electronvolt}')
ax1.set_xlabel(r'a␣/␣\si{\angstrom}')
plt.tight_layout(pad=0.2)
plt.savefig('out.pdf')
```

A number of graphs in the introductory chapter have been manually drawn with Inkscape [129].

D Appendix D
Symbols and Abbreviations

A list of the symbols and abbreviations used in this thesis.

symbol	description
A	diode ideality factor
A_{SCR}	diode ideality factor for dominant recombination in the space charge region
A_{IF}	diode ideality factor for dominant recombination at the interface
A^*	effective Richardson constant
a	lattice constant
AM1.5	solar spectrum for an air mass coefficient of 1.5
α	factor, dividing the voltage drop at a junction
α	absorption coefficient
α_{Zn}	Auger parameter for Zn
b	bowing factor
CBD	chemical bath deposition
CIGSSe	$Cu(In,Ga)(S,Se)_2$
χ	calculated factor for the correction of thicknesses obtained from X-ray flourescence measurements
ΔE_{CB}	conduction band offset
$\Delta E_{CB,ab}$	conduction band offset at the absorber/buffer interface
$\Delta E_{CB,bw}$	conduction band offset at the buffer/window interface
ΔE_{VB}	valence band offset
d	film thickness
d	film thickness, determined by quartz crystal microbalance
d_{ZnOS}	effective Zn(O,S) layer thickness from X-ray fluorescence measurements
$d_{ZnInOS,calc}$	calculated thickness of a ZnInOS layer

symbol	description
DC	direct current
e	elementary charge
E_{CB}	conduction band minimum energy
E_{VB}	valence band maximum energy
E_{VBM}	valence band maximum energy obtained from XPS measurements
E_{F}	Fermi level
$E_{\mathrm{F,e}}$	quasi Fermi level for electrons
$E_{\mathrm{F,h}}$	quasi Fermi level for holes
E_{g}	band gap energy
$E_{\mathrm{g,PL}}$	band gap energy, determined from photoluminescence measurements
E_{i}	Fermi level position without doping (approximately in the middle of the band gap)
E_{t}	energetic position of recombination centers
E_{min}	minimum energy, necessary to pass over an energetic barrier
E_{kin}	kinetic energy
E_{CL}	core level binding energy
$E_{\mathrm{CL}}^{\mathrm{VBM}}$	difference between valence band maximum energy obtained from XPS measurements and core level binding energy
ϵ	absolute dielectric permittivity
ϵ_{r}	relative dielectric permittivity
$\mathcal{E}$	electric field strength
η_i	electrochemical potential for charge carrier type i, that is for electrons and holes
η_{e}	electrochemical potential for electrons
η_{h}	electrochemical potential for holes
η	efficiency
η_{max}	maximum efficiency
EQE	external quantum efficiency
FF	fill factor
G	generation rate
G_0	generation rate in thermal equilibrium
G_{th}	thermal generation rate

symbol	description
$\hbar$	reduced Planck constant
HEEDTA	N-(2-hydroxyethyl)ethylenediaminetriacetic acid
HR-window	high resistive window layer
I_0	intensity of irradiation
IV	current–voltage
i-ZnO	ZnO without elemental dopants
$\mathrm{In_{Cu}}$	indium–copper antisite defect
J	current density
J_0	reverse saturation current density
$J_{0,\mathrm{if}}$	reverse saturation current density for interface recombination
$J_{\mathrm{te},0}$	reverse saturation current density for thermionic emission
J_∞	temperature independent part of the reverse saturation current density
J_{sc}	short circuit current density
J_{photo}	photo current, integral over the generation profile
J_{field}	field current density
$J_{\mathrm{diffusion}}$	diffusion current density
J_{wall}	Maxwallian thermal particle flux to a wall
k_B	Boltzmann constant
L_{eff}	effective diffusion length
$L_{\mathrm{eff,norm}}$	normalized effective diffusion length
LR-window	low resistive window layer
m^*	effective mass
μ_i	chemical potential for charge carrier type i, that is for electrons and holes
$m_{\mathrm{mol,X}}$	molar mass of a material X
n	dominantly doped with donor impurities
n+	doped with high concentration of donor impurities
n	density of electrons
n_{In}	atomic fraction of In in a material
n_{Zn}	atomic fraction of Zn in a material
N_{CB}	effective density of states in the conduction band
N_{VB}	effective density of states in the valence band

symbol	description
N_D	density of donor impurities
$N_{D,b}$	density of donor impurities in the buffer layer
$N_{D,w}$	density of donor impurities in the window layer
$N_{D,ab}$	surface density of donor impurities at the absorber/buffer interface
N_A	density of acceptor impurities
$N_{A,ab}$	surface density of acceptor impurities at the absorber/buffer interface
$N_{A,bw}$	surface density of acceptor impurities at the buffer/window interface
$N_{A,p+}$	density of acceptor impurities in the p+ layer
N_t	density of recombination centers
$n_t(E)$	energy dependent density of recombination centers
$n_{samples}$	number of samples
ω	angular frequency
p	dominantly doped with acceptor impurities
p+	doped with high concentration of acceptor impurities
p–n	junction with p-doped material on one side and n-doped material on the other side
p	density of holes
$p\|_{if}$	density of holes at the interface
ϕ	electric potential
Φ_b^p	energetic barrier height for interface recombination dominated by the density of holes
$\Phi_{b,0}^p$	energetic barrier height for interface recombination dominated by the density of holes without applied bias voltage
ϕ_b	energetic barrier height
ϕ_{max}	maximum energetic barrier height
P_{max}	maximum electrical power per area delivered by the solar cell
$P_{illumination}$	power of the incoming photon flux
PL	photoluminescence
PVD	physical vapor deposition
QNR	quasi neutral region
QE	quantum efficiency
R	reflectance

symbol	description
R′	reflectance from a single reflection process
R	recombination rate
R_0	recombination rate in thermal equilibrium
R_{net}	net recombination rate (or generation rate, if negative)
R_{r}	radiative recombination rate
r_{r}	radiative recombination coefficient
$R_{\mathrm{t,max}}$	maximum non-radiative recombination rate
R_{p}	shunt resistance in the diode model
R_{s}	series resistance in the diode model
ρ_{X}	density of a material X
$\rho_{\mathrm{X,Y}}$	density of element X in a material Y
RF	radio frequency
S_{e}	surface recombination velocity for electrons
S_{h}	surface recombination velocity for holes
SCAPS	solar cell capacitance simulator
SCR	space charge region
SEM	scanning electron microscopy
SIMS	secondary ion mass spectroscopy
σ	capture cross section
σ	conductivity
T	transmittance
T	temperature
T^*	characteristic temperature, describing the energetic distribution of a recombination center density
τ_{p}	effective lifetime of holes
τ_{n}	effective lifetime of electrons
TAA	thioacetamide C_2H_5NS
u_{a}	activation energy of the reverse saturation current
U_{a}	activation energy relevant for the open circuit voltage
U_{00}	tunneling energy
V	voltage
V_{bi}	built-in potential

symbol	description
V_{oc}	open circuit voltage
v_{th}	thermal velocity
v_x	carrier velocity in x-direction
V_X	vacancy in the lattice for element X
V_{In,In_2O_3}	The volume fraction, attributed to In in In_2O_3
V_{In,In_2S_3}	The volume fraction, attributed to In in In_2S_3
$V_{Zn,ZnO}$	The volume fraction, attributed to Zn in ZnO
$V_{Zn,ZnS}$	The volume fraction, attributed to Zn in ZnS
$W_{D,n}$	space charge region width on the n-side of the junction
$W_{D,p}$	space charge region width on the p-side of the junction
XPS	X-ray photoelectron spectroscopy
XRF	X-ray fluorescence
Zn(O,S)	Zn(O,S) based material, possibly with inclusion of hydroxides
ZnInOS	(Zn,In)(O,S) material with undefined elemental concentrations and unknown phase formation
z_i	sign of charge for carrier type i, that is, holes or electrons

Bibliography

[1] World Energy Council, *Energy Resources*, https://www.worldenergy.org/data/resources/ (visited on 03/29/2016) (Cited on page 1).

[2] Umweltbundesamt der Bundesrepublik Deutschland, *Entwicklung des Energieverbrauchs*, http://www.umweltbundesamt.de/daten/ (visited on 03/29/2016) (Cited on page 1).

[3] Deutsche Bank - Markets Research, *2014 Outlook: Let the Second Gold Rush Begin*, Jan. 2014, https://www.deutschebank.nl/nl/docs/Solar_-_2014_Outlook_Let_the_Second_Gold_Rush_Begin.pdf (visited on 03/29/2016) (Cited on page 2).

[4] Solar Frontier K.K., *Solar Frontier Achieves World Record Thin-Film Solar Cell Efficiency: 22.3%*, online press release, Dec. 2015, http://www.solar-frontier.com/eng/news/2015/C051171.html (visited on 03/15/2016) (Cited on page 2).

[5] A. Chirilă, P. Reinhard, F. Pianezzi, P. Bloesch, A. R. Uhl, C. Fella, L. Kranz, D. Keller, C. Gretener, H. Hagendorfer, D. Jaeger, R. Erni, S. Nishiwaki, S. Buecheler, and A. N. Tiwari, "Potassium-induced surface modification of Cu(In,Ga)Se_2 thin films for high-efficiency solar cells", Nature Materials Letter **12**, 1107–1111 (2013) (Cited on page 2).

[6] P. Würfel, *Physics of Solar Cells: From Principles to New Concepts*, (WILEY-VCH Verlag GmbH & Co. KGaA, 2005), ISBN: 978-3-527-61854-5 (Cited on pages 5, 9, 10, 42).

[7] U. Rau and H.-W. Schock, "Cu(In,Ga)Se_2 solar cells", in *Clean Electricity from Photovoltaics*, (World Scientific, 2001), ISBN: 978-1-86094-161-0 Chap. 7, pp. 277–345 (Cited on pages 5, 9, 15–17, 20, 42).

[8] R. Scheer and H.-W. Schock, *Chalcogenide Photovoltaics*, (Wiley-VCH Verlag GmbH & Co. KGaA, 2011), ISBN: 978-3-527-63370-8 (Cited on pages 5, 9, 13–15, 17, 18, 25).

[9] S. M. Sze and K. K. Ng, *Physics of Semiconductor Devices*, (John Wiley & Sons, 2006), ISBN: 978-0-470-06832-8 (Cited on pages 5, 15, 18).

[10] W. Shockley and H. J. Queisser, "Detailed Balance Limit of Efficiency of p–n Junction Solar Cells", Journal of Applied Physics **32**, 510–519 (1961) (Cited on page 13).

[11] M. Burgelman, P. Nollet, and S. Degrave, "Modelling polycrystalline semiconductor solar cells", Thin Solid Films **361–362**, 527–532 (2000) (Cited on page 14).

[12] V. Nadenau, U. Rau, A. Jasenek, and H. W. Schock, "Electronic properties of $CuGaSe_2$-based heterojunction solar cells. Part I. Transport analysis", Journal of Applied Physics **87**, 584–593 (2000) (Cited on page 17).

[13] A. Kanevce, M. Gloeckler, A. O. Pudov, and J. R. Sites, "Conduction-Band-Offset Rule Governing J-V Distortion in CdS/CI(G)S Solar Cells", in Symposium F – Thin-Film Compound Semiconductor Photovoltaics, Vol. 865, MRS Proceedings (2005), F5.32 (Cited on page 19).

[14] J. E. Jaffe and A. Zunger, "Theory of the band-gap anomaly in ABC_2 chalcopyrite semiconductors", Phys. Rev. B **29**, 1882–1906 (1984) (Cited on pages 20, 122).

[15] P. Jackson, D. Hariskos, R. Wuerz, O. Kiowski, A. Bauer, T. M. Friedlmeier, and M. Powalla, "Properties of $Cu(In,Ga)Se_2$ solar cells with new record efficiencies up to 21.7%", physica status solidi (RRL) – Rapid Research Letters **9**, 28–31 (2015) (Cited on page 20).

[16] S.-H. Wei and A. Zunger, "Band offsets and optical bowings of chalcopyrites and Zn-based II-VI alloys.", Journal of Applied Physics **78**, 3846 (1995) (Cited on pages 20, 92, 126).

[17] M. I. Alonso, M. Garriga, C. D. Rincón, E. Hernández, and M. León, "Optical functions of chalcopyrite $CuGa_xIn_{1-x}Se_2$ alloys", Applied Physics A **74**, 659–664 (2002) (Cited on page 20).

[18] C. A. Durante Rincón, E. Hernández, M. I. Alonso, M. Garriga, S. M. Wasim, C. Rincón, and M. León, "Optical transitions near the band edge in bulk $CuIn_xGa_{1-x}Se_2$ from ellipsometric measurements", Materials Chemistry and Physics **70**, 300–304 (2001) (Cited on page 20).

[19] P. D. Paulson, R. W. Birkmire, and W. N. Shafarman, "Optical characterization of $CuIn_{1-x}Ga_xSe_2$ alloy thin films by spectroscopic ellipsometry", Journal of Applied Physics **94**, 879–888 (2003) (Cited on page 20).

[20] S. B. Zhang, S.-H. Wei, A. Zunger, and H. Katayama-Yoshida, "Defect physics of the$CuInSe_2$ chalcopyrite semiconductor", Phys. Rev. B **57**, 9642–9656 (1998) (Cited on page 20).

[21] P. Salomé, H. Rodriguez-Alvarez, and S. Sadewasser, "Incorporation of alkali metals in chalcogenide solar cells", Solar Energy Materials and Solar Cells **143**, 9–20 (2015) (Cited on page 20).

[22] S. Siebentritt, M. Igalson, C. Persson, and S. Lany, "The electronic structure of chalcopyrites-bands, point defects and grain boundaries", Progress in Photovoltaics: Research and Applications **18**, 390–410 (2010) (Cited on page 20).

[23] A. Klein, "Energy band alignment in chalcogenide thin film solar cells from photoelectron spectroscopy", Journal of Physics: Condensed Matter **27**, 134201 (2015) (Cited on pages 21, 26, 28, 29, 105, 107, 125).

[24] B. K. Meyer, A. Polity, B. Farangis, Y. He, D. Hasselkamp, T. Krämer, and C. Wang, "Structural properties and bandgap bowing of $ZnO_{1-x}S_x$ thin films deposited by reactive sputtering", Applied Physics Letters **85**, 4929–4931 (2004) (Cited on page 21).

[25] C. Persson, C. Platzer-Björkman, J. Malmström, T. Törndahl, and M. Edoff, "Strong valence-band offset bowing of $ZnO_{1-x}S_x$ enhances p-type nitrogen doping of ZnO-like alloys", English, Physical Review Letters **97**, 146403(4) (2006) (Cited on pages 21, 64, 106, 122).

[26] D. Kieven, A. Grimm, I. Lauermann, M. C. Lux-Steiner, J. Palm, T. Niesen, and R. Klenk, "Band alignment at sputtered ZnS_xO_{1-x}/Cu(In,Ga)$(Se,S)_2$ heterojunctions", physica status solidi (RRL) – Rapid Research Letters **6**, 294–296 (2012) (Cited on page 21).

[27] T. Adler, M. Botros, W. Witte, D. Hariskos, R. Menner, M. Powalla, and A. Klein, "Valence band offsets at Cu(In,Ga)Se_2/Zn(O,S) interfaces", physica status solidi (a) **211**, 1972–1980 (2014) (Cited on pages 21, 27–29, 69, 112, 115).

[28] S. Lany and A. Zunger, "Light-and bias-induced metastabilities in Cu(In,Ga)Se_2 based solar cells caused by the (V_{Se}-V_{Cu}) vacancy complex", Journal of Applied Physics **100**, 113725 (2006) (Cited on pages 22, 55).

[29] U. Rau, M. Schmitt, J. Parisi, W. Riedl, and F. Karg, "Persistent photoconductivity in Cu(In,Ga)Se_2 heterojunctions and thin films prepared by sequential deposition", Applied Physics Letters **73**, 223–225 (1998) (Cited on page 22).

[30] M. Igalson, A. Urbaniak, P. Zabierowski, H. A. Maksoud, M. Buffiere, N. Barreau, and S. Spiering, "Red-blue effect in Cu(In,Ga)Se_2-based devices revisited", Thin Solid Films **535**, 302–306 (2013) (Cited on pages 22, 40, 55, 63).

[31] S. Lany and A. Zunger, "Intrinsic DX Centers in Ternary Chalcopyrite Semiconductors", Physical Review Letters **100**, 016401 (2008) (Cited on pages 22, 55).

[32] I. Eisgruber, J. Granata, J. Sites, J. Hou, and J. Kessler, "Blue-photon modification of nonstandard diode barrier in $CuInSe_2$ solar cells", Solar Energy Materials and Solar Cells **53**, 367–377 (1998) (Cited on pages 22, 63, 64).

[33] T. Adler, "Zn(O,S) Puffer Eigenschaften in Cu(In,Ga)Se_2 Solarzellen", PhD thesis (Technische Universität Darmstadt, Dec. 2013) (Cited on pages 26, 27, 30, 107, 125).

[34] A. Klein, "Energy band alignment at interfaces of semiconducting oxides: A review of experimental determination using photoelectron spectroscopy and comparison with theoretical predictions by the electron affinity rule, charge neutrality levels, and the common anion rule", Thin Solid Films **520**, 3721–3728 (2012) (Cited on pages 26, 105, 107).

[35] C. D. Wagner, "Auger lines in x-ray photoelectron spectrometry", Analytical Chemistry **44**, 967–973 (1972) (Cited on page 27).

[36] A. M. H. Fuchs, "Der Frontkontakt der CdTe-Dünnschichtsolarzelle: Charakterisierung und Modifizierung von Puffer- und Fensterschichten und deren Grenzflächen", PhD thesis (Technische Universität Darmstadt, 2015) (Cited on page 28).

[37] J. Fritsche, T. Schulmeyer, D. Kraft, A. Thißen, A. Klein, and W. Jaegermann, "Utilization of sputter depth profiling for the determination of band alignment at polycrystalline CdTe/CdS heterointerfaces", Applied Physics Letters **81**, 2297–2299 (2002) (Cited on pages 28, 29).

[38] C. Platzer-Björkman, T. Törndahl, D. Abou-Ras, J. Malmström, J. Kessler, and L. Stolt, "Zn(O,S) buffer layers by atomic layer deposition in Cu(In,Ga)Se_2 based thin film solar cells: Band alignment and sulfur gradient", Journal of Applied Physics **100**, 044506 (2006) (Cited on pages 28, 29, 61, 64).

[39] P. Y. Yu and M. Cardona, *Fundamentals of Semiconductors*, 4th ed., (Springer-Verlag Berlin Heidelberg, 2010), ISBN: 978-3-642-00710-1 (Cited on page 32).

[40] J. Tauc, "Optical properties and electronic structure of amorphous Ge and Si", Materials Research Bulletin **3**, 37–46 (1968) (Cited on page 32).

[41] V. Probst, I. Koetschau, E. Novak, A. Jasenek, H. Eschrich, F. Hergert, T. Hahn, J. Feichtinger, M. Maier, B. Walther, and V. Nadenau, "A New Mass Production Technology for High-Efficiency Thin-Film CIS-Absorber Formation", IEEE Journal of Photovoltaics **4**, 687–692 (2014) (Cited on page 32).

[42] S. Spiering, A. Nowitzki, F. Kessler, M. Igalson, and H. A. Maksoud, "Optimization of buffer-window layer system for CIGS thin film devices with indium sulphide buffer by in-line evaporation ", Solar Energy Materials and Solar Cells **144**, 544–550 (2016) (Cited on pages 39, 40).

[43] AVANCIS GmbH, *Module with record efficiency from AVANCIS: Fraunhofer ISE certifies CIGS solar module with an efficiency of 17.9%*. online press release, May 2016, http://www.avancis.de/en/press/news/article/avancis-erzielt-erneuten-wirkungsgradrekord-fraunhofer-ise-zertifiziert-cigs-solarmodul-mit-wirkungsgrad-von-179/ (visited on 05/16/2016) (Cited on page 39).

[44] N. Barreau, "Indium sulfide and relatives in the world of photovoltaics", Solar Energy **83**, 363–371 (2009) (Cited on pages 39, 55).

[45] M. Bär, N. Barreau, F. Couzinié-Devy, L. Weinhardt, R. G. Wilks, J. Kessler, and C. Heske, "Impact of Annealing-Induced Intermixing on the Electronic Level Alignment at the In_2S_3/Cu(In,Ga)Se_2 Thin-Film Solar Cell Interface", ACS Applied Materials & Interfaces **8**, 2120–2124 (2016) (Cited on pages 39, 40).

[46] S. Spiering, S. Chowdhury, A. Drese, D. Hariskos, A. Eicke, and M. Powalla, "Evaporated indium sulphide as buffer layer in Cu(In,Ga)Se_2-based solar cells", in 21st European Photovoltaic Solar Energy Conference (Sept. 2006), pp. 1847–1852 (Cited on pages 39, 55).

[47] P. Pistor, A. Grimm, D. Kieven, F. Hergert, A. Jasenek, and R. Klenk, "Dry vacuum buffers for industrial chalcopyrite absorbers from a sequential absorber process route", in Photovoltaic Specialists Conference (PVSC), 2011 37th IEEE (June 2011), pp. 002808–002812 (Cited on page 39).

[48] P. Pistor, "Formation and Electronic Properties of In_2S_3/Cu(In,Ga)Se_2 Junctions and Related Thin Film Solar Cells", PhD thesis (Freie Universität Berlin, 2009) (Cited on pages 40, 55).

[49] H. A. Maksoud, M. Igalson, and S. Spiering, "Influence of post-deposition heat treatment on electrical transport properties of In_2S_3-buffered Cu(In,Ga)Se_2 cells", Thin Solid Films **535**, 158–161 (2013) (Cited on page 40).

[50] M. Topič, F. Smole, J. Furlan, and M. A. Contreras, "Examination of CdS/-CIGS Solar Cell Temperature Dependence", in 14th European Photovoltaic Solar Energy Conference (June 1997), pp. 2139–2142 (Cited on pages 40, 55).

[51] A. Niemegeers, M. Burgelman, R. Herberholz, U. Rau, D. Hariskos, and H.-W. Schock, "Model for electronic transport in Cu(In,Ga)Se_2 solar cells", Progress in Photovoltaics: Research and Applications **6**, 407–421 (1998) (Cited on pages 40, 55).

[52] R. Klenk, "Characterisation and modelling of chalcopyrite solar cells", Thin Solid Films **387**, 135–140 (2001) (Cited on page 40).

[53] K. Ramanathan, F. Hasoon, S. Smith, A. Mascarenhas, H. Al-Thani, J. Alleman, H. Ullal, J. Keane, P. Johnson, and J. Sites, "Properties of Cd and Zn partial electrolyte treated CIGS solar cells", in Photovoltaic Specialists Conference, 2002. Conference Record of the Twenty-Ninth IEEE (May 2002), pp. 523–526 (Cited on page 40).

[54] M. Bär, L. Weinhardt, C. Heske, H.-J. Muffler, M. C. Lux-Steiner, E. Umbach, and C. Fischer, "Cd^{2+}/NH_3 treatment of Cu(In,Ga)$(S,Se)_2$ thin-film solar cell absorbers: a model for the performance-enhancing processes in the partial electrolyte", Progress in Photovoltaics: Research and Applications **13**, 571–577 (2005) (Cited on page 40).

[55] M. Bär, U. Bloeck, H.-J. Muffler, M. Lux-Steiner, C.-H. Fischer, M. Giersig, T. Niesen, and F. Karg, "Cd^{2+}/ NH_3-treatment of Cu(In,Ga)$(S,Se)_2$: Impact on the properties of ZnO layers deposited by the ion layer gas reaction method", Journal of Applied Physics **97**, 014905 (2005) (Cited on page 40).

[56] S. Siebentritt, "What limits the efficiency of chalcopyrite solar cells?", Solar Energy Materials and Solar Cells **95**, 1471–1476 (2011) (Cited on page 51).

[57] R. Klenk, H.-W. Schock, and W. H. Bloss, "Photocurrent collection in thin film solar cells-calculation and characterization for CuGaSe2/(Zn,Cd)S", in 12th European Photovoltaic Solar Energy Conference (Apr. 1994), pp. 1588–1591 (Cited on page 51).

[58] S. S. Hegedus and W. N. Shafarman, "Thin-film solar cells: device measurements and analysis", Progress in Photovoltaics: Research and Applications **12**, 155–176 (2004) (Cited on page 51).

[59] C. Persson, Y.-J. Zhao, S. Lany, and A. Zunger, "*n*-type doping of $CuInSe_2$ and $CuGaSe_2$", Phys. Rev. B **72**, 035211 (2005) (Cited on page 55).

[60] L. Kronik, U. Rau, J.-F. Guillemoles, D. Braunger, H.-W. Schock, and D. Cahen, "Interface redox engineering of Cu(In,Ga)Se_2–based solar cells: oxygen, sodium, and chemical bath effects", Thin Solid Films **361–362**, 353–359 (2000) (Cited on page 55).

[61] S. Siebentritt, "Alternative buffers for chalcopyrite solar cells", Solar Energy **77**, 767–775 (2004) (Cited on page 61).

[62] D. Hariskos, S. Spiering, and M. Powalla, "Buffer layers in Cu(In,Ga)Se_2 solar cells and modules", Thin Solid Films **480–481**, 99–109 (2005) (Cited on page 61).

[63] N. Naghavi, D. Abou-Ras, N. Allsop, N. Barreau, S. Bücheler, A. Ennaoui, C.-H. Fischer, C. Guillen, D. Hariskos, J. Herrero, et al., "Buffer layers and transparent conducting oxides for chalcopyrite Cu(In,Ga)$(S,Se)_2$ based thin film photovoltaics: present status and current developments", Progress in Photovoltaics: Research and Applications **18**, 411–433 (2010) (Cited on page 61).

[64] S. Pawar, B. Pawar, J. Kim, O.-S. Joo, and C. Lokhande, "Recent status of chemical bath deposited metal chalcogenide and metal oxide thin films", Current Applied Physics **11**, 117–161 (2011) (Cited on page 61).

[65] T. M. Friedlmeier, P. Jackson, A. Bauer, D. Hariskos, O. Kiowski, R. Wuerz, and M. Powalla, "Improved Photocurrent in Cu(In,Ga)Se_2 Solar Cells: From 20.8% to 21.7% Efficiency with CdS Buffer and 21.0% Cd-Free", IEEE Journal of Photovoltaics **5**, 1487–1491 (2015) (Cited on page 61).

[66] J. Nam, Y. Kang, D. Lee, J. Yang, Y.-S. Kim, C. B. Mo, S. Park, and D. Kim, "Achievement of 17.9% efficiency in 30×30 cm^2 Cu(In,Ga)$(Se,S)_2$ solar cell sub-module by sulfurization after selenization with Cd-free buffer", Progress in Photovoltaics: Research and Applications **24**, 175–182 (2015) (Cited on pages 61, 62).

[67] S. Merdes, V. Malinen, F. Ziem, I. Lauermann, M. Schüle, F. Stober, F. Hergert, N. Papathanasiou, and R. Schlatmann, "Zn(O,S) buffer prepared by atomic layer deposition for sequentially grown Cu(In,Ga)$(Se,S)_2$ solar cells and modules", Solar Energy Materials and Solar Cells **126**, 120–124 (2014) (Cited on page 61).

[68] R. Klenk, A. Steigert, T. Rissom, D. Greiner, C. A. Kaufmann, T. Unold, and M. C. Lux-Steiner, "Junction formation by Zn(O,S) sputtering yields CIGSe-based cells with efficiencies exceeding 18%", Progress in Photovoltaics: Research and Applications **22**, 161–165 (2014) (Cited on page 61).

[69] M. Powalla, W. Witte, P. Jackson, S. Paetel, E. Lotter, R. Wuerz, F. Kessler, C. Tschamber, W. Hempel, D. Hariskos, R. Menner, A. Bauer, S. Spiering, E. Ahlswede, T. Friedlmeier, D. Blázquez-Sánchez, I. Klugius, and W. Wischmann, "CIGS cells and modules with high efficiency on glass and flexible substrates", IEEE Journal of Photovoltaics **4**, 440–446 (2014) (Cited on pages 61, 64, 85).

[70] C. Hubert, N. Naghavi, A. Etcheberry, O. Roussel, D. Hariskos, M. Powalla, O. Kerrec, and D. Lincot, "A better understanding of the growth mechanism of Zn(S,O,OH) chemical bath deposited buffer layers for high efficiency Cu(In,Ga)$(S,Se)_2$ solar cells", physica status solidi (a) **205**, 2335–2339 (2008) (Cited on pages 61, 62).

[71] C. Hubert, N. Naghavi, B. Canava, A. Etcheberry, and D. Lincot, "Thermodynamic and experimental study of chemical bath deposition of Zn(S,O,OH) buffer layers in basic aqueous ammonia solutions. Cell results with electrodeposited $CuIn(S\ Se)_2$ absorbers", Thin Solid Films **515**, 6032–6035 (2007) (Cited on page 62).

[72] P. O'Brien and J. McAleese, "Developing an understanding of the processes controlling the chemical bath deposition of ZnS and CdS", Journal of Materials Chemistry **8**, 2309–2314 (1998) (Cited on page 62).

[73] R. Sáez-Araoz, D. Abou-Ras, T. Niesen, A. Neisser, K. Wilchelmi, M. Lux-Steiner, and A. Ennaoui, "In situ monitoring the growth of thin-film ZnS/Zn(S,O) bilayer on Cu-chalcopyrite for high performance thin film solar cells", Thin Solid Films **517**, 2300–2304 (2009) (Cited on page 62).

[74] M. Buffière, E. Gautron, T. Hildebrandt, S. Harel, C. Guillot-Deudon, L. Arzel, N. Naghavi, N. Barreau, and J. Kessler, "Composition and structural study of solution-processed Zn(S,O,OH) thin films grown using H_2O_2 based deposition route", Thin Solid Films **535**, 171–174 (2013) (Cited on page 62).

[75] T. Nakada and M. Mizutani, "18% Efficiency Cd-Free Cu(In, Ga)Se_2 Thin-Film Solar Cells Fabricated Using Chemical Bath Deposition (CBD)-ZnS Buffer Layers", Japanese Journal of Applied Physics **41**, L165–L167 (2002) (Cited on page 62).

[76] T. Kobayashi and T. Nakada, "Efficient Cu(In,Ga)Se_2 thin film solar cells with reduced thickness of ZnS(O,OH) Buffer Layer", Solar Energy Materials and Solar Cells **117**, 526–530 (2013) (Cited on page 62).

[77] A. Ennaoui, M. Bär, J. Klaer, T. Kropp, R. Sáez-Araoz, and M. C. Lux-Steiner, "Highly-efficient Cd-free $CuInS_2$ thin-film solar cells and mini-modules with Zn(S,O) buffer layers prepared by an alternative chemical bath process", Progress in Photovoltaics: Research and Applications **14**, 499–511 (2006) (Cited on page 62).

[78] D. Hariskos, R. Menner, P. Jackson, S. Paetel, W. Witte, W. Wischmann, M. Powalla, L. Bürkert, T. Kolb, M. Oertel, et al., "New reaction kinetics for a high-rate chemical bath deposition of the Zn(S,O) buffer layer for Cu(In,Ga)Se_2-based solar cells", Progress in Photovoltaics: Research and Applications **20**, 534–542 (2012) (Cited on pages 62, 112).

[79] C. Hubert, N. Naghavi, O. Roussel, A. Etcheberry, D. Hariskos, R. Menner, M. Powalla, O. Kerrec, and D. Lincot, "The Zn(S,O,OH)/ZnMgO buffer in thin film Cu (In,Ga)$(S,Se)_2$-based solar cells part I: Fast chemical bath deposition of Zn(S,O,OH) buffer layers for industrial application on Co-evaporated Cu(In,Ga)Se_2 and electrodeposited $CuIn(S,Se)_2$ solar cells", Progress in Photovoltaics: Research and Applications **17**, 470–478 (2009) (Cited on page 62).

[80] A. Ennaoui, T. Kropp, M. C. Lux-Steiner, and R. Saéz-Araoz, "Method for applying zinc sulfide and zinc oxide buffer layer on semiconductor substrate, involves dissolving certain amount of zinc salt and thiocarbamide in distilled water", WO 2010108480 A2 (2010) (Cited on page 62).

[81] M. Buffière, S. Harel, L. Arzel, C. Deudon, N. Barreau, and J. Kessler, "Fast chemical bath deposition of Zn(O,S) buffer layers for Cu(In,Ga)Se_2 solar cells", Thin Solid Films **519**, 7575–7578 (2011) (Cited on page 62).

[82] J. M. Doña and J. Herrero, "Process and Film Characterization of Chemical-Bath-Deposited ZnS Thin Films", Journal of The Electrochemical Society **141**, 205–210 (1994) (Cited on page 62).

[83] P. Němec, I. Němec, P. Nahalkova, Y. Němcová, F. Trojanek, and P. Malý, "Ammonia-free method for preparation of CdS nanocrystalline films by chemical bath deposition technique", Thin Solid Films **403**, 9–12 (2002) (Cited on page 62).

[84] G. Agawane, S. W. Shin, A. Moholkar, K. Gurav, J. H. Yun, J. Y. Lee, and J. H. Kim, "Non-toxic complexing agent Tri-sodium citrate's effect on chemical bath deposited ZnS thin films and its growth mechanism", Journal of Alloys and Compounds **535**, 53–61 (2012) (Cited on pages 62, 106).

[85] T. Hildebrandt, N. Loones, M. Bouttemy, J. Vigneron, A. Etcheberry, D. Lincot, and N. Naghavi, "Search for new bath formulations of Zn(S, O, OH) buffer layer to outperform record performances of CdS-based CIGSe solar cells", in Photovoltaic Specialists Conference (PVSC), 2013 IEEE 39th (June 2013), pp. 1114–1119 (Cited on pages 62, 106).

[86] J. Liao, S. Cheng, H. Zhou, and B. Long, "Al-doped ZnS thin films for buffer layers of solar cells prepared by chemical bath deposition", IET Micro Nano Letters **8**, 211–214 (2013) (Cited on pages 62, 64, 106).

[87] H. Khallaf, G. Chai, O. Lupan, H. Heinrich, S. Park, A. Schulte, and L. Chow, "Investigation of chemical bath deposition of ZnO thin films using six different complexing agents", Journal of Physics D: Applied Physics **42**, 135304 (2009) (Cited on page 62).

[88] A. Yamada, H. Miyazaki, Y. Chiba, and M. Konagai, "High-efficiency Cu(InGa)Se_2 solar cells with a zinc-based buffer layer", Thin Solid Films **480**, 503–508 (2005) (Cited on page 62).

[89] A. Goudarzi, G. M. Aval, R. Sahraei, and H. Ahmadpoor, "Ammonia-free chemical bath deposition of nanocrystalline ZnS thin film buffer layer for solar cells", Thin Solid Films **516**, 4953–4957 (2008) (Cited on page 62).

[90] W. Witte, D. Hariskos, A. Eicke, R. Menner, O. Kiowski, and M. Powalla, "Impact of annealing on Cu(In,Ga)Se_2 solar cells with Zn(O,S)/(Zn,Mg)O buffers", Thin Solid Films **535**, 180–183 (2012) (Cited on pages 62, 63).

[91] N. Naghavi, C. Hubert, A. Darga, G. Renou, C. Ruiz, A. Etcheberry, D. Hariskos, M. Powalla, and J. Guillemoles, "On a Better Understanding of Post-Treatment Effects on CI(G)S/Zn(S,O,OH)/ZnMgO Based Solar Cells", in 23rd European Photovoltaic Solar Energy Conference and Exhibition (Sept. 2008), pp. 2160–2164 (Cited on pages 62, 63).

[92] T. Kobayashi, T. Kumazawa, Z. Jehl Li Kao, and T. Nakada, "Post-treatment effects on ZnS(O,OH)/Cu(In,Ga)Se_2 solar cells deposited using thioacetamide-ammonia based solution", Solar Energy Materials and Solar Cells **123**, 197–202 (2014) (Cited on pages 62, 63).

[93] N. Naghavi, S. Temgoua, T. Hildebrandt, J. F. Guillemoles, and D. Lincot, "Impact of oxygen concentration during the deposition of window layers on lowering the metastability effects in Cu(In,Ga)Se_2/CBD Zn(S,O) based solar cell", Progress in Photovoltaics: Research and Applications **23**, 1820–1827 (2015) (Cited on pages 62–64, 81, 85, 86).

[94] A. Pudov, J. Sites, M. Contreras, T. Nakada, and H.-W. Schock, "CIGS J–V distortion in the absence of blue photons", Thin Solid Films **480**, 273–278 (2005) (Cited on pages 63, 64).

[95] Q. Nguyen, K. Orgassa, I. Koetschau, U. Rau, and H. Schock, "Influence of heterointerfaces on the performance of Cu(In,Ga)Se_2 solar cells with CdS and In(OH_x,S_y) buffer layers", Thin Solid Films **431–432**, 330–334 (2003) (Cited on page 63).

[96] M. Igalson and C. Platzer-Björkman, "The influence of buffer layer on the transient behavior of thin film chalcopyrite devices", Solar Energy Materials and Solar Cells **84**, 93–103 (2004) (Cited on page 63).

[97] M. Buffière, N. Barreau, L. Arzel, P. Zabierowski, and J. Kessler, "Minimizing metastabilities in Cu(In,Ga)Se_2/(CBD)Zn(S,O,OH)/i-ZnO-based solar cells", Progress in Photovoltaics: Research and Applications **23**, 462–469 (2015) (Cited on pages 63, 64, 67, 81).

[98] A. Zunger, "Practical doping principles", Applied Physics Letters **83**, 57–59 (2003) (Cited on page 64).

[99] P. Prathap, N. Revathi, Y. Subbaiah, K. R. Reddy, and R. Miles, "Preparation and characterization of transparent conducting ZnS:Al films", Solid State Sciences **11**, 224–232 (2009) (Cited on page 64).

[100] D. E. Ortíz-Ramos, L. A. González, and R. Ramirez-Bon, "p-Type transparent Cu doped ZnS thin films by the chemical bath deposition method", Materials Letters **124**, 267–270 (2014) (Cited on page 64).

[101] J.-H. Lee, W.-C. Song, J.-S. Yi, and Y.-S. Yoo, "Characteristics of the CdZnS thin film doped by thermal diffusion of vacuum evaporated indium films", Solar Energy Materials and Solar Cells **75**, 227–234 (2003) (Cited on page 64).

[102] H. Khallaf, G. Chai, O. Lupan, L. Chow, S. Park, and A. Schulte, "Investigation of aluminium and indium in situ doping of chemical bath deposited cds thin films", Journal of Physics D: Applied Physics **41**, 185304 (2008) (Cited on pages 64, 106).

[103] S. A. Al Kuhaimi and Z. Tulbah, "Structural, Compositional, Optical, and Electrical Properties of Solution-Grown $Zn_xCd_{1-x}S$ Films", Journal of The Electrochemical Society **147**, 214–218 (2000) (Cited on pages 64, 105).

[104] H. Khallaf, G. Chai, O. Lupan, L. Chow, H. Heinrich, S. Park, and A. Schulte, "In-situ boron doping of chemical-bath deposited CdS thin films", physica status solidi (a) **206**, 256–262 (2009) (Cited on page 64).

[105] G. Sozzi, F. Troni, and R. Menozzi, "On the combined effects of window/buffer and buffer/absorber conduction-band offsets, buffer thickness and doping on thin-film solar cell performance", Solar Energy Materials and Solar Cells **121**, 126–136 (2014) (Cited on page 64).

[106] K. Ellmer, A. Klein, and B. Rech, *Transparent Conductive Zinc Oxide*, (Springer Berlin Heidelberg, 2008), ISBN: 978-3-540-73612-7 (Cited on page 81).

[107] T. Minemoto, Y. Hashimoto, T. Satoh, T. Negami, H. Takakura, and Y. Hamakawa, "Cu(In,Ga)Se_2 solar cells with controlled conduction band offset of window/Cu(In,Ga)Se_2 layers", Journal of Applied Physics **89**, 8327–8330 (2001) (Cited on page 85).

[108] J. Palm, S. Jost, R. Hock, and V. Probst, "Raman spectroscopy for quality control and process optimization of chalcopyrite thin films and devices", Thin Solid Films **515**, 5913–5916 (2007) (Cited on page 90).

[109] R. Menner, B. Dimmler, R. Mauch, and H. Schock, "II–VI compound thin films for windows in heterojunction solar cells", Journal of Crystal Growth **86**, 906–911 (1988) (Cited on page 105).

[110] N. Naghavi, C. Hubert, A. Etcheberry, V. Bermudez, D. Hariskos, M. Powalla, and D. Lincot, "Compositional engineering of chemical bath deposited (Zn,Cd)S buffer layers for electrodeposited CuIn(S,Se)$_2$ and coevaporated Cu(In,Ga)Se$_2$ solar cells", Progress in Photovoltaics: Research and Applications **17**, 1–9 (2009) (Cited on page 105).

[111] R. Boorman and J. Sutherland, "Subsolidus phase relations in the ZnS-In$_2$S$_3$ system: 600 to 1080°C", Journal of Materials Science **4**, 658–671 (1969) (Cited on page 106).

[112] Y. Chen, S. Hu, W. Liu, X. Chen, L. Wu, X. Wang, P. Liu, and Z. Li, "Controlled syntheses of cubic and hexagonal ZnIn$_2$S$_4$ nanostructures with different visible-light photocatalytic performance", Dalton Transactions **40**, 2607–2613 (2011) (Cited on page 106).

[113] S. Peng, L. Li, Y. Wu, L. Jia, L. Tian, M. Srinivasan, S. Ramakrishna, Q. Yan, and S. G. Mhaisalkar, "Size-and shape-controlled synthesis of ZnIn$_2$S$_4$ nanocrystals with high photocatalytic performance", CrystEngComm **15**, 1922–1930 (2013) (Cited on page 106).

[114] K.-W. Cheng and C.-J. Liang, "Preparation of Zn–In–S film electrodes using chemical bath deposition for photoelectrochemical applications", Solar Energy Materials and Solar Cells **94**, 1137–1145 (2010) (Cited on page 106).

[115] R. Bayon, J. Herrero, and J. Klaer, "Optical Properties of CBD-InZn$_x$(OH, S) Buffer Thin Films for Photovoltaic Applications", in 16th European Photovoltaic Solar Energy Conference (May 2000) (Cited on page 106).

[116] K. Govender, D. S. Boyle, and P. O'Brien, "Developing cadmium-free window layers for solar cell applications: some factors controlling the growth and morphology of β-indium sulfide thin films and related (In,Zn)S ternaries", Journal of Materials Chemistry **13**, 2242–2247 (2003) (Cited on page 106).

[117] B. Asenjo, A. Chaparro, M. Gutiérrez, J. Herrero, and J. Klaer, "Study of CuInS$_2$/buffer/ZnO solar cells, with chemically deposited ZnS-In$_2$S$_3$ buffer layers", Thin Solid Films **515**, 6036–6040 (2007) (Cited on page 106).

[118] D. Hariskos, M. Ruckh, U. Rühle, T. Walter, H. W. Schock, J. Hedström, and L. Stolt, "A novel cadmium free buffer layer for Cu(In,Ga)Se$_2$ based solar cells", Solar Energy Materials and Solar Cells **41–42**, 345–353 (1996) (Cited on page 106).

[119] Y. Tokita, S. Chaisitsak, A. Yamada, and M. Konagai, "High-efficiency Cu(In,Ga)Se$_2$ thin-film solar cells with a novel In(OH)$_3$:Zn^{2+} buffer layer", Solar Energy Materials and Solar Cells **75**, 9–15 (2003) (Cited on page 106).

[120] Y. Hashimoto, T. Satoh, and T. Negami, "COMPOUND SEMICONDUCTOR FILM, SOLAR CELL, AND METHODS FOR PRODUCING THOSE", EP 1 662 580 A1 (2005) (Cited on page 106).

[121] C. Vanleugenhaghe and M. Pourbaix, "Indium", in *Atlas of electrochemical equilibria in aqueous solutions*, Translated from the French by James A. Franklin, (Pergamon Press, 1966), ISBN: 978-0-08-010985-5 Chap. 16.2, pp. 436–442 (Cited on page 106).

[122] M. Asabe, P. Chate, S. Delekar, K. Garadkar, I. Mulla, and P. Hankare, "Synthesis, characterization of chemically deposited indium selenide thin films at room temperature", Journal of Physics and Chemistry of Solids **69**, 249–254 (2008) (Cited on page 106).

[123] A. V. Naumkin, A. Kraut-Vass, S. W. Gaarenstroom, and C. J. Powell, *NIST X-ray Photoelectron Spectroscopy Database*, http://srdata.nist.gov/xps/ (visited on 10/14/2015) (Cited on page 114).

[124] M. Turcu, I. M. Kötschau, and U. Rau, "Composition dependence of defect energies and band alignments in the Cu($In_{1-x}Ga_x$)($Se_{1-y}S_y$) alloy system", Journal of Applied Physics **91**, 1391–1399 (2002) (Cited on pages 122, 124).

[125] T. Schulmeyer, "Mechanismen der Grenzflächenausbildung des Cu(In,Ga)Se_2-Systems", PhD thesis (Technische Universität Darmstadt, Apr. 2005) (Cited on page 122).

[126] D. Schmid, M. Ruckh, F. Grunwald, and H. W. Schock, "Chalcopyrite/defect chalcopyrite heterojunctions on the basis of $CuInSe_2$", Journal of Applied Physics **73**, 2902–2909 (1993) (Cited on page 122).

[127] Python Software Foundation, *Python Language Reference, version 3.3*, https://www.python.org/downloads/ (Cited on page 149).

[128] J. D. Hunter, "Matplotlib: A 2D graphics environment", Computing In Science & Engineering **9**, 90–95 (2007) (Cited on page 151).

[129] The Inkscape Team, *Inkscape, version 0.48*, https://inkscape.org/ (Cited on page 152).

Acknowledgments

The final chapter of this thesis is dedicated to those who made my work possible. I want to explicitly thank Prof. Susanne Siebentritt for accepting me as her far-away PhD student, for continuous support with finding the right direction and asking the right questions, and for her high tolerance towards the special circumstances associated with a dissertation work in the industry. The same debt of gratitude is owed to Jürgen Hackenberg and Siegmund Zweigart, who were great tutors to me at the Robert Bosch GmbH and supported me with a framework of knowledge I could build on and with reliable financial means. Without Jürgen's guidance in chemistry I would never have succeeded. I also want to thank the members of my Dissertation Supervisory Committee, Prof. Hans-Werner Schock and Prof. Ludger Wirtz, who regularly supported me with valuable input on the progress and direction of my work. My colleagues Rolf Keller, Vemulamada Pardhasaradhi, and Günter Wiltschko were of invaluable help with the different processes, developed and employed in this work, while Lutz Dorfmüller and Frank Schnell earned my thanks by helping me out, when I had problems with my measurement equipment. I am grateful for the XPS measurements, conducted by Anne Fuchs, and the following discussions about the band alignment with her, many thanks also to Prof. Andreas Klein for the right pointers within this topic. I also want to thank my fellow PhD students Björn Müller, Ulrich Berner, and Rou Hua Chua for the regular discussion sessions. Along the same lines, many thanks to my colleagues at the Bosch CISTech GmbH, especially to Frank Hergert, André Wachau, Frederik Stober, and Manuela Grosskinsky, providing me not only with CIGSSe absorber material and the occasional measurement but also with almost weekly discussions on buffer layer related topics during the larger part of my time as PhD student. I am sad, that it looks like CISTech will cease to operate, and my best wishes for the future are with all those who are involved.
Additionally, I want to thank Stephanie Spiering and Andreas Nowitzky, who were responsible for the process of finishing and measuring many batches of cells for me at the ZSW (~25000 commissioned IV curves).
Financial support by the German Federal Ministry of Education and Research is gratefully acknowledged here. Part of this work was conducted within the publicly funded NeuMas project (Grant No. 13N11767), and I want to thank all participants for the helpful discussions about Cd-free buffer layers.
Thanks also to Robert Schittny, who provided me with a very mature LaTeX template, and who gave me the idea to make most of the graphs in this work with the help of python/matplotlib. Finally, I am very grateful to Kristina for sustaining me morally in the last three years and to Anja and Lars, who gave me a reason to work on solar cells, and sometimes a reason not to.